



Farrell, Andrew J. (2022) *Ultrafast molecular dynamics in amorphous media. A spectroscopic study of molecular motions, vitreous vibrations, and saline structure*. PhD thesis.

<http://theses.gla.ac.uk/82776/>

Copyright and moral rights for this work are retained by the author

A copy can be downloaded for personal non-commercial research or study, without prior permission or charge

This work cannot be reproduced or quoted extensively from without first obtaining permission in writing from the author

The content must not be changed in any way or sold commercially in any format or medium without the formal permission of the author

When referring to this work, full bibliographic details including the author, title, awarding institution and date of the thesis must be given

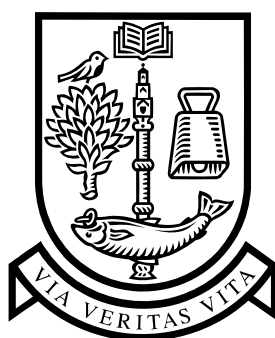
Enlighten: Theses

<https://theses.gla.ac.uk/>
research-enlighten@glasgow.ac.uk

ULTRAFAST MOLECULAR DYNAMICS IN AMORPHOUS MEDIA

A Spectroscopic Study of Molecular Motions, Vitreous Vibrations, and Saline
Structure

Thesis submitted for the degree of
Doctor of Philosophy
at the University of Glasgow



By
Andrew J. Farrell
College of Science & Engineering
University of Glasgow

March 2022

ABSTRACT

This thesis presents three studies conducted over the course of 3 years within the chemical photonics research group of the University of Glasgow.

Molecular dynamics and structure are intertwined; one can infer the microscopic structure by the molecular dynamics and *vice versa*. This thesis is primarily a spectroscopic study of carefully chosen inter- and intra-molecular vibrations in condensed phase media that are highly sensitive to microscopic structure and closely linked to their thermodynamic properties. The two major techniques used throughout are optical Kerr-effect spectroscopy, and Fourier transform infrared spectroscopy.

Optical Kerr-effect spectroscopy (OKE), to pick one of the technique's many names, has been a mainstay in the study of intermolecular interactions for many decades. Despite this there is no standard approach to the interpretation of OKE spectra. The research within this thesis seeks to address this issue by converging upon a general blueprint for OKE line-shape interpretation through robust experimentation and iterative line-shape fitting attempts. As is the case within most OKE studies, the line-shape fitting procedure used throughout is self-consistent. What makes this work worthwhile and useful to the field is the apparent robustness of the final fitting procedure across a very broad range of experimental data. This includes alterations in firstly the molecular size of alkanes and cycloalkanes, secondly the temperature of liquid propane, and finally molecular anisotropy through studying liquid methane and six-carbon ring molecules from cyclohexane to benzene—5 sets of experiments; 24 OKE spectra in total. Though not perfect, the method employed provides (at the *very least*) a justified starting point for the interpretation of more complex liquids. Indeed, this analytical framework guides subsequent work here.

One of the most notorious THz spectral anomalies is the so-called 'boson peak'. It has been reported in Raman and neutron scattering spectra for wide range of amorphous condensed phases, manifesting as an excess in the vibrational density of states, typically occurring in the 1 THz region. Little is known of the nature of this vibrational mode other than the fact that it has a transverse character. The boson peak is very difficult to spot due to sharing its characteristic frequency with various other oscillatory dynamics, esp. librations.

This thesis aims to observe an entirely isolated boson peak through the selection of near-isotropically polarisable glass-forming molecular liquids with vastly simplified intermolecular spectra. With librations rendered OKE-invisible, the remaining sub-THz dynamics result from intermolecular collisions, *i.e.*, washed-out phonon-like modes. This work will compare and contrast the nature of these localised vibrations present within various glass-forming liquids with the behaviour expected of the boson peak. Results show that the remaining collision-induced band may be consistent with transverse acoustic vibrations, however there are additional low-frequency modes visible in some glass forming liquids whose origin is less clear and warrants further investigation. Furthermore, this highlights the importance of these two modes being distinguished from each other, as boson peaks have not always been assigned in a consistent manner.

Lastly, this thesis takes aim at the putative liquid-liquid transition in water. Its proposed existence is a product of an explanation of the peculiar thermodynamics of water. Frustratingly, such a liquid-liquid transition is believed to occur at an experimentally inaccessible region of the H₂O phase diagram, where ice nucleation will occur rapidly and spontaneously. This work utilises aqueous salt solutions that suppress the onset of crystallisation and enable the probing of amorphous solvent H₂O from ambient to cryogenic temperatures. H₂O structure and dynamics are studied using OKE and FTIR spectroscopies, while using various dopants to probe local electrostatic environments. Spectra of magnesium perchlorate and lithium chloride solutions are probed and analysed in this chapter, the latter of which is often touted as an experimental proxy for pure H₂O dynamics. Their spectra are far from dull, but exhibit temperature dependent phenomena that are explainable outwith the liquid-liquid transition concept. In concentrated lithium chloride solution, the evidence suggests the occurrence of nanophase segregation on cooling that is driven by reduced solubility. This results in an expulsion of solutes into a rich brine phase. Magnesium perchlorate solution at the eutectic composition meanwhile appears to only vitrify on cooling, suggesting that this solution may only be analogous to pure water at pressures too high to access the liquid-liquid transition.

CONTENTS

ABSTRACT	II
LIST OF FIGURES	VI
LIST OF TABLES	X
ACKNOWLEDGEMENTS	XI
AUTHOR'S DECLARATION	XII
ABBREVIATIONS	XIII
I INTRODUCTION	I
1.1 OVERVIEW	1
1.2 INTERPARTICLE FORCES	3
1.3 INTRAMOLECULAR DYNAMICS	4
1.4 SOLID-STATE DYNAMICS	6
1.5 LIQUID DYNAMICS AND TRANSITIONS	9
1.6 LASERS AND OPTICS	12
1.7 FOURIER-TRANSFORM INFRARED SPECTROSCOPY	17
1.8 OPTICAL KERR-EFFECT SPECTROSCOPY	21
1.9 COMPUTATIONAL CHEMISTRY	26
2 EXPERIMENTAL.....	28
2.1 OKE SET-UP	28
2.2 FTIR SET-UP	32
2.3 SAMPLE PREPARATION	32
3 DATA ANALYSIS.....	34
3.1 OKE SIGNAL PROCESSING.....	34
3.2 SPECTRAL LINE-SHAPES	36
4 LIQUID HYDROCARBON DYNAMICS.....	42
4.1 INTRODUCTION	42
4.2 EXPERIMENTAL.....	44
4.3 MODELLING OF THERMODYNAMIC PROPERTIES	45
4.4 CALCULATION OF MOLECULAR POLARISABILITIES	48
4.5 N-ALKANES	49

4.6	METHANE	58
4.7	PROPANE.....	59
4.8	CYCLOALKANES	63
4.9	6-MEMBERED RINGS	67
4.10	DISCUSSION & CONCLUSION	70
5	THE BOSON PEAK.....	73
5.1	INTRODUCTION	73
5.2	METHODS	76
5.3	THE HIDDEN BOSON PEAK IN TOLUENE	80
5.4	TITANIUM ALKOXIDES.....	85
5.5	TETRABUTYL ORTHOSILICATE	91
5.6	CONCLUSION AND FURTHER WORK.....	93
6	THE LIQUID-LIQUID TRANSITION IN WATER.....	95
6.1	INTRODUCTION	95
6.2	EXPERIMENTAL.....	98
6.3	NEAT WATER	99
6.4	HYDRAZINIUM TRIFLUOROACETATE SOLUTION.....	101
6.5	AQUEOUS SOLUTIONS OF SYMMETRIC IONS	104
6.6	THIOCYANATE-PROBED LITHIUM CHLORIDE SOLUTIONS.....	110
6.7	CONCLUSION & FURTHER WORK.....	114
7	CONCLUSION.....	116
8	REFERENCES.....	119
9	APPENDICES.....	134
A.	PHONONS IN A 1-DIMENSIONAL CHAIN.....	134
B.	HYDROCARBON MOLARITIES	135
C.	HYDROCARBON OKE SPECTRA LINE-SHAPE FITTING PARAMETERS	136
D.	HAVRILIAK-NEGAMI LINE-SHAPE PROPORTIONALITIES.....	138
E.	TOLUENE SUPPLEMENTARY DATA.....	139
F.	TiBUO SUPPLEMENTARY DATA	140
G.	OKE LINE-SHAPE FITTING PARAMETERS FOR TITANIUM TETRABUTOXIDE, TETRAETHOXIDE, AND THEIR 1:1 MIXTURE.	142
H.	TBOS SUPPLEMENTARY DATA.....	143
I.	DOPED LITHIUM CHLORIDE SOLUTIONS	145

LIST OF FIGURES

FIGURE 1.1. LONGITUDINAL AND TRANSVERSE ACOUSTIC PHONONS.	6
FIGURE 1.2. THE DISPERSION RELATION FOR LATTICE PHONONS.....	7
FIGURE 1.3. THE VIBRATIONAL DENSITY OF STATES.....	8
FIGURE 1.4. CRYSTALLISATION AND VITRIFICATION UPON COOLING A LIQUID.	10
FIGURE 1.5. A BINARY PHASE DIAGRAM.	12
FIGURE 1.6. ILLUSTRATION OF A CLASSIC 4-LEVEL LASER SYSTEM.....	13
FIGURE 1.7. A BASIC LASER CAVITY.....	14
FIGURE 1.8. LASER CAVITY MODES.	14
FIGURE 1.9. CHIRPED LASER PULSES.....	15
FIGURE 1.10. QUARTER WAVEPLATE ILLUSTRATED.....	17
FIGURE 1.11. VIBRATIONAL ENERGY LEVELS IN AN ANHARMONIC POTENTIAL.	18
FIGURE 1.12. A MICHELSON INTERFEROMETER.....	19
FIGURE 1.13. EXAMPLE INTERFEROGRAM.	20
FIGURE 1.14. JABLONSKI DIAGRAM OF RAMAN SCATTERING.	21
FIGURE 1.15. POLARISABILITY SHOWN BY AN ELECTRIC FIELD INDUCED DIPOLE.	22
FIGURE 1.16. CARTOON OF THE OPTICAL KERR-EFFECT.	24
FIGURE 1.17. JABLONSKI DIAGRAM OF OKE SPECTROSCOPY.	26
FIGURE 2.1. SCHEMATIC OF THE OKE EXPERIMENTAL SET-UP.	28
FIGURE 2.2. MODULATION OF PUMP AND PROBE SIGNALS, WITH 'LOCK-IN' AT THE DIFFERENCE FREQUENCY.	31
FIGURE 2.3. SCHEMATIC OF THE FTIR SPECTROMETER.....	32
FIGURE 3.1. TIME-DOMAIN OKE DATA FITTING OF THE ELECTRONIC RESPONSE AND THE SIGNAL DECAY.	35
FIGURE 3.2. RESULTANT FREQUENCY DOMAIN SPECTRUM AFTER FOURIER-TRANSFORM DECONVOLUTION.....	35
FIGURE 3.3. THE COLE-COLE AND DEBYE LINE-SHAPES, AND THEIR 'INERTIAL' VARIATIONS.	38
FIGURE 3.4. THE BROWNIAN OSCILLATOR LINE-SHAPE.....	39
FIGURE 3.5. THE ANTI-SYMMETRISED GAUSSIAN LINE-SHAPE.	40
FIGURE 3.6. THE BUCARO-LITOVITZ LINE-SHAPE.....	41

FIGURE 4.1. GENERIC FORM OF THE INTERMOLECULAR VIBRATIONAL SPECTRUM OF A WEAKLY INTERACTING LIQUID.	43
FIGURE 4.2. TRENDS IN HYDROCARBON MOLARITIES AT 25°C.	45
FIGURE 4.3. VISCOSITY TRENDS IN <i>N</i> -ALKANES AND CYCLOALKANES, AND WITH TEMPERATURE IN PROPANE.	46
FIGURE 4.4. SLIP TO STICK FRICTION FACTOR RATIOS AS A FUNCTION OF ASPECT RATIO.	47
FIGURE 4.5. MOLECULAR ANISOTROPIC POLARISABILITY TRENDS IN VARIOUS HYDROCARBONS.	49
FIGURE 4.6. OKE SPECTRA OF VARIOUS <i>N</i> -ALKANES AT 25°C.	50
FIGURE 4.7. LINE-SHAPE FITTING OF <i>N</i> -ALKANE OKE SPECTRA AT 25°C.	50
FIGURE 4.8. SED FOR SLIP AND STICK CONDITIONS WITH EXPERIMENTAL <i>N</i> -ALKANE <i>A</i> -RELAXATION LIFETIMES.	51
FIGURE 4.9. FITTING PARAMETER TRENDS IN <i>N</i> -ALKANE OKE SPECTRA <i>VS</i> CHAIN LENGTH. ..	52
FIGURE 4.10. CARTOON OF THE TIME-AVERAGED INTERMOLECULAR POTENTIAL LANDSCAPE.	54
FIGURE 4.11. CARTOON OF THE RADIAL DISPLACEMENT OF THE LIBRATION OF A SIMPLE CHAIN MOLECULE.	56
FIGURE 4.12. OKE SPECTRUM OF LIQUID METHANE AT 95K WITH VARIOUS FITS.	58
FIGURE 4.13. OKE SPECTRA OF LIQUID PROPANE AT VARIOUS TEMPERATURES.	60
FIGURE 4.14. LINE-SHAPE FITTING OF LIQUID PROPANE OKE SPECTRA AT VARIOUS TEMPERATURES.	61
FIGURE 4.15. FITTING PARAMETER TRENDS IN LIQUID PROPANE OKE SPECTRA WITH TEMPERATURE.	62
FIGURE 4.16. OKE SPECTRA OF VARIOUS CYCLOALKANES AT 25°C.	64
FIGURE 4.17. LINE-SHAPE FITTING OF CYCLOALKANE OKE SPECTRA.	65
FIGURE 4.18. FITTING PARAMETER TRENDS IN CYCLOALKANE OKE SPECTRA WITH RING SIZE.	66
FIGURE 4.19. OKE SPECTRA OF VARIOUS 6-MEMBERED RINGS AT 25°C.	68
FIGURE 4.20. LINE-SHAPE FITTING OF 6-MEMBERED RING OKE SPECTRA WITH FIT PARAMETER TRENDS.	68
FIGURE 5.1. ILLUSTRATION OF THE BOSON PEAK IN THE VDOS.	74
FIGURE 5.2. IN A SUPERCOOLED LIQUID, LOCALLY FAVOURED STRUCTURES FORM IN A SEA OF THE NORMAL LIQUID.	76
FIGURE 5.3. MOLAR HEAT CAPACITIES OF STABLE AND METASTABLE SEQUENCES OF TOLUENE.	80

FIGURE 5.4. TEMPERATURE DEPENDENT TERAHERTZ SPECTRA OF TOLUENE.	81
FIGURE 5.5. OKE SPECTRA OF TOLUENE AT VARIOUS TEMPERATURES, AND THEIR LINE-SHAPE FITS.	83
FIGURE 5.6. FITTING PARAMETERS FOR THE LINE-SHAPE FITS OF TOLUENE AT VARIOUS TEMPERATURES.	84
FIGURE 5.7. TITANIUM ALKOXIDES INVESTIGATED.	85
FIGURE 5.8. MEASURING THE GLASS TRANSITION TEMPERATURE OF TiBuO.	86
FIGURE 5.9. OKE SPECTRA OF TITANIUM BUTOXIDE AT VARIOUS TEMPERATURES.	86
FIGURE 5.10. OKE SPECTRA OF LIQUID AND VITREOUS TITANIUM 2-ETHYLHEXYLOXIDE.	87
FIGURE 5.11. OKE SPECTRA OF TITANIUM BUTOXIDE AND ETHOXIDE AND THEIR 50:50 VOL% MIXTURE AT 20 °C.	88
FIGURE 5.12. LINE-SHAPE FITS TO THE TEMPERATURE DEPENDENT OKE SPECTRA OF TITANIUM BUTOXIDE.	89
FIGURE 5.13. TRENDS IN LINE-SHAPE FITTING PARAMETERS OF TiBuO.	90
FIGURE 5.14. OKE SPECTRA OF TETRABUTYL ORTHOSILICATE AT VARIOUS TEMPERATURES. ...	91
FIGURE 5.15. LINE-SHAPE FITS FOR TBOS OKE SPECTRA AT VARIOUS TEMPERATURES.	92
FIGURE 5.16. LINE-SHAPE AMPLITUDES AND FREQUENCIES FOR TBOS AT VARIOUS TEMPERATURES.	93
FIGURE 6.1. ILLUSTRATIVE PHASE DIAGRAM OF H ₂ O.	96
FIGURE 6.2. IR SPECTRUM OF PURE H ₂ O AT ROOM TEMPERATURE.	100
FIGURE 6.3. OD STRETCH TRANSITION IN WATER AND ICE.	100
FIGURE 6.4. IR SPECTRA OF THE OD STRETCH IN CONCENTRATED HTFA _(AQ) UPON COOLING.	101
FIGURE 6.5. IR SPECTRA OF THE OD STRETCH IN CONCENTRATED HTFA _(AQ) UPON HEATING.	102
FIGURE 6.6. OKE SPECTRA OF HTFA _(AQ) SOLUTION AT VARIOUS TEMPERATURES.	103
FIGURE 6.7. FTIR SPECTRA OF THE OH STRETCH IN Mg(CLO ₄) _{2(AQ)} ON COOLING.	106
FIGURE 6.8. TEMPERATURE DEPENDENT OH STRETCH MODE ABSORBANCE AT 3330 CM ⁻¹ IN Mg(CLO ₄) ₂ SOLUTION COOLED AT A CONSTANT RATE.	107
FIGURE 6.9. FTIR SPECTRA OF THE OH STRETCH IN Mg(CLO ₄) _{2(AQ)} ON REHEATING.	108
FIGURE 6.10. TEMPERATURE DEPENDENT OH STRETCH MODE ABSORBANCE AT 3330 CM ⁻¹ IN Mg(CLO ₄) ₂ SOLUTION WHEN REHEATED AT A CONSTANT RATE.	108
FIGURE 6.11. OKE SPECTRA OF Mg(CLO ₄) ₂ SOLUTION BETWEEN 280 AND 120 K.	109
FIGURE 6.12. IR SPECTRA OF EUTECTIC LiCl-SCN:7H ₂ O DOPED WITH D ₂ O AT VARIOUS TEMPERATURES.	111

FIGURE 6.13. TEMPERATURE-DEPENDENT FTIR SPECTRA OF DOPED AND UNDOPED LiCl:9H ₂ O.....	112
FIGURE 6.14. FITTING PARAMETER TRENDS FOR THE T-DEPENDENT LiCl-SCN:7H ₂ O IR- SPECTRA.....	113

LIST OF TABLES

TABLE 1.1. EXAMPLES OF VARIOUS NORMAL MODES IN <i>N</i> -ALKANES.....	5
TABLE 2.1. LASER PULSE POLARISATIONS THROUGHOUT THE OKE SET-UP.	29
TABLE 4.1. CALCULATED POLARISABILITY ELEMENTS OF VARIOUS HYDROCARBONS.....	48
TABLE 4.2. FITTING PARAMETER VALUES FOR VARIOUS FITS OF THE METHANE OKE SPECTRUM.	59
TABLE 6.1. VARIOUS SALTS DISSOLVED IN WATER.....	104

ACKNOWLEDGMENTS

I would firstly like to thank my supervisor Prof. Klaas Wynne for his support, guidance, and enthusiasm throughout my postgraduate studies. I feel fortunate to have such knowledgeable supervisor with which to explore the research topics herein. Additionally your cheerful nature and good sense of humour made being a member of the ultrafast chemical physics group a pleasure.

I would next like to thank Dr. Mario González-Jiménez, undoubtedly my unofficial second supervisor. You went above and beyond to assist me with his expertise in all matters chemistry, OKE, and *especially* programming. Your selfless efforts certainly streamlined my research, and for that I am very grateful.

Thank you to Gopa, Finlay, Judith, John, and later Zhiyu and Ben of the UCP group—and former member Chris. It has been a great pleasure working with you all. Thank you also to Nicola and Sarah with whom I thoroughly enjoyed working alongside.

I'd like to also thank my family who are always there for me, and my friends who help me unwind. I feel lucky to have such supportive people in my life.

Finally, a special thank you to my wife who has supported me throughout my entire undergraduate degree and now PhD, while completing her own degrees. With our university studies finally coming to an end, I can't wait to have more time to spend with you.

AUTHOR'S DECLARATION

"I declare that, except where explicit reference is made to the contribution of others, this dissertation is the results of my own work and has not been submitted for any other degree at the University of Glasgow or any other institution."

Name: Andrew John Farrell

Signature:

Chapter 4 was reproduced in part with permission from:

Farrell, A. J.; González-Jiménez, M.; Ramakrishnan, G.; Wynne, K. J. *Phys. Chem. B* 2020, 124 (35), 7611–7624.

© 2020 American Chemical Society.

The data of chapter 5 is available online ([chemrxiv](#)) as a pre-print.

Parts of chapter 6 were reproduced in part with permission from:

Lane, P. D.; Reichenbach, J.; Farrell, A. J.; Ramakers, L. A. I.; Adamczyk, K.; Hunt, N. T.; Wynne, K. *Phys. Chem. Chem. Phys.* 2020, 22 (17), 9438–9447.

© 2020 Royal Society of Chemistry.

ABBREVIATIONS

ASG	anti-symmetrised Gaussian
BE	Bose-Einstein
BL	Bucaro-Litovitz
BO	Brownian oscillator
BP	boson peak
BZ	Brillouin zone
CC	Cole-Cole
CI	collision-induced
CIP	contact ion pair
DFT	density functional theory
DHO	damped harmonic oscillator
EM	electromagnetic
FDS	frequency domain spectrum/spectra
FT	Fourier transform
FTIR	Fourier transform infrared
FWHM	full width at half maximum
HDA	high density amorphous
HDL	high density liquid
HN	Havriliak-Negami
iCC	inertial Cole-Cole
iD	inertial Debye
iHN	inertial Havriliak-Negami
IR	infrared
KWW	Kohlrausch-Williams-Watts
LA	longitudinal acoustic
LDA	low density amorphous
LDL	low density liquid
LFS	locally favoured structures
LLT	liquid-to-liquid transition
MD	molecular dynamics

OKE	optical Kerr-effect
OPD	optical path difference
PE	polyethylene
PTFE	polytetrafluoroethylene
SE	Stokes-Einstein
SED	Stokes-Einstein-Debye
TA	transverse acoustic
TBOS	tetrabutyl orthosilicate
TDT	time domain trace
TEOS	tetraethyl orthosilicate
TFA	trifluoroacetate
VDoS	vibrational density of states
vdW	van der Waals
VFT	Vogel-Fulcher-Tammann
VHDA	very high density amorphous

I INTRODUCTION

I.1 Overview

Intermolecular interactions facilitate energy transfer and are crucial in driving chemical reactions in the condensed phase, making the investigation of the nature of these interactions key to our understanding of chemical reactivity.^{1,2} The dynamics of matter depends strongly on the state of the matter, such as solid, liquid, or gas (ignoring the more exotic ones), owing to their vastly different structures and interparticle interactions. Solid state matter is effectively locked in place by strong interparticle forces. In the case of crystals—the lowest energy solids—dynamics are strongly coupled throughout the entire crystal lattice. If supplied with sufficient heat, and therefore kinetic energy, such particles can break free from their interparticle cage and diffuse throughout the material; the result is a condensed phase that doesn't exhibit long range structural order, *i.e.*, a liquid. Particles in the liquid phase are still restricted by, and coupled to, their immediate neighbours to varying degrees, however. Ultimately with enough kinetic energy these particles escape the electrostatic clutches of their neighbours and evaporate, where they can freely explore and occupy the entirety of their container volume, while exhibiting simplified interparticle interactions consisting largely of elastic collisions.

Dynamics and structure within the amorphous (disordered) condensed phases are arguably the most complex. They can exhibit shorter-range, transient structures vestigial of the corresponding crystal, resulting in similar collective motions but on more localised scale and with greater damping. Simultaneously, the constituent molecules (or atoms, ions, *etc.*) are afforded enough freedom to showcase their own quirks, which can result in some very complex dynamics indeed. For example, take the liquid *n*-alkanes (studied in chapter 4). One might initially rank these as some of the *least* complex liquids, but as one considers longer-chained alkanes, the individual molecules begin to crumple into diverse conformations, each of which with their own normal intramolecular vibrational modes, centre of mass, diffusion rate, *etc.* For *n*-alkanes with odd carbon numbers from 11 upwards, the long chains can arrange themselves with crystal-like order, yet retain the ability to rotate about its major molecular axis—this is known as a “rotator phase”.³ Even methane can exhibit a similar

effect, where 1 in 4 molecules can freely rotate.⁴ Going to longer molecules such as polymers, these long-chain molecules are highly entangled, and (in the liquid phase) they diffuse primarily by “reptation”, a name derived in analogy to snakes slithering past one another.⁵ Upon cooling they will undergo a glass transition and effectively have their liquid disorder frozen-in.

Furthermore, otherwise identical molecules can behave differently if their local electrostatic environment is not identical. Take for example a single water molecule surrounded by its identical peers (this central H₂O may be considered as bulk-like). At any given moment it may be hydrogen bonded to typically anywhere between 0 and 4 other H₂O molecules. This can affect its *intra*-molecular dynamics; the O-H stretching vibration is known to be highly sensitive to the local structure (as will become evident in chapter 6). Next compare bulk water to a water molecule bound to a solute, which can be slowed down by order of magnitude or more—factors of 8 and 5 slowdowns are observed in the case of haemoglobin for the rotational correlation time and translational diffusion coefficient respectively.⁶ Diffusive relaxation motions of H₂O measured using optical-Kerr effect spectroscopy and dynamic light scattering are found to slow down 7-fold in lysozyme-bound H₂O,⁷ 17-fold for DNA-bound H₂O,⁸ and 50-fold within a 1 M trimethylamine N-oxide solution.⁹

Of course, it is not only polymers that undergo a glass transition instead of crystallising. Molecular dynamics occur on an extremely broad range of timescales, depending on the molecule and dynamics in question. Molecules in highly viscous liquids diffuse relatively slowly; once diffusion timescales reach 100 s, the material is conventionally considered a glass. Glasses in general are not new materials by any stretch of the imagination; however, they still retain some mysterious thermodynamic properties. One of these is the apparent excess heat capacity over that of the corresponding crystal, originating from an additional underdamped intermolecular vibrational mode. This is known as the Boson peak (the focus of chapter 5), which is observed in some of the most simple and ubiquitous glasses, such as quartz.

In summary, molecular dynamics can be very complex even in relatively simple liquids and glasses. After presenting an introduction to the scientific principles and experimental techniques underpinning this thesis in chapters 1 to 3, the research of chapter 4 focusses on the development of a foundational interpretation of intermolecular dynamics. This is achieved through the study of a very broad range of molecular liquids that exhibit some of

the more basic dynamics. Next, this understanding is put to work to uncover more peculiar structural and dynamical phenomena in more specialised materials in chapters 5 and 6.

1.2 Interparticle Forces

There are various competing and compounding forces at play at the molecular level that govern the nature of inter- and intra-molecular interactions, and the resulting microscopic structure.

An important force to first consider is the Pauli repulsion force, which is the major repulsive force that prevents matter collapsing into a much smaller volume.^{10,11} This force is a result of the Pauli exclusion principle that states that no two fermions (particles with half-odd-integer values of spin) can simultaneously occupy the same quantum state. This is the strong repulsive force that dominates at short interatomic distances, r , which Lennard-Jones modelled using a simple r^{-12} dependence for computational speed.¹²

Molecules are collections of two or more atoms which are bound together by covalent bonds, which involve the sharing of valence electrons. The simplest case of head-on overlapping of atomic orbitals produces σ -bonds, the strongest type of covalent bond. There are also π -bonds in which atomic orbitals overlap laterally and are generally weaker than σ -bonds. Double/triple bonds consist of one σ -bond and one/two π -bonds. These covalent bonds can be understood in terms of simple Coulombic attraction between the positive nuclei and negative electrons. The sharing of multiple pairs of electrons produces progressively stronger atomic binding. These are some of the strongest bonds present within a system, with bond energies typically in excess of 200 kJ/mol; intermolecular forces for example tend to be one or two orders of magnitude weaker depending on their nature.

Intermolecular interactions are often grouped under the umbrella term of van der Waals (vdW) forces. These include various types of permanent and/or induced multipole-multipole interactions that can be classified into three types. Firstly, the Keesom interaction, which describes the attractive or repulsive force arising from the electrostatic interaction between permanent multipoles. Secondly, the Debye interaction, which is the attraction between a permanent and an induced multipole. Thirdly, the final vdW force is the London dispersion interaction, which describes the force of attraction between induced multipoles only. Finally, there is of course the repulsion or attraction between charges (depending on their relative polarities), which is the electrostatic or Coulombic interaction.

Hydrogen bonding is another interparticle force that is present in some materials. It is so named because the presence of covalently bonded hydrogen in a molecule, due to its relatively weak electronegativity, may give rise to charge separation and thus polarised molecules that can attract strongly. Specifically, a hydrogen bond is a directional, attractive, intermolecular force between a hydrogen atom in a molecule that, due to being covalently bonded with a strongly electronegative atom, has a slight positive charge, and a non-bonding electron pair on another strongly electronegative atom,¹³ *e.g.*, fluorine, oxygen, and nitrogen atoms. Hydrogen bonds can be either intermolecular (*e.g.*, H₂O-to-H₂O or between two nucleotides in DNA) or intramolecular (giving proteins their folded structure for example). Hydrogen-bonding groups within a molecule are hydrophilic—favouring interactions with H₂O (or any other polar molecules) over non-polar substances such as oil.

1.3 Intramolecular Dynamics

As mentioned previously, there are a wide variety of ways in which matter vibrates within a system. The atoms that make up a molecule are held in place by a combination of attractive and repulsive forces, but they are by no means static. Depending on the timescales of reference, the atoms within the molecule can be seen to oscillate about their natural equilibrium position. There are various well-defined modes through which they can do this, known as the normal modes. Idealised quadratic normal modes are orthogonal to each other, which is to say an excitation of one normal mode cannot couple to another, however this is not strictly true in practice. In principle, all intramolecular vibrations can be decomposed into some combination of these fundamental modes.

Because they are intramolecular, they involve the oscillations of atoms bound by covalent bonds, which are far stronger than intermolecular forces. This means that many of the normal mode vibrational frequencies are greater than those of the intermolecular interactions.

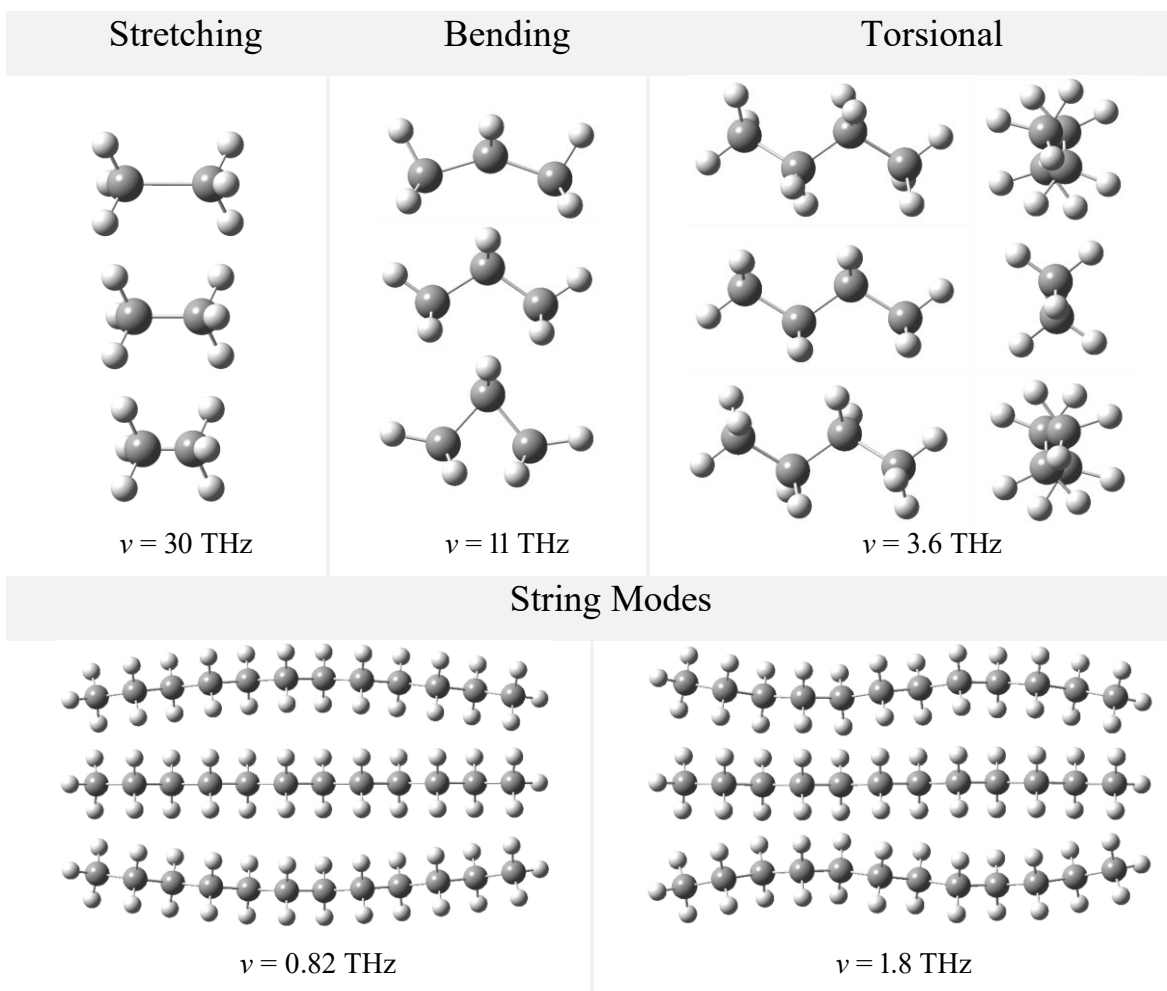


Table 1.1. Examples of various normal modes in *n*-alkanes.

Shown are types of normal modes that molecules may exhibit using the *n*-alkanes as an example, along with their frequencies calculated using Gaussian09 with 6-311++G(2df,p) level of theory. The central molecules represent the equilibrium position, while the top and bottom represent extrema. For simplicity each example shown here is with respect to the carbon atoms (or carbon-carbon bonds) in the chain. The torsional mode is shown with both side view and end-on view for clarity. The first string mode is the lowest (calculated) frequency normal mode of dodecane, while the next mode is the corresponding second harmonic.

A few examples of normal modes are shown in Table 1.1. Stretching vibrational modes tend to have some of the highest frequencies. This remains true even for highly delocalised stretches; for example, the dodecane whole molecule stretching mode has a frequency of 5.6 THz. This is greater than its whole molecule bending modes (the ‘string modes’, analogous to a guitar string) and torsional modes, although their higher-order harmonics will eventually exceed this. The bending modes involve bond angle oscillations, while torsional modes are due to twisting motions where the bond angles remain constant. These can often be of similar frequencies for the same molecule. Since intermolecular modes typically occur with frequencies ~ 1 THz and lower, some of these intramolecular modes will become washed out by solvent interaction.

1.4 Solid-State Dynamics

Crystals are solids which exhibit long-range structural order, that can be fully described in terms of a single repeating arrangement of matter (atoms/molecules/ions etc) that tiles across 3 dimensions—this tiling unit is known as the unit cell of the crystal. The dynamics of the crystal’s constituent particles on the other hand, cannot be fully understood with reference to the unit cell alone, but must instead be considered within the context of the entire crystal lattice. Because of the periodic structure of the crystal, certain internal nuclear motions can couple to their neighbouring nuclei and ultimately propagate throughout the entire solid with high fidelity.

Phonons are indistinguishable bosonic quasiparticles, and so by definition they obey Bose-Einstein (BE) statistics for the occupation of energy states (just as photons do). Since phonons are bosons (having integer values of spin), this means that they are not limited by the Pauli exclusion principle to occupy different quantum states from each other. Consequently, phonons are free to ‘condense’ into the ground state. Phonons propagate as the collective sum of individual oscillations of the lattice particles as either transverse or longitudinal waves as shown in Figure 1.1. The longitudinal waves are due to particles oscillating along the phonon axis, while in transverse waves they are perpendicular to the direction of phonon propagation.

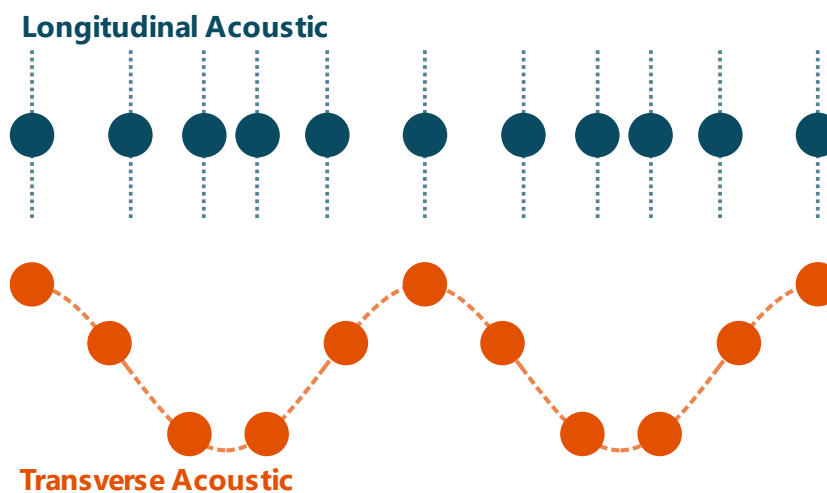


Figure 1.1. Longitudinal and transverse acoustic phonons.

Shown are LA and TA phonons of the same wavelength in 1D chains with the same (equilibrium) lattice spacing. The distinction between LA and TA is the direction in which the constituent particles oscillate with respect to the direction of phonon propagation.

Einstein attempted to explain the heat capacity of a crystal by treating each atom (or molecule, ion, *etc.*) as an independent oscillator in a harmonic potential well. In this picture, energy quanta are stored as vibrational excitations of the atom within the well. Predictions

from this model can show agreement with experimental heat capacity data at higher temperatures, however at low temperatures it breaks down. As $T \rightarrow 0$ K, the specific heat approaches zero with an exponential relationship due to the treatment of all phonons as quasiparticles of equal energy (and thus frequency). Debye showed that heat in crystals is better explained as being stored in the form of lattice phonons.¹⁴ These may propagate with different frequencies, depending on the phonon type and wavevector, as shown in Figure 1.2.

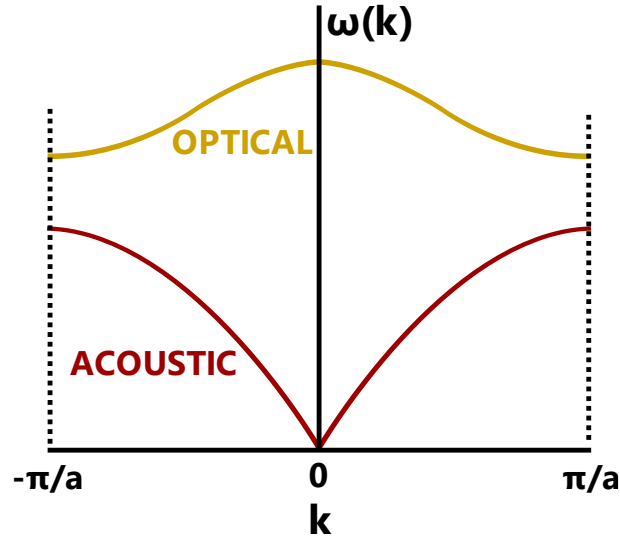


Figure 1.2. The dispersion relation for lattice phonons.

Different branches exist for different phonon types (acoustic vs optical) as shown, but these branches split for different wave types (transverse vs longitudinal) not shown here.

It should be mentioned here that there are two further categories of phonons, acoustic and optical. Optical phonons can occur only where the unit cell contains more than one atom (or molecule, ion, etc), that can move out of phase with respect to each other. Just like the acoustic modes, they can have transverse and longitudinal forms, however this work only encounters acoustic type modes in the liquid and glassy phases, and so the optical branch will not be explored in further depth. The phonon group velocity, v_g , is given by

$$v_g = \frac{\partial \omega}{\partial k} \quad (1.1)$$

where ω is the angular frequency and k is the wavevector.

As shown in Figure 1.3, the low frequency trend in the vibrational density of states (VDoS), $g(\omega)$, for the perfect Debye solid ($\propto \omega^2$) is in good agreement with that of a typical real crystal. Clearly at higher frequencies this agreement breaks down. The Debye frequency, ω_D , is the theoretical maximum achievable vibrational frequency for the lattice, governed by the interparticle spacing (see Appendix A.1 for illustrated explanation). The area under these $g(\omega)$ curves is the same, in other words, the total number of states is the

same. It can be shown (via lengthy derivation not reproduced here) that the phonon contribution to the heat capacity of a crystal produces a T^3 dependence at low temperature. This is the dominant contribution at low temperatures.

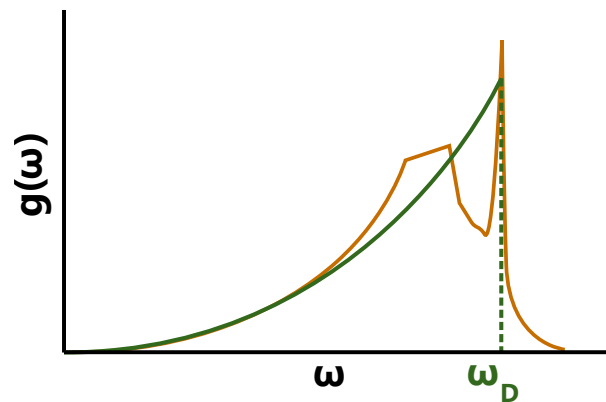


Figure 1.3. The vibrational density of states.

The VDoS, $g(\omega)$, for both the perfect Debye solid (green), where ω_D is the Debye frequency, and a typical real crystal (orange).

The ‘kinks’ in the real crystal VDoS occur when the group velocity ($d\omega/dk$) is zero. These points are also known as van Hove singularities.¹⁵ The group velocity of acoustic phonons approaches zero when k approaches $\pm\pi/a$. At these points there are many states with similar frequencies that are free to condense, producing sharp peaks in the VDoS.

Finally, one cannot ignore the fact that solids are not necessarily crystals. Plastics and glasses for example are solids that do not exhibit long range structural order. Despite their amorphism, *phonon-like* vibrational modes can persist to some extent, but with some degree of damping. Shorter wavelength modes can exist in some washed-out localised form since they involve collective oscillations of fewer neighbouring units, indeed at the Brillouin zone edge ($k = \pm\pi/a$) only the motions of the immediate neighbours are required for one full wavelength of motion. One example of this is the hydrogen-bond bend and stretch modes which are commonly observed in water. These can be traced back to the TA and LA phonon modes respectively of ice. Longer wavelength motions on the other hand are less sensitive to microscopic disorder, a fact laid bare by the infamous collapse of the Tacoma bridge due to its violent oscillation at ~ 0.5 Hz. To complicate things further, liquids and plastics may form local structures/clusters that may indeed result in the preservation of longer-than-expected wavelength oscillations. These lower frequency contributions to the VDoS (and thus the heat capacity at low temperatures) of liquids and glasses are still not fully understood and will be discussed further in chapter 5.

1.5 Liquid Dynamics and Transitions

A simple and widely used distinction between the solid and liquid phases is that, although both cannot be compressed (much), a liquid conforms to the shape of its containing vessel. Its structure is therefore dynamic, with particles able to slip past each other and diffuse. On a macroscopic scale, the liquid flows while the solid doesn't.

The movement of a particle within a liquid is of course still not completely free due to strong interparticle forces with the solvent particles; diffusive motions will have varying strengths of 'internal friction' slowing it down. Macroscopically speaking, liquids will flow with more or less ease depending on the physical properties of the material, the most pertinent of which is the viscosity. Viscosity, η , is a measure of a material's resistance to a viscous stress. Unlike an elastic stress, which is proportional to the magnitude of material's deformation from some equilibrium position (analogous to Hooke's law for a simple spring), viscous stress is one that is related to the *rate* of deformation of a material. Viscosity commonly shows a strong temperature dependence that is often modelled using a variety of empirical functions. One of the more common expressions is the Vogel-Fulcher-Tammann (VFT) equation given by

$$\eta(T) = \eta_0 \cdot e^{\frac{DT_0}{T-T_0}}, \quad (\text{I.2})$$

where η_0 , D , and T_0 are empirical fitting parameters. Generally, viscosities increase (exponentially) as temperatures drop, as indicated in the VFT equation.

As mentioned earlier, the major difference between the solid and liquid states is the ability of the liquid to flow under an external force. At the microscopic scale this appears as translational diffusion of molecules. The Stokes-Einstein (SE) equation relates the diffusion rate D to the thermal energy and a friction factor, ζ specific to the material as¹⁶

$$D = \frac{k_B T}{\zeta}. \quad (\text{I.3})$$

For translational diffusion of a simple sphere, the translational friction factor is of the form¹⁷

$$\zeta_t = C\pi\eta r, \quad (\text{I.4})$$

where r is the hydrodynamic radius, η is the dynamic viscosity, and C is a constant that takes on values between 4 and 6 pertaining to perfect slip and perfect stick conditions respectively. Despite being a macroscopic material property, the use of dynamic viscosity term may often be applicable for friction factors in relation to the diffusion of single

molecules in a pure liquid, or a solute through a solvent. Particle displacements due to random translations follow a normal distribution which, after some time, t , will have a standard deviation given by

$$\sigma_t = \sqrt{6D_t t}. \quad (1.5)$$

For orientational diffusion, typically the diffusion rate can be estimated using the Stokes-Einstein-Debye (SED) relation for spheres, where the rotational friction factor is given as¹⁸

$$\zeta_r = 6\eta V, \quad (1.6)$$

where V is the molecular volume. The molecule is generally approximated to have spherical geometry, giving a volume in terms of the effective hydrodynamic radius.

These expressions include the dynamic viscosity which is very much a macroscopic concept. When the solute molecule is comparable in size to (or as is often the case in this work, identical to) the solvent molecules, the SE and SED relations risk becoming increasingly irrelevant. It is therefore unsurprising that they are commonly experimentally observed to break down.^{16,19–22} The experimental accuracy of the SE relation will generally improve as solute-solvent interactions average out, *i.e.*, when $r_{solute} \gg r_{solvent}$, and observed to deteriorate when $r_{solute} < r_{solvent}$, where r is the molecular radius.²³

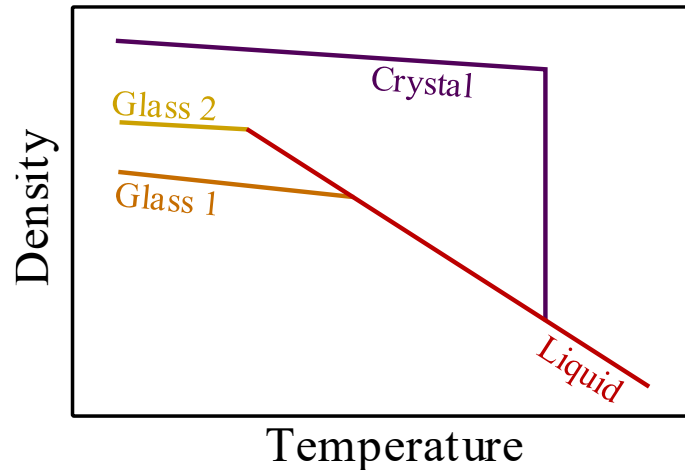


Figure 1.4. Crystallisation and vitrification upon cooling a liquid.

Possible behaviours of a typical liquid upon cooling, illustrated by the effects of crystallisation and vitrification on the density. Adapted from ref.²⁴

There are a few different behaviours that a liquid can exhibit upon cooling as illustrated in Figure 1.4 in terms of density. Generally, a liquid upon cooling will undergo a first-order phase transition into a crystalline state around the melting temperature T_m . This is the most thermodynamically favourable pathway. Crystallisation requires the repositioning and reorientation of the constituent molecules into the lattice structure; however, it is not always

possible for them to do so. For example, if a liquid is cooled at a rapid enough rate, the molecules may simply not have enough time to reposition before the material viscosity diverges and diffusive motion is arrested. The resulting material resembles a ‘frozen-in’ liquid phase, more commonly referred to as a glass. The transition between liquid and glass is called vitrification and can be thought of as a purely kinetic transition, as opposed to one between states of thermodynamic equilibrium. Depending on the material, cooling rates to produce vitrification may be fairly pedestrian, or need to be preposterously fast. H₂O will crystallise with ease unless it is hyperquenched at rates above 10⁶ K/s into the glassy state. Alternatively, the viscosity of water may be increased by the addition of salt as shown in chapter 6, allowing for gentle cooling ~1 K/min into the glass. Some of the viscous molecular liquids studied in chapter 5 meanwhile (such as tetrabutyl orthosilicate and titanium tetrabutoxide) could not be crystallised experimentally at all, only vitrified. The complexity of their intermolecular potential landscapes, with multiple local energy minima, prevents crystallisation.

Transitions in a material need not result in a change of state. Liquids can undergo structural transitions while remaining liquids; these are known simply as liquid-to-liquid transitions (LLTs) and have become the focus of much study in recent years. This has been driven particularly by suggestion that a LLT exists in supercooled water (discussed in detail in chapter 6). LLTs have been reported in a wide range of materials, such as phosphorus²⁵, silicon,²⁶ sulphur,²⁷ butanol²⁸, triphenyl phosphite,^{29,30} aqueous salt solution,³¹ and after decades of attempts, in neat H₂O.³²

In order to probe the putative LLT in H₂O, a trick employed here (for reasons that will become apparent in chapter 6) is to instead study aqueous salt solutions. Dissolving salt in water decreases the melting point of the solution below that of the pure solute or solvent; sometimes *well* below. This effect is illustrated by the binary phase diagram shown in Figure 1.5.

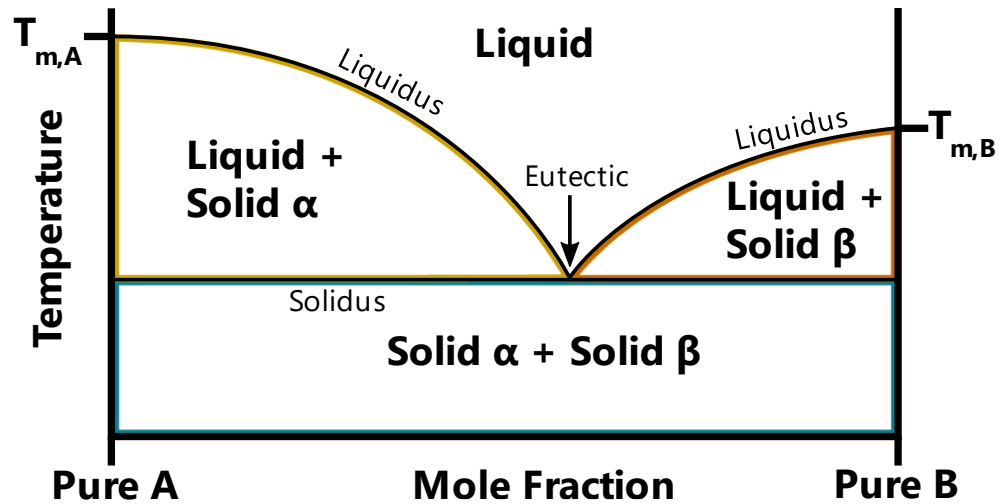


Figure 1.5. A binary phase diagram.

The phase diagram of a mixture of two components, A and B, whose melting points in their pure form is labelled as $T_{m,A}$ and $T_{m,B}$. Solids α and β indicate A- and B-rich precipitates respectively.

The liquidus and solidus lines on the binary phase diagram define the temperature bounds within which liquid and solid states may coexist, as shown in Figure 1.5. The eutectic point occurs at a particular mole fraction, where the fully liquid phase transitions to a fully solid binary phase or *vice versa*. This means that the eutectic system can be cooled to lowest possible temperature before the onset of crystallisation, which also corresponds to a high viscosity as described previously with the VFT equation (1.2).

1.6 Lasers and Optics

To understand the physical principles underpinning the spectroscopic technique used throughout this work, an appreciation of laser physics is necessary. Laser is an acronym for light amplification by the stimulated emission of radiation. To understand the meaning behind this, electronic absorption and emission of light will be discussed.

An electron can become more energetic by absorbing an incident (pump) photon whose energy is equal to the difference between the two electronic energy states as shown in Figure 1.6 (a). Spontaneous emission is the simplest form of photon emission, where the photon release is a stochastic process; this is not useful if the goal is to achieve lasing. Alternatively, a photon can be emitted by ‘stimulating’ the electron with another photon to emit a photon in sympathy (same phase and direction). One won’t get far in creating a laser by passing energy back and forth between the same two energy levels unfortunately. After continuous pumping, only a 50:50 population split of electrons across both levels will be reached. This is described by the Einstein B coefficients, which is the rate of absorption, B_{12} , or stimulated emission, B_{21} . These two values reach parity for a 50:50 population split. For lasing to occur,

stimulated emission must exceed that of absorption between the two laser transition states, otherwise no amplification can occur. To overcome this, the electrons must be cycled through more than just two energy levels.

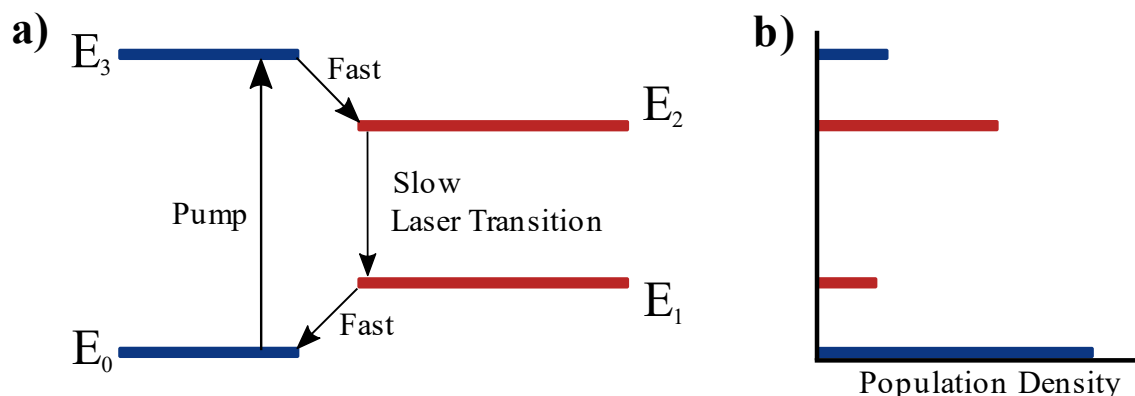


Figure 1.6. Illustration of a classic 4-level laser system.

a) The energy level diagram with b) corresponding population densities. Lasing occurs between the two red energy levels. Figure adapted from ref.³³

The four-level laser entirely separates the pumping transition from the emission transition as shown in Figure 1.6 (a). This facilitates population inversion, thus producing viable amplified stimulated emission. Starting from the ground state, E_0 , the electron absorbs pump energy (usually a pump photon) to reach an excited state E_3 , before rapidly decaying to a lower electronic energy level E_2 . The electron is free to decay to E_1 by photon emission but will subsequently decay quickly back to the ground state. The bleaching of states E_3 and E_1 keep the population densities of E_2 high and E_1 low respectively, resulting in a maintained population inversion as shown in Figure 1.6 (b). With population inversion achieved, an emitted photon is more likely to stimulate the emission of another photon than be reabsorbed, *i.e.*, $B_{21} > B_{12}$. This is how amplification occurs in the four-level laser.

In solid-state lasers, the electrons involved in lasing are outer shell electrons of rare-earth or transition metal ions present as dopants within a host crystal or glass. Common dopants include neodymium, erbium, and titanium ions, each of which have their own characteristic lasing wavelengths (and bandwidths).

Lasers can be operated in a continuous wave mode, or a pulsed mode. The pulsed mode operation of some lasers can produce extremely short and intense pulses, which can be very useful in fields of scientific research, medicine, defence, and manufacturing. This work utilises laser ‘mode-locking’, a technique that can produce a train of ultrashort pulses.

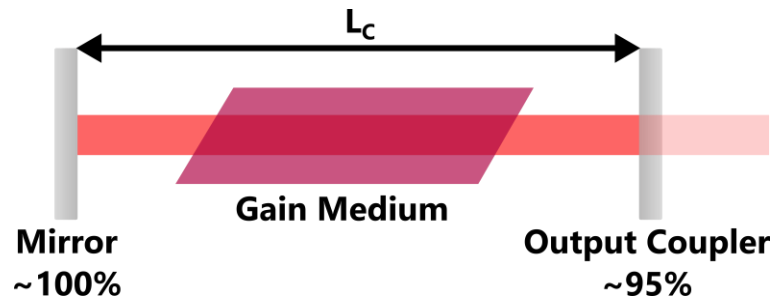


Figure 1.7. A basic laser cavity.

Cavity consisting of the gain medium between two mirrors, one of which is partially transmissive to allow laser light output.

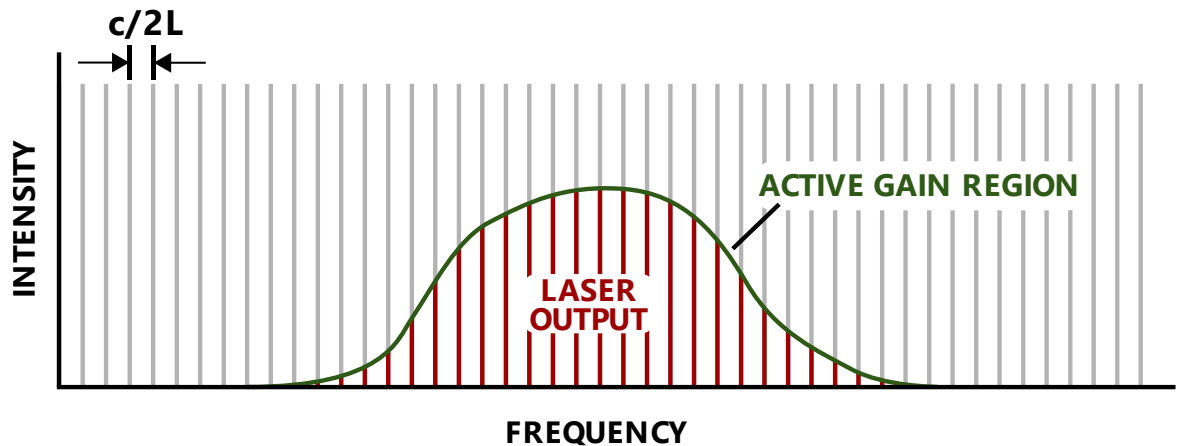


Figure 1.8. Laser cavity modes.

Modes allowed within the cavity are shown as vertical lines with spacing $\Delta\nu = c/2L_C$. However, only the cavity modes (red) that lie within the emission bandwidth of the gain medium (green) may lase.

Within the laser cavity (see Figure 1.7) of length L_C , only modes with wavelength $\lambda = 2L_C/A$ (where $A \in \{1, 2, 3, \dots\}$) will produce standing waves, while all other wavelengths are suppressed through destructive interference.

Intense and temporally narrow laser pulses are created by the summation of these longitudinal modes when their phase relationship is such that they periodically and simultaneously interfere constructively. This is known as mode-locked operation, and there are various mode-locking techniques that can be employed to accomplish this. The laser used here uses Kerr-lens mode-locking, which utilises the optical Kerr-effect (discussed in greater depth in section 1.8) to selectively focus down intensity spikes into the high-gain region of the Ti:sapphire crystal, thereby enhancing them until mode-locked operation dominates. The origin of the initial spike may be due to random intensity fluctuations, or can be induced by other experimental means including rapidly fluctuating the cavity length.

Ti^{3+} has a particularly broad laser emission bandwidth, due to various possible laser transitions between multiple vibronic energy levels. The broad emission bandwidth is

illustrated in Figure 1.8 as the active gain region that spans a broad frequency range, encompassing various cavity modes. Given that the temporal pulse width is inversely proportional to the frequency bandwidth, this has made Ti:sapphire an important gain medium in the creation of ultrashort laser pulses.

Refractive index and birefringence are relatively simple concepts but one that is central throughout this work. OKE spectroscopy induces and observes the decay of transient birefringence in a medium of study. Additionally, the OKE set-up manipulates the polarisation of ultrashort laser pulses using uniaxial-crystal (*i.e.*, birefringent) optics—more commonly referred to as waveplates. It is therefore important that these concepts are discussed here.

The speed of light, c , is a universal constant that defines the phase velocity of any electromagnetic (EM) wave through a vacuum—it is also the upper limit at which information, energy, or matter can travel. The phase velocity of EM waves travelling through a medium, however, is (almost) always slower than c . In the classical picture, this is because light will be partially absorbed and re-emitted by the electrons within the solid with a slight phase-shift. The resulting superposition of the waves in the medium reveals a retardation effect of the wave (except in some very particular circumstances and/or metamaterials which can produce increases in the phase velocity,³⁴ or even flip its direction³⁵). The extent to which a material will change the phase velocity of light is the refractive index. This is a dimensionless quantity that states the ratio between the phase velocities of EM waves in a vacuum and through the particular medium. The refractive index, $n(\lambda)$, typically shows a mild wavelength dependence (over the wavelengths of interest in this work at least), however this can still produce significant experimental hurdles to the execution of OKE spectroscopy.

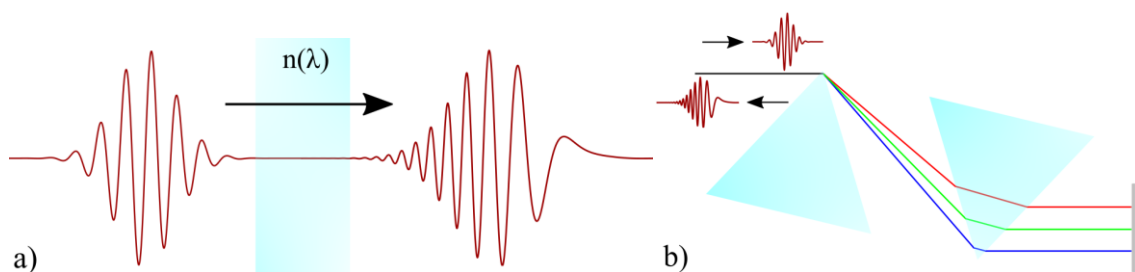


Figure 1.9. Chirped laser pulses.

a) The electric field of a laser pulse before and after chirping by traversing a medium with a refractive index that varies sufficiently with wavelength. b) Negative chirp produced by prism pair with end mirror. Note that the chirped pulses in both figures are different because they are travelling in opposite directions.

The wavelength dependence of the refractive index can be relatively small, however the number of transmitting optics, and thus the total glass thickness, through which laser pulses

must traverse before they interrogate matter in OKE spectroscopy can be large. This can result in significant (positive) chirping if left unchecked—see Figure 1.9 (a). The main issue with chirped pulses in OKE spectroscopy is the broadening of the intensity profile, rather than the wavelength-sweep across the electric field profile. This is because OKE is a Raman scattering technique (as discussed in section 1.8), and thus the frequency of the light is not supposed to be resonant with the transitions under study, making it less important.

Some crystals can have polarisation-dependent refractive indices, the simplest ones are uniaxial crystals. A uniaxial crystal has a single ‘optic axis’; a polarised wave (in any orientation) travelling parallel to this axis will only experience one uniform refractive index. However, should a polarised wave travel in any other path through the uniaxial crystal, it will experience two different refractive indices for orthogonal components of its electric field—this is known as birefringence, and a uniaxial crystal is said to be birefringent. This means that the perpendicular components of the electric field can be retarded at different rates, which is a useful tool in performing polarisation alterations and manipulations. For example, consider a linearly polarised EM wave traversing a crystal such that exactly equal parts of its optical intensity experience different refractive indices. As shown in Figure 1.10, the component of the wave that ‘sees’ the lower refractive index will travel faster (hence this crystal axis is called the fast-axis), while the other component (with electric field in the slow-axis) will be retarded with respect to this. The resulting polarisation depends on the thickness of the medium. After traversing enough of the birefringent crystal, the slow-axis wave may have been retarded by, *e.g.*, one half of a wave ($\lambda/2$). At this point, the net result for the EM field is that its linear polarisation will be rotated by $\pi/4$ radians. This describes the function of half waveplates. There are also quarter waveplates which can turn linearly polarised light into circularly polarised light and *vice versa* (see Figure 1.10). Both $\lambda/2$ and $\lambda/4$ waveplates are used in the OKE set-up used here, as shown later in section 2.1.

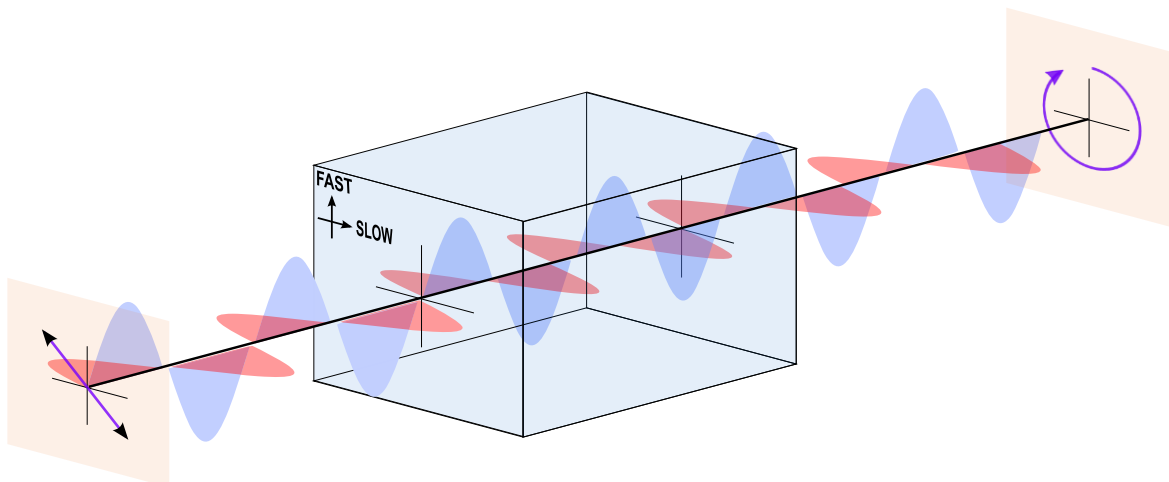


Figure 1.10. Quarter Waveplate Illustrated.

Linearly polarised light becomes circularly polarised after traversing a quarter waveplate, illustrated by the different retardation of orthogonal components (blue and red) of the electrical field within the fast and slow crystal axes respectively.

Finally, it will be discussed in section 1.8 how birefringence can exist in a liquid. In OKE spectroscopy, a disordered (and thus optically isotropic) liquid can be forced into anisotropy for a short period of time. Studying the relaxation of this transient birefringence can reveal information on the relaxation dynamics, which are represent the normal thermal molecular motions

1.7 Fourier-Transform Infrared Spectroscopy

Infrared spectroscopy is a widely utilised technique to measure the frequencies of vibrational energy level transitions due to its relative simplicity. Of all possible molecular vibrations, those that produce a change in molecular dipole moment are said to be IR-active. As discussed for electronic transitions in section 1.6, absorption of infrared light occurs when an incident IR photon is of energy, $h\nu$, equal to the difference between the two vibrational energy levels, *e.g.*, $E_1 - E_0$ as shown in Figure 1.11.

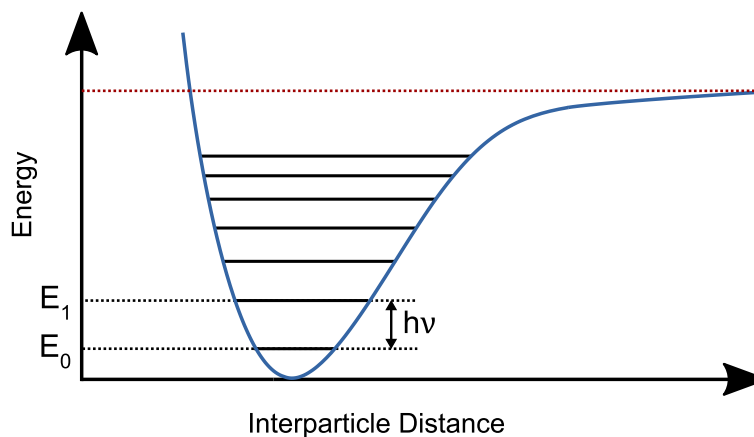


Figure 1.11. Vibrational energy levels in an anharmonic potential.

The shape of the potential landscape is shown by the blue curve, and solid black lines display the lowest quantised energy levels.

For some transitions, particularly those between low lying energy levels, one can often assume a quadratic potential landscape form, which greatly simplifies vibrations into harmonic motions; vibrational energy levels, E_n , under the quadratic model are equally spaced. In reality however, interatomic/intermolecular potentials are anharmonic, as illustrated by the asymmetry of the interparticle potential in Figure 1.11. This is intuitive, as a particle cannot be indefinitely trapped in a finite potential well. A particle will escape the well once it gains sufficient energy (red dotted line in Figure 1.11). This anharmonic potential results in a ΔE (and thus, $h\nu$) reduction at higher energies.

In addition to the frequency of the light, it is also important to understand *how much* light may be absorbed. The absorbance, A , upon travelling through some volume will be proportional to both the path length, l , and the concentration of absorbers, c , within the volume. This is described by the Beer-Lambert law, which simply states this dependence, where the constant of proportionality is called the molar absorption coefficient, ϵ (although in practice it is known by various names). If I_0 is the initial light intensity, and I is the final intensity after attenuation by absorption, then the Beer-Lambert law is

$$A = \log_{10} \frac{I_0}{I} = \epsilon l c. \quad (1.7)$$

These values (other than l and c) are, of course, wavelength dependent. IR spectroscopy in its most conceptually basic form can be accomplished by passing individual IR wavelengths through a sample and measuring the transmitted intensities for each wavelength; indeed, this is the basis of dispersive (or scanning) spectrometers, which are still widely used for ultraviolet/visible spectroscopies. *Fourier-transform* infrared spectroscopy (FTIR) is a more sophisticated technique that passes the complete spectrum of a broad-band IR source through a sample and measures its entire transmission spectrum

simultaneously. The $\text{SNR} \propto \sqrt{t}$, where t is the time taken to measure a single spectral element. If a dispersive IR and FTIR spectrometer were to measure the same sample for equal time durations (t_{total}) with equal optical throughput, the FTIR signal is vastly superior as each spectral element is measured in tandem. This means that the SNR in FTIR is $\propto \sqrt{t_{\text{total}}}$, while the dispersive SNR remains $\propto \sqrt{t}$. Furthermore, assuming the same IR source the intensity of the IR light can be far greater in FTIR spectroscopy because there is no monochromator requirement (typically a prism/grating and aperture pair) and thus no loss in IR intensity, again enhancing the SNR.

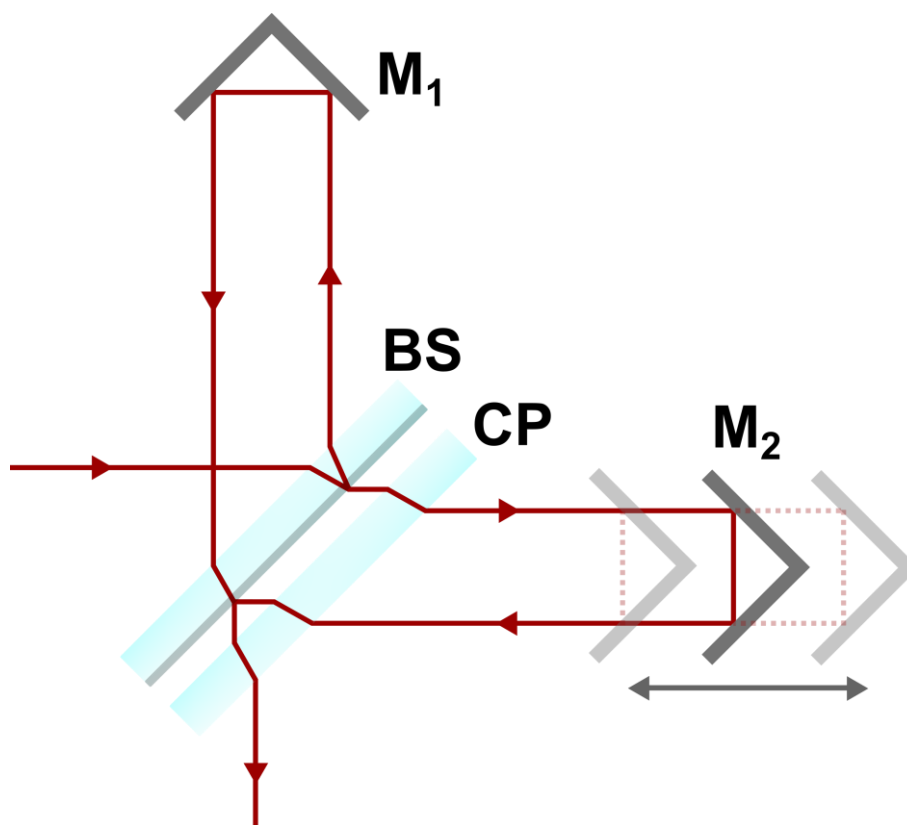


Figure 1.12. A Michelson interferometer.

A single ray trace showing the Michelson interferometer concept. BS is a 50:50 beam-splitter, and CP is a compensator plate. M_1 is a static mirror while M_2 can be translated about the axis of the incident light propagation.

At the heart of the FTIR spectrometer is the Michelson interferometer, depicted in Figure 1.12. It consists of a 50:50 beam-splitter (the ‘half-silvered mirror’ type is illustrated here) and two end mirrors for each arm, one of which is on a translation stage. This moveable mirror enables the alteration of the optical path length of one of the two ‘arms’ of the interferometer, and thus, controls the optical path difference (OPD). The intensity of the recombined beams is a function of the OPD; plotting these against each other produces an interferogram, whose generic form is illustrated in Figure 1.13.

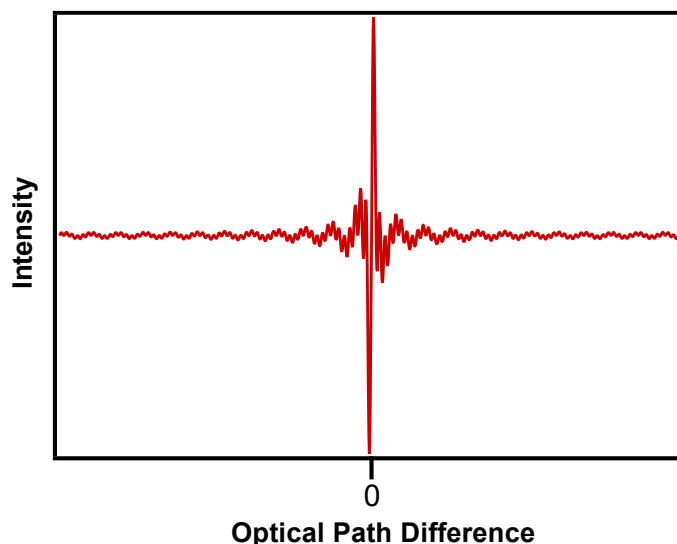


Figure 1.13. Example interferogram.

The measured optical intensity after the Michelson interferometer depends on the optical path difference between both interferometer arms.

When the mirrors are positioned such that each arm of the interferometer has the same optical path length, the broad-spectrum light is ultimately recombined in phase (constructive interference), producing an intense signal. This is the ‘centre-burst’ observed in Figure 1.13 at zero path difference. When the path length of each arm begins to differ, achieved via the translation of one of the end mirrors (M_2 in Figure 1.12), the light is recombined with a different phase shift for each wavelength. The result of this is shown in the wings of the interferometer, where there is little change in the intensity as the path difference changes. This is because the equal rates of both constructive and destructive interference for the spectral elements have an averaging effect on the overall intensity. Although relatively dull in shape, just as much spectral information is encoded within the wings (fortunately, as interferograms are mostly wings anyway!). In fact, the larger the interferogram, *i.e.*, the further the translation of M_2 , the greater the resolution of the resultant frequency spectrum. This is important for instances when, for example, when the spectral elements under study are relatively narrow.

Signals that exist naturally in, *e.g.*, the spatial or temporal domain can also be fully expressed in their corresponding inverse domains (reciprocal space or frequency respectively in this example). The Fourier transform (\mathcal{F}) and inverse Fourier transform (\mathcal{F}^{-1}) are mathematical operations that convert the signal between the two inverse domains:

$$F(\xi) = \mathcal{F}[f(x)] = \int_{-\infty}^{\infty} f(x)e^{-2\pi i x \xi} dx, \quad (\text{1.8})$$

$$f(x) = \mathcal{F}^{-1}[F(\xi)] = \int_{-\infty}^{\infty} F(\xi) e^{2\pi i \xi x} d\xi. \quad (1.9)$$

The interferogram is in terms of OPD, and thus will be Fourier transformed into a spectrum in the inverse length domain (wavenumber). In practice, the mirror M_2 may be translated at a constant velocity, with the interferogram taken as a function of time. The FT will produce a frequency spectrum which is simply proportional to the wavenumber spectrum by a factor of the speed of light, c .

1.8 Optical Kerr-Effect Spectroscopy

Traditional Raman spectroscopy is a well utilised and relatively simple technique to measure the frequencies of (Raman-active) vibrational modes. This is achieved by using a non-resonant laser light source which is absorbed and emitted with a Raman-shift in frequency that is equal to the rovibrational transition energies, as illustrated in Figure 1.14. Such transitions must be ‘Raman-active’, which is to say that the transition must involve some change in the molecular polarisability; this is complementary to IR-active modes, where it is the molecular dipole moment that must be altered. However, its performance at lower frequencies is complicated by the intense quasi-elastic Rayleigh wing that scales with the Bose-Einstein thermal population factor. OKE spectroscopy is a time-domain technique that is superior for the observation of sub-THz dynamics, but considerably more complex. This section will explain the theory behind OKE spectroscopy, while the experimental set-up and data analysis are introduced in section 2.1 and chapter 3 respectively.

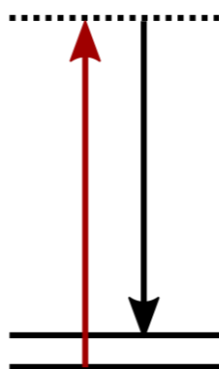


Figure 1.14. Jablonski diagram of Raman scattering.

Solid horizontal lines indicate vibrational energy levels and dashed horizontal lines represent virtual energy states. This scheme represents Stokes Raman scattering.

The Kerr-effect was discovered by Reverend John Kerr, who observed that an external electric field could alter the birefringence of a medium, and the strength of this effect is proportional to the square of the electric field strength.^{36,37} Note that this differs from the Pockels effect, which occurs in crystals lacking inversion symmetry and describes a direct

proportionality of birefringence and electric field strength. The optical Kerr-effect is simply the Kerr-effect when the electric field applied is due to a material's illumination with EM waves, which was observed experimentally some 90 years later.³⁸ This intensity dependence of the refractive index is given by

$$n = n_o + n_2 I, \quad (\text{I.10})$$

where n_2 is the second-order nonlinear refractive index with units of $(W/m^2)^{-1}$ and I is the electric field intensity.

The degree to which a molecule can become polarised (in other words, gain an induced dipole) by an electric field is called the molecular polarisability. Although there are higher order dependencies for the induced dipole for strong electric fields, the first (linear) term in the expression for induced dipole moment $\vec{\mu}$ in an electric field \vec{E} is

$$\vec{\mu} = \hat{\alpha} \vec{E}. \quad (\text{I.11})$$

The proportionality term $\hat{\alpha}$ is the polarisability of the molecule, a rank 2 tensor that relates the electric field strength in three dimensions to the molecular polarisability in three dimensions:

$$\hat{\alpha} = \begin{bmatrix} \alpha_{xx} & \alpha_{xy} & \alpha_{xz} \\ \alpha_{yx} & \alpha_{yy} & \alpha_{yz} \\ \alpha_{zx} & \alpha_{zy} & \alpha_{zz} \end{bmatrix}. \quad (\text{I.12})$$

The value of tensor element α_{ij} states the molecular polarisability in the i axis caused by and electric field in the j axis.

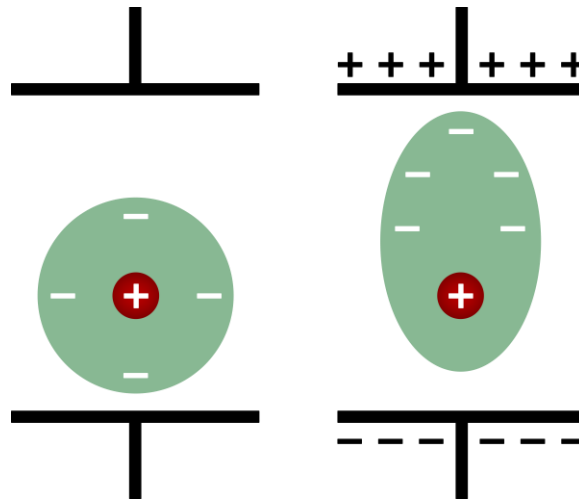


Figure 1.15. Polarisability shown by an electric field induced dipole.

Atoms are illustrated with a nucleus (red) surrounded by a volume of electrons (green). An atom (left) becomes polarised due to the displacement of electron density by a uniform external electric field (right) formed between two oppositely charge plates.

Generally, in any frame of reference, it is reasonable to expect the diagonal elements of the polarisability tensor to have the greatest values—that is to say that a molecule in an electric field will be polarised more in the direction of the field than orthogonal to it. Atoms have no off-diagonal contributions to their polarisability tensor, so within an electric field as illustrated in Figure 1.16, the induced dipole is simply parallel with the electric field. For molecules it is often not so simple; off-diagonal terms can exist. Fortunately, there will always exist some molecular reference frame where the off-diagonal elements reduce to zero, leaving only the diagonal elements as non-zero; the spatial axes in such reference frame are the *principal axes*.

$$\hat{\alpha} = \begin{bmatrix} \alpha_{xx} & 0 & 0 \\ 0 & \alpha_{yy} & 0 \\ 0 & 0 & \alpha_{zz} \end{bmatrix} \quad (\text{I.13})$$

A molecule is isotropically polarisable if, with respect to the molecular principal axes, $\alpha_{xx} = \alpha_{yy} = \alpha_{zz}$. Consequently, the induced molecular dipole will be in exact alignment with the electric field. If this condition is not met however, then the molecule is anisotropically polarisable, and the induced dipole will be misaligned with the electric field. Figure 1.16 shows firstly an EM pulse with a defined polarisation, and thus electric field orientation, that will induce a transient dipole in any molecule. Isotropically polarisable molecules, such as CF_4 in the illustration, will have an induced dipole which is parallel to the electric field. An anisotropic molecule on the other hand, CS_2 in the illustration, will have an induced dipole which is *not* parallel with the field (unless it happens to be in a very exact orientation with respect to the field already). In this case the molecule effectively receives a ‘torque-kick’ *via* the Lorentz force to bring its transient dipole into alignment with the field. Note that in OKE spectroscopy (for laser pulses with very narrow temporal widths on the order of 10^{-14} s or faster) the transient dipole may have already disappeared before the molecules have had much chance to rotate in response. The transient dipole duration is the short window during which the molecules receive angular momentum, they may reach a maximum degree of alignment long after this.

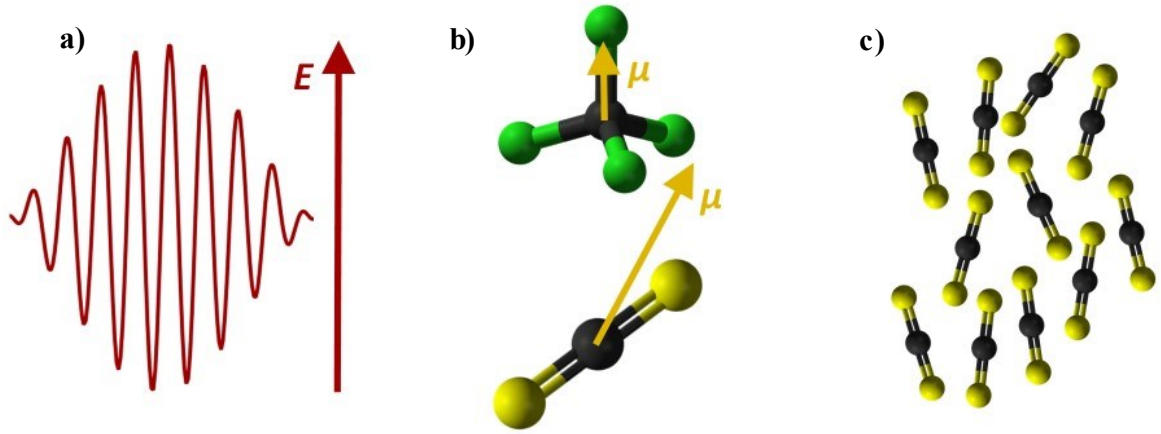


Figure 1.16. Cartoon of the optical Kerr-effect.

a) The polarised electric field of an intense laser pulse. b) The resulting induced dipoles on both an isotropically (weakly) polarisable molecule, CF_4 (top) and an anisotropically (highly) polarisable molecule, CS_2 (bottom). c) Anisotropic molecules are brought into some degree of alignment some time after their interaction with the electric field.

The liquid illustrated in Figure 1.16 (c) is birefringent. However, OKE spectroscopy does not measure single molecules, so it is useful to now consider the many-body polarisability tensor, $\Pi(t)$, of the medium. This can be thought of as the sum of two contributions: one molecular (intrinsic) term, and one interaction-induced term

$$\Pi(t) = \Pi^M(t) + \Pi^I(t). \quad (1.14)$$

The molecular term is simply the sum of all the atomic polarisabilities in the laboratory reference frame (not with respect to the molecular principal axes).

$$\Pi^M(t) = \sum_{n=1}^N \alpha_n(t). \quad (1.15)$$

When molecular orientations are randomised in the liquid, the many-body polarisability will become isotropic, which is to say, each diagonal element of $\Pi^M(t)$ will be equal, while the off-diagonal elements will average out to zero. This is true even for anisotropically polarisable molecules. There must be some orientational ordering in the ensemble as shown in Figure 1.16 (c) before an overall anisotropy exists.

Intermolecular interactions have an influence on the molecular polarisability. This can become quite complicated given the many forces at play, as outlined in section 1.2. For ‘simple’ liquids, where dipole-induced-dipole (Debye) interactions are the only light scattering mechanisms,³⁹ the interaction-induced term is given by^{40,41}

$$\Pi^I(t) \cong \sum_{n=1}^N \sum_{n \neq m} \alpha_n(t) \cdot T \cdot \alpha_m(t) \quad (1.16)$$

where α_n is the polarisability of molecule n . \mathbf{T} is the dipole-dipole interaction tensor given by

$$\mathbf{T} = \frac{3\vec{r}\vec{r} - \hat{\mathbf{1}}}{r^3}, \quad (\text{I.17})$$

where \vec{r} is the unit vector between the centres of mass of both molecules, r is the intermolecular separation, and $\hat{\mathbf{1}}$ is the unit tensor.⁴²

It is fluctuations in $\mathbf{\Pi}(t)$ that give rise to the OKE signal, $S_{OKE}(t)$. Specifically, the OKE signal is proportional to the derivative of the polarisability-polarisability time correlation function of the off-diagonal elements

$$S_{OKE}(t) \propto \frac{1}{k_B T} \frac{d}{dt} \langle \Pi_{xy}(t) \Pi_{xy}(0) \rangle, \quad (\text{I.18})$$

where $\langle \dots \rangle$ indicates the average.⁴¹

Given that there are both intrinsic and induced terms contributing to $\mathbf{\Pi}(t)$ (and thus $\Pi_{xy}(t)$) as defined in eq. (1.14), this suggests that liquid consisting of *isotropic* molecules can still give rise to an OKE signal via the interaction-induced, $\mathbf{\Pi}^I(t)$ term; this does not contradict Figure 1.16, which illustrates the evolution of the $\mathbf{\Pi}^M(t)$ term. This is relevant to the work of chapters 4 and 5, which will present OKE spectroscopic studies into isotropic (and near-isotropic) molecules.

Finally, OKE spectroscopy excited Raman-active vibrational modes via the mechanism illustrated in Figure 1.17. This is a coherent Raman scattering technique, and thus requires that the frequency of the scattered photon lies within the bandwidth of the probe pulse (which is the same as the pump pulse in these experiments). The bandwidth of the pulses therefore imposes a limit on the range of measurable dynamics. Because the pump pulse creates a population of molecules in an excited vibrational state, scattered photons may have either a Stokes or anti-Stokes Raman shift, the latter of which is illustrated in Figure 1.17.

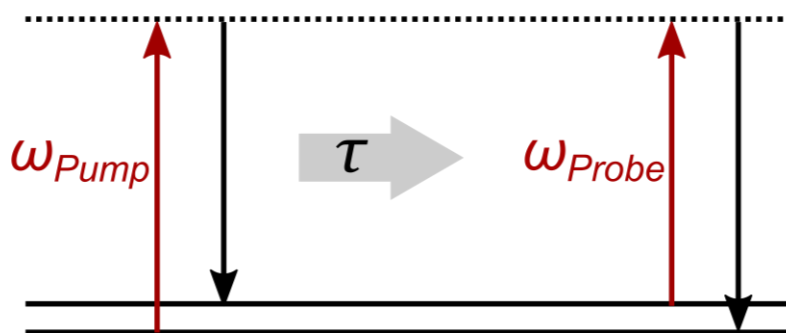


Figure 1.17. Jablonski diagram of OKE spectroscopy.

The probe pulse arrives after some controlled time delay, τ , after the pump pulse.

1.9 Computational Chemistry

Throughout this work, the application of computational chemistry will often feature to compliment experimental data. The simulation of the intramolecular normal vibrational modes of molecules is useful to this work, especially the lowest frequency modes which can occur on timescales comparable to the intermolecular motions of interest (which tend to be on the order of 1 ps and greater). Raman active vibrations with frequencies below ~ 20 THz (670 cm^{-1}) will also be observable in the OKE spectra in this work, meaning that computed normal modes can help in the characterisation of spectral line-shapes. Another example of the utility of computational chemistry to this work is in the calculation of molecular polarisability tensors. This can provide an insight into the strength of the OKE response of the molecule, specifically the spectral intensity of various dynamical contributions to the OKE signal.

As mentioned previously, in the condensed phase there are many different types of dynamics at play. Many intramolecular vibrations occur on much faster timescales than intermolecular interactions. Very high frequency vibrations such as X-H stretching modes have periods faster than 10 fs, meanwhile even a relatively low-mass molecule will take far longer to traverse a single van der Waals radius—at 20°C , a water molecule is likely to take longer than 100 fs. Because of this, faster vibrations are, in general, only very weakly coupled to surrounding heat bath. This means that their calculated vibrational frequencies often accurately reflect those witnessed spectroscopically. Lower frequency mode calculations however, do not tend to be as reliable since they are far more dependent on solvent interaction; they also tend to involve more molecular mass (or the entire molecule as shown previously in Table 1.1) and thus more electrons, meaning that small errors (due to implementing mathematical assumptions for example) can start to compound. Furthermore, the background potential surrounding a single molecule in the condensed phase is not

uniform, rather depending strongly on the local structure. This is not accounted for throughout the single-molecule computations performed here. It should be noted that these non-uniform potential landscapes can be accounted for by conducting many-body molecular dynamics simulations, however this comes at the cost of increased computational power requirements (and expertise).

This work utilises Gaussian09 (Revision D.01)⁴³ software to perform computational chemistry calculations using density functional theory (DFT). DFT is a method of calculating the electron density and structure in a material by treating the N electron wavefunction as the sum of N wavefunctions. This means that the electron density is reduced from a $3N$ dimensional function into a 3 dimensional one. Atomic orbitals are often modelled by some number of Gaussian functions, while each electron is assigned its own effective potential landscape determined by its position relative to nuclei and other electrons in the system. The total electron density around the molecule, and thus the molecular structure, is a function of all these functions, which is referred to as a ‘functional’ (hence density functional theory).

2 EXPERIMENTAL

This section will introduce the major experimental set-ups applied throughout this work, namely the OKE set-up, and the FTIR spectrometer.

2.1 OKE Set-up

The optical Kerr-effect is induced by very intense optical fields such as those achieved by powerful lasers. As discussed in section 1.7, mode-locked lasers can produce very short and intense laser pulses; these are perfect for both inducing and probing a transient birefringence in the time domain. The laser oscillator (Coherent Micra-10) used in this work is a mode-locked Ti:sapphire laser that delivers a train of ~ 10 nJ pulses with a repetition rate of 82 MHz and with 800 nm nominal wavelength providing a temporal pulse width of ~ 18 fs within the sample, broadening to ~ 25 fs when the sample is placed within a cryostat. This corresponds to an optical power of 820 mW.

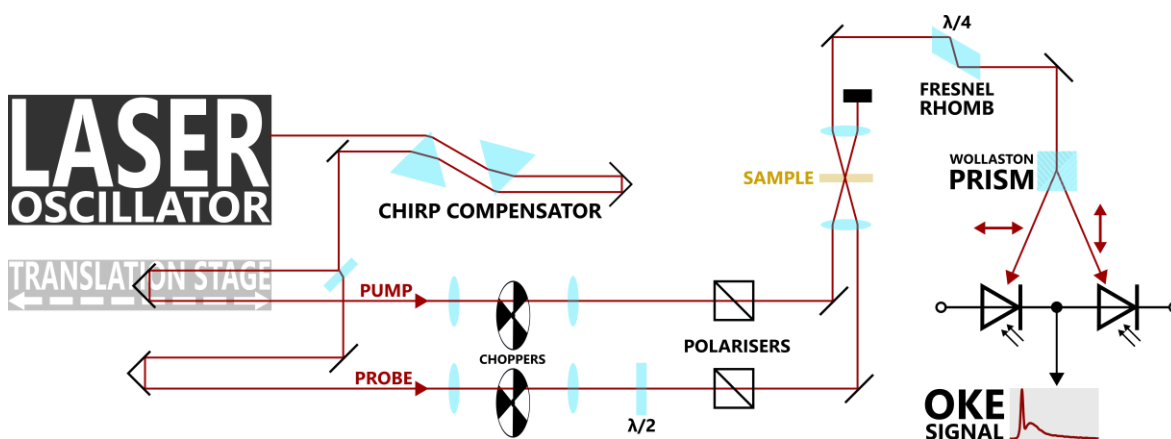


Figure 2.1. Schematic of the OKE experimental set-up.

The path of the laser pulses (red line) is mapped, alongside the major optical components.

As discussed in section 1.6, the laser pulse will undergo chromatic dispersion after traversing media whose refractive indices vary significantly with wavelength; this applies to the optical components implemented here. To negate this introduction of positive chirp, the laser pulses are negatively chirped beforehand by the prism pair shown in Figure 2.1 (but better illustrated previously in Figure 1.9). This effectively ‘slows down’ the longer wavelengths, with the knowledge that they will have ‘caught up’ later, after traversing the remaining optics before the sample. This achieves the narrowest possible intensity profile at

the sample, which is optimal to induce (and probe) the optical Kerr-effect. Figure 2.1 shows the use of a lens to focus both pulses onto the sample, however in the set-up used here both pulses are actually focussed by a single off-axis parabolic mirror.

This set-up places the translation stage on the pump path. In principle it could equally be placed on the probe path, however in this set-up it is preferable to fix the probe geometry since any beam-wander would affect its detection at the photodiodes. The time delay between pump and probe at the sample was altered by as little as 5 fs, and as much as 1 ns. This translation stage (Newport) can therefore be controlled with sub-micron spatial resolution, while the stage (by specification) operates over a 600 mm range.

	BEFORE SAMPLE	AFTER SAMPLE	AFTER FRESNEL RHOMB
NO SAMPLE OR NO PUMP			
WITH SAMPLE AND WITH PUMP			

Table 2.1. Laser pulse polarisations throughout the OKE set-up.

The pump (black) and probe (red) pulse polarisations at various points before detection. The pump is included for reference.

Both pulses must arrive at the sample with a $\pi/4$ (45°) relative rotation in their polarisation, as shown in Table 2.1. To this end, the probe traverses a $\lambda/2$ waveplate, with either crystal axis aligned at some orientation, θ , with respect to the probe polarisation. This has the effect of rotating the polarisation about an angle of 2θ (the reference axis only determines whether it is a clockwise or anticlockwise rotation). Therefore, to achieve a $\pi/4$ relative pump and probe polarisation, the $\lambda/2$ waveplate is oriented at $\pi/8$ with respect to the incident probe polarisation. It is preferable to rotate the polarisation in this manner before passing the pulse through a linear polariser, because when the natural polarisation of the laser system ($> 100:1$ at the oscillator output) is aligned with the polariser, there is minimal loss in intensity. Polarisers are then used to further linearise the polarisation of the

pump and probe at the sample, because it is important to have highly directional electric fields to induce and probe the transient birefringence.

When the pump arrives at the sample the optical Kerr-effect is induced, and the molecules within the pumped volume receive the torque kick to align their transient molecular dipoles with the electric field (Figure 1.16). Sometime later, as determined by the delay stage position, the probe arrives at a now-birefringent sample. This sample effectively acts as a waveplate, with a fast and slow axis that produces a phase shift in orthogonal components of the probe, giving rise to a small, *off-linear* ellipticity (see Table 2.1). This off-linear ellipticity is then transformed into an *off-circular* ellipticity by a Fresnel rhomb, which is essentially a $\lambda/4$ waveplate that introduces very little chromatic dispersion (even less than a zero-order waveplate).

At this stage there are three contributions to the signal: the transmitted probe intensity, the homodyne signal, and the heterodyne signal. The heterodyne signal varies linearly with the response function, $R(t)$, as opposed to $\propto R(t)^2$ for homodyne. This makes it preferable for OKE spectroscopy, as the homodyne signal decays too rapidly. Heterodyne detection has been traditionally been accomplished without circularly polarising the transmitted probe pulse. Instead the probe pulse traverses *almost*-crossed polarisers before and after the sample; the resulting signal is detected by a photodiode and the signal is passed to a lock-in amplifier. This experiment must be repeated again where the almost-crossed polarisers are altered; if they were oriented at exactly 91° with respect to each other in the first experiment, they must now be at exactly 89° . The results from both experiments can be subtracted from each other to yield the pure heterodyne contribution.^{44,45} This is fundamentally because the heterodyne component is dependent on the polarisation angle, changing sign for each experiment, while the homodyne contribution remains invariant.

In the balanced detection method employed here, this polarisation dependence *vs.* invariance is exploited directly within the set-up. By circularly polarising the probe pulse after the sample, the homodyne contribution is split into exactly equal orthogonal components, which subsequently cancel each other out electronically at the photodiodes. This leaves only the heterodyne signal to be passed on to the lock-in amplifier.

Splitting up the perpendicular polarisation components of the elliptical (or circular) probe pulse is achieved using a Wollaston prism. A Wollaston prism is actually two birefringent prisms fused together, whose fast and slow axes are perpendicular to each other's. Light of

orthogonal polarisations will propagate along either the fast or slow axis in the first prism, and then swap to the opposite crystal axis for the second prism. At the interface between the two prisms the orthogonal components will refract towards or away from the normal (by Snell's law), effectively splitting them up spatially (see Figure 2.1). A crystal axis of the Wollaston prism (either the fast or slow, although one should ensure that the probe pulse is split within the plane of the OKE setup for both practicality and safety) should be oriented at 0° with respect to the initial probe polarisation. This will ultimately result in the splitting of the elliptical electric field into its major and minor orthogonal components.

As mentioned previously, balanced detection is employed in this set-up. This technique utilises two photodiodes that measure the difference in the photocurrent produced by vertical and horizontal polarisation components, illustrated in Figure 2.1, which cancels out both the probe intensity and homodyne signal, sending only the heterodyne signal to the lock-in amplifier.⁴⁶ With the aid of Table 2.1 one can notice that when there is no OKE signal (*e.g.*, because of no pump pulse), then a circularly polarised probe pulse undergoes balanced detection, thereby producing no signal. Conversely, when a birefringent sample is probed, it is an elliptically polarised pulse that will undergo balanced detection. By definition, one of the orthogonal components will have a greater optical intensity than the other, and some net (non-zero) photocurrent will be measured; this is the OKE signal.

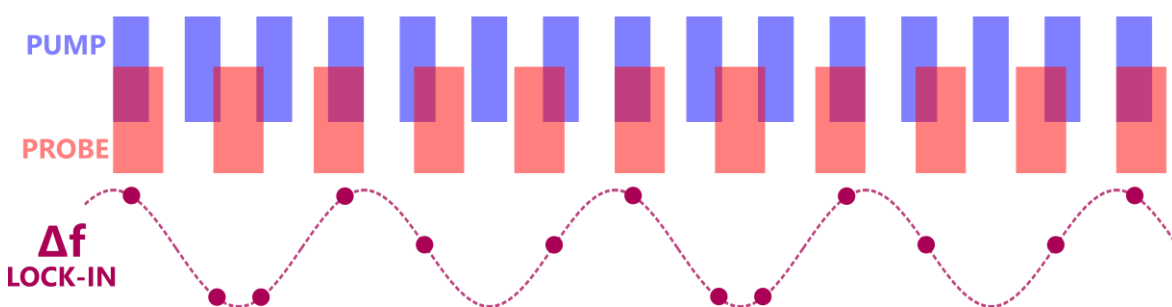


Figure 2.2. Modulation of pump and probe signals, with 'lock-in' at the difference frequency.

Pump (blue) and probe (orange) beams are modulated by optical chopping at different rates, producing an OKE signal modulated at the difference frequency (purple).

The OKE signal of interest is of course not the only light that the photodiodes will detect. Scattered pump and probe light will reach the detector, along with ambient light and other sources noise sources. To better isolate the OKE signal, lock-in amplification is employed. The pump and probe beams are chopped at kHz frequencies in the ratio of 7:5. This suggests that both pulses often do not interact with the sample throughout the duration of an OKE experiment, however this asynchronous pulse chopping serves a useful purpose, to modulate the OKE signal of interest by the difference frequency (see Figure 2.2). The exact chopping

rates are fed into a lock-in amplifier, which selectively amplifies signals at the difference frequency only, *i.e.*, the OKE signal. Furthermore, signals from other frequency bands, such as scattered pump/probe light or ambient light, are filtered out. The end result is an OKE signal with a drastically enhanced signal-to-noise ratio (SNR).⁴⁷

2.2 FTIR Set-up

This work utilises a commercial off-the-shelf FTIR spectrometer (Bruker Vertex 70). The instrument uses a silicon carbide globar as an IR (black body) light source. It incorporates a Michelson interferometer (as outlined in section 1.7) with a KBr beam-splitter, after which the recombined light passes through a sample in the transmission geometry illustrated in Figure 2.3 (although alternative geometries exist). The intensity of the transmitted light is detected by a pyroelectric detector.

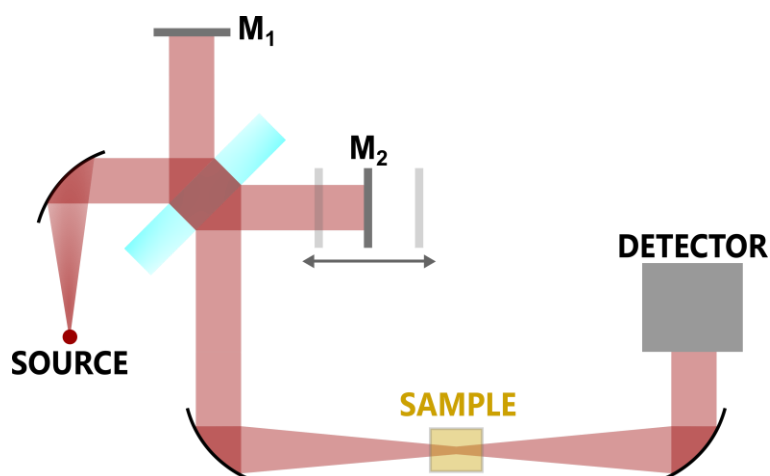


Figure 2.3. Schematic of the FTIR spectrometer.

FTIR data are gathered by first measuring the sample-free background spectrum formed from the source emission and atmospheric absorption spectra. The sample transmission spectrum is the ratio of the with-sample and background spectra.

2.3 Sample Preparation

OKE spectroscopy is highly sensitive to sample quality.⁴⁴ The sample is placed at the lens focus as shown previously in Figure 2.1, meaning that a very small cross-section of the sample is probed. The inclusion of foreign particles and/or bubbles, can cause severe laser light scattering from both the pump and probe pulse. Furthermore, solute concentration gradients in solution and poorly mixed viscous liquids can introduce refractive index gradients. This can wreak havoc with the balanced detection set-up used here. Sample inhomogeneities with domains on the order of the laser cross section can result in the uneven

probing of these domains, thereby providing an unrealistic picture of the mixture dynamics. There are various experimental procedures taken to mitigate this. Firstly, if necessary, samples are mixed using a lab bench vortex mixer. Secondly all samples are filtered upon their transfer to a cuvette with a short (1–2 mm) path length. Thirdly, the cuvette is immersed in an ultrasonic bath to degas the sample. This step can take particularly long for the viscous liquids of chapter 5. Finally, the cuvette is cleaned using optics-grade acetone.

FTIR spectroscopy is far less sensitive to sample quality. Smaller bubbles and scattering particles will generally not compromise the spectrum quality. Nonetheless, samples were mixed, degassed, and filtered. The samples are measured in the transmission geometry outlined in Figure 2.3; to achieve this they are loaded between two CaF₂ plates within the standard plate-spacer-plate sandwich configuration, where the spacer is a PTFE ring with a well-defined thickness.

Hygroscopic salts and liquids studies here were handled entirely within a N₂ gas purged glove box, with a measured dew point of < -40°C, which converts to a moisture content of < 128 ppm H₂O.

3 DATA ANALYSIS

OKE spectroscopy is a time-domain, pump-probe technique that measures the derivative of the polarisability-polarisability time correlation function (see eq. (1.18)). OKE data can be analysed directly in the time-domain, or it can be Fourier transformed into the frequency domain. By preference, this work primarily presents OKE data in the form of frequency-domain spectra (FDS). Before one can perform a FT however, the raw time-domain trace (TDT) must first undergo processing and analysis. Once successfully converted from TDT to FDS, there are various analytical and empirical function that are commonly used to explain the spectral line-shape. The functions applied throughout this work will be introduced in this chapter.

3.1 OKE Signal Processing

The time-domain material response, $R(t)$, contains both the nuclear and electronic response of the system ($R_n(t)$ and $R_e(t)$ respectively). The electronic response to the electric field is essentially instantaneous, while nuclei have much greater mass and thus move on longer timescales; these motions are the molecular dynamics of interest. The time domain OKE experiment (as outlined in section 2.1) does not directly access $R(t)$, rather its convolution with the pump-probe autocorrelation trace, $G^{(2)}(t)$:⁴⁸

$$S_{OKE}(\tau) \propto \int_{-\infty}^{\infty} dt R(t - \tau) G^{(2)}(t). \quad (3.1)$$

$G^{(2)}(t)$ is experimentally available *via* the instantaneous electronic contribution to $S_{OKE}(\tau)$, which mirrors the temporal intensity profile of the laser pulse itself. This is convenient as both $G^{(2)}(t)$ and $S_{OKE}(\tau)$ are gathered in the same experiment (see Figure 3.1). A transform-limited, ultrashort pulse from a mode-locked laser typically exhibits a squared hyperbolic-secant temporal shape. $G^{(2)}(t)$ in this work tends to follow this line-shape given as

$$G^{(2)}(t) \propto \operatorname{sech}^2\left(\frac{t}{t_w}\right), \quad (3.2)$$

where t_w is a width parameter. The response function can then be recovered through the following Fourier transform relationship:

$$\mathcal{F}[R(t)] \propto \frac{\mathcal{F}[S_{OKE}(\tau)]}{\mathcal{F}[G^{(2)}(\tau)]}. \quad (3.3)$$

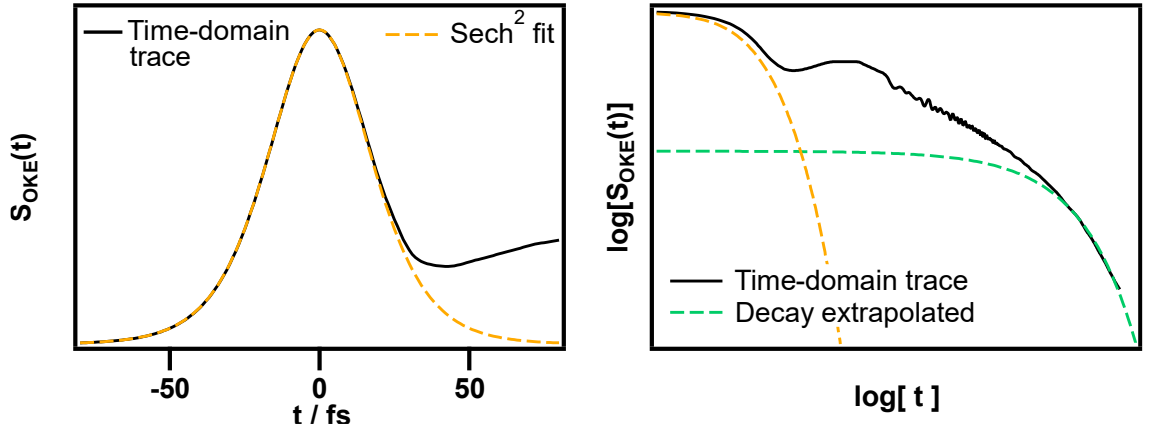


Figure 3.1. Time-domain OKE data fitting of the electronic response and the signal decay.

Example of the time-domain signal processing method. **Left:** The instantaneous electronic response part of the TDT fit to a hyperbolic-secant-squared line-shape, which is then used as a model for $G^{(2)}(t)$. **Right:** The entire TDT at positive pump-probe delay times, plotted on a log-log scale. The signal is extrapolated *via* fitting of the decay slope at longer times.

Using the Born-Oppenheimer approximation, the material response function can be considered as the sum of electronic and nuclear components, $R(t) = R_e(t) + R_n(t)$, of which $R_e(t)$ is a real term. The imaginary term of $\mathcal{F}[R(t)]$ provides the OKE (nuclear) response in the frequency domain:^{44,48}

$$S_{OKE}(\omega) = \text{Im}\{\mathcal{F}[R(t)]\} \equiv \text{Im}\{\mathcal{F}[R_n(t)]\}. \quad (3.4)$$

Figure 3.2 shows the resultant OKE FDS. This work will primarily present OKE results in their *linear* FDS form, *i.e.*, $S_{OKE}(\omega/2\pi)$, but will often be referred to simply as S_{OKE} .

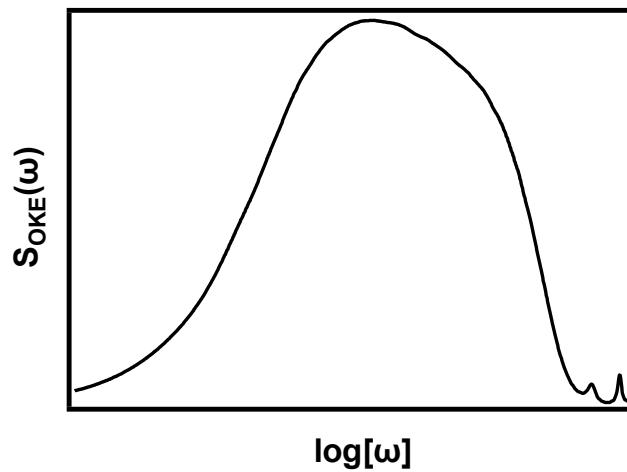


Figure 3.2. Resultant frequency domain spectrum after Fourier-transform deconvolution.

Example OKE FDS is shown with a logarithmic frequency axis.

In this work many traces are gathered (always >50 , but typically ~ 100) and averaged to produce a single TDT before any data analysis commences. The set-up used here probes dynamics across several orders of magnitude in time. To accomplish this, the data is taken with fs temporal resolution at short delay times to capture high frequency dynamics, and extends to logarithmic temporal steps as the maximum pulse delay of 1 ns is approached (the final step is often the order of 100 ps). This method ensures that molecular dynamics on all experimentally accessible timescales are indeed probed.

The quality of the resultant FDS can be further improved through the use of additional signal processing methods. One such example shown in Figure 3.1 is that the signal decay may be extrapolated beyond the maximum experimentally accessible delay time. This may be appropriate for high SNR TDTs, where the decay slope can be easily characterised; this is not appropriate for materials that exhibit more complex/ambiguous diffusive dynamics. Typical time-domain decay curves used for extrapolation are introduced in section 3.2 below. The data may also be zero-padded (lengthening the data set by appending zeros), which is standard practice to smooth the frequency domain spectrum by artificially increasing its resolution.

3.2 Spectral Line-Shapes

There exist many line-shape functions, both analytical and empirical, that can be applied to produce a frequency-domain interpretation of molecular dynamics. Dynamics occur in real time of course and should therefore also be considered in the time domain.

3.2.1 Relaxations and Diffusive Motions

The simplest case of anisotropy relaxation follows a simple exponential decay in the time domain,

$$\phi(t) = A \cdot \exp\left(\frac{-t}{\tau}\right), \quad (3.5)$$

where τ is the characteristic relaxation lifetime of the system and A is the initial amplitude. Indeed, many of the OKE TDTs in this work are observed to decay according to this relationship. The FT of this function yields the well-known Debye function,

$$D(\omega) = \frac{A_D}{1 + i\omega\tau}, \quad (3.6)$$

the imaginary part of which is used to fit the FDS OKE spectra.

In their study of the dielectric relaxation of polymers, Williams and Watts observed that dielectric relaxation can be a more protracted phenomenon, conforming instead to an empirically stretched version of the exponential decay.⁴⁹ The stretched exponential function was actually first used by Kohlrausch, but in the context of capacitor charge,⁵⁰ over a century prior. The stretched exponential equation,

$$\phi_{KWW}(t) = A \cdot \exp \left[- \left(\frac{t}{\tau_{KWW}} \right)^\gamma \right] \quad (3.7)$$

is therefore also known as the Kohlrausch-Williams-Watts (KWW) function. The parameter γ introduces the stretching and takes on values $0 < \gamma \leq 1$. There is no analytical expression for the FT of the KWW function,⁵¹ however there is an analogous empirical modification to the Debye function introduced by Havriliak and Negami⁵² that is used to model such dynamics in the frequency domain, given as

$$H_{\alpha,\beta}(\omega) = \frac{A_H}{(1 + (i\omega\tau)^{\beta_{CC}})^{\alpha_{CD}}}, \quad (3.8)$$

where $0 < \alpha_{CD}, \beta_{CC} \leq 1$. The HN equation reverts to the Debye function when $\alpha_{CD}, \beta_{CC} = 1$, the Cole-Cole (CC) function when $\alpha_{CD} = 1 > \beta_{CC}$, and the Cole-Davidson (CD) function when $\beta_{CC} = 1 > \alpha_{CD}$. In this work, the Cole-Davidson parameter is always set to a value of one, making it superfluous here.

For pure rotations, the orientational diffusion lifetime observed in OKE spectroscopy is related to the diffusion rate through the relation¹⁶

$$\tau_r = \frac{1}{6D_r}, \quad (3.9)$$

where D_r is the rotational diffusion constant, whose general form was introduced previously as the Stokes-Einstein relation (see eq.(1.3)). This τ_r lifetime is thus calculable theoretically, and it can often (but not always) reflect the experimental τ obtained through modelling of real OKE relaxation data.

Birefringence relaxation can only commence after the sample material has become birefringent, which as mentioned in section 1.8, is not instantaneous with the pump pulse. A small delay will be present between the pump pulse ‘torque kick’ at $t = 0$ and the time of maximum birefringence. This delay is simply due to molecular inertia, and can be accounted for using an inertial rise factor:^{53,54}

$$\phi_I(t) = \phi(t)(1 - e^{-t/\tau_I}). \quad (3.10)$$

Again, the effect of inertia on the frequency domain spectrum has been accounted for using the a phenomenological modification to the CC function, a simplified version of which is given by⁵⁵

$$iCC_{\beta}(\omega) = \frac{A_I}{1 + (i\omega\tau)^{\beta_{CC}}} - \frac{A_I}{1 + (i\omega\tau + \Omega_I\tau)^{\beta_{CC}}}, \quad (3.11)$$

where Ω_I acts as a high-frequency limit beyond which the diffusive line-shape intensity is suppressed. The inertial Cole-Cole (iCC) and inertial Debye (iD, when $\beta_{CC} = 1$) functions are particularly useful when the high frequency tail of diffusive overextends well into the THz region. One would not expect, for example, molecular orientational diffusion to occur on faster timescales than single-molecule librational motions, since the librational timescales effectively define the how quickly the molecules themselves can rotate.

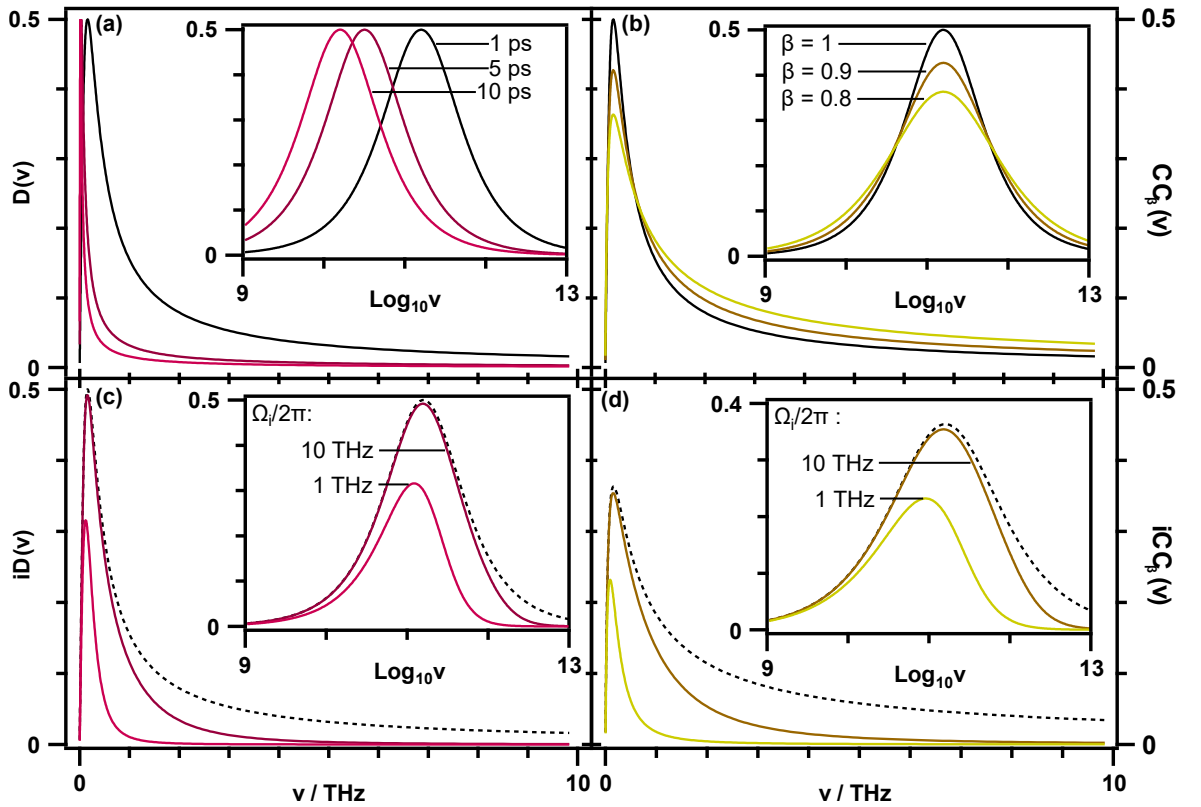


Figure 3.3. The Cole-Cole and Debye line-shapes, and their ‘inertial’ variations.

Each curve is displayed on a linear (main) and logarithmic (inset) scale. Due to their β_{CC} values, black solid curves are Debye line-shapes, red curves indicate Debye/inertial Debye line-shapes, and yellow curves indicate Cole-Cole/inertial Cole-Cole line-shapes. The dashed lines show the non-inertia-limited cases. **(a)** Debye line-shape for various τ values, where $A_D = 1$. **(b)** Cole-Cole line-shapes for various β values, where $A_{CC} = \tau/ps = 1$. **(c)** Inertial Debye line-shapes for various Ω_I values, where $A_{iD} = \tau/ps = 1$. **(d)** Inertial Cole-Cole line-shapes for various Ω_I values, where $A_{iCC} = \tau/ps = 1$ and $\beta = 0.8$.

Figure 3.3 shows and compares the forms of equations (3.8) and (3.11) for the case of regular and inertial Debye and Cole-Cole line-shapes. The Cole-Cole function is broadened

as the β_{CC} parameter is lowered from unity, while the inertial modification to these functions is observable as the reduction of the high frequency wing of the line-shape.

3.2.2 The Brownian Oscillator

The Brownian Oscillator (BO) can be used to model homogeneously-broadened intra- and intermolecular vibrational modes.^{56,57} It is the frequency domain expression of a damped harmonic oscillator (DHO), taking the form:

$$BO(\omega) = \frac{A_{BO}\omega_0^2}{\omega_0^2 - \omega(\omega + i\gamma)}, \quad (3.12)$$

where ω_0 is the central frequency of the *undamped* oscillator and γ is the damping rate. Critical damping occurs at $\gamma = 2\omega_0$, and the limit of $\gamma \gg \omega_0$ returns the Debye function. Its line-shape is illustrated in Figure 3.4, alongside its variation with ω_0 and γ .

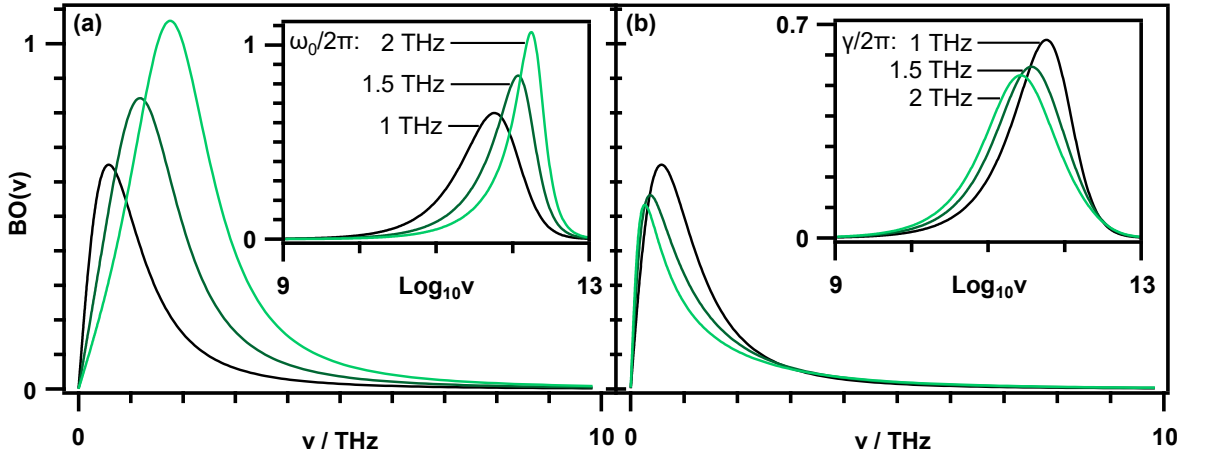


Figure 3.4. The Brownian oscillator line-shape.

(a) BO line-shape for various ω_0 values, where $A_{BO} = \gamma/2\pi/\text{THz} = 1$. (b) BO line-shape for various γ values, where $A_{BO} = \omega_0/2\pi/\text{THz} = 1$. Each curve is displayed on a linear (main) and logarithmic (inset) scale.

Clearly from Figure 3.4 (b), the damping has an effect on the frequency of the oscillation—the greater the damping the lower the frequency. This is intuitive, as in the overdamped regime there is no oscillation by definition, only a decay to the equilibrium state. Only underdamped modes ($\omega_0 > \gamma/2$) oscillate. The frequency of the damped harmonic oscillator is given by

$$\omega_{\text{DHO}} = \sqrt{\omega_0^2 - \gamma^2/4}. \quad (3.13)$$

The undamped ($\gamma = 0$) oscillator frequency therefore represents the maximum frequency.

3.2.3 The Anti-symmetrised Gaussian

The anti-symmetrised Gaussian (ASG) function is used to model inhomogeneously-broadened vibrational modes and has the form^{58,59}

$$\text{ASG}(\omega) = A_G \left[e^{-\frac{(\omega-\omega_G)^2}{\sigma_G^2}} - e^{-\frac{(\omega+\omega_G)^2}{\sigma_G^2}} \right], \quad (3.14)$$

where ω_G is the Gaussian frequency and σ_G is related to the full width at half-maximum (FWHM) of the ASG by $\sigma_{FWHM} = 2\sigma_G\sqrt{\ln(2)}$. Figure 3.5 shows the ASG function and its variation with ω_G and σ_G .

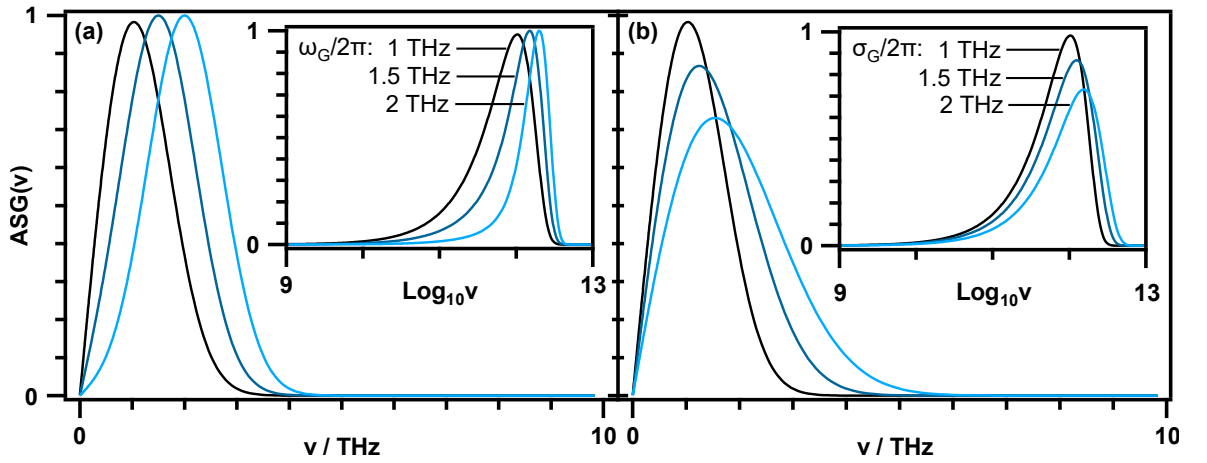


Figure 3.5. The anti-symmetrised Gaussian line-shape.

(a) ASG line-shape for various ω_G values, where $A_G = \sigma_G/2\pi/\text{THz} = 1$. (b) ASG line-shape for various σ_G values, where $A_G = \omega_G/2\pi/\text{THz} = 1$. Each curve is displayed on a linear (main) and logarithmic (inset) scale

The Gaussian amplitude can also be expressed as

$$A_G = \frac{A'_G}{\sigma_G\sqrt{2\pi}}. \quad (3.15)$$

3.2.4 The Ohmic and Bucaro-Litovitz functions

The Bucaro-Litovitz (BL) line-shape was derived to model the spectra of isotropically polarisable liquids, whose signal is collision induced (CI).⁶⁰ The BL function has the form

$$\text{BL}(\omega) = A_{BL}\omega^\delta e^{-\frac{\omega}{\omega_{BL}}}, \quad (3.16)$$

where ω_{BL} is the BL frequency and δ is a parameter related to the strength of the molecular frame distortion during pairwise collisions, taking on values close to 1.

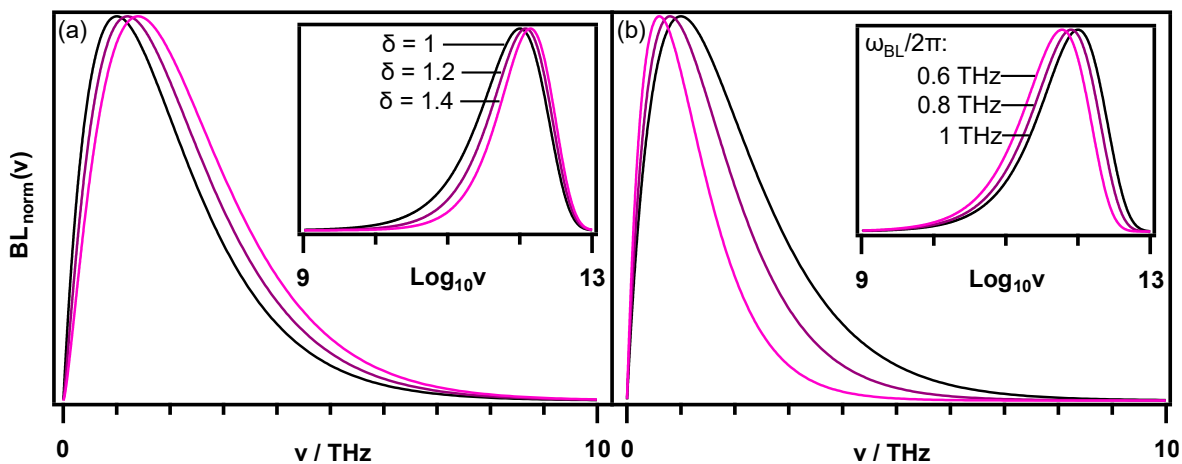


Figure 3.6. The Bucaro-Litovitz line-shape.

(a) The normalised BL function for various δ values, where $\omega_{BL}/2\pi = 1\text{THz}$. (b) The normalised BL line-shape for various ω_{BL} values, where $\delta = 1$. Each curve is displayed on a linear (main) and logarithmic (inset) scale. BL curves with $\delta = 1$ are Ohmic functions.

When $\delta = 1$ the BL reduces to the Ohmic function. BL line-shape intensities are highly sensitive to small changes in δ and ω_{BL} ; those shown on Figure 3.6 are normalised to enable illustration.

4 LIQUID HYDROCARBON DYNAMICS

With the exception of some additional data and further exploration of various concepts, the research which comprises this chapter has been published as an article entitled: “Low-Frequency (Gigahertz to Terahertz) Depolarized Raman Scattering off *n*-Alkanes, Cycloalkanes and Six-Membered Rings: A Physical Interpretation”, within the Journal of Physical Chemistry B. See ref.⁶¹ for details.

Throughout this chapter, the label of ‘ β -relaxation’ is applied to diffusive motions related to translational diffusion. Translational diffusion is found (in this work) to exhibit a largely similar dependence on viscosity as rotational diffusion, which is labelled as α -relaxation. It should be noted that within the research field focussed on the dynamics of glasses and glass-forming liquids, ‘ β -relaxation’ is a term which is often applied for relaxation process that strictly *do not* exhibit the same viscosity dependence as α -relaxation dynamics, while translational diffusive modes are instead subsumed into the α -band. Therefore, the labelling in this chapter, though entirely self-consistent, may be confusing to some experts in glass dynamics. One need only remember this fact while reading this chapter. This was appreciated post-publication. It should be noted, however, that a recent paper⁶² relates β -relaxation (a.k.a. Johari-Goldstein relaxation) to the local rearrangement of molecular cages and cage-breaking events, which is in-keeping with this chapter.

4.1 Introduction

Intermolecular dynamics consist of a broad range of interactions on many different time scales, typically anything ~ 1 ps or slower (≤ 1 THz). The corresponding low-frequency spectra are also broad, appearing as “blobs” lacking discernible features. The featureless character of gigahertz to terahertz spectra complicates the assignment of line shape contributions and therefore any subsequent interpretation.

Through instantaneous normal-mode analyses of molecular-dynamics simulations^{63–66} and comparisons with Stokes-Einstein-Debye theory for diffusion, it is understood that the highest frequencies are dominated by molecular librations (and possibly low-frequency

intramolecular modes, torsions in particular), while the lowest frequency response is due to molecular orientation relaxation. At intermediate frequencies, dynamics are predominantly translational in origin. In the 1970s, Bucaro and Litovitz suggested that motions at these frequencies could be approximated as pairwise collisions causing molecular frame distortions.^{60,67} Like the librational modes, collision-induced contributions at high frequencies are more localised ‘cage-rattling’ motions, becoming progressively more diffusive at lower frequencies; to distinguish them from the orientational motions, these will be referred to as translational (*i.e.*, collisional) in origin. This line-shape division is applied in dielectric relaxation spectroscopy (DRS), where orientational and translational diffusion are known as α and β -relaxation respectively, and ‘cage-rattling’ is referred to as a ‘fast- β ’ process (see Figure 4.1).^{68–70}

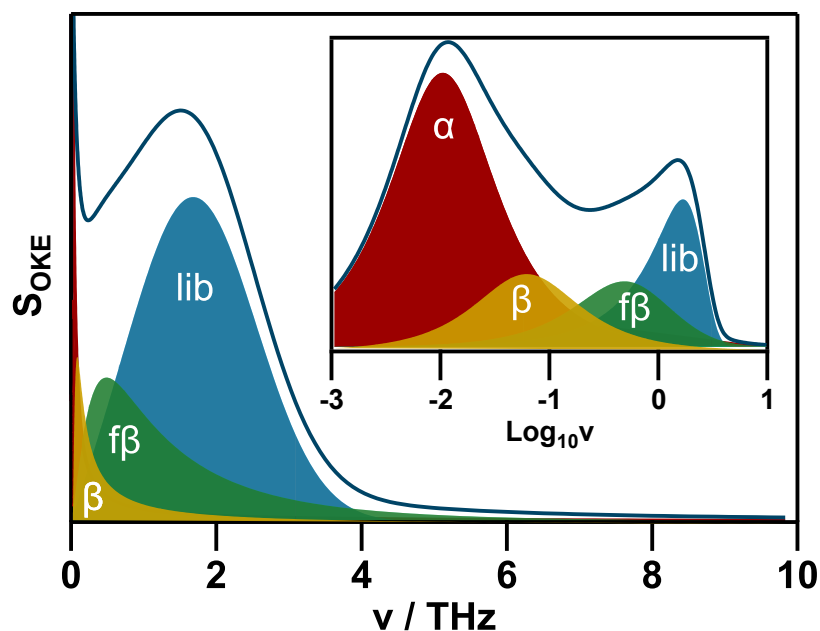


Figure 4.1. Generic form of the intermolecular vibrational spectrum of a weakly interacting liquid.

Contributions are generally identified as α -relaxation (orientational relaxation, red), β -relaxation (translational diffusion, yellow), fast- β (cage rattling, green), and librations (blue). Inset displays the same spectrum on a logarithmic frequency scale which is advantageous for highlighting the sub-terahertz part of the spectrum.

In reality however, all such dynamics are highly interdependent, and this method of spectral compartmentalisation produces a highly simplified interpretation. A potential alternative is the application of mode-coupling theory, which has been successfully used to describe depolarised light-scattering spectra of liquids.^{71–76} However, mode-coupling theory describes the low-frequency spectrum through an abstract Langevin equation with a memory kernel related to the static structure factor, whose physical meaning is more difficult to extract.^{77–79} Thus, spectral compartmentalisation may well give better physical insights, but is it *too* simplistic? In this work, the applicability of this approach is tested by applying it to

a wide range of molecular liquids whose intermolecular interactions are not expected to be particularly complex, especially *n*-alkanes and cycloalkanes, using ultrafast optical Kerr-effect (OKE) spectroscopy^{8,9,44,80–82} to measure the low-frequency depolarised Raman spectrum. This work shows that this ‘simplistic’ division in fact provides a realistic and consistent picture over a wide range of molecular sizes and temperatures. This picture can be extrapolated to interpret the dynamics of weakly anisotropic molecular liquids such as cyclohexane, and the (notoriously difficult to fit) spectra of liquids such as benzene. It will also be shown, by studying liquid methane, that both the α -relaxation and librations can be ‘switched-off’ through molecular symmetry^{83,84} to enable the study of the β -processes in isolation thereby emphasising the validity of the model.

4.2 Experimental

Liquids were purchased from Sigma-Aldrich with a rated purity $\geq 98\%$ with the exceptions of hexane, cyclopentene, and 1,4-cyclohexadiene, which have a purity $\geq 95\%$, and were used without further purification. Liquid samples were filtered with a PTFE filter (Millex) with 20 μm pore size and degassed for 1 min in an ultrasound bath before measurements. Room-temperature samples were contained in a 1 mm thick rectangular quartz cuvette (Starna) and held in a temperature-controlled (± 0.5 K) aluminium block. Low-temperature measurements were performed using a liquid-N₂ cryostat (Oxford Instruments, ± 0.1 K) in a nitrogen environment to avoid water condensation. Gaseous species were also purchased from Sigma-Aldrich with a purity $>99.9\%$; these were condensed into a similar cuvette within the cryostat attached to a sample-purged bladder valve.

In order to fit the OKE spectra a number of analytical functions have been used, all of which have been examined in detail in section 3.2. OKE signal contributions due to molecular orientational diffusion in this work mostly follow an exponential decay in the time domain that upon Fourier transform produces the well-known Debye line-shape (eq.(3.6)). Where possible, $S_{OKE}(t)$ decays are fit to exponential decays before FT deconvolution. For particularly fast decays with diffusion lifetimes only one order of magnitude-or-so slower than the librational/fast- β timescales, Havriliak-Negami line-shapes begin to protrude well into the THz region, which is unphysical (as discussed in section 3.2.1) and also produces a poor fit to the data. For these reasons, the inertial Havriliak-Negami line-shapes (eq.(3.11)) have been applied for all diffusive modes throughout for consistency, even for slowly diffusing molecules where the additional (inertia) parameter has little influence on the line-shape. For oscillatory dynamics, the Brownian oscillator is always applied to model the fast- β spectral contribution, while librations were found to conform to either a BO or an

antisymmetrised Gaussian function. The Bucaro-Litovitz line-shape also features in this chapter, but primarily to display its poor fit to data.

4.3 Modelling of Thermodynamic Properties

The OKE response is sensitive to the thermodynamic properties of the system under study, so the effect of altering temperature and hydrocarbon chain/ring size on such properties, particularly density and viscosity, must first be accounted for. Figure 4.2 shows the molarity trends across the various molecular series investigated in this work; six membered rings show a linear trend with molecular weight (or alternatively, number of π -electrons) while the n -alkanes and cycloalkanes are fit to power laws.

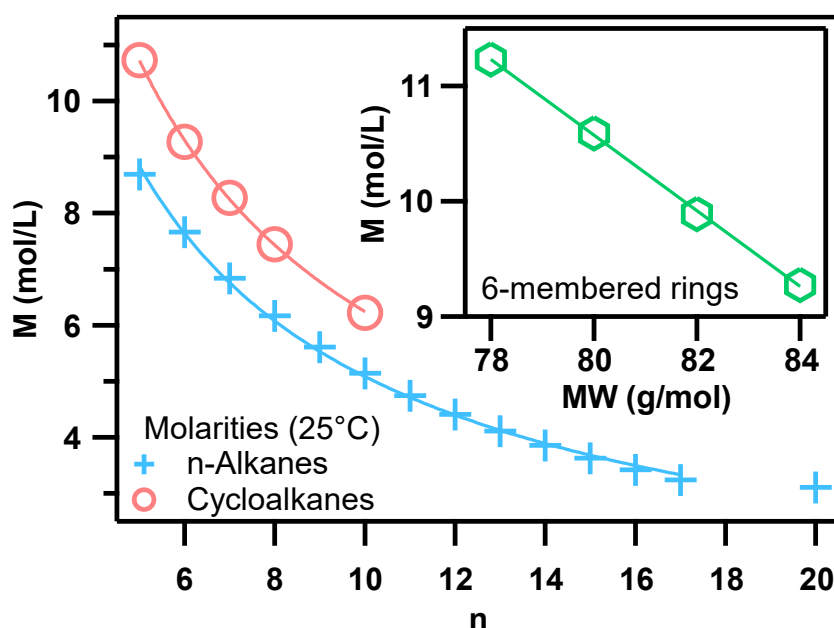


Figure 4.2. Trends in hydrocarbon molarities at 25°C.

Values are obtained from literature for n -alkanes⁸⁵ (+), cycloalkanes⁸⁶ (○), and 6-membered rings^{85,87} (◊) where the ring of 80 g/mol is 1,4-cyclohexadiene.

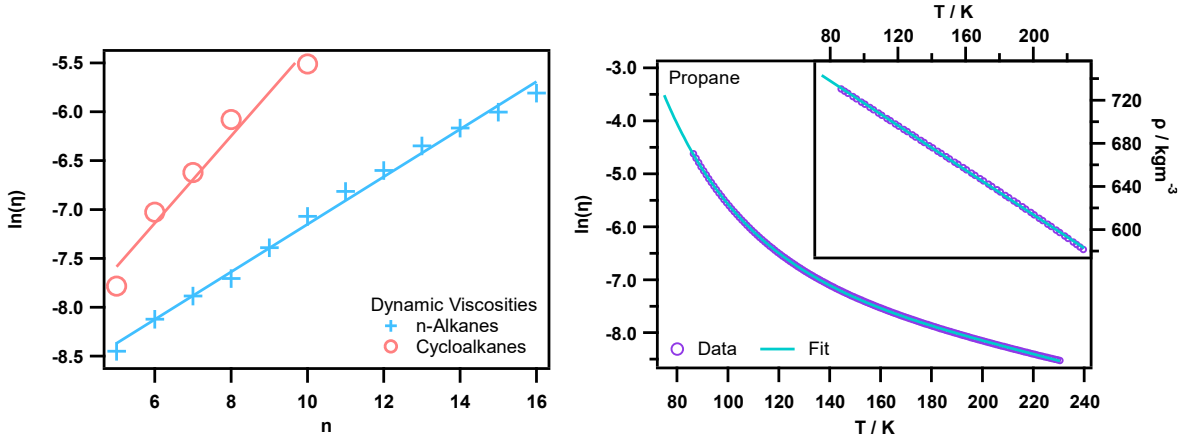


Figure 4.3. Viscosity trends in n -alkanes and cycloalkanes, and with temperature in propane.

Left: The relation between viscosity and molecular sizes are modelled using literature values for n -alkanes^{85,88–91} (+) and cycloalkanes⁸⁶ (○). **Right:** The temperature dependent viscosity (main) and density (inset) of liquid propane is modelled.⁸⁵

$$M_{alk} = 31.9n^{-0.79} \quad (4.1)$$

$$M_{cyc} = 37.7n^{-0.78} \quad (4.2)$$

The n -alkanes and cycloalkanes exhibit a very similar molarity dependence on molecular size as one might expect, with best fit values shown in eqs. (4.1) and (4.2) respectively. Dynamic viscosities appear to vary exponentially (to a reasonable approximation) with the number of carbons for n -alkanes and cycloalkanes. This of course produces straight line fits (equations (4.3) and (4.4)) when using the logarithm of viscosity as shown in Figure 4.3.

$$\ln(\eta_{alk}) = 0.24n_{alk} - 9.59 \quad (4.3)$$

$$\ln(\eta_{cyc}) = 0.45n_{cyc} - 9.81 \quad (4.4)$$

The relationship between viscosity and temperature in liquids must often be fit to empirical models, of which there are many. This work only requires an adequate fit of viscosity data, and so the $\eta(T)$ curve for liquid propane shown in Figure 4.3 has been fit to a commonly used four parameter model shown in eq.(4.5) with best fit values; this fit has been extrapolated into the supercooled regime.

$$\ln(\eta(T)) = -16.1 + 782T^{-1} + 3.44 \cdot 10^{-2}T - 6.99 \cdot 10^{-5}T^2 \quad (4.5)$$

$$\rho(T) = -1.03T + 821 \quad (4.6)$$

Finally, it will be necessary to consider the nature of translational and rotational diffusion for the molecules under study with more ‘exaggerated’ dimensionalities. Longer n -alkanes for example cannot be expected to diffuse as perfect spheres, they will instead be exposed to far greater solvent friction for rotations about both axes orthogonal to the molecular axis.

This will result in our observation of slower diffusive lifetimes than predicted by Stokes-Einstein-Debye. The friction factor of a tumbling rod-shaped molecule, $\zeta_{r,rod}$, is

$$\zeta_{r,rod} = \frac{\pi\eta L^3}{3[\ln(2L/d) - 0.5]}, \quad (4.7)$$

where L is the length of the rod (/cylinder), and d is the diameter.^{92–94} This friction factor is for ‘stick’ diffusion, but it can be used to calculate the ‘slip’ diffusion by applying a correction factor. Hu and Zwanzig⁹⁵ have derived the aspect ratio dependent slip friction factors of both oblate and prolate spheroids—illustrated in Figure 4.4 as the ratio of the slip friction factor to the stick friction factor of the same spheroid. These values can aid in the determination of orientational diffusion lifetimes for all chemical species under investigation, if such values do not conform to those predicted by SED theory.

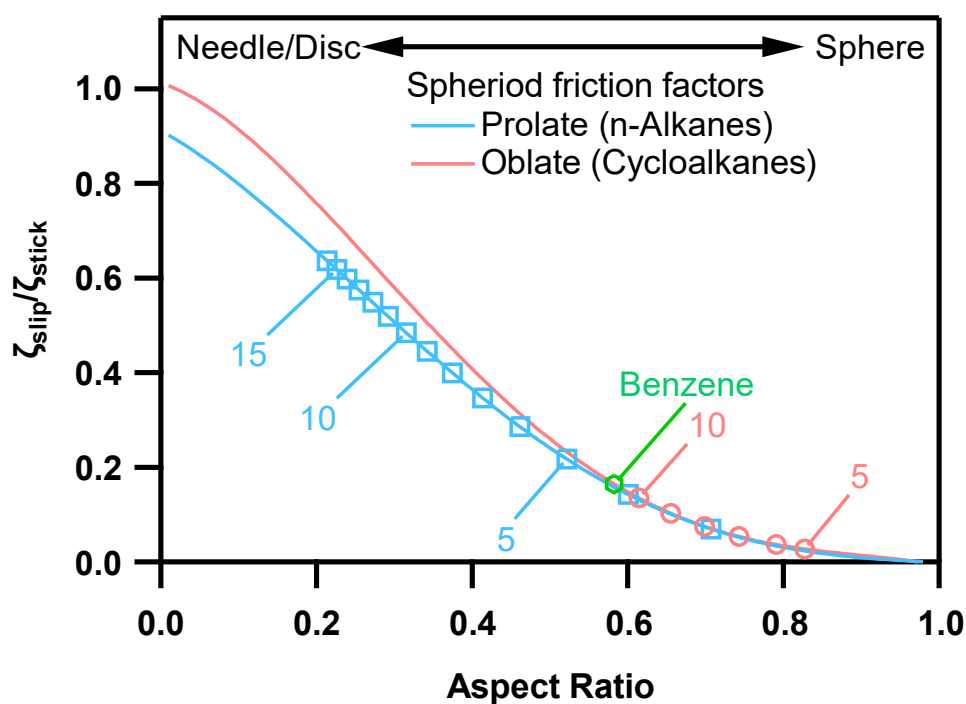


Figure 4.4. Slip to stick friction factor ratios as a function of aspect ratio.

Adapted from ref.⁹⁵. The positions of the n -alkanes (blue \square), cycloalkanes (red \circ), and benzene (green \circ) are marked along the appropriate prolate or oblate curve. The positions on the n -alkanes are strictly for the straight chain conformers.

The rod-like geometry ought to again be considered for translational diffusion lifetimes, $\zeta_{t,rod}$, and is given by⁹⁴

$$\zeta_{t,rod} = \frac{3\pi\eta L}{\ln(2L/d)}. \quad (4.8)$$

4.4 Calculation of Molecular Polarisabilities

The OKE signal is sensitive to the anisotropic part of the polarisability tensor,⁸⁰ and so it is important to gain insight into the molecular polarisabilities of the hydrocarbons under study. Molecular polarisability tensors, $\hat{\alpha}$, were computed using Gaussian09 software with 6-311++G(2df,p) level of theory. The polarisability tensor is given as

$$\hat{\alpha} = \begin{pmatrix} \alpha_{XX} & 0 & 0 \\ 0 & \alpha_{YY} & 0 \\ 0 & 0 & \alpha_{ZZ} \end{pmatrix}, \quad (4.9)$$

from which the isotropic and anisotropic polarisabilities, $\alpha(\hat{\alpha})$ and $\beta(\hat{\alpha})$ respectively, can be calculated using⁹⁶

$$\alpha(\hat{\alpha}) = \text{Tr}(\hat{\alpha})/3, \quad (4.10)$$

and

$$\beta(\hat{\alpha}) = \frac{1}{\sqrt{2}} \sqrt{(\alpha_{XX} - \alpha_{YY})^2 + (\alpha_{XX} - \alpha_{ZZ})^2 + (\alpha_{YY} - \alpha_{ZZ})^2}. \quad (4.11)$$

Computed polarisability tensor elements are given in Table 4.1, and the principal axes used here are illustrated in Figure 4.5. For the hydrocarbons considered here, the major contribution to polarisability comes from the carbon-carbon bonding electrons, which are more polarisable along the bond than perpendicular to it. Of course, π -bond electrons are more polarisable than σ -bond electrons perpendicular to the bond.

Linear alkanes C_nH_{2n+2}	α_{XX} / \AA^3	α_{YY} / \AA^3	α_{ZZ} / \AA^3	$\alpha(\hat{\alpha})$ / \AA^3	$\beta(\hat{\alpha})$ / \AA^3	Cyclo-alkanes C_nH_{2n}	α_{XX} / \AA^3	α_{YY} / \AA^3	α_{ZZ} / \AA^3	$\alpha(\hat{\alpha})$ / \AA^3	$\beta(\hat{\alpha})$ / \AA^3
n= 1	2.40	2.40	2.40	2.40	0.00	n= 3	6.04	6.04	5.30	5.79	0.74
2	4.65	4.21	4.21	4.36	0.45	4	8.00	8.00	6.91	7.64	1.09
3	6.93	6.28	5.96	6.39	0.85	5	10.0	10.0	8.73	9.58	1.27
4	9.46	8.08	7.65	8.40	1.64	6	12.0	12.0	10.6	11.5	1.40
5	11.9	9.96	9.28	10.4	2.38	7	14.3	14.0	12.2	13.5	1.97
6	14.5	11.8	10.9	12.4	3.24	8	16.4	16.0	13.8	15.4	2.43
7	17.1	13.5	12.5	14.4	4.18	9	18.4	18.2	15.5	17.4	2.81
8	19.8	15.4	14.2	16.5	5.11	10	21.0	19.7	16.9	19.2	3.63
9	22.4	17.1	15.8	18.4	6.06	11	23.1	22.2	18.6	21.3	4.12
10	24.7	18.8	17.3	20.3	6.78	12	25.0	24.7	20.2	23.3	4.66
11	27.3	20.5	18.9	22.3	7.77	cC ₆ H ₆	13.5	13.5	7.14	11.4	6.36
12	30.5	22.3	20.6	24.5	9.17	1,4-cC ₆ H ₈	14.8	10.9	8.15	11.3	5.79
						cC ₆ H ₁₀	12.7	10.6	8.91	10.7	3.29

Table 4.1. Calculated polarisability elements of various hydrocarbons.

For the n -alkanes, cycloalkanes, and unsaturated 6-membered rings, individual polarisability tensor elements as well as the isotropic and anisotropic polarisabilities of each molecule are shown. All units are cubic Angstroms.

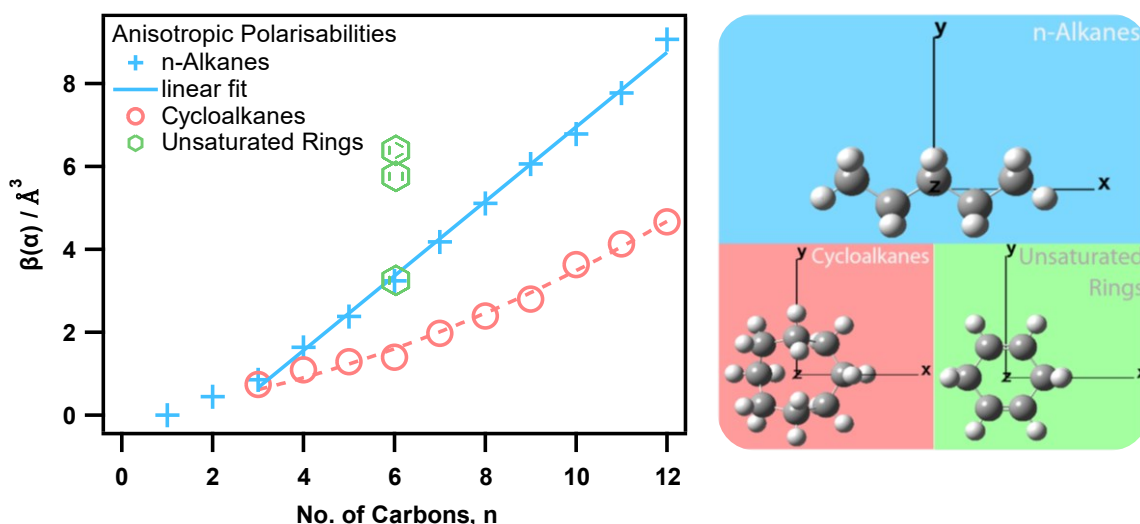


Figure 4.5. Molecular anisotropic polarisability trends in various hydrocarbons.

Left: Alkanes (+) and cycloalkanes (o) polarisabilities as a function of chain/ring size are shown as well as cyclohexene, 1,4-cyclohexadiene and benzene. The blue line shows the linear dependence of the anisotropic polarisabilities of *n*-alkanes longer than ethane with *n*, while the red curve is a quadratic line to guide the eye. **Right:** The *x*- and *y*-axes correspond to the *n*-alkanes' major and minor axes and the cycloalkanes' two major axes. The *x*-axis is aligned with the double bond(s) of the unsaturated rings. The *z*-axis is out-of-plane for all molecules.

Since increasing *n* simply reflects the addition of a single CH₂ group to each of these molecules one might expect the polarisability tensor elements, as well as the anisotropic polarisabilities, to exhibit a linear trend with *n*. This is certainly the case in the *n*-alkanes from propane onwards as seen in Figure 4.5; ethane is an exception for the simple reason that its calculated principal *x*-axis projects along the C-C bond. Whilst optimised linear geometries have been used for the *n*-alkanes, most cycloalkanes buckle under varying degrees of ring strain into various conformations. This may be responsible for the observed non-linearity in $\beta(\hat{\alpha})$ vs. *n*, which instead seems to follow an approximately quadratic curve.

4.5 *n*-Alkanes

First, one of the simplest series of molecular liquids will be considered: linear alkanes. Although, some of these liquids have been studied previously,^{97–100} the far superior signal-to-noise ratio in the experiments presented here allow new insights to be gained.

Figure 4.6 presents both the OKE time domain responses of various room temperature *n*-alkanes alongside their corresponding frequency domain spectra after Fourier transform deconvolution. The initial fast decay up to ~30 fs is the instantaneous electronic response of each liquid, which simply follows the laser pulse intensity profile. All slower dynamics are the nuclear motions of interest. Immediately clear in the FD spectra is the growing and red-

shifting orientational-relaxation band as *n*-alkane chains lengthen, however a deeper understanding of the dynamics at play requires these spectra to be fit to line-shapes.

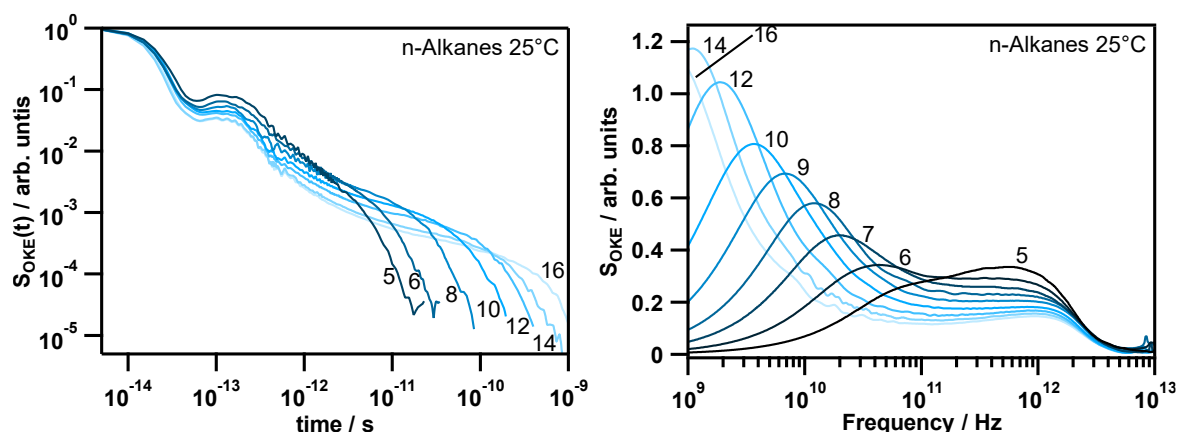


Figure 4.6. OKE spectra of various *n*-alkanes at 25°C.

The time domain OKE response (left), and the frequency domain OKE spectra after Fourier-transform deconvolution (right), are shown for labelled *n*-alkanes.

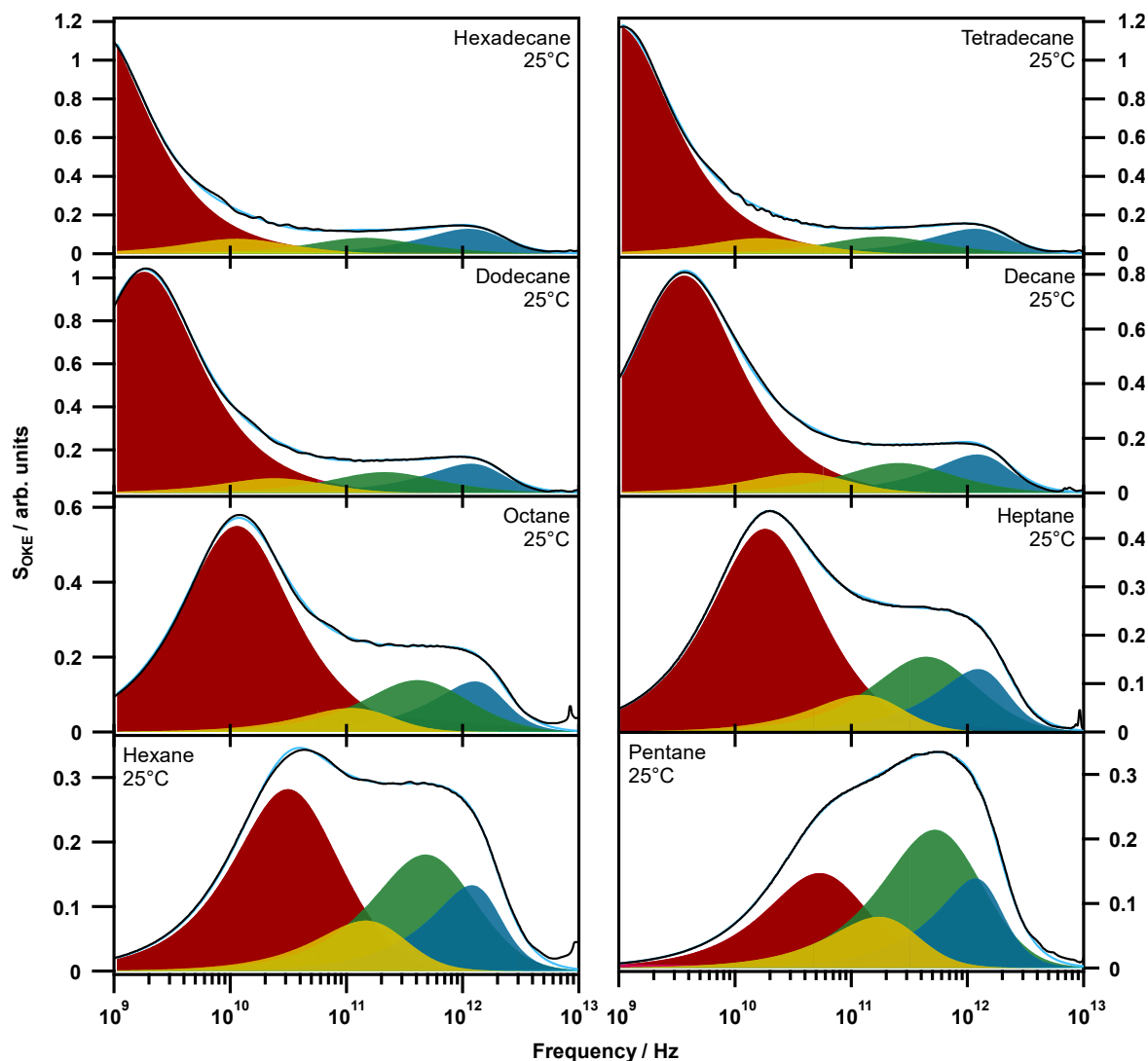


Figure 4.7. Line-shape fitting of *n*-alkane OKE spectra at 25°C.

The fits (blue line) of the data (black line) are comprised of the α -relaxation (red), β -relaxation (yellow), fast- β mode (green), and librational mode (blue).

Figure 4.7 shows the n -alkane OKE spectra fit to 4 functions: a single inertial Debye function for α -relaxation, either an iD or iCC function for β -relaxation, a single Brownian oscillator for the fast- β (cage-rattling) process, and another Brownian oscillator for librations. These spectra significantly broaden as chain lengths increase; this may need to be compensated for by either introducing (yet) more modes or simply by empirically broadening an existing mode. The former is potentially justifiable as one could resolve the α - and β -relaxations into separate orthogonal spatial components, however the latter essentially accomplishes the same outcome while maintaining continuity in the fit functions. β -relaxation is often typified by a Cole–Cole function in the frequency domain, it is sensible that it should be the preferentially broadened mode. Surprisingly, in these particular spectra, the line-shape fit improvement accomplished by broadening the inertial Debye β -relaxation into an inertial Cole-Cole is relatively minor and was therefore deemed unnecessary; it is necessary for other spectra explored later in this chapter.

Various forms of SED equation (particularly the friction factors therein) have been mentioned throughout this work, so it is important to pin down exactly which version is best suited to the n -alkanes' experimental diffusive lifetimes.

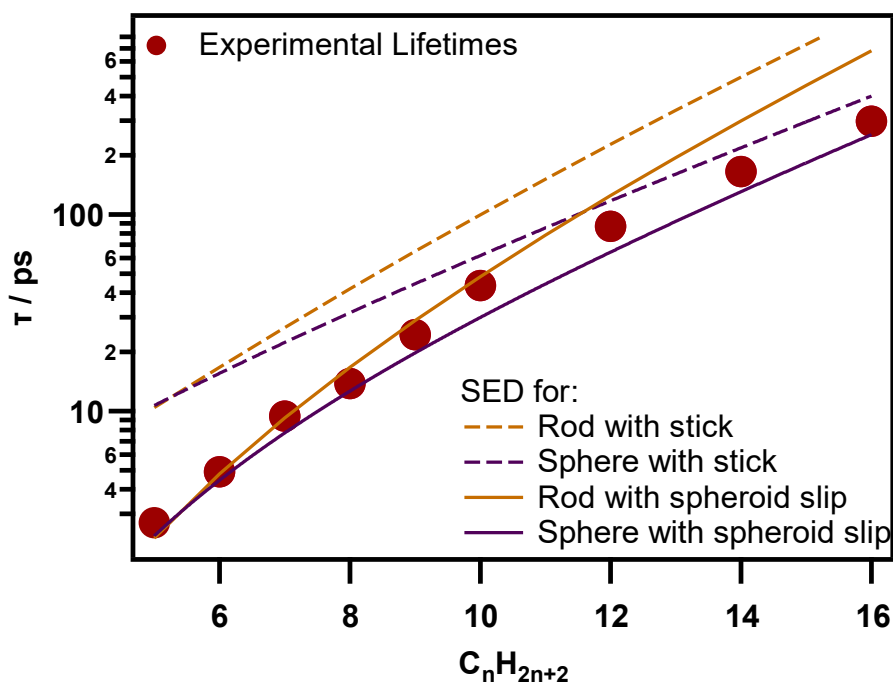


Figure 4.8. SED for slip and stick conditions with experimental n -alkane α -relaxation lifetimes.

Theoretical SED ‘stick’ (dashed lines) and ‘slip’ (solid lines) conditions for both spheres (purple) and rods (orange) are shown alongside the experimental lifetimes (●).

Figure 4.8 shows that firstly, the n -alkanes exhibit a closer overall conformity to ‘slip’ conditions. This is expected given the relatively weak intermolecular forces at play.

Secondly, the orientational diffusion lifetimes for *n*-alkanes up to decane can be well modelled with either rod or sphere SED—the former perhaps marginally superior. Finally, the largest *n*-alkanes here begin to diffuse more like spheres than rods. This can be attributed to the increased prevalence of gauche conformations; more “bent” *n*-alkanes should have shorter α -relaxation times as they become slightly less rod-like and more spherical.

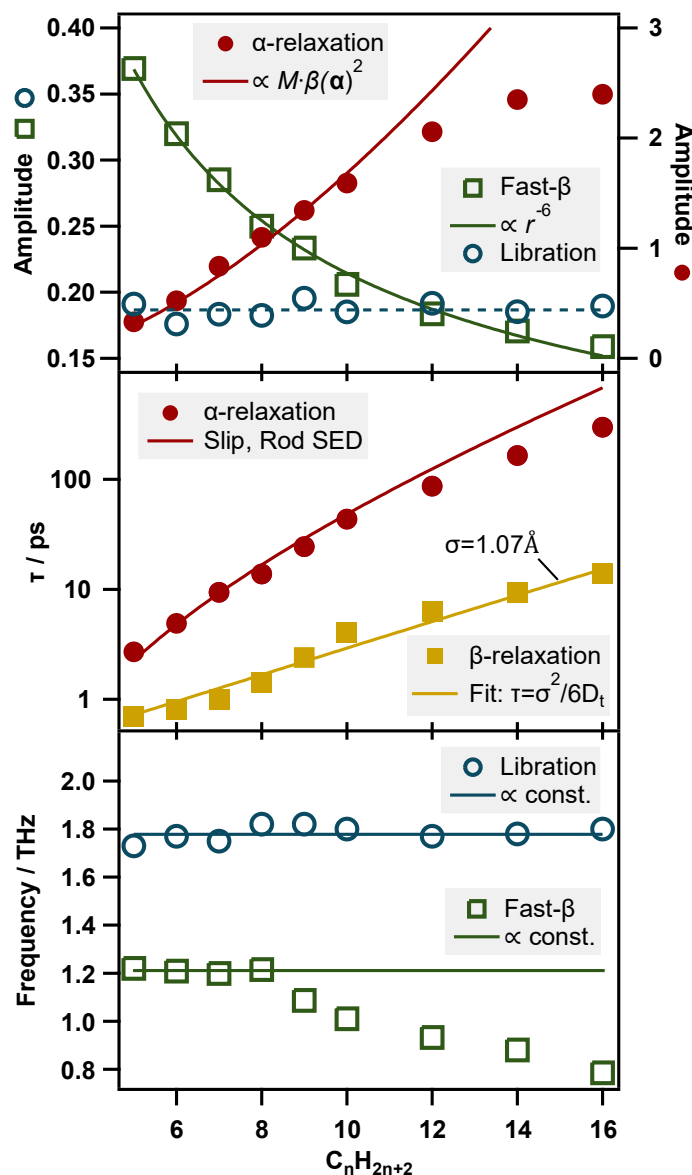


Figure 4.9. Fitting parameter trends in *n*-alkane OKE spectra vs chain length.

Shown are the fitting parameter values of the α -relaxation (red ●), β -relaxation (yellow ■), fast- β (green □), and libration (blue ○) line-shapes as a function of *n*-alkane chain length, *n*. The parameters displayed are the amplitudes (top), diffusive lifetimes (middle), and vibrational frequencies (bottom). See Appendix C.1 for fitting parameter values.

In this work the α -relaxation amplitude is expected to scale with $M \cdot \beta(\hat{\alpha})^2$, where *M* is the molarity of the liquid, which corrects for the changing number of molecules within the laser focus. Given that *M* varies as $n^{-0.79}$ (eq.(4.1)) and, as shown in Figure 4.5, $\beta(\hat{\alpha})$ scales linearly with *n*, the amplitude of the α -relaxation is proportional to $n^{1.21}$. This relationship is used to fit the data (see Figure 4.9) with some success for pentane to decane but ultimately

breaks down for longer chains. This comes as little surprise as chain-bending becomes more significant as discussed previously. Average end-to-end distances of the n -alkanes deviate from the straight chain by 5% for pentane up to 13% for dodecane,¹⁰¹ ultimately leading to a preferred hairpin conformation in hexadecane.¹⁰² Of course this bending effectively lends polarisability from the α_{XX} tensor element to the orthogonal elements, thereby reducing $\beta(\hat{\alpha})$.

Since the β -relaxation is translational and diffusive, its lifetime was fit to the Stokes-Einstein equation for rod diffusion. Setting the time as the experimental β -relaxation lifetime, $t = \tau_\beta$ (see eq(1.5)), produces a best fit value of σ_t of 1.07 Å, which is close to a van der Waals radius. Because of the proximity of the two β -modes, the amplitude of the β -relaxation is heavily dependent on its inertial rise frequency Ω_I which, as discussed in section 3.2, is fixed to the fast- β frequency. As a result, these amplitudes are not representative of the actual strength of the mode and are considered essentially useless. They have been omitted from analyses throughout this chapter.

The fast- β mode is a collision-induced signal, and as such its strength must depend on the interparticle distance. An expression for this dependence can be derived, starting with the most probable velocity, v , of a molecule in a Maxwell-Boltzmann distribution:

$$v^2 = \frac{2k_B T}{m}, \quad (4.12)$$

where T is the temperature and m is the mass of the molecule, which scales with the number of carbons, n . Next consider that each CH₂ unit has the same polarisability, and broadside collisions of long chains and short chains have different velocities at the same temperature. It follows that the CH₂ units in shorter chains (with greater velocities) more closely approach their nearest neighbours, and therefore yield a greater collision-induced signal. If the intermolecular repulsion falls off exponentially as

$$V(r) = V_0 \exp\left(-\frac{r}{r_0}\right), \quad (4.13)$$

where r is the interparticle distance, r_0 is close to the Bohr radius and V_0 (referred to as the repulsive or Buckingham potential) is $\sim 10^{-17}$ J.¹⁰³ This value is derived from calculations involving noble gas atoms, however it will be used here as a starting point for fitting the data presented here (but left as an unbound fitting parameter). Considering collisions at the most probable energy will lead to a minimum collision distance of

$$V(r) = V_0 \exp\left(-\frac{r}{r_0}\right) = \frac{1}{2}mv^2$$

$$\rightarrow r = -r_0 \ln\left(\frac{mv^2}{2V_0}\right).$$
(4.14)

The OKE signal scales with Π^2 (see section 1.7). From equations (1.16), (1.17), and (1.18), the collision induced OKE signal is proportional to r^{-6} . Combined with eq. (4.14) this becomes

$$S_{\text{CI}} \propto \ln^{-6}\left(\frac{mv^2}{2V_0}\right).$$
(4.15)

Referring only to a single CH₂ unit, this can be rewritten as

$$S_{\text{CI}} \propto \ln^{-6}\left(\frac{14av^2}{2V_0}\right),$$
(4.16)

where a is the atomic mass unit. Finally, using the entire molecule as the velocity of the CH₂ unit, this gives

$$S_{\text{CI}} \propto \ln^{-6}\left(\frac{7k_B T}{V_0(7n + C)}\right),$$
(4.17)

where n is the number of carbons and C is a constant with value 1 for n -alkanes (accounting for terminal hydrogens) or value 0 for cycloalkanes. By fitting the fast- β amplitude to this model, a V_0 value of 1×10^{-18} J is obtained (with fit shown in Figure 4.9).

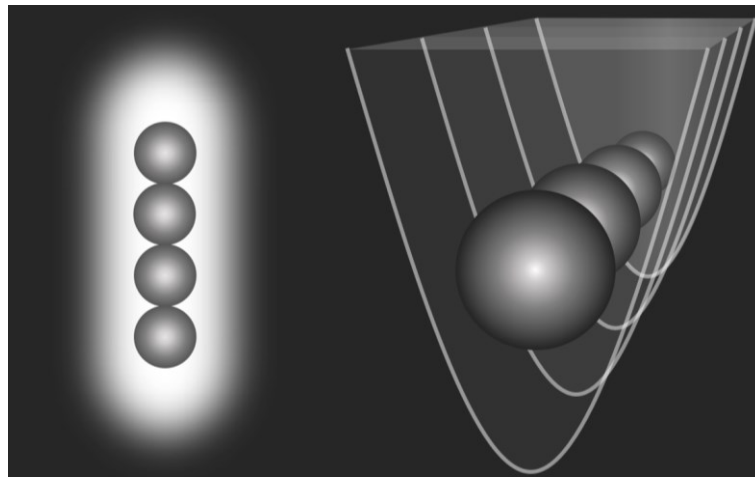


Figure 4.10. Cartoon of the time-averaged intermolecular potential landscape.

Left: the average liquid phase molecular cage around a simple chain molecule, represented by white free space. **Right:** discretised one-dimensional quadratic potentials about each unit.

To understand the effect of molecular size on the fast- β (cage rattling) oscillation, the intermolecular landscape around each molecule should be considered. Figure 4.10 illustrates the time-average intermolecular potential about a single alkane molecule, approximated by a linear chain of (CH_n) spheres. The fast- β process frequency appears to stay roughly

constant for short chains, eventually drops off with longer chains. The trend for short chains can be explained using the assumption of rigidity, whereas longer chains will become progressively floppier. Since the fast- β mode is collision-induced, collisions orthogonal to the molecular axis should produce the greatest collision-induced anisotropy. Assuming a harmonic potential, the intermolecular force, F_n felt by the molecule during a broadside translation can be defined simply as the sum of interatomic forces

$$F_n = -nkx, \quad (4.18)$$

where k is the force (or spring) constant and x is the displacement. Since $\omega_0 = \sqrt{k/m}$, where ω_0 is the angular frequency of the harmonic oscillator, and from eq.(4.18), the effective spring constant $k_{eff} = nk$, it is found that

$$\omega_0 \propto \sqrt{\frac{n}{n}} = 1. \quad (4.19)$$

The frequency of the fast- β mode is therefore expected to be independent of chain length or ring size. This does indeed match the experimental data for the fast- β of pentane up to octane. This suggests that nonane and beyond may become significantly floppy on these timescales. In fact, the simulated spectra of the n -alkanes only exhibit normal intramolecular modes at frequencies $\leq \omega_{\beta}$ at nonane onwards, effectively marking the end of the rigid rod regime.

Librations appear to remain at constant frequency throughout the series, which is not intuitive. In the rigid rod regime, where one can reasonably speak in terms of librations, one might expect an increasing moment of inertia for longer chains to result in a redshift, as with the orientational diffusion. On the contrary one can show mathematically that the librational frequency should remain constant. The total repulsive restoring force *via* the nearest-neighbour collision (using the simple time-averaged potential landscape of Figure 4.10) is calculable as the summation of individual restoring forces on each unit within the chain. A librating rigid rod is illustrated in Figure 4.11.

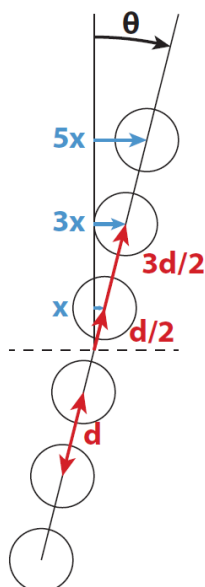


Figure 4.II. Cartoon of the radial displacement of the libration of a simple chain molecule.

Using the small angle approximation for an angle of libration, θ , atomic displacements (blue) are directly proportional to the radial atomic distances (red).

The moment of inertia of a simple chain-like molecule is of course dependent on the length of (or number of units in) the chain. Approximating the n -alkanes as a linear chain, where each unit in the chain corresponds (approximately) to a CH_2 group, then the moment of inertia I_n of the first 3 even number of carbon alkanes ($n = 2, 4, 6$) can be written as

$$I_2 = 2m \left(\frac{d}{2} \right)^2 = 2md^2 \frac{1}{4}, \quad (4.20)$$

$$I_4 = 2m \left[\left(\frac{d}{2} \right)^2 + \left(\frac{3d}{2} \right)^2 \right] = 2md^2 \frac{10}{4}, \quad (4.21)$$

$$I_6 = 2m \left[\left(\frac{d}{2} \right)^2 + \left(\frac{3d}{2} \right)^2 + \left(\frac{5d}{2} \right)^2 \right] = 2md^2 \frac{35}{4}, \quad (4.22)$$

where m is the mass of a CH_2 unit and d is the C-C bond length. The generalises to

$$I_n = 2md^2 \left[\sum_{i=2,4,6,\dots}^n \left(\frac{i-1}{2} \right)^2 \right] = 2md^2 \frac{1}{24} (n^2 - 1)n. \quad (4.23)$$

Now that the relationship between moment of inertia and alkyl chain length is derived, the restoring torque must be accounted for. The magnitude of the torque, T , is of course the perpendicular force times the distance from the centre of rotation; the restoring torque on each CH_2 unit is therefore given by Hooke's law. Again, for simplicity, total restoring torque on the first 3 'even' alkanes can be defined as follows:

$$T_2 = -2\kappa \left(x \frac{d}{2} \right) = -\kappa \frac{d^2}{2} \sin \theta \cong -\frac{1}{2} \kappa d^2 \theta \quad (4.24)$$

$$\begin{aligned} T_4 &= -2\kappa \left(x \frac{d}{2} + 3x \frac{3d}{2} \right) = -10\kappa x d \\ &= -10\kappa \frac{d^2}{2} \sin \theta \cong -5\kappa d^2 \theta \end{aligned} \quad (4.25)$$

$$\begin{aligned} T_6 &= -2\kappa \left(x \frac{d}{2} + 3x \frac{3d}{2} + 5x \frac{5d}{2} \right) = -35\kappa x d \\ &= -35\kappa \frac{d^2}{2} \sin \theta \cong -\frac{35}{2} \kappa d^2 \theta. \end{aligned} \quad (4.26)$$

Here, θ is the angle of libration, x is the displacement of the first (inner) CH₂ unit, κ is the angular Hooke's constant for each CH₂ group (with units of Nm/rad), and the factor of 2 arise through symmetry (as illustrated in Figure 4.11). The general form is therefore

$$\begin{aligned} T_n &= -2\kappa \left(x \frac{d}{2} + 3x \frac{3d}{2} + 5x \frac{5d}{2} + \dots \right) \\ &= -2\kappa \frac{d}{2} (1 + 3^2 + 5^2 + \dots) x \\ &= -2\kappa \theta \left(\frac{d}{2} \right)^2 (1 + 3^2 + 5^2 + \dots) \\ &= -2\kappa \theta \left(\frac{d}{2} \right)^2 \sum_{i=2,4,6,\dots}^n (i-1)^2 \\ &= -2\kappa \theta \left(\frac{d}{2} \right)^2 \frac{1}{6} n(n^2 - 1) = -\frac{1}{12} \kappa d^2 \theta n(n^2 - 1). \end{aligned} \quad (4.27)$$

The relationship between the restoring torque and n is therefore

$$T_n = -\kappa_{eff} \theta \propto n(n^2 - 1), \quad (4.28)$$

where

$$\kappa_{eff} = \frac{1}{12} \kappa d^2 n(n^2 - 1). \quad (4.29)$$

Finally, and with the combination of equations (4.23) and (4.29), the librational frequency, ω_{lib} depends on n as

$$\omega_{lib} = \sqrt{\frac{\kappa_{eff}}{I}} \propto \sqrt{\frac{n(n^2 - 1)}{(n^2 - 1)n}} = 1 \quad (4.30)$$

This proof can explain the ω_{lib} independence on n , however this continues beyond (what was previously referred to as) the rigid rod regime, which is perhaps surprising.

Finally, understanding how the amplitude of the libration *should* scale with n is complicated. For example, the reduction in free angle of libration as n -alkane chains extend will have a depressive impact on A_{lib} ; longer chains have a greater $\beta(\hat{\alpha})$ enhancing A_{lib} ; fewer larger molecules will be probed by the laser in the same volume, depressing A_{lib} , *etc.* Molecular collisions can also enhance the (anisotropic) polarisability⁴² to varying degrees. This work suggests that all such influences appear to produce a cancelling effect, making the librational amplitude appear largely independent on n . It should be noted that the contributions to the spectra from Raman active intramolecular mode(s) at librational frequencies or lower, that are expected (by calculation at least) to occur from n -octane onwards, cannot be resolved here. Instead their contributions to the OKE spectra are subsumed into the ‘intermolecular’ bands.

4.6 Methane

Although α -relaxation and librations are strictly speaking delocalised collective motions, their amplitude depends directly on the molecular anisotropic polarisability tensor, which is zero (or very near zero) in molecules with a high degree of symmetry such as tetrahedral and octahedral.^{47,56,84,104,105} For this reason, it is useful to consider the OKE spectrum of liquid methane, which will be purely collision-induced due to its tetrahedral symmetry. Traditional fitting procedures of such isotropic liquids dictate that a single Bucaro–Litovitz function should account for the dynamics. Figure 4.12(a) shows the best fit of the spectrum using a Bucaro–Litovitz function.

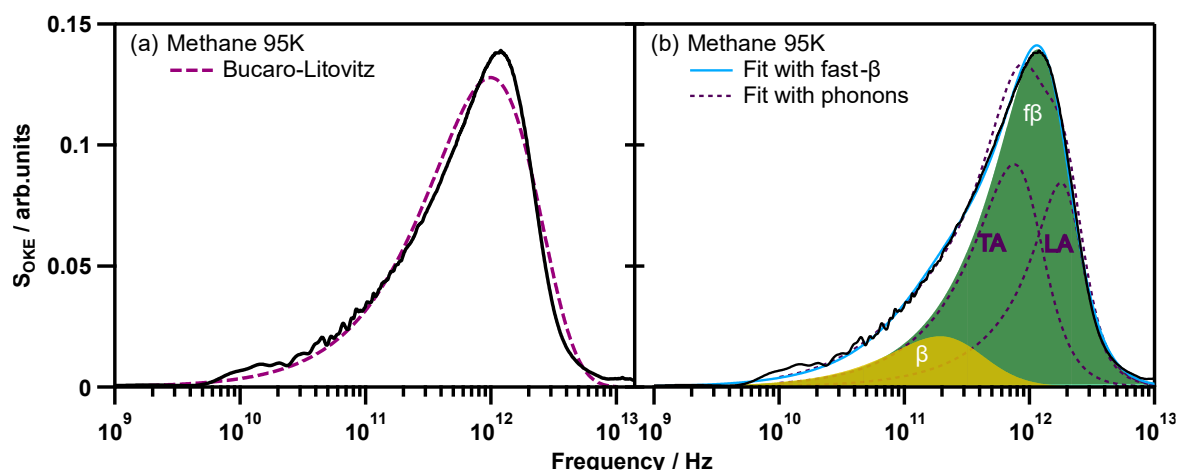


Figure 4.12. OKE spectrum of liquid methane at 95K with various fits.

The liquid methane data (black lines) are shown with: (a) the best fit Bucaro-Litovitz curve (dashed line), and (b) line-shape fitting composed of a fast- β mode (green) and β -relaxation (yellow). Also shown in (b) are line-shapes representing the transverse and longitudinal acoustic (TA and LA) phonon modes of solid methane. See Table 4.2 for values.

	β -relaxation				Fast- β			Bucaro-Litovitz			TA Phonon			LA Phonon		
	A_{CC} / 10^{-1}	τ / ps	β	Ω_I / THz	A_B / 10^{-1}	$\omega_0/2\pi$ / THz	$\gamma/2\pi$ / THz	A_{BL} / 10^{-4}	$\omega_{BL}/2\pi$ / THz	δ	A_B / 10^{-1}	$\omega_0/2\pi$ / THz	$\gamma/2\pi$ / THz	A_B / 10^{-1}	$\omega_0/2\pi$ / THz	$\gamma/2\pi$ / THz
a)	-	-	-	-	-	-	-	2.60	0.95	1.05	-	-	-	-	-	-
b)	0.67	0.64	0.93	1.65	1.88	1.65	1.32	-	-	-	-	-	-	-	-	-
b)	0.67	0.64	0.93	1.65	-	-	-	-	-	-	1.15	1.00	0.72	0.86	2.10	1.15

Table 4.2. Fitting parameter values for various fits of the methane OKE spectrum.

Values correspond to the fitting parameters used in Figure 4.12 (a) and (b). The β -relaxation Ω_I is fixed to the fast- β ω_0 . TA and LA phonon modes are used for illustrative purposes only, so the same β -relaxation iCC function was applied. Phonon ω_0 values are fixed to literature values.¹⁰⁶

The Bucaro–Litovitz function was derived almost 50 years ago and is used abundantly to date. Its contribution has been substantial, but in highly simplified spectra such as in this work, the BL function performs no better than a single antisymmetrised Gaussian or Brownian oscillator in fitting the spectra and is clearly inappropriate. If the same interpretation is applied as that for the other n -alkanes, liquid methane should still have a vastly simplified spectrum that only exhibits β -processes that can be well-modelled using two modes as shown in Figure 4.12 (the fit parameters are listed in Table 4.2).

As the name suggests, the strength of a collision-induced signal exhibits an inverse relationship with intermolecular separation; in terms of a crystal, Brillouin-zone edge phonons would produce the greatest collision-induced signal. The Brillouin-zone edge transverse and longitudinal acoustic (TA and LA) phonon frequencies of the plastic phase of solid methane were used to fit the OKE spectrum of liquid methane.¹⁰⁶ This is of course unreasonable in the liquid phase and it unsurprisingly produces a poor fit, but this nonetheless illustrates the potential origin of the rattling dynamics described by the fast- β mode in the disordered liquid. The data are well-modelled by this fast- β mode represented as a single Brownian oscillator. The low frequency β -relaxation accounts for more diffusive motions and is thus modelled by the inertial Debye function introduced previously, which suppresses the high-frequency slope to prevent any unphysical encroachment beyond the fast- β oscillation. The β -relaxation lifetime corresponds to a diffusion length of 1.08 Å, similar to that seen in the n -alkanes.

4.7 Propane

It is also important that consistent fits can be obtained as a function of temperature with this procedure. Propane was chosen first because of its broad liquid phase range (85–231 K).

Measurements were taken between 210 and 78 K (into the supercooled regime), corresponding to a 100-fold increase in viscosity that produces a significant evolution of the spectral line-shape. At the same time, propane has an anisotropic polarisability even smaller than cyclohexane and cyclopentane, making it relevant to other more popularly studied weakly anisotropic molecules. Figure 4.13 shows the OKE response at five temperatures. At 210 K the spectrum exhibits a monomodal appearance but broadens significantly on cooling. Even before line-shape fitting, these spectra suggest two distinct types of dynamics: those whose frequencies are either highly dependent or mostly independent of temperature. These spectra were fitted, as shown in Figure 11, in the same manner as the longer alkanes with the exceptions of the libration, which fit to an antisymmetrised Gaussian function and the β -relaxation at 78 K, which required an inertial Cole–Cole function. Discrete contributions to the spectrum are impossible to spot in the 210 K data alone, but the individual modes can be tracked from the supercooled liquid. The diffusive modes exhibit the most significant change with temperature, accounting for an increasing proportion of the spectrum at lower temperatures until the β -relaxation becomes an inertial Cole–Cole function to fit the broad, flat line-shape from ca. 200 down to 20 GHz.

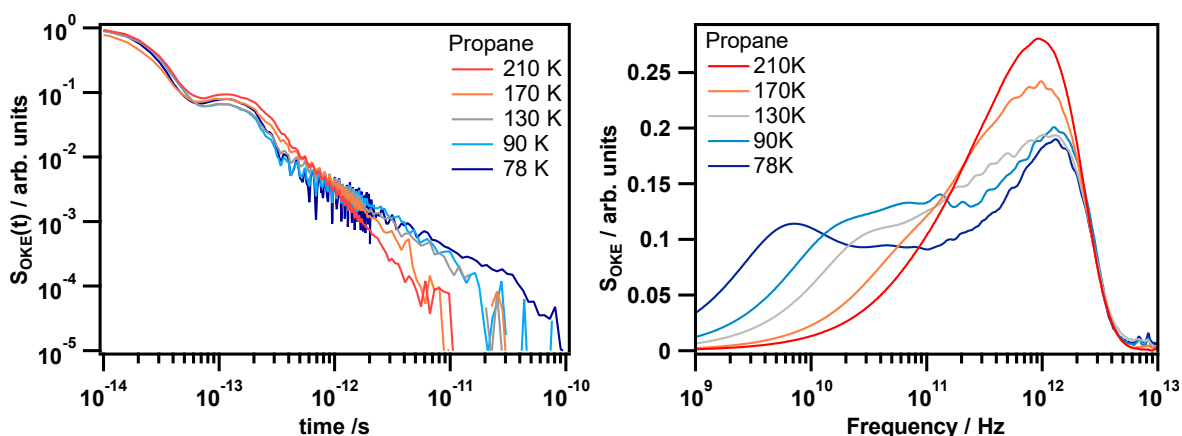


Figure 4.13. OKE spectra of liquid propane at various temperatures.

The time domain OKE response (left), and the frequency domain OKE spectra after Fourier-transform deconvolution (right), are shown for propane at various temperatures.

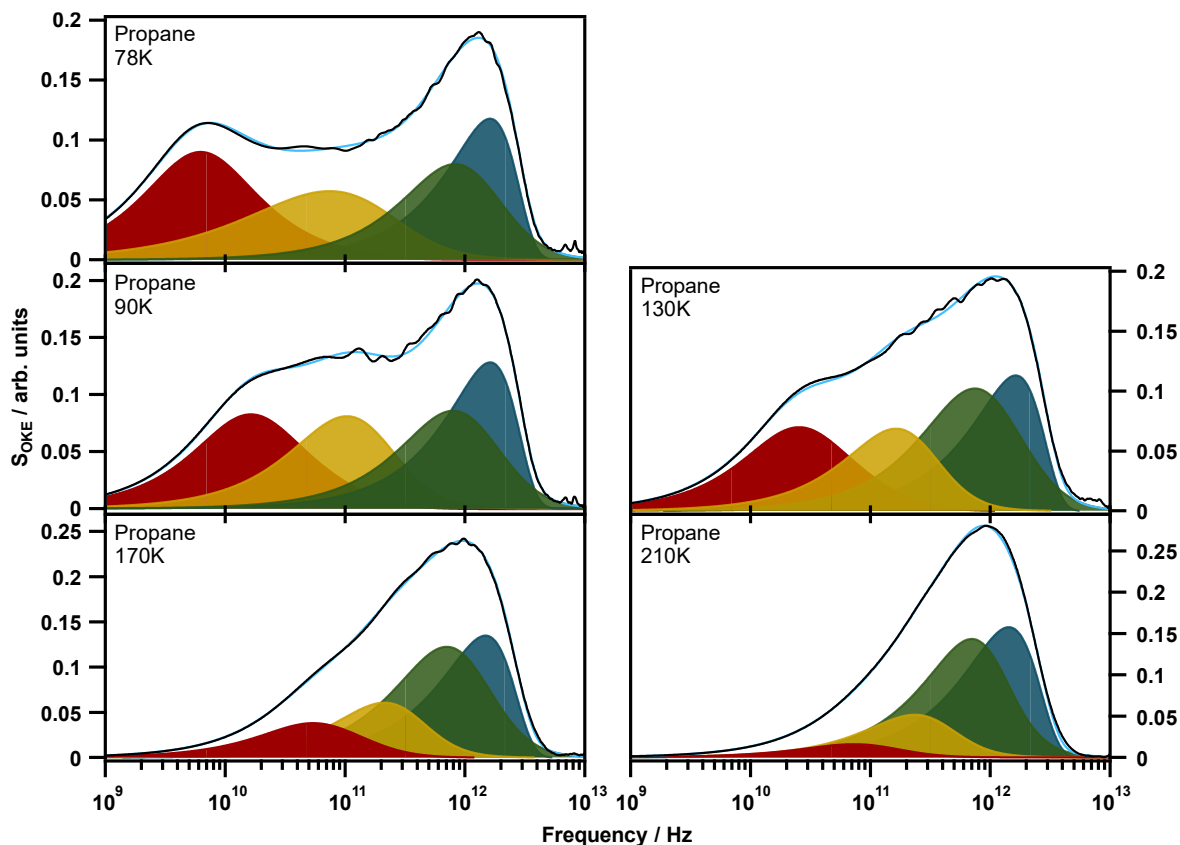


Figure 4.14. Line-shape fitting of liquid propane OKE spectra at various temperatures.

The fits (blue line) of the data (black line) are comprised of the α -relaxation (red), β -relaxation (yellow), fast- β mode (green), and librational mode (blue). See Appendix C.2 for fitting parameter values.

Compared to the other alkanes, the propane time-domain trace exhibits a particularly large and long-lived oscillation owing to a strongly Raman active intramolecular mode at 11 THz (360 cm^{-1}) assigned to the C-C-C torsional mode. In the time domain this oscillation appears to disappear abruptly, however this is an artifact of the data collection method, where the step-scan data collection changes from linear to logarithmic in time- as discussed previously in section 3.1.

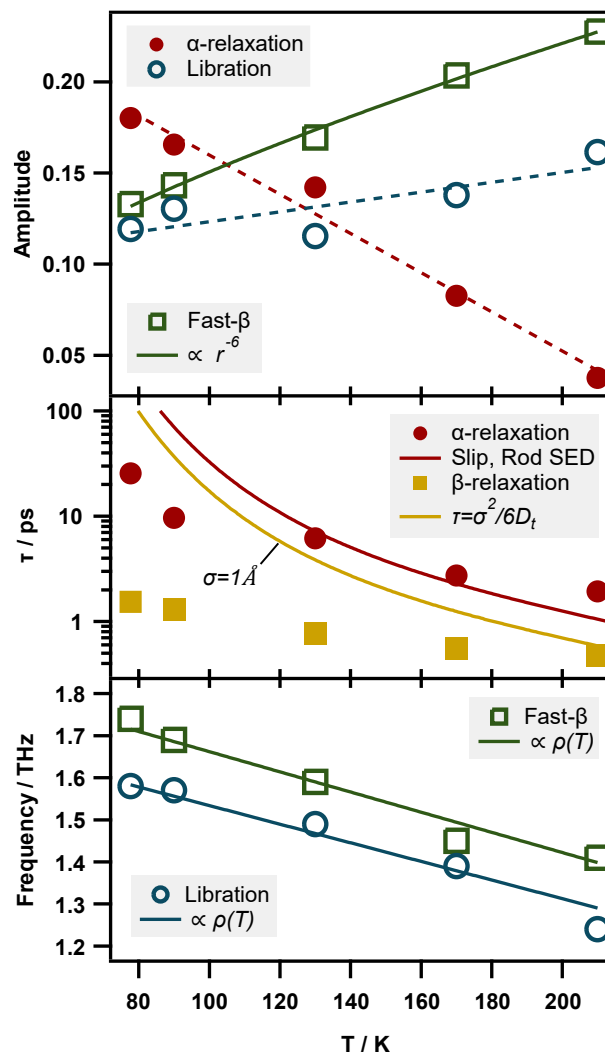


Figure 4.15. Fitting parameter trends in liquid propane OKE spectra with temperature.

Shown are the fitting parameter values of the α -relaxation (red \bullet), β -relaxation (yellow \blacksquare), fast- β (green \square), and libration (blue \circ) line-shapes as a function of temperature. The parameters displayed are the amplitudes (top), diffusive lifetimes (middle), and vibrational frequencies (bottom).

The fit parameters are shown in Figure 4.15, with parameter values tabulated in Appendix C.2. As shown previously (Figure 4.3 and Eq.4.6), propane densities were fit to a linear relationship with temperature that was in turn used to model the librational and fast- β frequency temperature dependence.

The α -relaxation band (Figure 4.15) is very weak at high temperatures but it becomes gradually more prominent on cooling, an effect seen previously^{107,108} and proposed to arise from polarisability enhancement due to cooperative molecular ordering but is yet to be fully understood.⁵³ The experimental α -relaxation lifetimes are comparable with Stokes–Einstein–Debye using slip conditions at higher temperatures but deviating by an order of magnitude at 78 K. For the β -relaxation the characteristic diffusion length, σ , was set at 1 Å for comparison with the other alkanes, revealing a poor conformity to the Stokes–Einstein relation by up to 2 orders of magnitude at 78 K. Given that the broader lower temperature spectra best expose the diffusive dynamics and thus offer the greatest

confidence in diffusive line-shape fitting, these deviations from theory are real phenomena that require explanation as opposed to a limitation of the fitting procedure. It is well-known that Stokes–Einstein and Stokes–Einstein–Debye relations excel in predicting the diffusive behaviours of macromolecules in solution, for example, but commonly break down for small molecules^{16,109,110} which are said to “hop” through the surrounding solvent, especially at low or supercooled temperatures.^{110–114} This is the reason that the $\tau \propto \eta V/T$ relationship violation in propane is witnessed in Figure 4.15, where the macroscopic viscosity is of little relevance to the microscopic motions.

The librational amplitudes decrease slightly with decreasing temperature, which could be explained by liquid densification producing a reduction in the average angle of libration. Librational frequencies increase on cooling, an effect observed previously in experimental and simulated OKE studies on benzene.¹¹⁵ This is again attributed to the increasing liquid density, where less free space means less free motion of a molecule in a cage, and intermolecular potential landscapes become more quadratic in nature. This also applies to the fast- β mode, where the $\omega \propto \rho(T)$ proportionality also holds. The fast- β process increases in amplitude with increasing temperature, which is expected from higher energy collisions. Eq. (4.15) was used previously to model the collision induced signal (at constant temperature) as a function of chain length; one can substitute back the thermal energy term, $k_B T$, into this equation to get

$$S_{\text{CI}} \propto r^{-6} \propto \ln^{-6} \left(\frac{k_B T}{V_0} \right). \quad (4.31)$$

Fitting the amplitudes to eq. (4.31) yields $V_0 \sim 10^{-16}$ J, again within an order of magnitude of typical values. The difficulty in achieving greater agreement between V_0 values between the propane and *n*-alkane investigations (and the cycloalkanes introduced next) is likely due to the shapeless nature of the intermolecular part of the OKE spectra. Bear in mind that this amplitude is of a line-shape fit that is not tightly bound by the *data*, rather it is mostly dependent on the surrounding line-shape fits.

4.8 Cycloalkanes

At room temperature, the cycloalkanes may have one or multiple discrete conformations (C_8H_{16} has 10 known conformations¹¹⁶) that could contribute distinct intermolecular interactions—such an effect may or may not be negligible. Their dynamics are also more complex than their linear counterparts; for example cyclopentane at room temperature is known to undergo nearly free pseudorotation in the gas and liquid phases via an intramolecular ring-puckering mode;^{117–119} its intermolecular dynamics are coupled not only

to each other but to an intramolecular mode and its overtones. It should be noted that other cycloalkanes also undergo pseudorotation but with some energy barrier; *e.g.*, cycloheptane $\Delta E = 2.2k_B T$ at 298 K.¹²⁰

The low-frequency spectra of room-temperature cycloalkanes are shown in Figure 4.16. Cyclopentane and cyclohexane exhibit a monomodal appearance similar to liquid propane at higher temperatures and typical of near-isotropically polarisable molecules. Upon increasing the ring size, the spectral evolution resembles that of propane upon cooling, where the lowest frequency (diffusive) modes grow in amplitude and red shift, uncovering the high-frequency oscillatory dynamics.

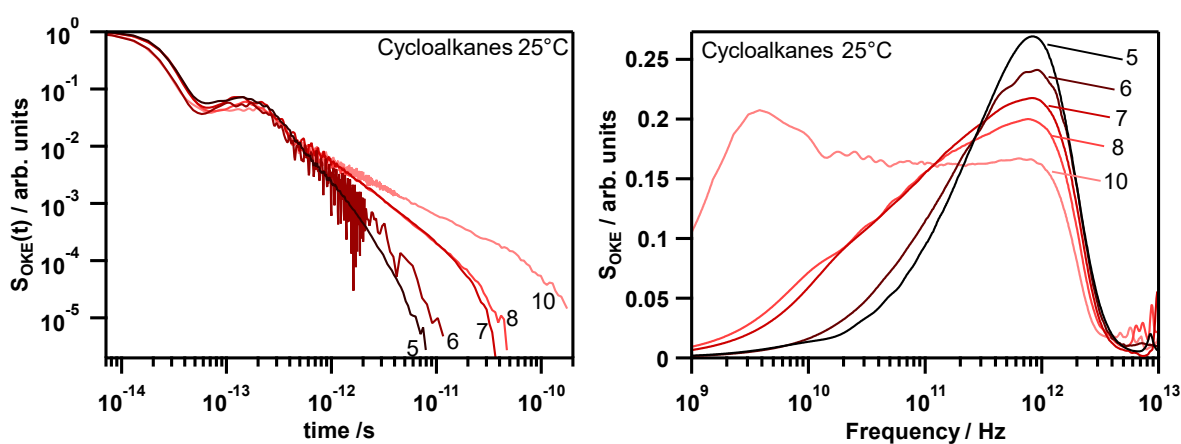


Figure 4.16. OKE spectra of various cycloalkanes at 25°C.

The time domain OKE response (left), and the frequency domain OKE spectra after Fourier-transform deconvolution (right), are shown for labelled cycloalkanes.

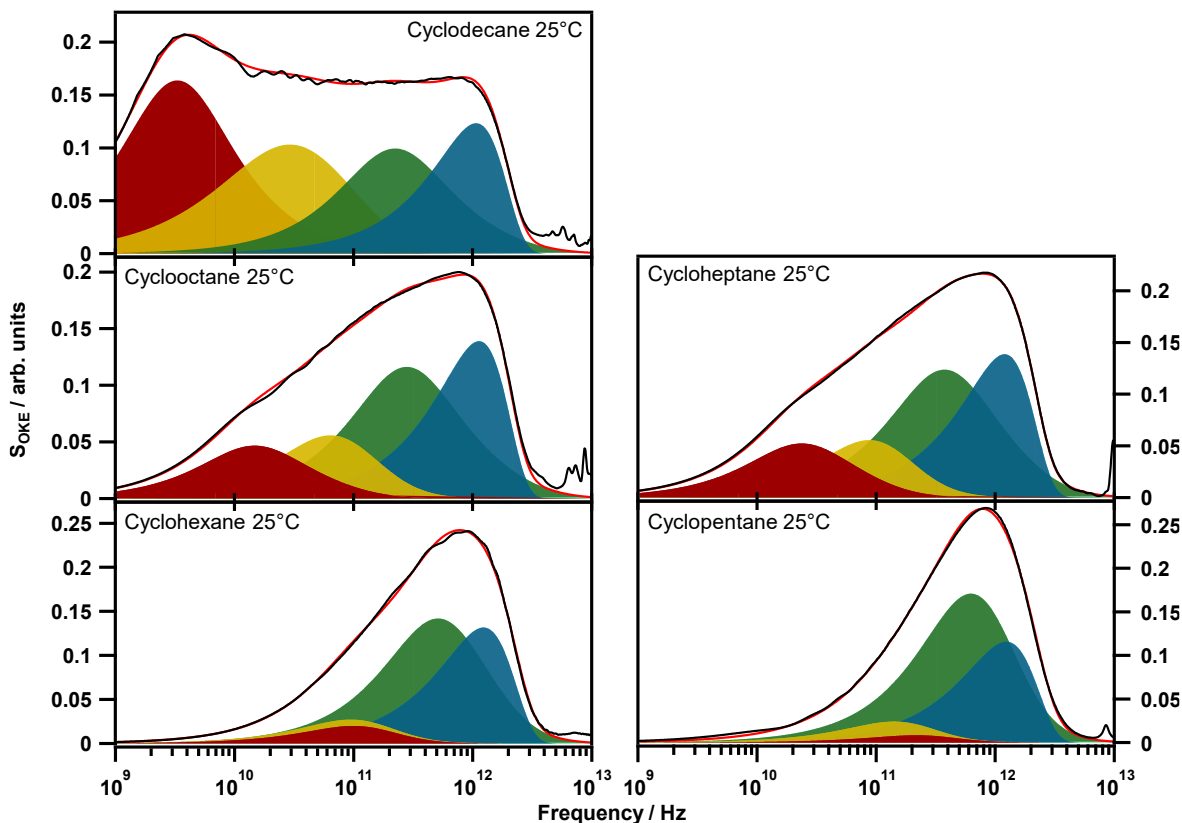


Figure 4.17. Line-shape fitting of cycloalkane OKE spectra.

The fits (red line) of the data (black line) are comprised of the α -relaxation (red), β -relaxation (yellow), fast- β mode (green), and librational mode (blue).

Cycloalkane spectra take on forms varying from monomodal to trapezoidal throughout. The line-shape fitting, shown in Figure 4.17 (and with values tabulated in Appendix C.3), for the smallest rings is particularly difficult; these spectra could be modelled with relative ease using a higher frequency antisymmetrised Gaussian oscillator (attributed to librational contributions) and a Bucaro–Litovitz function to mop up the remaining dynamics. This procedure ultimately fails when the diffusive and oscillatory components diverge for larger rings whose broader spectra require additional line-shape contributions and thus a higher resolution interpretation of the dynamics at play. By extrapolating from the larger rings and using the line-shape evolution of the n -alkanes series as a blueprint, a consistent picture across all the cycloalkanes may be constructed.

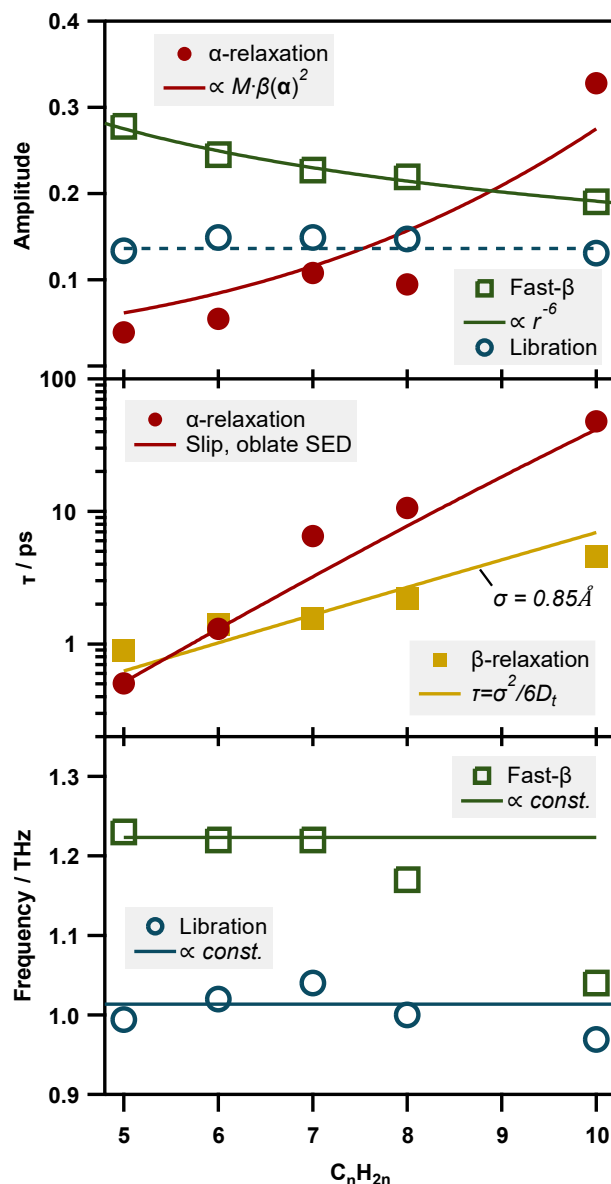


Figure 4.18. Fitting parameter trends in cycloalkane OKE spectra with ring size.

Shown are the fitting parameter values of the α -relaxation (red \bullet), β -relaxation (yellow \blacksquare), fast- β (green \square), and libration (blue \circ) line-shapes as a function of temperature. The parameters displayed are the amplitudes (top), diffusive lifetimes (middle), and vibrational frequencies (bottom).

As discussed previously, the amplitude of the α -relaxation band scales with $M \cdot \beta(\hat{\alpha})^2$, and since these polarisabilities were modelled as $\propto n^{-2}$ (and $M \propto n^{-0.78}$), amplitudes were fit to the $n^{3.22}$ proportionality shown in Figure 4.18. There is a clear deviation from monotonicity from the cyclooctane α -relaxation amplitude, however, which is possibly related to the conformational complexity of the molecule. Lifetimes compare well with Stokes–Einstein–Debye theory with the slip friction factor for oblate spheroids.

β -relaxation lifetimes fit to a translational diffusion distance just under 1 Å, in keeping with the alkanes' values. It is interesting to note that the β -relaxation is predicted to have a shorter lifetime than the α -relaxation for cyclopentane. Fits can be made to reflect theory as is the case in this work; however, this is generally avoided in OKE spectroscopy, as the α -

relaxation is expected to terminate the material's response in the time domain. Observation of dynamics slower than the α -relaxation are therefore anomalous. Arguably the strong overlap and coupling of these diffusive modes make their dynamics largely indistinguishable in such instances, which should allow for some leeway.

Librational and fast- β mode amplitudes can be modelled in an identical fashion to the n -alkanes, with the former maintaining a constant amplitude throughout while the latter again varies with the strength of intermolecular collisions, with a V_0 value of 5×10^{-17} J. The librational and fast- β frequencies conform to the same n dependence seen in short alkanes and drop off at cyclooctane. Recall that in the n -alkanes the decrease in fast- β frequency was attributed to molecular floppiness, marked by the occurrence of normal intramolecular modes with the same (or lower) frequency (see section 4.5). This same explanation cannot be used here, because the lowest calculated normal mode of the most populous cyclooctane conformation, boat-chair, is 3.7 THz and is visible in Figure 4.17 as a small shoulder on the librational band – the lowest energy intramolecular normal mode of the (less populous) chair conformer is 2.2 THz. This is instead attributable to conformational complexity and/or deviations from ideal ring geometry. The simple intermolecular interaction outlined in Figure 4.10 underpins the assumption of Eq (4.18): that the intermolecular repulsion scales with n . This of course relies on each atomic unit participating in collisions, *i.e.*, all mass must reside on the molecule's surface. More spherical molecules have atoms which are more shielded from direct bulk interaction, which is likely the effect witnessed in the more “crumpled” hydrocarbons such as boat-chair cyclooctane. As molecules become more spherical or crumpled, the shielded mass still acts as an inertial load, but its contribution to the spring constant, k diminishes. Simply put, for the molecule as a whole, the $m \propto n$ relationship still holds, while $k \propto n$ does not. In cyclooctane the (slightly) shielded CH_n units contribute less or less occasionally to the intermolecular forces that produce intermolecular cage-rattling motions but still fully contribute to the inertial load; this will result in the reduction of the librational and fast- β frequencies.

4.9 6-Membered Rings

Due to their complicated spectra, some of the most commonly studied liquids are benzene^{87,121–130} and cyclohexane.^{87,100,127,131} Just as with the alkanes and cycloalkanes, it is necessary to observe line-shape trends across a series in order to make reasonable assignments of the intermolecular dynamics at play. The OKE spectra of cyclohexane, cyclohexene, 1,4-cyclohexadiene, and benzene are shown in Figure 4.19.

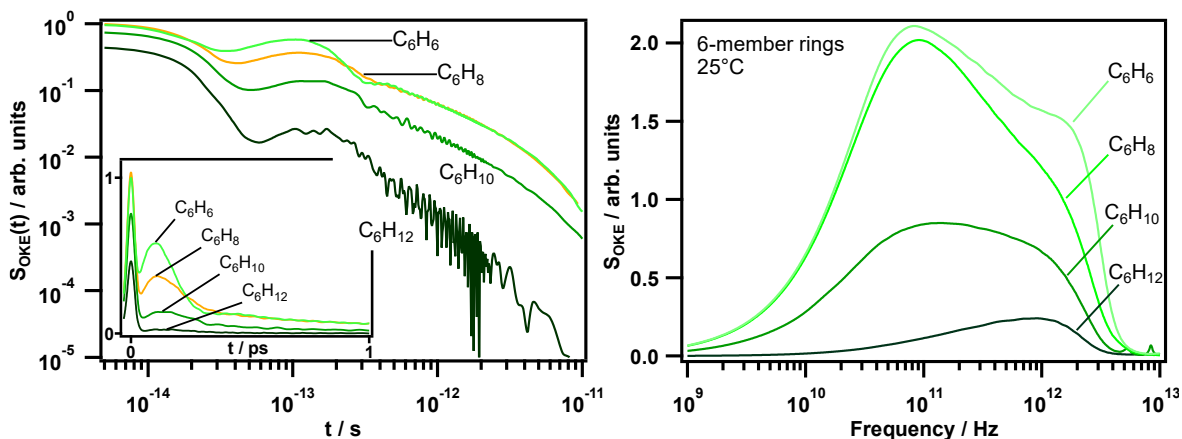


Figure 4.19. OKE spectra of various 6-membered rings at 25°C.

(Left) Time-domain OKE response of the 6-membered rings on a log-log scale, with a portion of the initial response displayed on a linear scale (inset). (Right) The corresponding frequency-domain spectra. C₆H₈ is 1,4-cyclohexadiene, and its TDT is orange purely for clarity.

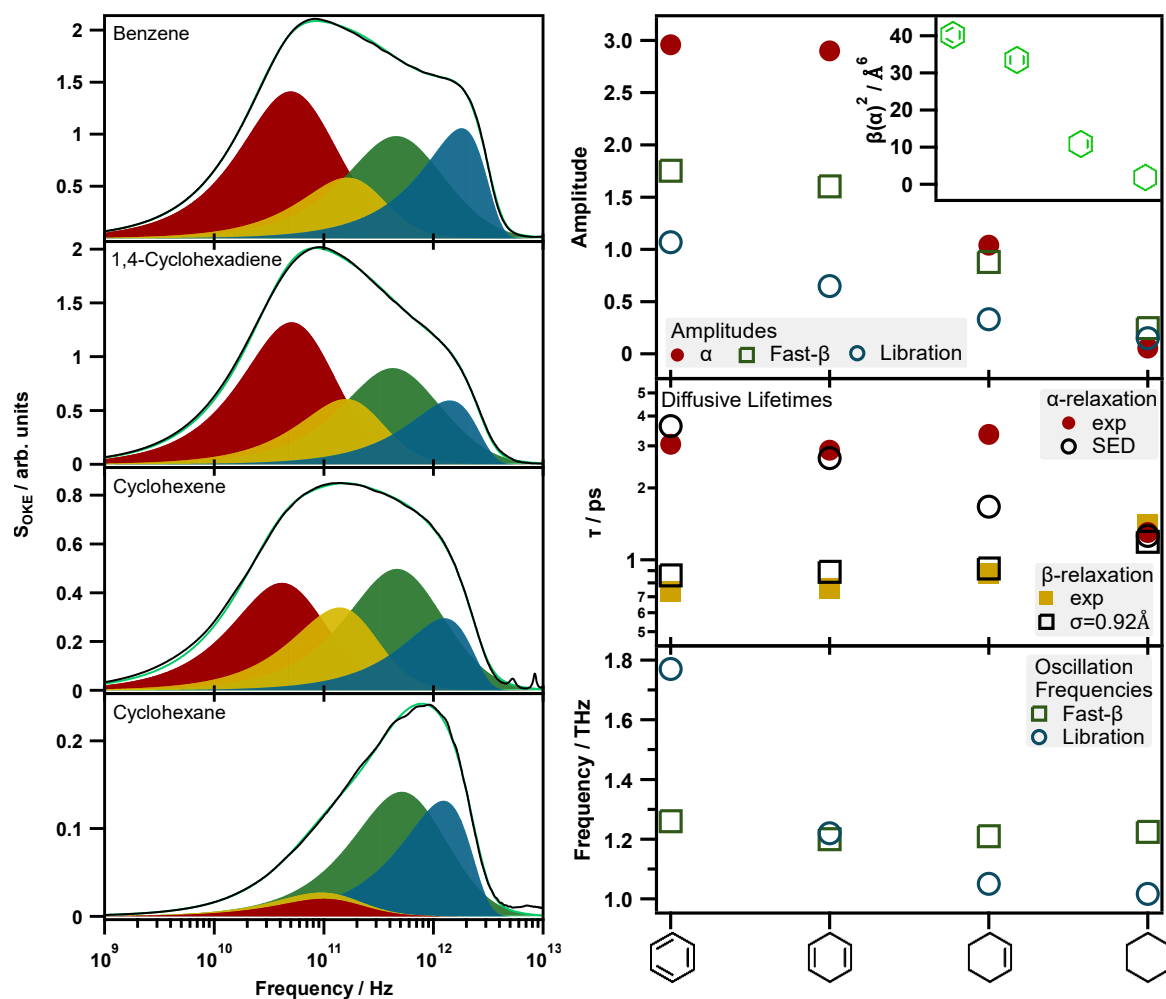


Figure 4.20. Line-shape fitting of 6-membered ring OKE spectra with fit parameter trends.

Left: the fits (green line) of the data (black line) are comprised of the α -relaxation (red), β -relaxation (yellow), fast- β mode (green), and librational mode (blue). Right: the fitting parameter values of the α -relaxation (red ●), β -relaxation (yellow ■), fast- β (green □), and librational (blue ○) line-shapes across the series. The parameters displayed are the amplitudes (top), diffusive lifetimes (middle), and vibrational frequencies (bottom). Anisotropic polarisabilities are also shown (top inset) for each molecule.

Previous work has seen cyclohexane modelled using one,¹³¹ two,¹⁰⁰ and three⁸⁷ line-shapes; benzene has been fit with two,^{115,122,128–130} three,^{87,126} and five¹²⁸ line-shapes. Most recent work has fit the series from cyclohexane to 1,4-cyclohexadiene to benzene using combinations of BL+BL+ASG to BL+BL+ASG+ASG to BL+ASG+ASG functions, respectively.⁸⁷ This work shows how a far more consistent picture can be achieved using the four line-shape model as shown in Figure 4.20.

The anisotropic polarisabilities, along with the amplitudes of all modes, increase in a near-linear trend across these rings from 6 to 0 π -electrons as shown in Figure 4.20. The α -relaxation is expected to scale with $\beta(\hat{\alpha})^2$, and this appears to be the case certainly for the three heaviest rings at least; the α -relaxation amplitude for benzene may be slightly less than expected. Similar results were found by Kakinuma *et al.*, who suggest that the time integral of the nuclear part of the entire response function, $S_{\text{OKE}}(t)$ scales with $\beta(\hat{\alpha})^2$ for all rings.⁸⁷ One might have expected the β modes to depend on the isotropic polarisability, $\alpha(\hat{\alpha})$, but as shown in Table 4.1, isotropic polarisabilities are mostly invariant across the six-membered rings. These observations suggest that all intermolecular dynamics in this series remain strongly coupled; the β -modes retain some orientational dependence.

Orientalional relaxation lifetimes in benzene match Stokes–Einstein–Debye theory with the oblate spheroid slip condition and other experimental and simulated benzene studies.^{115,132} Notably the cyclohexene τ_{α} is approximately double that predicted by Stokes–Einstein–Debye. Cyclohexane and benzene are roughly oblate spheroids but interpolating for the intermediate rings may contribute to the experimental deviation from theory given the more irregular geometry of cyclohexene. It is also worth noting that the centre of mass is slightly askew in cyclohexene only, so in principle, rotations would require more free volume and should therefore occur on slower time scales; it would be surprising if this effect alone would double τ_{α} . In more realistic terms, the presence of π -electrons has a significant effect on the intermolecular potential, evidenced by the $\sim 20\%$ drop in dynamic viscosity between cyclohexane and cyclohexene, which then remains approximately constant for the remaining rings. These two distinct viscosity regimes suggest that one need not expect a smooth trend in orientation relaxation from saturated cyclohexane to benzene; rather one can expect dynamics that are heavily dependent on the presence or absence of π -electrons. The librational frequency of benzene matches previous work,¹²² while studies on the remaining rings are lacking or unreliable. For instance, the three and four-fit model mentioned previously finds that the Gaussian (librational) frequency, ω_G , halves from cyclohexane to cyclohexene and then doubles for 1,4-cyclohexadiene, which is unrealistic.

On the other hand, the fitting procedure described here arrives at realistic values and trends for the oscillatory frequencies.

4.10 Discussion & Conclusion

This chapter sets out to demonstrate a logical and useful interpretation of gigahertz to terahertz spectra that produces a disentangled picture of intermolecular dynamics. The α -relaxation ranges from the most obvious feature of the OKE spectra of highly anisotropic and/or viscous liquids to one of the most obscure in isotropic and/or low-viscosity liquids. In the former cases, these experiments show the orientational relaxation lifetime, τ_α , abiding Stokes–Einstein–Debye theory with the slip condition (and accounting for aspect ratio in the *n*-alkanes); less spherical molecules eventually require aspect ratio dependent correction factors. In spectra with the weakest α -relaxation contribution, there is every reason to expect a continuation of the trend, which is effectively extrapolated in this work. SED theory does however fail to account for the dynamics in liquid propane at lower temperatures, but this is due to the viscosity becoming progressively irrelevant for microscopic molecular motions within supercooled liquids (see section 4.7).

The collision-induced contribution to these spectra have been fit to two line-shapes that have been treated analogously to the rotational contributions from librations (an oscillatory mode) and orientational diffusion. While it is intuitive to assign the oscillatory part of the CI contribution to a ‘cage-rattling’ type motion, the nature of the ‘diffusive’ part is less clear; here it has been treated as single-molecule diffusion. It should be noted that often these parts of the intermolecular spectrum are fit to single broad bands resulting from exponential^{53,133} or power-law fits^{55,107} to the time-domain decay. In this work, it is found that the β -relaxation is the most difficult to fit due its concealed and relatively weak contribution to the dynamics. It is not possible to make meaningful conclusions on the basis of its amplitude, which is a limitation of this model. On the other hand, τ_β values correspond to standard deviations in position (translational diffusion) of $0.85 \text{ \AA} \leq \sigma_t \leq 1.08 \text{ \AA}$, which are remarkably consistent with the fact that OKE spectroscopy is sensitive only to collisions and translations on the order of a van der Waals radius.

Whilst this work has reasonable success in applying just one line-shape for each of the four types of dynamics mentioned here, it is worth noting that molecules of exaggerated dimensionality with, *e.g.*, needle or disc-like geometries, may diffuse and vibrate on entirely different timescales for in-plane vs out-of-plane and parallel vs perpendicular motions. In fact, this is almost certainly a contributing factor to the broadening of *n*-alkane spectra as

chain lengths increase. An idealised (and intrepid) approach to the line-shape fitting of such spectra would include the eventual splitting of single modes into their two spatial components. This is not attempted here for various reasons, not least of which is to avoid both overparameterisation and the compounding difficulty of achieving consistent and meaningful fits. Furthermore, one may reasonably expect a signal dominance of one spatial contribution over another. For example, in-plane orientational motions will produce a small signal due to the relatively small difference between the associated polarisability tensor elements when compared with the out-of-plane case. In terms of the collision-induced β -modes, it can be argued that for these species the “broadside” collisions involve a greater number of interparticle interactions across the molecule and should be the dominant β contribution to the OKE spectra. For these reasons, to account for the broad spectra of long-chain *n*-alkanes and supercooled propane, the β -relaxation mode was gradually broadened from an inertial Debye to an inertial Cole–Cole function. This is the simplest possible approach, introducing just one extra broadening parameter.

Fast- β mode characteristics are governed by the strength and frequency of approximately harmonic intermolecular cage rattling. Intermolecular potential, V_0 , values obtained through fitting parameter modelling are consistently within an order of magnitude of literature values, which is surprising given the central location of the fast- β mode within these shapeless spectra. The effect of temperature is a proxy for density, which is known to have clear influence on the librational frequencies;¹¹⁵ this work shows that, unsurprisingly, this holds true for the fast- β mode as well.

The antisymmetrised Gaussian function is commonly used to fit librational motions and indicates the presence of inhomogeneous environments. Librational modes in the *n*-alkanes from pentane to hexadecane, however, fit the Brownian oscillator line-shape. This notably excludes propane whose librational mode has an antisymmetrised Gaussian profile. This appears to correlate with aspect ratio, where ratios > 0.55 (more spherical) follow an antisymmetrised Gaussian line-shape, while ratios < 0.55 (more needle- or disc-like) have Brownian profiles. This binary outlook is of course simplistic, and indeed previous *n*-alkane work has modelled the librational mode using a Gaussian–Brownian convolution.¹⁶ In any event, far more data would be required on different molecules with a range of aspect ratios to determine if this correlation is real or simply coincidental. What is clear from these data is that conformationally simple molecules, which are rigid on picosecond time scales, librate and rattle in their intermolecular cage according to relatively straightforward mechanics, which gradually break down for progressively larger molecules. Diffusive modes on the

other hand seem to closely follow Stokes–Einstein–Debye and Stokes–Einstein theories throughout, with the exception of cyclohexene, which behaves far more like benzene than cyclohexane.

In summary, this work tests the validity of a physical line-shape fitting approach to gigahertz to terahertz dynamics for simple weakly interacting molecular liquids. The study of liquid methane reveals how collision-induced (β) signals do not follow the Bucaro–Litovitz line-shape, derived to account for precisely such dynamics. Instead, these dynamics must be split into vibrational and diffusive parts, directly analogous to librations and orientation relaxation. One should therefore expect to be able to reasonably compartmentalise the gigahertz to terahertz spectra of weakly interacting liquids into four simple dynamical categories: orientational α -relaxation, translational β -relaxation, fast- β oscillations, and librations. This work has shown the model’s applicability across the room-temperature *n*-alkanes and cycloalkanes, across a 130 K temperature ramp of propane into the supercooled regime, and across various six-membered rings from cyclohexane to benzene. These spectra can indeed be meaningfully partitioned across dimensions of oscillatory/diffusive and rotational/translational dynamics in a single coherent picture for the first time. Though not without limitation, this interpretation provides a foundation on which our understanding of intermolecular dynamics can be built.

5 THE BOSON PEAK

This data of this chapter is available online as a preprint, see ref.¹³⁴ for details. Based on insightful peer-review feedback this data has been re-interpreted here.

5.1 Introduction

The expected behaviour of a liquid when cooled is to freeze at the melting temperature, where the molecules arrange themselves in an ordered crystalline state. However, many liquids can be supercooled where crystallisation is postponed. On further cooling, the supercooled liquid becomes increasingly viscous and at the glass-transition temperature vitrifies into an amorphous solid called a glass. The liquid–glass transition is one of the most difficult and well-studied problems of condensed matter physics.^{135–139}

A common and quintessential feature of glasses is the observation of the so-called boson peak (BP) typically seen in spontaneous Raman scattering spectroscopy and inelastic neutron scattering at a frequency around 1 THz. It is named as such because one of the few known characteristics of its Raman spectral line-shape at its time of discovery was that its temperature dependence appeared to obey BE statistics for thermal population of energy levels (see eq. 5.2).¹⁴⁰ The BP represents a peak in the vibrational density of states, $g(\omega)$, normalised by the frequency squared, $g(\omega)/\omega^2$.¹⁴¹ This corresponds to an excess in the density of states over that expected from phonons in a perfect Debye crystal, as illustrated in Figure 5.1. This gives rise to anomalous behaviour of the low-temperature heat capacity C_p and a peak in C_p/T^3 at a few 10s of K. The boson peak has a predominantly transverse character^{142–144} and is strongest in depolarised Raman scattering. The boson peak typically becomes visible when a (supercooled) liquid is vitrified. Thus, the position, amplitude, and shape of the boson peak could provide crucial information on the physics of supercooling and vitrification.

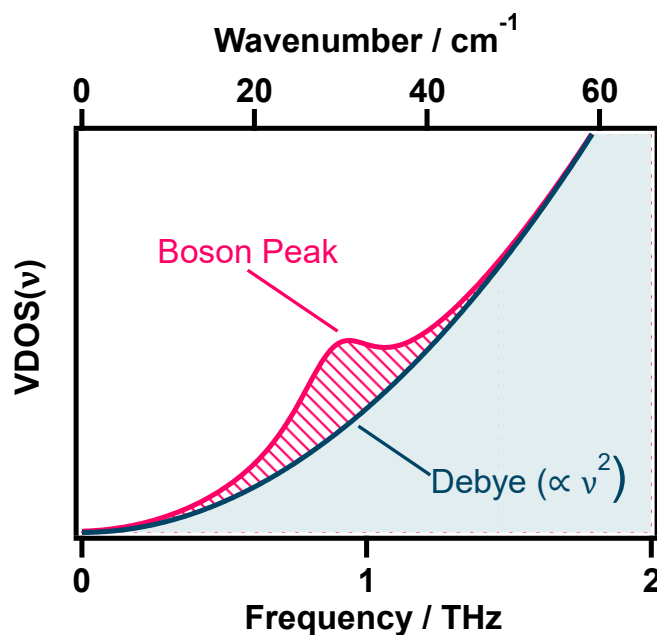


Figure 5.1. Illustration of the Boson peak in the VDOS.

The Boson peak illustrated as excess vibrational states above the Debye model.

The origin of the boson peak is still the subject of much scrutiny to date, with many proposed mechanisms to explain how it emerges. Some believe it to be caused by random spatial fluctuations of elastic constants brought about by disorder.^{145–147} It has also been argued to be the remnant of a van Hove singularity of the corresponding crystal, that has been washed out by amorphous structure.^{148,149} Other explanations include the coupling of acoustic phonon modes with quasi-localised soft modes arising from defects,^{150,151} the weak interaction between quasi-localised harmonic modes producing anharmonicity,¹⁵² or competition between elastic mode propagation and diffusive damping.¹⁵³ In supercooled liquids, it has been argued that crystal nucleation is inhibited by locally favoured structures that geometrically inhibit the formation of the thermodynamically most stable state¹⁵⁴ and give rise to the emergence of the boson peak.¹⁵⁵ Thus, the spectral features of the boson peak could provide crucial insight into the nature and abundance of these locally favoured structures.

However, in most liquids (including those that vitrify) it is difficult to distinguish the various processes that contribute to the vibrational spectrum in the low-terahertz range. In this range in liquids, one can distinguish spectral contributions from^{61,69} primary- or α -relaxations due to orientational and translational diffusion, an oscillatory intermolecular mode (sometimes referred to as “cage rattling”), librational motion, and finally low-frequency vibrational modes. The α -relaxation process freezes out on vitrification while vibrational contributions are sometimes narrow and relatively easy to distinguish. That

leaves the intermolecular cage-rattling mode and librations in addition to possible contributions from a boson peak, all of which peak around 1 THz, making an unobscured observation of the boson peak difficult or impossible.

There are numerous reports of observations of boson peaks in the literature, however, many of these are obscured. In depolarised Raman scattering, the intensity of both the orientational-relaxation and librational bands scale with the anisotropic part of the molecular polarisability tensor and therefore the presence of one implies the other. The boson peaks reported in the Raman spectra of vitrified B_2O_3 ,^{156,157} As_2S_3 ,¹⁵⁸ $Ca_2K_3(NO_3)_7$,¹⁵⁷ propylene glycol,¹⁵⁹ glycerol,^{156,160} m-tricresyl phosphate,¹⁵⁶ toluene,¹⁶¹ and salol¹⁶² all show orientational relaxation in the liquid implying the presence of a librational band that is partially obscuring the boson peaks. Raman and inelastic neutron scattering spectra of $Y_2O_3-Al_2O_3$,¹⁶³ $Na_{0.5}Li_{0.5}PO_3$,¹⁶⁴ $ZnCl_2$ and $ZnBr_2$,¹⁶⁵ *ortho*-terphenyl,^{166,167} polyisoprene,¹⁶⁷ polystyrene,¹⁶⁷ and other polymers¹⁶⁸ are also complicated by phonon bands again complicating the identification of the boson peak in the glass. The Raman spectra of glassy sulfur¹⁶⁹ (S_8) and selenium¹⁷⁰ show a complex band shape between 0 and 100-150 cm^{-1} , the high frequency region of which has been correctly assigned to librations. Bumps at *circa* 20 cm^{-1} (~ 0.6 THz) are assigned to boson peaks but reliable analysis of their (temperature dependent) shape and amplitude is difficult. Lastly, the features observed at ~ 50 cm^{-1} (1.5 THz) in glassy SiO_2 , GeO_2 , *etc.*,^{140,171-175} appear to be some of the best isolated boson peaks—the local SiO_2 structure is likely to be close to tetrahedral, where each silicon is surrounded by 4 oxygens (and where the anisotropic part of the polarisability tensor would vanish and which would make the librational band invisible in depolarised Raman scattering).

In summary, although observation of the BP in vitrified liquids has been reported many times over, many of these line-shapes are complicated by the presence of other, often overlapping, modes. Perhaps as a result, some of these boson peaks have been cross-checked by other techniques such as neutron scattering¹⁷⁶ or inelastic x-ray scattering.^{177,178} However, a common theme is that it is difficult to determine the temperature-dependent shape and amplitude of the BP for detailed analysis. However, the example of glassy SiO_2 shows the way forward: symmetry can be used to simplify depolarised Raman spectra.

The glass-forming liquids under investigation in this work are toluene, titanium alkoxides (particularly tetrabutoxide), and tetrabutyl orthosilicate. Toluene will be first introduced as an example of a glass-forming liquid whose intermolecular spectrum exhibits the

aforementioned issue of overlapping spectral features that can obscure the BP. The focus will then shift onto glass-forming titanium alkoxide liquids in which the molecules and/or molecular clusters have a greater degree of symmetry, thereby reducing the signals from orientational diffusion and librations. Diffusive translations freeze out on vitrification, leaving a single, largely isolated, intermolecular mode whose signal in depolarised Raman spectroscopy scales with the intermolecular collision strength. This intermolecular mode is consistent with the fast- β mode (of chapter 4), the rattling of molecules in the cage formed by their neighbours.^{62,69,179} Thus, in a model in which the supercooled liquid consists of liquid-like regions and locally favoured structures (LFS), whose size and/or population increases on lowering temperature (see Figure 5.2), then both should show such cage-rattling intermolecular modes. Finally, the OKE study of vitreous tetrabutyl orthosilicate reveals an additional intermolecular mode at a lower frequency which may originate from a cluster fast- β mode.

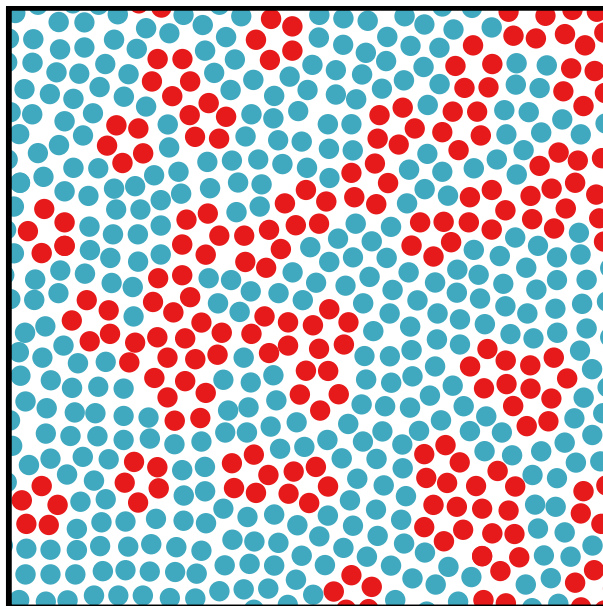


Figure 5.2. In a supercooled liquid, locally favoured structures form in a sea of the normal liquid.

Circles represent individual liquid molecules. Structures (red) with 5-fold symmetry are shown for illustration within a normal liquid (blue), as they cannot tile space. Adapted from ref.¹⁸⁰

5.2 Methods

5.2.1 Experimental

Liquids were purchased from Sigma-Aldrich and have a rated purity $\geq 98\%$ with the exceptions of titanium tetraethoxide, which has a purity $\geq 80\%$ (5% contamination with titanium tetraisopropoxide resulting in 20% titanium triethoxide monoisopropoxide) and were used without further purification. As will become clear in section 5.4, this substantial

impurity is entirely acceptable for its application, which is to deliberately reduce the symmetry of a titanium alkoxide liquid mixture. Liquid samples were filtered with a PTFE filter (Millex) with 20 μm pore size and degassed for 1 min in an ultrasound bath before OKE measurements. Room-temperature samples were contained in a 1 mm thick rectangular quartz cuvette (Starna) and held in a temperature-controlled (± 0.5 K) aluminium block. Low-temperature measurements were performed using a liquid- N_2 cryostat (Oxford Instruments, ± 0.1 K) in a nitrogen environment to avoid water condensation. The OKE spectra of toluene were gathered by Dr. David Turton (University of Glasgow) several years prior to this work.

It is important to quantify the glass transition temperature of the liquids used here. Without access (at the time) to a differential scanning calorimeter that could operate at cryogenic temperatures, instead viscometry measurements were performed with the help of Dr. Emily Draper on a rheometer (Anton Paar MCR 201) using a 50 mm cone at a fixed shear rate of 10 rad/s. The temperature was lowered from 75°C to -40°C at a rate of 1°C/min and the viscosity recorded every minute. Measurements were performed under an atmosphere of nitrogen to prevent oxidation of the sample using a custom-made 3D printed plate hood courtesy of Dr. Bart Dietrich. A cylinder of nitrogen gas was attached to an inlet on the hood to allow for a stream of nitrogen to pass over the measurement system and sample throughout the measurement. To help the temperature reach and maintain -40°C, the nitrogen gas line was passed through a liquid nitrogen bath before it reached the hood on the rheometer. This does not reach temperatures as low as T_g , but the viscosity data can be modelled and extrapolated to approximate the glass transition temperature.

Differential scanning calorimetry (DSC) measurements were eventually performed by Dr. Ben Russell using a TA Instruments DSC 2500 differential scanning calorimeter equipped with a quench-cooling accessory.

5.2.2 OKE and Raman Scattering Relationships with the Density of States.

The vibrational density of states (VDoS) $g(\omega)$ can be measured in several related experiments such as Raman scattering (including OKE spectroscopy), inelastic neutron scattering, *etc.* Such spectroscopies never measure $g(\omega)$ directly but instead a product of the VDoS with the strength of the coupling associated with the particular spectroscopy. Thus, the various spectroscopies measure the same dynamics or spectra but with different amplitudes for the various components. One can write more general relations between the

measured spectra and the VDoS; for example, the spontaneous Raman scattering (SRS) spectrum and the inelastic neutron scattering (INS) spectrum are related to the VDoS by¹⁴⁰

$$S_{SRS}(\omega) \propto S_{INS}(\omega) \propto g(\omega)C(\omega) \frac{n(\omega, T) + 1}{\omega}, \quad (5.1)$$

where

$$n(\omega, T) = \frac{1}{e^{\hbar\omega/k_B T} - 1} \quad (5.2)$$

is the Bose-Einstein occupation number, and $C(\omega)$ is the coupling term specific to the technique. The coupling term in SRS will have some frequency dependence, while in INS it is frequency independent. Most importantly, INS can measure propagating (phonon) modes whereas SRS cannot because of momentum matching. It has been suggested that the frequency dependence of the coupling in the SRS spectrum may follow ω^2 at very low frequencies ($< 20 \text{ cm}^{-1}$) and ω at low frequencies in glasses.^{172,173,181–183}

The OKE spectrum is given by¹⁸⁴

$$S_{OKE}(\omega) = S_{SRS}(\omega) \frac{1 - e^{-\hbar\omega/k_B T}}{2\hbar} \quad (5.3)$$

$$\propto g(\omega) \frac{C(\omega)}{\omega},$$

thus, one can convert an OKE spectrum to the equivalent spontaneous Raman scattering spectrum.

5.2.3 Line-Shapes and Fit Functions

As discussed previously in section 3.2, overdamped or diffusive modes (corresponding to orientational and translational diffusion) are typically fit to the imaginary part of the Havriliak-Negami function (see eq. (3.8)) with $0 < \alpha_{CD}, \beta_{CC} \leq 1$. Diffusive motions are described by the HN line-shape which varies around the frequency origin as ω for a regular Debye or Cole-Davidson function and ω^0 as $\beta_{CC} \rightarrow 0$ (see Appendix D), and therefore does not produce a peak in $g(\omega)/\omega^2$. Thus, diffusive modes do not represent any ‘excess’ heat capacity. Underdamped Brownian oscillators and antisymmetrised Gaussian functions (eqs. (3.12) and (3.14) respectively) will display a peak in $g(\omega)/\omega^2$; these line-shapes therefore *can* describe a boson peak.

The intermolecular mode (named the fast- β mode in chapter 4, and will be named as such herein for consistency) originating from washed-out pseudo-Brillouin zone edge phonon

modes, can be considered for simplicity as the rattling of a molecule in the cage of its neighbours. If the BP does indeed arise due to LFS, then there is no obvious *a priori* model for the temperature dependence of the centre frequency of a fast- β mode. Often, in OKE studies the frequency of the librational band is related to the density of the liquid as a function of temperature, and (chapter 4 argued that) a similar model could apply to the intermolecular mode as well. This is convenient when $\rho(T)$ is known, however some of the materials under study here are quite obscure. An alternative approach would be to attempt to model the averaged intermolecular potential.

The Morse potential is a rough and ready representation of the anharmonicities of the intermolecular potential. The vibrational eigen energies in a Morse potential as a function of the quantum number n are

$$E_n = h\nu_0 \left(n + \frac{1}{2} \right) - \frac{[h\nu_0 \left(n + \frac{1}{2} \right)]^2}{4D_e} \quad (5.4)$$

where D_e is the dissociation energy of the well and ν_0 is the vibrational frequency at the bottom of the well. This equation was solved for n ; the spacing of the eigen energies can be written as

$$E_{n+1} - E_n = h\nu_0 - \frac{(n+1)(h\nu_0)^2}{2D_e} \equiv h\nu. \quad (5.5)$$

Inserting the solution for n ,

$$E_{n+1} - E_n = \frac{(4\sqrt{D_e(D_e - E_n)} - h\nu_0)h\nu_0}{4D_e}. \quad (5.6)$$

If it is assumed that $E_n \cong k_B T$, one obtains

$$\nu = \frac{(4\sqrt{D_e(D_e - k_B T)} - h\nu_0)}{4D_e} \nu_0 \quad (5.7)$$

as the expected frequency of the boson peak. This expression goes to zero at

$$k_B T = D_e - \frac{(h\nu_0/4)^2}{D_e}. \quad (5.8)$$

Typical parameters would be $\nu_0 \sim 1$ THz (the presumed frequency of the boson peak) and D_e/h estimated as 10-50 THz. The problem with this model is that the temperature of eq.(5.8) is not the boiling temperature, as the density of a liquid is very much finite just below the boiling temperature (and the frequency not expected to be zero). Therefore, eqs. (5.7) and (5.8) should be regarded as reasonable fit functions to account for the anharmonicity of intermolecular vibrations, rather than reflecting meaningful physics.

5.3 The Hidden Boson Peak in Toluene

Toluene is a liquid that vitrifies at $T_g = 120$ K. The boson peak is directly related to the extra heat capacity of the glass over the crystal—in toluene, the heat capacity C_p has been measured for stable¹⁸⁵ (liquid, crystal) and metastable¹⁸⁶ (supercooled, glass) sequences. As can be seen in Figure 5.3 (based on data from these previous studies)^{185,186} vitrified toluene has ~10% extra heat capacity over the crystal, which peaks at a temperature $T_{boson} = \sim 20$ K. This must be due to an “extra” vibrational density of states, that is, a boson with a frequency that would be estimated as $k_B T_{boson}/h$ or ~ 0.4 THz in the case of toluene. Analysis of C_p/T^3 for toluene similarly leads to an estimate of the boson peak frequency of ~ 0.5 THz.¹⁸⁷

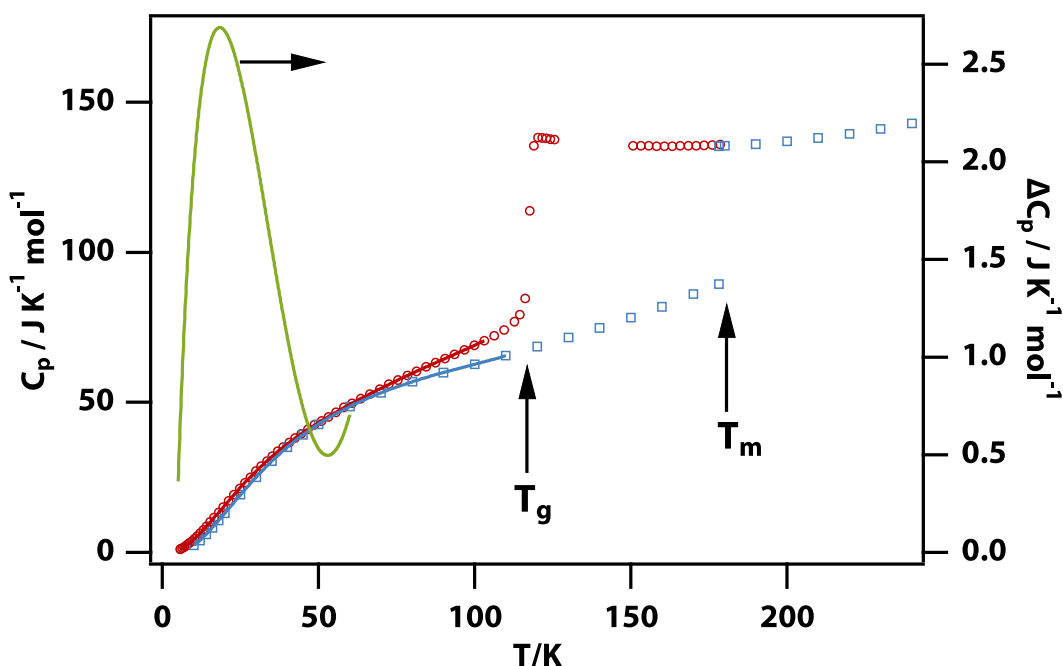


Figure 5.3. Molar heat capacities of stable and metastable sequences of toluene.

Shown are crystalline toluene (blue squares), and supercooled and vitrified toluene (red circles) from refs.¹⁸⁵ and ¹⁸⁶ respectively. Fits are to 8th order polynomials, and the difference between these fits (green line) is shown to peak at 20 K (0.42 THz).

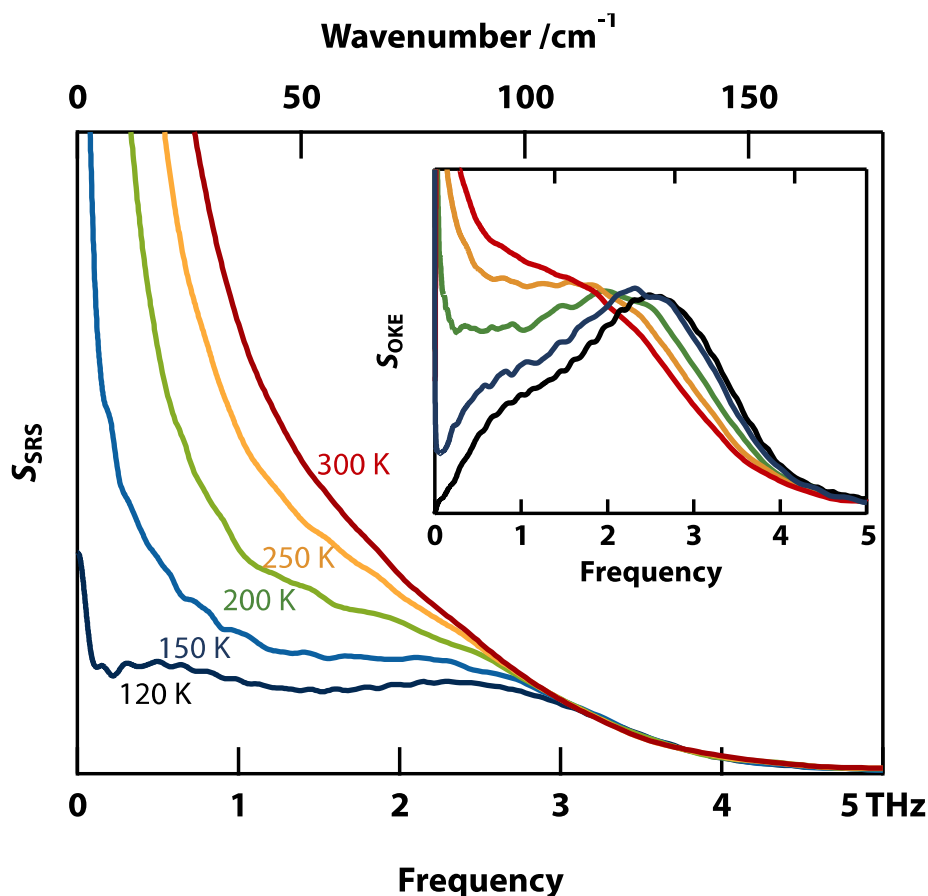


Figure 5.4. Temperature dependent terahertz spectra of toluene.

Shown are the OKE spectra (inset) and spontaneous anisotropic Raman spectrum (SRS, main panel) derived from it.

The temperature-dependent terahertz spectra of toluene taken using OKE spectroscopy are shown in Figure 5.4. The reduced spectrum can be converted to a spontaneous Raman scattering spectrum by multiplying with a Bose-Einstein occupation factor (eq. (5.2)) as discussed in section 5.2. This converted spontaneous Raman spectrum is shown in Figure 5.4 and is consistent with published Raman spectra of toluene.^{161,188} In liquid and supercooled toluene, the spontaneous Raman spectrum is dominated by so-called quasi-elastic scattering. The quasi-elastic peak vanishes only when toluene is vitrified, to reveal a peak at 2.5 THz and a weaker shoulder at 0.5 THz. In similar temperature-dependent spontaneous Raman and inelastic neutron scattering spectra, the higher frequency peak is often identified as the boson peak but is in fact due to molecular librations.¹⁷⁷

The 0.5 THz shoulder appears to be the actual boson peak (the frequency is right based on excess heat capacity measurements, see above) but its shape is difficult to determine with great accuracy from Figure 5.4, and it cannot be ruled in or out from the spectra alone that it exists in the supercooled liquid as well. OKE spectra do not exhibit this quasi-elastic curtain that obscures the sub-terahertz dynamics in the liquid phase but instead have eminently analysable bands due to diffusive processes such as orientational- and translational-

relaxation. Using the line-shape fitting methodology developed in chapter 4, the spectra of liquid and glassy toluene over temperature was analysed, with results shown in Figure 5.5 and with parameter trends shown in Figure 5.6 (and parameter values in Appendix E.2).

The most prominent feature in Figure 5.5 is the α -relaxation peak which is observed to redshift on cooling as expected, but also increase in intensity. Again, this is less understood but commonly observed in other studies,^{53,107,108} and of course chapter 4. This is assigned to reorientational diffusion, whose time constant starts at 5.1 ps for room temperature toluene 1.1 ns at 150 K and freezing out completely by 120 K indicating vitrification (consistent with T_g in Figure 5.3). The existence of two relaxation mechanisms in toluene was first suggested over 50 years ago by Santarelli and coworkers.¹⁸⁹ A more recent THz time domain spectroscopic study by Rønne *et al.*¹²³ observes a dominant relaxation band at room temperature with a lifetime of 5.8 ps, which they also assign to reorientational diffusion and fit to a Debye curve. After this contribution is subtracted, they note the presence of a residual diffusive contribution—this reflects the additional diffusive mode contributing to the line-shape fits of these spectra, attributed to more translational motions here.

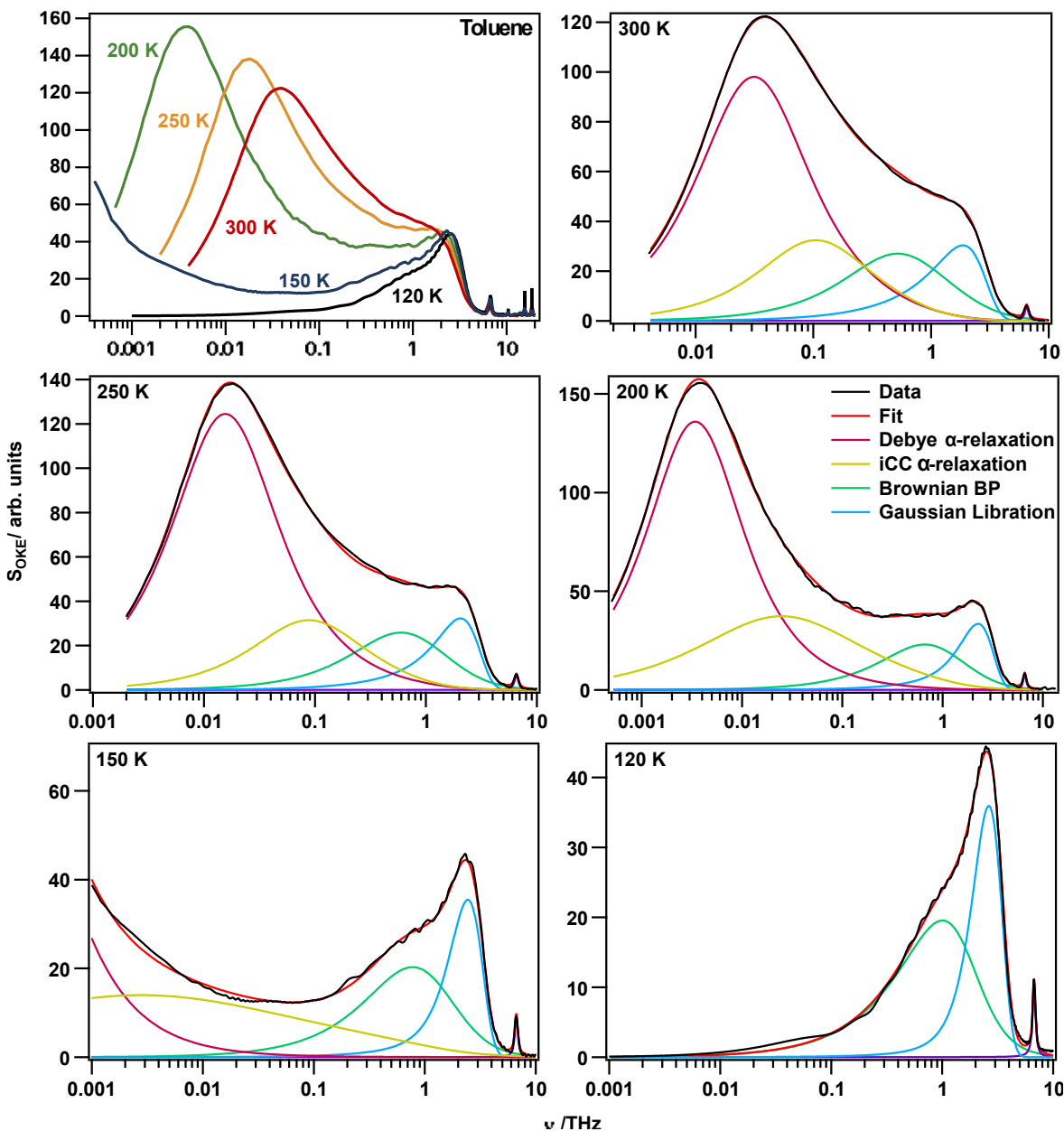


Figure 5.5. OKE spectra of toluene at various temperatures, and their line-shape fits.

Shown are the OKE spectra of toluene at several temperatures as shown, with fits to a Debye function (orientational relaxation), an inertial Cole-Cole (for translational diffusion), a Brownian (for the boson peak), and a Gaussian (librations) function.

The toluene spectrum at 120 K is the most pertinent to this work, where the diffusive motions are frozen out leaving only oscillatory modes. Toluene is highly anisotropically polarisable—slightly more so than benzene—and thus a strong peak due to librations is expected. The intense peak at 2.6 THz at 120 K is assigned to librations, which has a similar room temperature frequency to that seen in benzene previously (within 5%), as one would expect. Its amplitude is invariant with temperature, again consistent with the findings of the hydrocarbon studies of chapter 4. This suggests that the expected increase in the band amplitude resulting from increased density on cooling (more molecules probed within the same volume) must be counterbalanced by the reduced average angle of libration—a by-product of the density increase.

With the libration taken care of, the attention can be shifted to the remaining lower frequency shoulder mode which is the lowest (oscillatory) frequency feature observable here. Its frequency over temperature mimics that of the libration, exhibiting a very linear dependence. The temperature-dependent density of toluene is taken from literature⁸⁵ and used to fit the undamped frequencies of both modes which can be seen to abide the general trend as expected.

The amplitude of the shoulder mode exhibits a positive temperature dependence which can be modelled as the strength of a collision induced signal (eq.(4.31), but also stated within Figure 5.6). Thus, this shoulder mode is assigned to a fast- β mode.

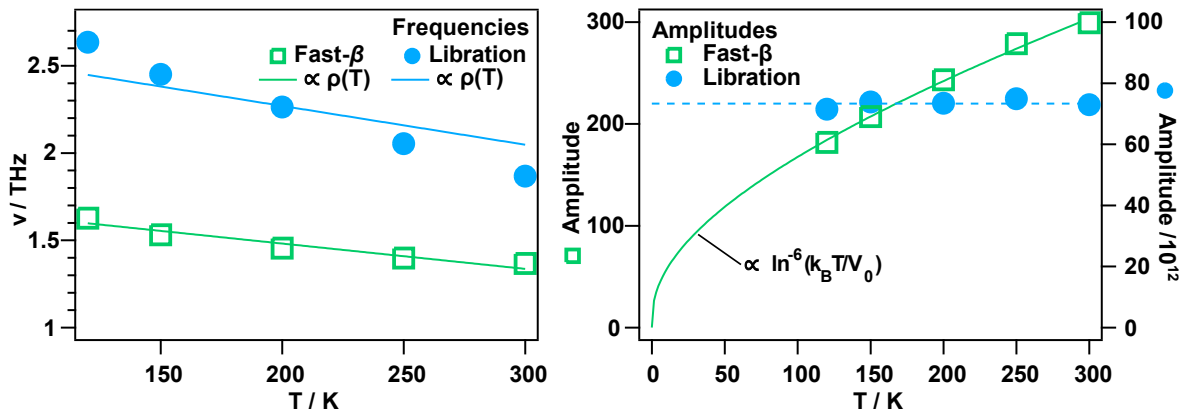


Figure 5.6. Fitting parameters for the line-shape fits of toluene at various temperatures.

Frequencies fit proportional to the density, which is found to be strongly linear with temperature (see ref.⁸⁵ and Appendix E.1). Note that Brownian frequencies are the undamped oscillator frequencies, ω_0 .

The fast- β is fit to a Brownian oscillator throughout. From 300 K to 150 K (in the liquid state) the fast- β BO is an overdamped vibration, and only at 120 K does it become underdamped, with a DHO frequency of 0.6 THz. In other words, the fast- β motion is an *oscillation* in the vitreous state, and only then exhibits an excess peak in the VDoS. In essence, the fast- β becomes a BP on vitrification. Recall that the fast- β is argued here to be washed out phonon(s) in the pseudo-BZ edge; in the crystal these phonons will exhibit an excess in the VdoS (and $C_p(T)$ curve) as a van Hove singularity at (approximately) the *undamped* oscillator frequency which is ~ 2.5 times greater than the DHO frequency. This result is consistent with the washed-out van Hove singularity hypothesis of the BP origin, which suggests that the BP originates from the transverse acoustic phonon in the corresponding crystal.¹⁴⁸ If this is the case, they are not excess states over the crystal at all.

The question must be asked: why should the fast- β only become underdamped on vitrification? Is this a pure coincidence or is it some fundamental property of glass

dynamics? Of course, damping is expected to decrease as temperatures drop, while vibrations become increasingly quadratic, but it is not obvious that the crossover into the underdamped regime should occur exactly at the glass transition. Certainly, further such studies on other glass forming systems would be necessary to conclude the significance of this result.

5.4 Titanium Alkoxides

In order to simplify the spectra, an extensive search for molecular liquids consisting of molecules with high symmetry (tetrahedral, octahedral, or icosahedral) was carried out, including ionic liquids with high symmetry ions and eutectic mixtures. Unfortunately, liquids of highly symmetric molecules or ions have a propensity to crystallise rather than vitrify. However, some of the liquids formed by titanium(IV) alkoxides are found to be glass formers (see Figure 5.7). Titanium tetraethoxide, tetrapropoxide, and tetraisopropoxide were found to crystallise readily on cooling. However, titanium tetrabutoxide (TiBuO) and tetra-2-ethylhexyloxide could be vitrified with ease. TiBuO has a glass transition at $T_g = 162.5$ K as measured using DSC (see Figure 5.8). TiBuO could not be crystallised and therefore the formal melting temperature is unknown. Analysis of measurements of the viscosity at relatively high temperatures compared to the glass transition temperature, suggests that TiBuO is a weakly fragile glass former (see Figure 5.8). This is indicated by the non-Arrhenius scaling fit of the rheology data when fit to the VFT equation.

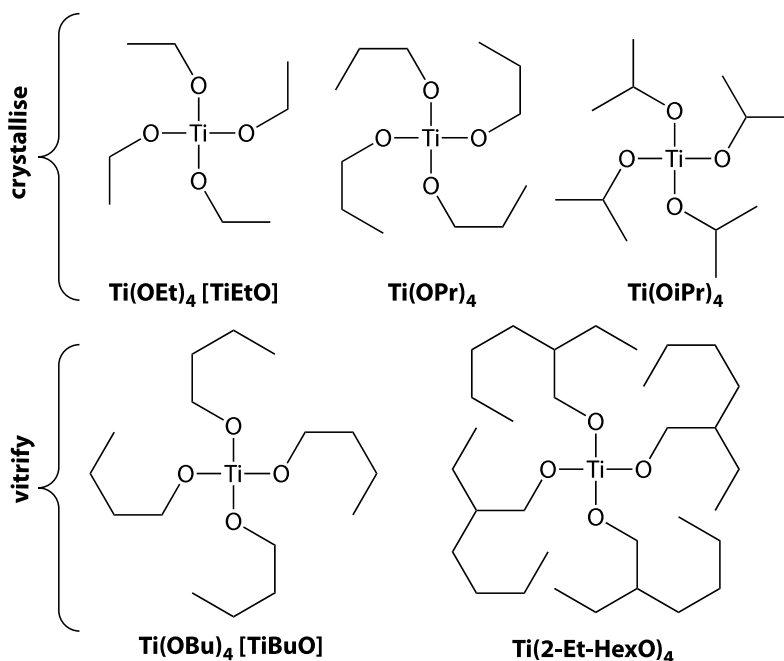


Figure 5.7. Titanium alkoxides investigated.

Shorter chain titanium alkoxides (top) tend to crystallise on cooling, while the longer chain ones (bottom) vitrify.

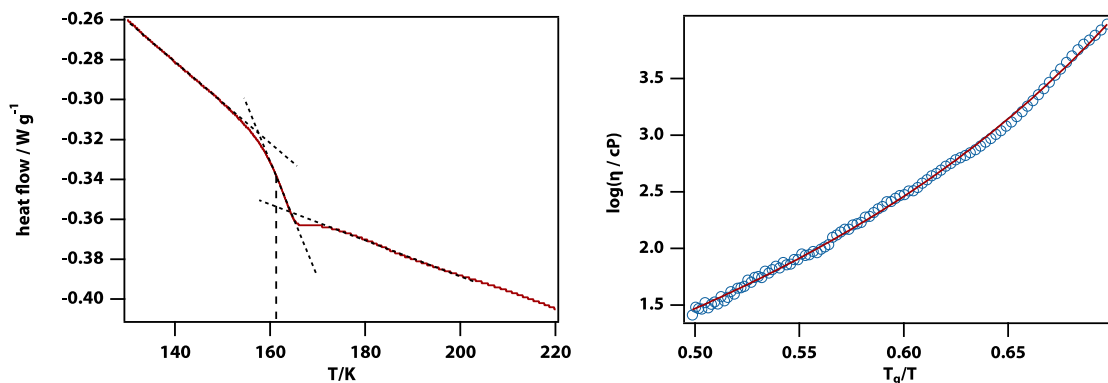


Figure 5.8. Measuring the glass transition temperature of TiBuO.

As found by DSC measurement (left), $T_g = 162.5$ K. Rheology data (right) was fit to a Vogel-Fulcher-Tammann expression for viscosity, $\eta = \eta_0 \exp(DT_0/(T - T_0))$, with $\eta_0 = 0.24 \pm 0.03$ cP, $D = 5.2 \pm 0.3$, and $T_0 = 156 \pm 2$ K.

TiBuO is known not to be monomeric. The crystals of titanium tetramethoxide and tetraethoxide are known to be tetrameric, with the titanium atom being octahedrally coordinated.¹⁹⁰ In the liquid phase, the titanium atoms in TiBuO are thought to be 5-fold coordinated in what are most probably trimers.^{191–193} The most probable 5-fold (D_{3h}) coordination of titanium in liquid TiBuO might give rise to a (small) anisotropic component in the molecular polarisability. The known rapid terminal–bridging alkoxide exchange¹⁹⁴ will be used below to demonstrate that the low-frequency OKE spectrum is predominantly collision-induced.

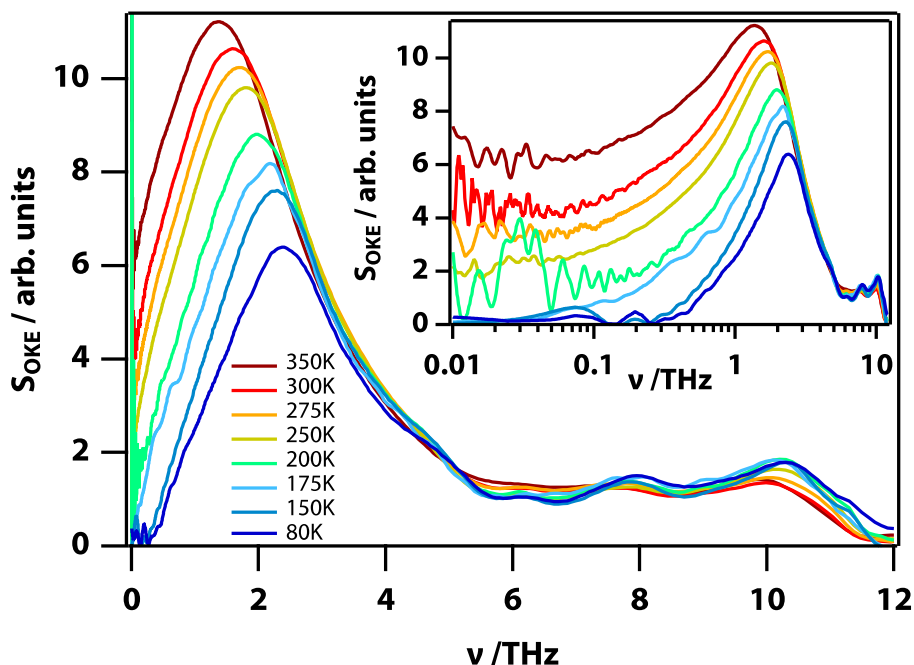


Figure 5.9. OKE spectra of titanium butoxide at various temperatures.

Spectra taken at a range of temperatures from 350 to 80 K (see legend). Data is shown on both a linear (main) and logarithmic (inset) frequency axis.

Figure 5.9 shows the OKE spectra of TiBuO over temperatures ranging from the glassy state (80 K), through the glass transition temperature (162.5 K) into the supercooled regime,

to room temperature and above (350 K). The spectra show several bands at frequencies 4 THz and higher whose amplitudes are essentially independent of temperature. These are almost certainly due to intramolecular vibrations. Vibrational normal mode calculations were carried out and used to calculate the depolarized Raman spectrum converted into an OKE spectrum. As can be seen in the calculated OKE spectrum in Appendix F.4, there are modes with moderate OKE intensity throughout the low terahertz frequency range. The four lowest frequency modes are butoxide librations. Based on the study on toluene (and propane, section 4.7), the strength of the librational mode should exhibit hardly any temperature dependence.

The dominant feature in the spectrum however is a band peaking between 1 and 3 THz, whose position and amplitude are strongly temperature dependent. When viewed with a logarithmic frequency axis, there is clearly an additional broad diffusive contribution below 1 THz. This shifts to lower frequency on cooling and is invisible below the glass transition temperature (as expected). Similar experiments (although much less detailed) were carried out on titanium tetra-2-ethylhexyloxy (see Figure 5.10), which shows the same effect.

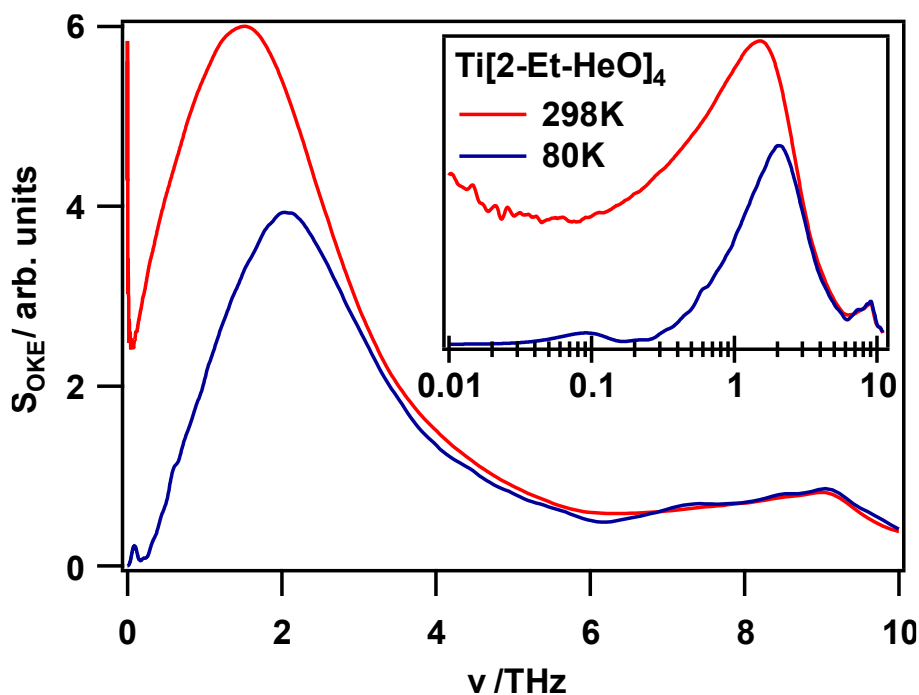


Figure 5.10. OKE spectra of liquid and vitreous titanium 2-ethylhexyloxy.

Spectra taken at 298 K (red) and 80 K (blue), shown with a linear (main) and logarithmic (inset) frequency axis

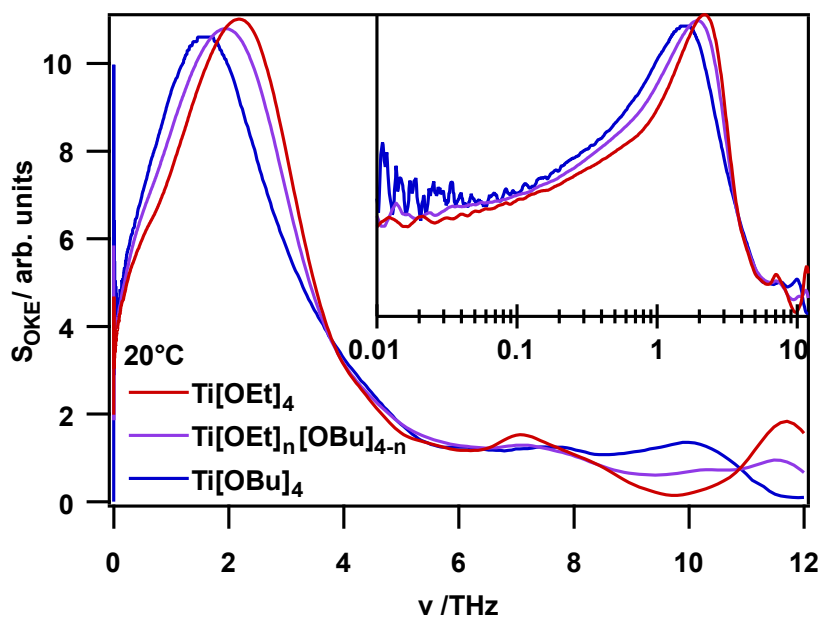


Figure 5.11. OKE spectra of titanium butoxide and ethoxide and their 50:50 vol% mixture at 20 °C.

Spectra shown on both linear (main) and logarithmic (inset) axes.

As the symmetry around the titanium atom is not tetrahedral or octahedral, the lower symmetry 5-fold coordination of titanium in liquid TiBuO could potentially give rise to a librational band in addition to the butoxide librations. To examine the extent of librational contributions to the OKE spectra, the symmetry was lowered more severely on purpose by making 50:50 mixtures of TiBuO and titanium tetraethoxide (TiEtO). As the terminal and bridging ligands are known to exchange rapidly,¹⁹⁴ this will lead to the formation of mixtures of $\text{Ti}(\text{OEt})_n(\text{OBu})_{4-n}$ most of which lack symmetry. The OKE spectra of TiBuO, TiEtO, and their 50:50 mixture at room temperature are shown in Figure 5.11. The 50:50 mixture does not show an increased amplitude of the 1–3 THz main band but simply a band that is exactly in between that of TiBuO and TiEtO. This confirms that this band is indeed predominantly of collision-induced character, and it is therefore assigned as the intermolecular cage-rattling fast- β band.

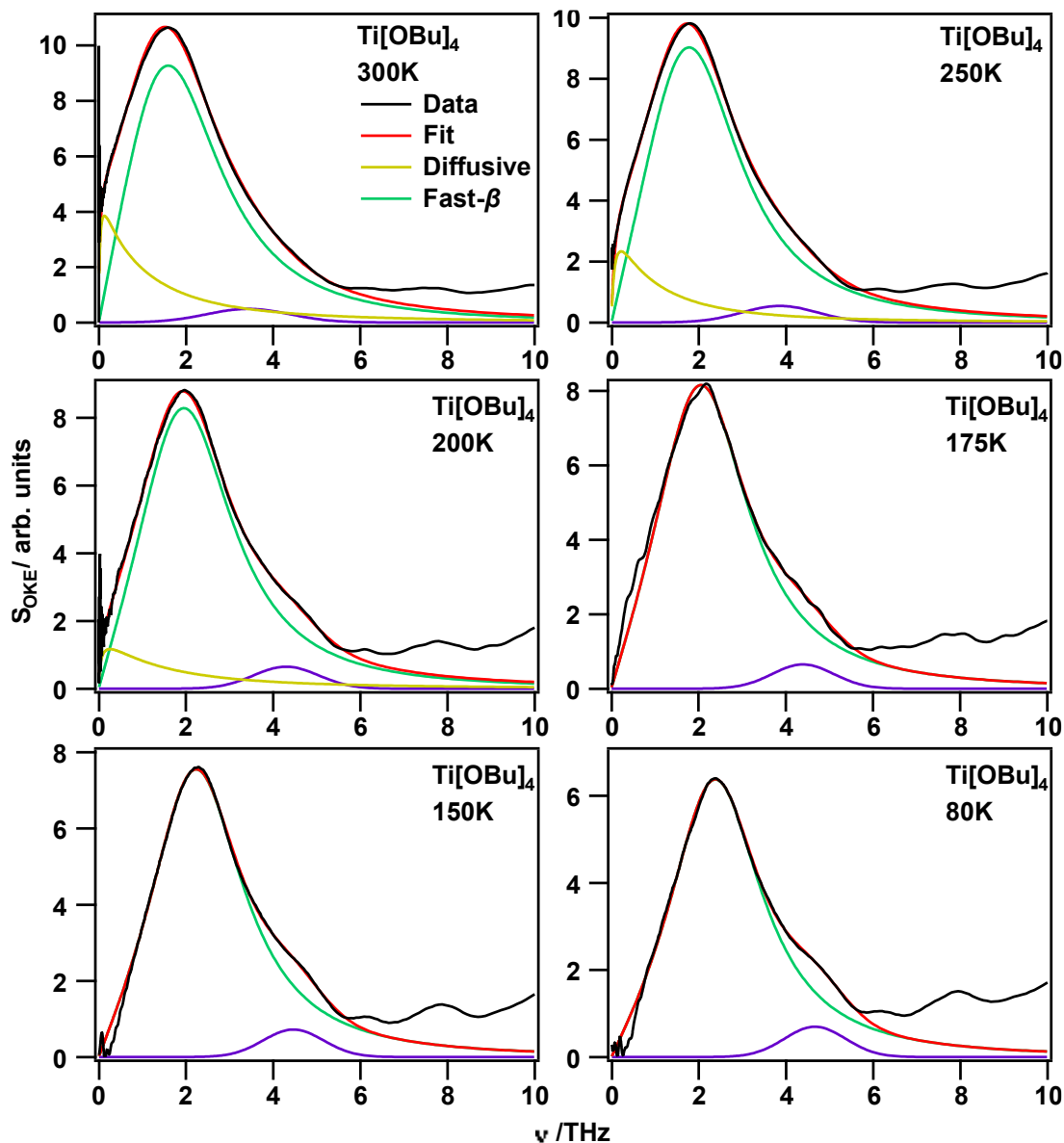


Figure 5.12. Line-shape fits to the temperature dependent OKE spectra of titanium butoxide.

Spectra taken from 300 K to 80 K (left to right), See legend for assignments; the high frequency shoulder mode (purple) is consistent with either an intramolecular mode or librational mode.

The (temperature-dependent) OKE spectra of TiBuO can be fitted with an inertial Cole-Cole function for the translational-relaxation and Brownian-oscillator functions for the intermolecular mode and intramolecular vibrations (see Figure 5.12, also shown on a logarithmic frequency scale in Appendix F.1, and parameters included as Appendix F.2). In the case of TiEtO and its mixture with TiBuO, the intermolecular mode could only be fitted satisfactorily with a Gaussian function, consistent with the presence of a mixture of $\text{Ti}(\text{OEt})_n(\text{OBu})_{4-n}$ species (see Appendix G.2 for and Appendix G.1 for line-shape fits and fitting parameters).

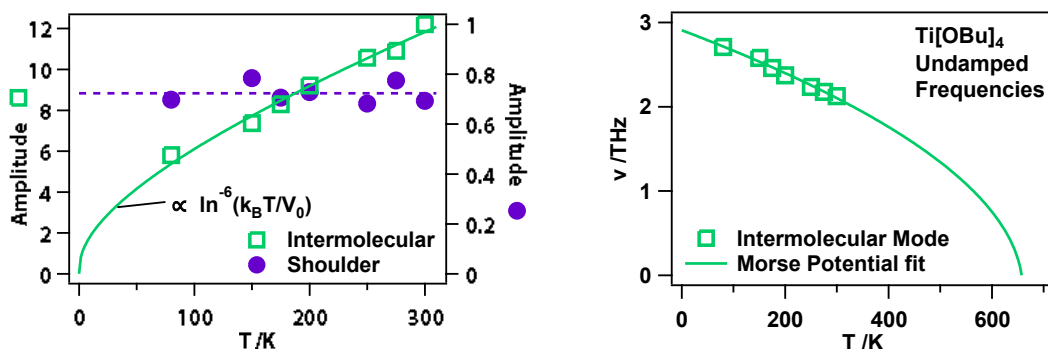


Figure 5.13. Trends in line-shape fitting parameters of TiBuO.

Shown are the amplitudes of the boson peak and the shoulder (left) and the boson peak frequency (right). The boson-peak amplitude data are fit to equation S16 with amplitude 59 ± 22 and $V_0 \times 10^{17} = 6.3 \pm 3.9$ J. Frequency data are fit to equation (5.7) with $D_e/h/\text{THz} = 14.8 \pm 0.7$ and $v_0/\text{THz} = 3.04 \pm 0.05$.

As shown in Figure 5.13, the amplitude of the shoulder peak is largely independent of temperature; this is possibly an intramolecular mode, however it is also consistent with a librational mode as discussed previously. Regardless, it does not obscure the intermolecular mode, which again can be modelled as a collision induced signal. This fast- β mode is in fact underdamped throughout the 80–300 K range, which suggests that the crossover between over- and underdamped regimes in toluene at its glass-transition temperature is possibly coincidental. Toluene may be a more fragile glass than TiBuO, as a result of weaker vdW forces (an indicator of fragility¹⁹⁵). No BPs can be found in literature with frequencies as large as the results for the TiBuO fast- β ; the DHO frequency here at 80 K is 2.4 THz. Ideally calorimetry measurements would be performed on TiBuO in the glassy and crystalline state to quantify its T_{boson} . This could be compared with the fast- β frequency to prove whether or not this mode matches the BP. As mentioned earlier however, TiBuO could not be crystallised in the laboratory, which poses a slight problem!

TiBuO has a weak OKE signal due to the low anisotropic polarisability and the SNR suffers as a result, compared to the toluene FDS whose signal is 5 times greater in the intermolecular (~ 1 THz) region. Whilst a single Brownian oscillator produces a good fit around the TiBuO signal peak, it is poor at the low frequency wing particularly at low temperatures. It is possible that lower frequency features are lost in the signal noise. Indeed, with the existence of trimers in the liquid and glass, a secondary fast- β mode at lower frequency would be expected. This would correspond to the ‘cage rattling’ of the whole trimer, which would be of lower frequency due to its greater mass.

5.5 Tetrabutyl Orthosilicate

Tetrabutyl orthosilicate (TBOS) is essentially the silicon analogue of TiBuO with a less ionic and more covalent character. It too is a glass-forming liquid, however the silicon tetraalkoxides generally do not form dimers, trimers, etc. in the liquid; one might expect this to simplify its intermolecular spectrum. On the contrary, as shown in Figure 5.14, the 80 K spectrum exhibits a clear low-frequency (*c.a.* 1 THz) shoulder mode which was not present—or at least observable—in glassy TiBuO.

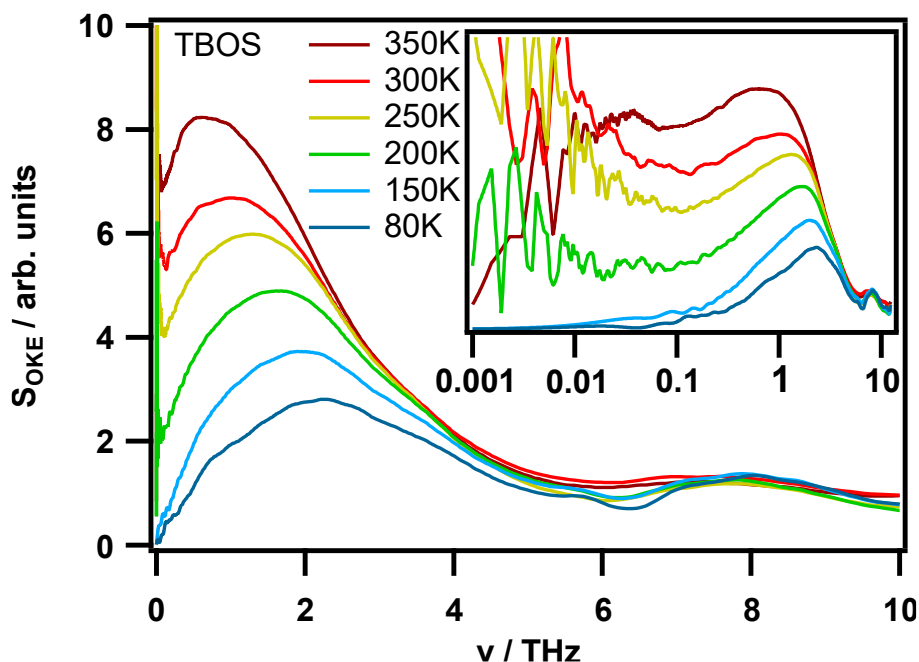


Figure 5.14. OKE spectra of tetrabutyl orthosilicate at various temperatures.

Spectra taken at temperatures from 350 to 80 K (see legend). Data is shown on both a linear (main) and logarithmic (inset) frequency axis

The spectra have been fit to line-shapes as shown in Figure 5.15 below (see Appendix H.1 for logarithmic frequency scale, and Appendix H.2 for parameter values). TBOS again exhibits a busy intramolecular region that does not interfere (much) with the intermolecular part. The lowest frequency band that red-shifts and disappears on cooling is consistent with a diffusive mode, which is modelled using the iCC function. This work remains agnostic to the nature of the high frequency (*c.a.* 3 THz) shoulder, which is consistent with both intramolecular and librational dynamics, however this mode is consistent with butoxide librations (which is technically intramolecular). What is interesting is that the spectral intensities of both intermolecular modes exhibit a strong temperature dependence. The *circa* 2 THz fast- β can be modelled by the usual collision-induced signal (see Figure 5.16), however the low frequency shoulder cannot be well modelled as such, likely again due to SNR. It is *qualitatively* consistent with a collision-induced signal, however.

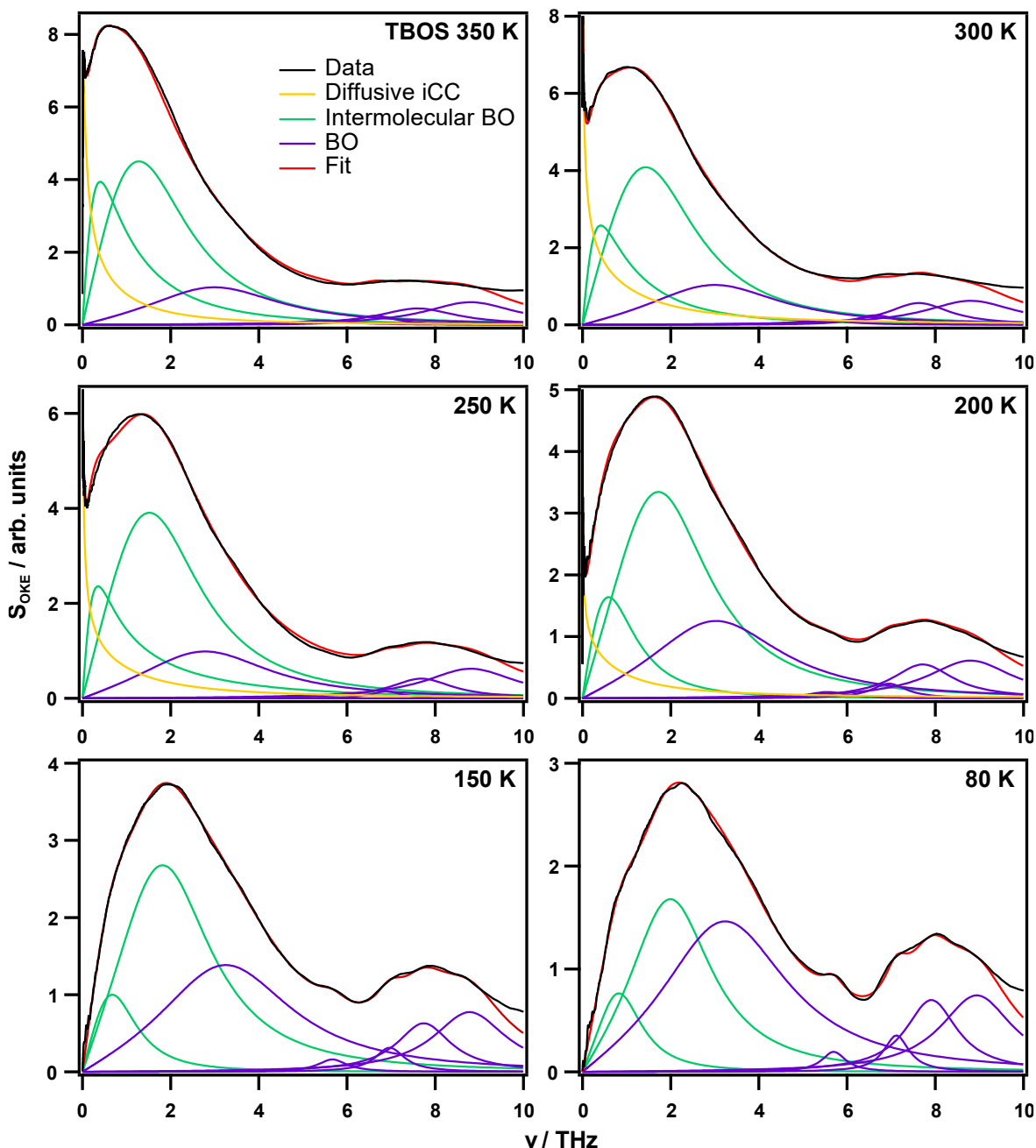


Figure 5.15. Line-shape fits for TBOS OKE spectra at various temperatures.

Spectra taken from 300 K to 80 K (left to right), See legend for assignments; the high frequency shoulder mode (purple) is consistent with an intramolecular mode.

The low frequency fast- β band becomes underdamped between 250 and 200 K, much greater than the TBOS T_g of 125 K (see Appendix H.3), while the fast- β is underdamped throughout. It might be considered that the low-frequency mode arises as the fast- β of locally favoured structures, i.e., $(\text{Si}(\text{BuO})_4)_n$ clusters. This line of reasoning would suggest that the cluster size can be inferred from the frequency ratio between the (single molecule) fast- β and the cluster fast- β . By Hooke's law, this would suggest the theoretical cluster size at 350 K is $n = 2.9$ molecules, and by 80 K it has increased to $n = 4.8$ molecules. Obviously not all clusters will be of equal size, and therefore this mode should ideally follow an ASG line-

shape (see equation (3.14)) to account for the inhomogeneous broadening associated with the distribution of cluster sizes; a better fit to these data is achieved with a BO (see equation (3.14)) however.

Alternatively, this mode could be simply another washed-out van-Hove singularity. Without the ability to crystallise TBOS however, this may be impossible to determine experimentally.

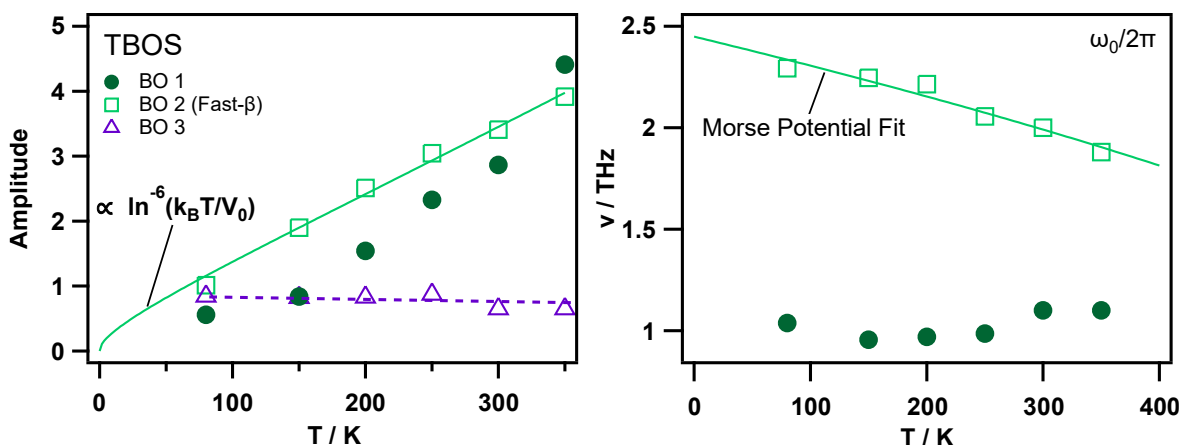


Figure 5.16. Line-shape amplitudes and frequencies for TBOS at various temperatures.

Left: Amplitudes of the Brownian fits to the first three (lowest) frequency vibrational modes: the low frequency shoulder (dark green ●), the main intermolecular mode (light green □) fit to eq.(4.31) with $V_0 \cdot 10^{18} J = 3.1 \pm 0.9$, and the broad high frequency shoulder mode (purple Δ). **Right:** Undamped BO frequencies are shown for the lowest two frequency modes, with the same symbols.

5.6 Conclusion and Further Work

In conclusion, this aim of this research was to uncover the BP, which is reported in many glass systems often sitting shoulder to shoulder with other more prominent spectral features, thereby making line-shape characterisations either difficult, unreliable, or simply impossible. Librational contributions to the spectra have indeed been suppressed, however the issue remains as to what part of (or indeed if) the remaining collision-induced dynamics are boson peaks. This depends entirely on what interpretation is taken as to what a BP is. In the van-Hove singularity hypothesis, the remaining fast- β mode may indeed be the BP. As seen in the case of toluene—whose OKE spectra are of such high quality that the librational band is not a nuisance—the BP is consistent with a fast- β mode that becomes underdamped at T_g .

The OKE spectra of the near-isotropically polarisable glass-formers exhibit line-shapes are mostly inconsistent consistent with the formation of LFS. TiBuO might indeed have many extra ‘cluster’ mode, however the SNR here makes it too difficult to access.

Furthermore, the additional vibration in TBOS fits to a BO function instead of an ASG function. This mode is however obscured in these spectra (a cruel irony) and the SNR is an issue as well; both facts mean that the BO vs. ASG issue remains unsettled. There is further scope for investigation of the boson peak in TBOS by means of greater quality OKE data (*e.g.* through greater scan averaging, better sample *etc.*). The resulting spectrum should be fit with both BO and ASG functions, and resultant fit qualities compared. An improvement in the SNR of lower frequency region would allow more confident fitting of the diffusive band as well.

Computational chemistry simulations on TBOS in particular may be useful to first characterise its crystal structure, which could then be used to calculate phonon dispersion curves for acoustic phonons. If the ‘cluster’ mode frequency matches that of a phonon, then there it is likely that the mode does not indicate molecular LFS after all.

6 THE LIQUID-LIQUID TRANSITION IN WATER

The results presented in this section are a concatenation of two experimental investigations into the liquid-liquid transition of water. The first presented here are experiments that directly measure the behaviour of H₂O solvent molecules in solutions of isotropically polarisable (and nearly OKE-invisible) ions. This line of experiments was completed with the help of Nicola Fairbairn, to whom I am grateful. Additionally, a thank you to Dr. David France is in order for synthesising hydrazinium trifluoroacetate solution for these experiments.

The second set of experiments employ the use of dopant thiocyanate ions to indirectly probe the water structure in aqueous LiCl solutions from room temperature down to 80 K. These results have been published as an article entitled: “Experimental observation of nanophase segregation in aqueous salt solution around the predicted liquid-liquid transition in water”, within *Physical Chemistry Chemical Physics*, see ref.¹⁹⁶ for details. Work belonging to co-author Paul Lane has been included here with consent.

6.1 Introduction

Water is the facilitator of all life.¹⁹⁷ It covers 70% of the surface of the earth, hosting an estimated 70% of all life on earth (believed to be down from 100% a few billion years ago). In searching for habitable planets or extra-terrestrial life, the existence of water is a primary criterion; “follow the water” is somewhat of a NASA slogan in this regard.

The human body is 60% H₂O by mass, and it occupies half of a biological cell’s volume. It contributes to countless biological functions, such as thermoregulation, lubrication, shock absorption, flushing out waste products; it is also the medium of all chemical reactions within the body. Biomolecular functionality, such as that of DNA,^{8,198} is contingent upon intermolecular forces with solvent H₂O, as are the incredibly complex mechanisms of protein folding,^{199,200} and even protein-DNA interactions.²⁰¹

For such a seemingly basic liquid, its microscopic structure and ultrafast dynamics can be surprisingly complex. Water will exchange protons on picosecond timescales²⁰² while forming dynamic, partially hydrogen bonded local structures. The inclusion of solutes complicates things further, producing slower-moving ion solvation-shell or biomolecular surface water.^{9,203}

Water exhibits many anomalous properties, including reaching a maximum density at 4 °C (277 K), a specific heat capacity that rapidly increases on supercooling,^{197,204,205} and an isothermal compressibility that does the same.²⁰⁶ Poole *et al.*²⁰⁷ interpreted this divergent behaviour as indicative of a hidden critical point which terminates the coexistence line separating high and low density liquid (HDL and LDL) water phases. Such a low-density liquid phase could be thought of as ice-like, resulting from a larger degree of tetrahedral ordering, while the high-density phase is more water-like (more disordered). Indeed, LDL has been referred to as the ‘mother of ice’, proposing it to be a necessary, but often very short-lived, intermediate state to crystallisation.²⁰⁸

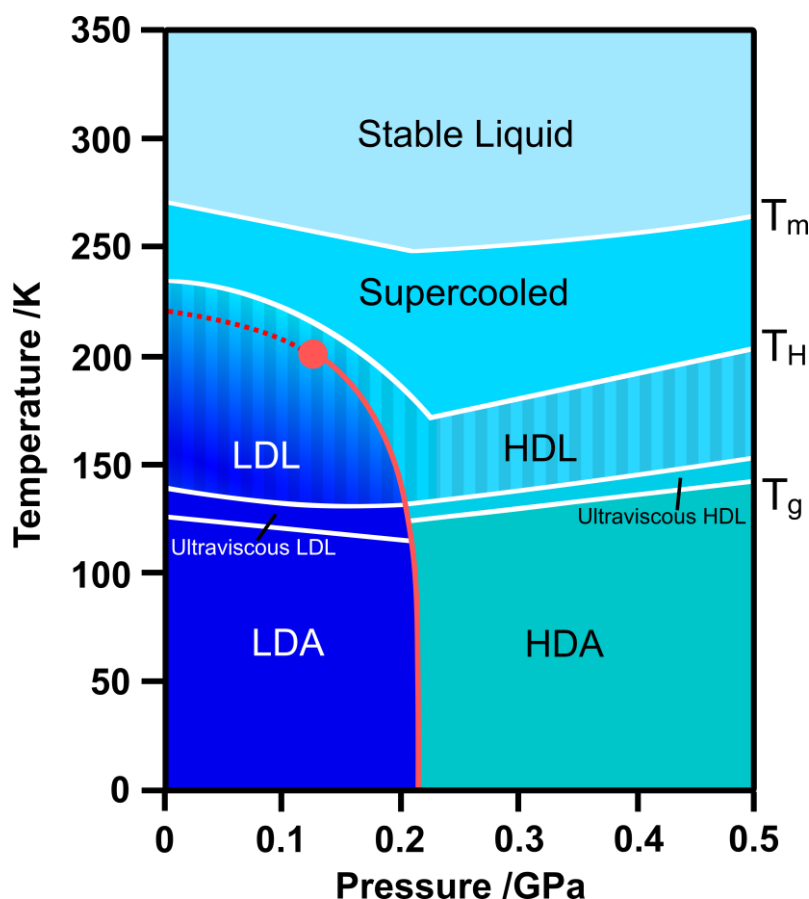


Figure 6.1. Illustrative Phase Diagram of H₂O.

The acronyms are for low- and high-density liquid and amorphous (glassy) phases. The transition between high- and low-density regimes (solid red line) terminates at a critical point (red circle), continuing as a Widom line (dashed red line) thereafter. The melting, homogenous nucleation, and glass transition temperatures are indicated (T with subscript m , H , and g respectively), with the “no man’s land” region indicated by the striped area.

Figure 6.1 shows the proposed H₂O phase diagram. T_H is the homogeneous nucleation temperature, at which ice nucleation will occur spontaneously in the bulk liquid, resulting in rapid crystallisation. Thus, the striped region of the phase diagram below T_H has been given the nickname of ‘no man’s land’, in reference to the experimental difficulty of studying liquid H₂O in this region. Unfortunately, the liquid-liquid critical point is predicted to lie within no man’s land, making experimental verification of its existence troublesome. If crystallisation is somehow avoided, cooling H₂O below 140 K results in the vitrification into an amorphous state (HDA or LDA) dependent on the structure of the preceding liquid. No man’s land can therefore be approached ‘from below’ after hyperquenching H₂O (at rates of 10⁶ K/s and above)^{209,210} into the glassy state—crystallisation occurs when T_g is crossed (however there is experimental evidence for an ‘ultraviscous’ intermediate phase²¹¹).

In recent years there has been a tremendous drive to experimentally observe the proposed LLT of water, with very mixed results. Murata and Tanaka believed they observed a LLT in water-glycerol mixtures,²¹² but this was later revealed to be caused by H₂O crystallisation.^{213,214} A method to delay the onset of nucleation is the addition of solutes that lower the liquidus temperature. The addition of salt to H₂O is also considered a proxy for increasing the pressure.²¹⁵

In a 2018 article, Woutersen *et al.*³¹ report on their observation of phenomena that appear to accomplish this. In their work, the infrared absorption spectra of highly concentrated aqueous solutions of deuterated hydrazinium trifluoroacetate (HTFA) are studied upon cooling and reheating. They observed a *reversible* transition between two spectral line-shapes strongly resembling HDL and LDL water.

Finally a very recent article (succeeding this work) by Kim *et al.*³² details their experimental observation of a LLT in supercooled neat H₂O using an IR (thermal) pump x-ray (scattering) probe technique. This involved the intense local heating of HDA into HDL using a high energy, 100 fs IR pulse, and probing the local structure during rapid expansion with 50 fs x-ray pulses. They witnessed an intermediate structure (LDL) that formed on timescales one order of magnitude faster than ice, which eventually followed. This is the first direct experimental observation of the LLT in pure water.

6.2 Experimental

6.2.1 Experiments on HTFA and $\text{Mg}(\text{ClO}_4)_2$

Hydrazinium trifluoroacetate was synthesised by Dr. David France for these experiments. Magnesium perchlorate hexahydrate was purchased from Sigma Aldrich with 99% purity and used without further purification.

FTIR measurements with the cryostat were performed between 300 and 100 K, at constant cooling/heating rates, and with 16-scan averaged spectra taken at constant time increments. The temperature ramps were given a ≥ 10 min starting margin before spectra were taken to help stabilise any temperature lag of the samples with respect to the cryostat temperature. The cooling and heating rates are not managed by the instruments used here. To complete temperature ramp experiments with (approximately) linear cooling/heating rates, the instruments required continuous monitoring and manual adjustment throughout measurements, *e.g.*, upon cooling, the liquid N_2 flowrate was gradually increased, and upon heating, the heater voltage was gradually increased. As such there will be some variability in the cooling rate throughout, here it is estimated as $\pm 10\%$ between each scan but averages out to $\pm 2\%$ over the entire ramp.

OKE measurements take a longer time to perform (~ 1 hr per spectrum), and so, unlike the FTIR spectra, they are not snapshots of the sample dynamics during a constant heating/cooling cycle rate. The temperature of the sample was instead allowed to stabilise at each chosen temperature step for 1 hr before measurements.

6.2.2 Experiments on Eutectic LiCl-SCN Solutions

A eutectic solution (6.76 M) of LiCl was prepared by dissolving anhydrous LiCl (Sigma-Aldrich) in distilled water. To allow use of SCN^- as an IR-sensitive probe, the LiCl concentration was reduced to 6.36 M and 0.4 M of LiSCN added to maintain the ionic concentration of the eutectic mixture. As both LiSCN and LiCl are hygroscopic, the solutions were prepared under 1 atm N_2 to minimise the absorption of water before and during weighing. A Volhard titration was performed to allow the amount of water absorbed by the LiCl and LiSCN to be accurately determined, this was then considered when preparing the solutions. In some cases, 9% D_2O was added to the H_2O solvent (keeping concentrations constant) to allow visualisation of the OD stretching vibration without signal saturation. The OH-stretching band of water was saturated under normal conditions,

preventing direct observation of this transition. Non-eutectic samples were prepared by keeping the SCN^- concentration constant at 0.4 M and changing the LiCl concentration.

For FTIR measurements, the samples were loaded between two CaF_2 windows separated by a polytetrafluoroethylene (PTFE) spacer of 25 μm thickness. For the room temperature measurements, this was housed in a standard transmission cell. For low temperature measurements, the samples were loaded into a cryostat (Oxford Instruments, ± 0.1 K) in which the sample space had been evacuated to less than 10^{-6} mbar, before being purged with a 0.2 bar overpressure of dry N_2 for a period of 15 minutes before the sample was inserted. This purge was maintained throughout the experiment. The sample was then adjusted to the required temperature, and it was ascertained that the results for the eutectic solution were consistent irrespective of whether the sample was simply cooled to a given temperature or first cooled to 90 K and subsequently heated to the required temperature. Once the temperature had stabilised the sample was held at this temperature for a further 10 minutes before measurements began.

All IR absorption spectra were acquired using a Bruker Vertex 70 Fourier Transform (FT)-IR spectrometer operating in the range of 800–4000 cm^{-1} with a resolution of 1.0 cm^{-1} . The average of three measurements, each consisting of 20 scans was used for all data shown.

6.3 Neat Water

The OH (and OD) stretching vibration in water exhibits a very broad, inhomogeneously-broadened IR absorption band, however it is highly sensitive to its electrostatic environment, making it a useful probe of local structure. In pure water the molar absorptivity of the OH stretch mode, $\epsilon(\nu_{\text{OH}})$ is too large for the instruments used here, producing the saturated peak in Figure 6.2. Doping water with a controlled amount of heavy water can introduce a ‘sister’ stretching mode at a lower frequency whose intensity lies within the dynamic range of the spectrometer.

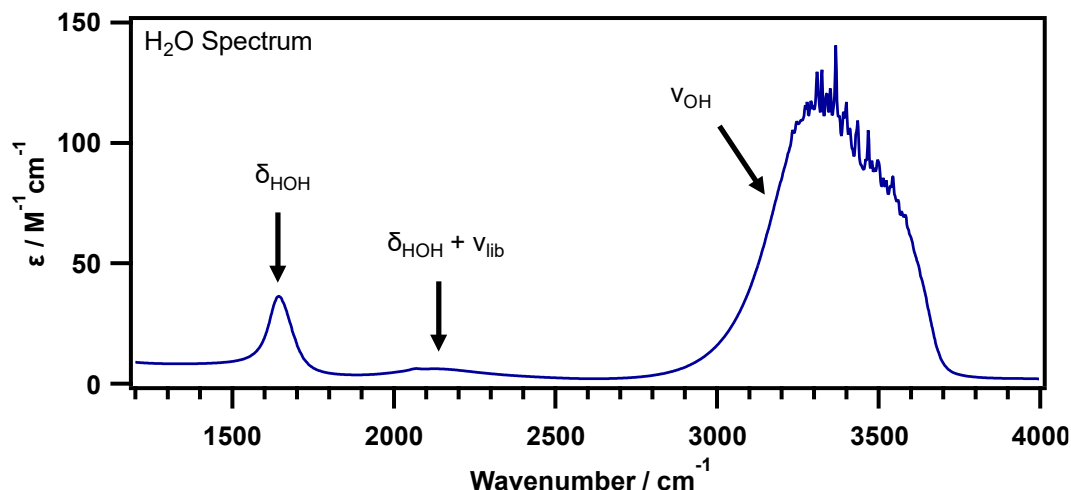


Figure 6.2. IR spectrum of pure H₂O at room temperature.

Labelled from left to right is the HOH bend mode (δ_{HOH}), the combination band of the HOH bend and molecular libration ($\delta_{HOH} + \nu_{lib}$), and the OH stretching mode (ν_{OH}). The ν_{OH} mode has a strong absorbance, and readily saturates the FTIR detector, as shown here.

The OD stretch is redshifted with respect to the OH by a factor of $\sqrt{2}$ into a mostly featureless part of the water IR spectrum (see Figure 6.3), sitting on the shoulder of a very weak combination band. One could dope pure D₂O with H₂O or *vice-versa*, however using a D₂O dopant to probe local structure has greater benefits in the HTFA studies, enabling the avoidance of X-H stretch bands due to both water and ions, which will occur in the same region as ν_{OH} . Furthermore, a broad saturated ν_{OD} band would encroach on the ν_{CN} stretching frequency of the thiocyanate ion, making it impossible to measure reliably.

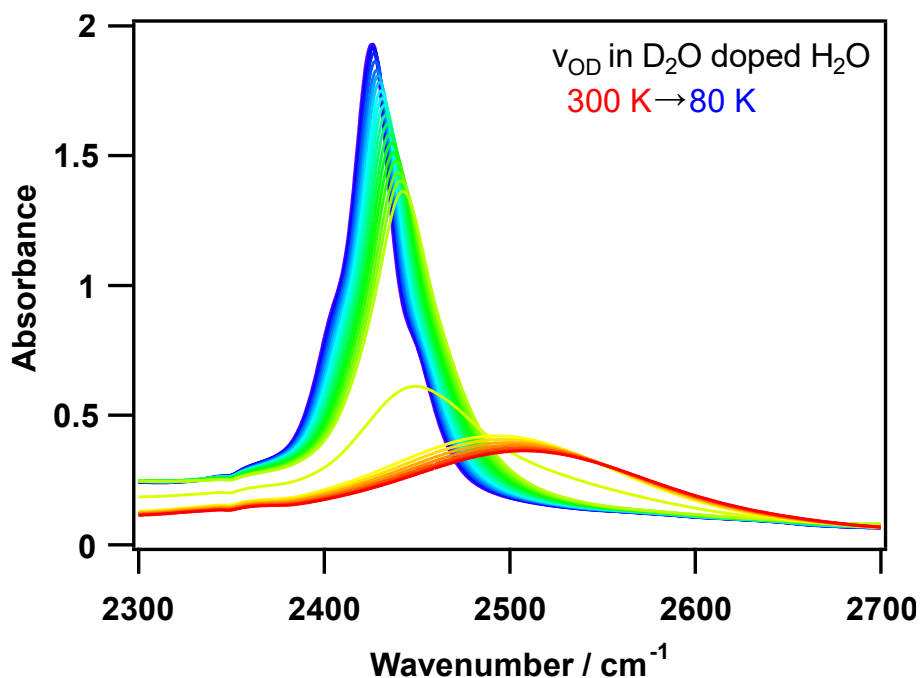


Figure 6.3. OD stretch transition in water and ice.

FTIR spectrum of the ν_{OD} mode is a single broad band in water. In ice it takes the form of readily identifiable intense and narrow peak. The intermediate state is an artifact of scan averaging. Sample is cooled at a rate of 1 K/min.

The frequency of the OH (and OD) stretches is typically interpreted in terms of the number of hydrogen bonds present. A molecule of D₂O in ice will be tetrahedrally hydrogen bonded to 4 neighbouring molecules, and in Figure 6.3 the ν_{OD} mode has a lower frequency than that of the liquid. Furthermore, non-hydrogen bonded gas-phase water molecules are observed to exhibit the highest possible stretching frequency at $\sim 3750\text{ cm}^{-1}$.^{216,217} Thus the broad line-shape of the OH (and OD) stretch may be understood as the summation of contributions from molecules with 0 to 4 hydrogen bonds (from high to low frequency).

For completeness it should be mentioned that H₂O and D₂O will readily exchange their hydrogen isotopes, and thus statistically the number of HOD molecules throughout the solvent will outnumber that of the original dopant. This will have negligible effect on the OD stretching mode though.

6.4 Hydrazinium Trifluoroacetate Solution

These first measurements set out to replicate the findings of Woutersen *et al.*,³¹ but with non-deuterated HTFA salt for convenience. Aqueous solutions of HTFA are doped with heavy water to study the isolated OD stretch band (ν_{OD}). Notably however, the CO₂ asymmetric stretch does encroach on the low frequency slope of the OD stretch as shown in Figure 6.4 centred at around 2350 cm^{-1} , but this is atmospheric and thus the two vibrations are not coupled; the CO₂ bands are also relatively narrow (gas phase) and thus are easy to identify and ignore. Conversely, the OH stretch overlaps with the NH stretching vibrations of the hydrazinium ion in solution, which is why the OD stretch is preferred in this work.

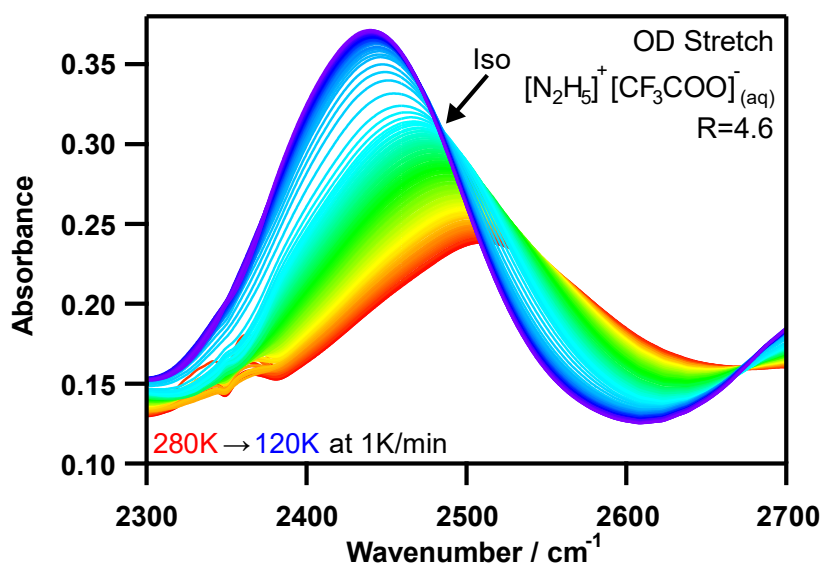


Figure 6.4. IR spectra of the OD stretch in concentrated HTFA_(aq) upon cooling.

The solution has 2.3 water molecules per ion ($R=4.6$). An isosbestic point (labelled 'Iso') is observed. The cooling rate is 1 K/min.

The results shown in Figure 6.4 and Figure 6.5 show the ν_{OD} mode of solvent water on cooling and heating respectively. Isosbestic points are spectral features indicative of a transition between two spectrally distinct populations. These are identifiable here as points on the $A(\nu)$ curve that are invariant with changing temperature. Figure 6.4 shows a nonlinear shift in both intensity and wavelength occurring at ~ 185 K, with an associated isosbestic point throughout a range of spectra at lower temperatures only. This is consistent with a transition between two states that only occurs when the liquid is cooled into no man's land, and certainly not before. Clearly the newly formed structure is not ice, but it appears as a liquid with a greater degree of tetrahedral order. This is consistent with a HDL to LDL transition, and occurs at a sensible temperature with respect to the phase diagram (although the experimental temperature lag is not accounted for as discussed in section 6.2.1). At colder temperatures the solution vitrifies, essentially freezing-in the structure at this point, thus there is minimal change in the ν_{OD} mode thereafter.

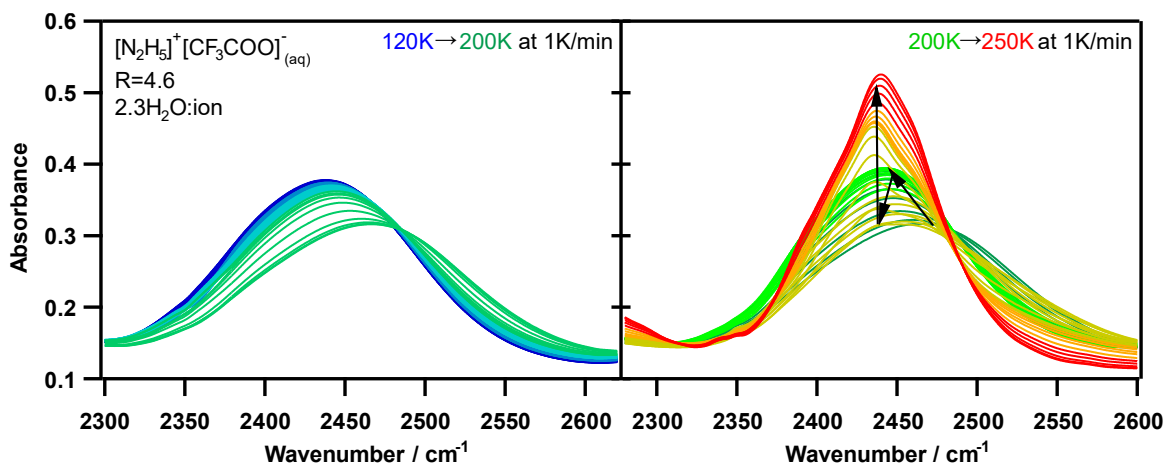


Figure 6.5. IR spectra of the OD stretch in concentrated HTFA(aq) upon heating.

This is split into two segments for greater clarity. **Left:** 120K to 200K. **Right:** 200K to 250K, with spectral evolution marked with arrows. This result is similar to that observed in ref.³¹, except this is the ν_{OD} stretch instead of ν_{OH} . The heating rate is 1 K/min.

The line-shape evolution on heating is more complex. Figure 6.5 (left) shows the apparent LDL to HDL transition accompanied with an isosbestic point at ~ 2480 cm^{-1} between 120 and 200 K. Figure 6.5 (right) then shows what appears to be a reversion to LDL before crystallising. This is reminiscent of the ‘mother of ice’ description of LDL by Bullock and Molinero.²⁰⁸ The dip in peak intensity coincides with an increase in the high frequency wing, followed by the clear onset of crystallisation. Recall that LDL may be 4-coordinated water in this solution, but where a significant proportion of the hydrogen bond donors and acceptors are solute ions. To crystallise, these ions must be expelled from solution, resulting in a coordination number flux, which may explain the sharp dip and broadening of the OD stretch before the emergence of ice.

Notably, these solutions do not actually contain much water—only 2.3 molecules per ion. Woutersen *et al.* argue that, although there may be no truly bulk-like water, H₂O interactions with the N and O atoms of the solutes may be considered a proxy for other water molecules.³¹ Nonetheless, if an aqueous solution with a greater water content could be observed to exhibit this spectral behaviour it may constitute a more compelling observation of the LLT in water. Additionally, OKE spectroscopy may be able to uncover further insights into the transition, but the OKE signal of H₂O is relatively weak, and contributions from the ions (especially trifluoroacetate) overcomplicates the intermolecular spectrum.

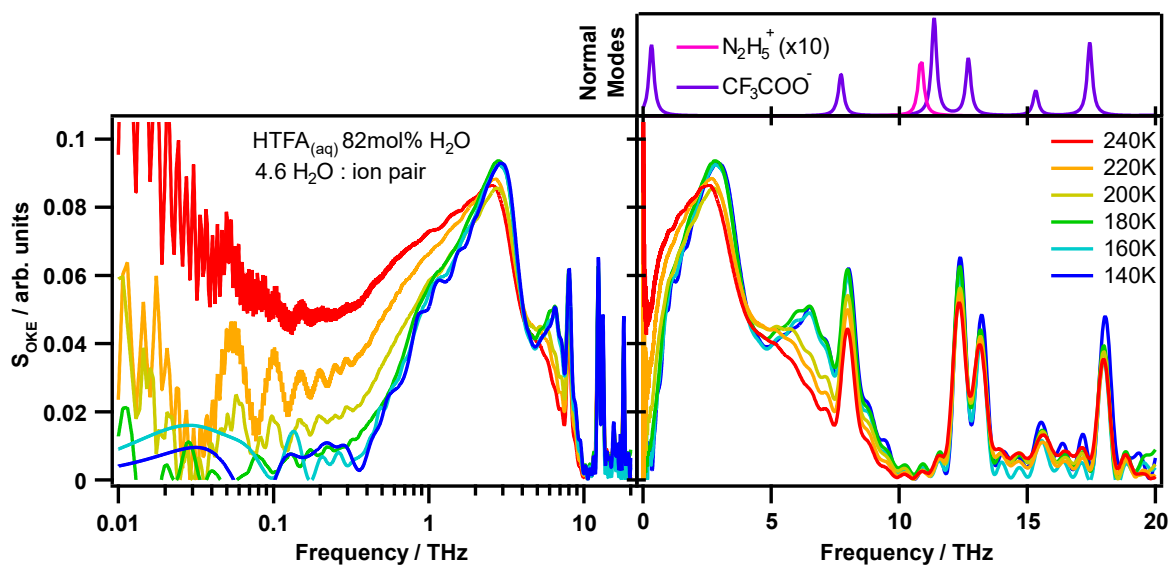


Figure 6.6. OKE spectra of HTFA_(aq) solution at various temperatures.

OKE spectra are shown with both logarithmic (left) and linear (right) frequency axes. Molecular normal modes (top right) are calculated using Gaussian09 with 6-311++G(2df,p) level of theory; note that the calculated normal mode spectrum of hydrazinium is scaled tenfold.

The OKE spectrum of (undoped) HTFA solution is shown in Figure 6.6. The calculated normal modes map well onto the observed intramolecular modes. It is to be expected that the very low frequency (torsional) normal mode of TFA at 0.3 THz will be too washed out by the heat bath to exhibit any distinct spectral signature, and clearly it doesn't. More interestingly, there appears to be two intermolecular spectral events that may be associated with the LLT. Most prominently, the growth of the triangular shoulder band at 6 THz. This band is consistent with the hydrogen-bond stretching mode (for crystalline H₂O this is the LA phonon).²¹⁸ It clearly blueshifts and intensifies first steadily on cooling but then is accelerated due to the LLT between 200 and 180 K. The most prominent feature at 2 THz that exhibits narrowing and an increase in intensity is consistent with the hydrogen-bond bending mode (TA phonon in ice)^{219,220}, however librational modes of the ions may be significant contributors to this peak.

Realistically it would require a host of OKE experiments, both temperature and salt-concentration dependent, to confidently assign all vibrational modes. It would be convenient if the spectra could be simplified through the use of symmetrical ions. Librations of molecular ions would become OKE invisible, leaving only their collisional motions and normal modes. Monatomic ions would be ideal insofar as they do not have normal modes to consider either. In HTFA, it is the TFA ion that is the most troublesome. It has a greater anisotropic polarisability than the hydrazinium ion by a factor of 4.5—hydrazinium on the other hand is very isotropic.

6.5 Aqueous Solutions of Symmetric Ions

An exhaustive search for H₂O-soluble salts consisting of symmetrical (or near-symmetrical) ions was carried out. Highly soluble salts of ions with low charge densities were sought after first. The logic behind this being that with too little ion density in the solution bulk water may freely crystallise, but excessive charge densities may destroy both the local H₂O structures and local H₂O dynamics. In terms of the alkali metal halides, only LiCl is (very widely) known to prevent crystallisation of H₂O on cooling, as will be discussed later. Some of the other candidate solutions were made from the salts listed in Table 6.1. Binary phase diagrams were not found to be readily available in literature for most of these solutions. Aqueous solutions of these were therefore made at their solubility limit, as opposed to their eutectic concentration. Solute-rich precipitation was expected on cooling; however, the remaining solution would be continuously diluted as a result, tending towards the eutectic composition. The ν_{OD} mode in each solution was monitored throughout cooling and in every instance a sharp band at the characteristic frequency of ice was observed to form. This was interpreted as the failure of the eutectic solution to supercool beyond the solidus temperature.

Anion	Cation
Li ⁺	ClO ₄ ⁻
Na ⁺	ClO ₄ ⁻
Ag ⁺	ClO ₄ ⁻
NH ₄ ⁺	PF ₆ ⁻
NH ₄ ⁺	OH ⁻
[N(CH ₃) ₄] ⁺	Cl ⁻
[N(C ₄ H ₉) ₄] ⁺	Br ⁻
[P(C ₄ H ₉) ₄] ⁺	Br ⁻

Table 6.1. Various salts dissolved in water.

The salts of these ions are relatively H₂O soluble. These ions have high symmetries and low charge densities.

By necessity, the salt specification of low charge density was somewhat relaxed ultimately leading to experiments on magnesium perchlorate solution. This solution has gained significant scientific interest since the discovery of Martian brine, which contains magnesium and perchlorate ions in high concentrations among others.²²¹ It has a known eutectic composition of 44 wt% salt, has a liquidus temperature as low as 206 K.²²² Mg^{2+} is regarded as kosmotropic, that is, its presence has an effect of reducing macromolecule (*e.g.* proteins or DNA) solubility, eventually causing them to precipitate- kosmotropes are said to cause ‘salting-out’. Kosmotropes are water ‘structure-makers’ meaning they enhance molecular order in water, promoting more tetrahedral structure. The ClO_4^- ion on the other hand is a chaotrope, which essentially has the opposite effect on water (and macromolecules). This means that for the $\text{Mg}(\text{ClO}_4)_2$ solution there are two competing effects at play. H_2O molecules solvated around Mg^{2+} ion may be thought of as more tightly bound and uniformly structured, while those surrounding ClO_4^- are loosely bound and disordered.

The charge density of the Mg^{2+} ion is a factor of 2.3 greater than that of Li^+ , meaning first solvation shell water should be tightly bound to the ion. ClO_4^- has an effective radius approximately 3 times larger than Mg^{2+} and thus an effective surface area 9 times greater, not to mention they are the 2:1 ion majority in solution. This means that most water molecules in this solution will exist in the solvation shell of the weakly charged anion. Neutron scattering experiments by Lenton *et al.*²²³ show the Mg^{2+} in this same solution has 6 surrounding H_2O molecules on average (leaving ~12 that are not), suggesting octahedral structure. Likewise, further away from the Mg^{2+} ion 6 surrounding ClO_4^- ions are typically found. This shows that there is a high degree of charge ordering in this solution.

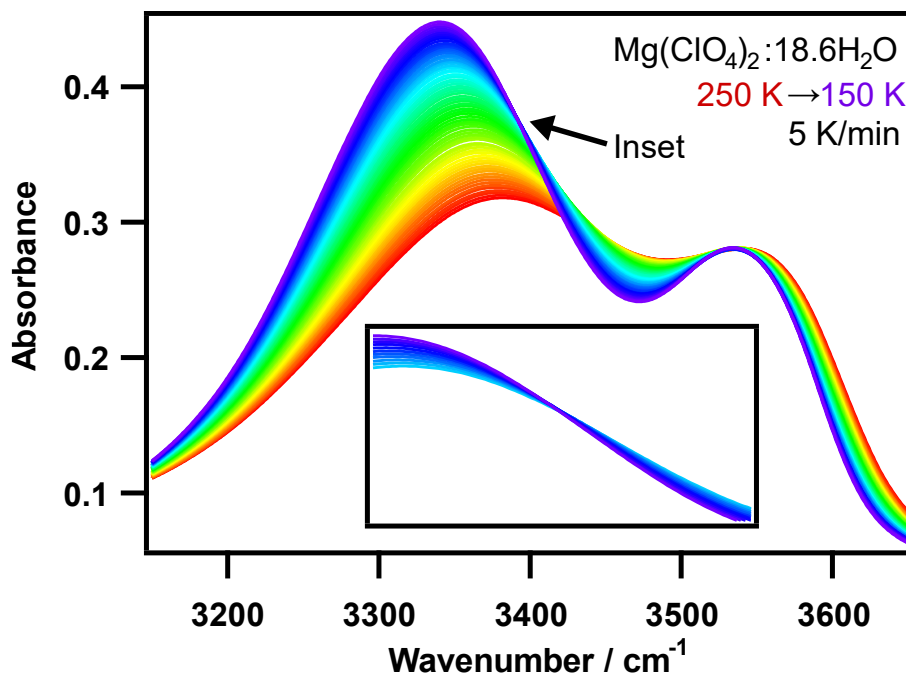


Figure 6.7. FTIR spectra of the OH stretch in $\text{Mg}(\text{ClO}_4)_2(\text{aq})$ on cooling.

FTIR spectra on cooling at 5 K/min (main), and a subtle isosbestic point at low temperatures (inset). Solution is 44 wt% salt, resulting in $\text{Mg}(\text{ClO}_4)_2:18.6\text{D}_2\text{O}$ (H_2O doped).

The high frequency shoulder band shown Figure 6.7 suggests that this solution permits a substantial population of weakly hydrogen-bonded OH groups. This has been assigned to hydrogen bonding with the ClO_4^- ion.^{224,225} The broad low frequency band must represent all inter- H_2O hydrogen bonded OH groups. The gradual red-shift on cooling may suggest either an overall increase in the number of hydrogen bonds per molecule, or a strengthening of the existing bonds. In the former case, on the pure- H_2O phase diagram (Figure 6.1) this would correspond to cooling at pressures below that of the liquid-liquid critical point, thereby not encountering the LLT. Instead, this would cross the Widom line in the single-phase region, which marks the onset of a *continuous* transition from HDL to LDL on cooling, as opposed to a first-order transition.

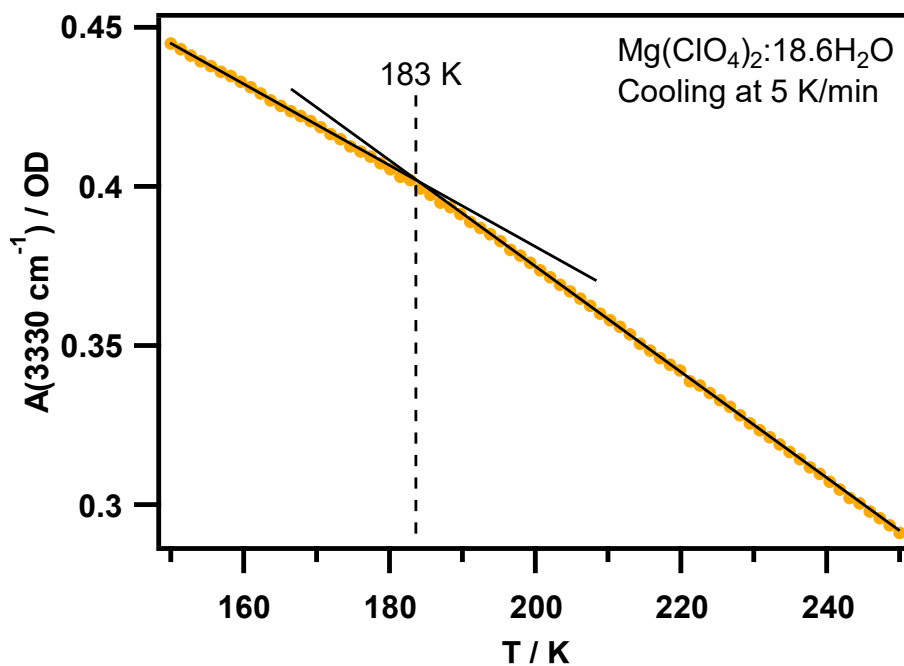


Figure 6.8. Temperature dependent OH stretch mode absorbance at 3330 cm^{-1} in $\text{Mg}(\text{ClO}_4)_2$ solution cooled at a constant rate.

Data is fit to straight lines for high and low temperature ranges. The intercept occurs at (approximately) 183 K, however the temperature scale is not exact due to experimental limitations.

There does appear to be an isosbestic point in these spectra only at lower temperatures (see Figure 6.7 inset). This is accompanied by a subtle change in the line-shape evolution as shown by the temperature dependent absorbance at fixed frequency as shown in Figure 6.8, which exhibits a very slight ‘hockey-stick’ trend that corresponds to a reduction in dA/dT on cooling. Given the clear increase in dA/dT present in HTFA solution, this observed decrease is unexpected for an HDL to LDL transition. Conversely, the neutron diffraction studies of this solution by Lenton *et al.*²²³ compares this solvent water structure to that seen in pure H_2O at 2 GPa. This is of course far too high for the LLT to be observed (by a factor of 10, see Figure 6.1). In this case, the liquid would remain HDL-like on cooling, until vitrifying into the so called very-HDA (VHDA) glass.²²⁶ Indeed, a reduction in the OH stretch dA/dT is a typical result of vitrification.^{196,227} Furthermore, according to the extended H_2O phase diagram of Ruiz *et al.*,²²⁸ a T_g of around 180 K would suggest an equivalent pure- H_2O pressure of ~ 2.5 GPa, in keeping with the aforementioned neutron diffraction studies.

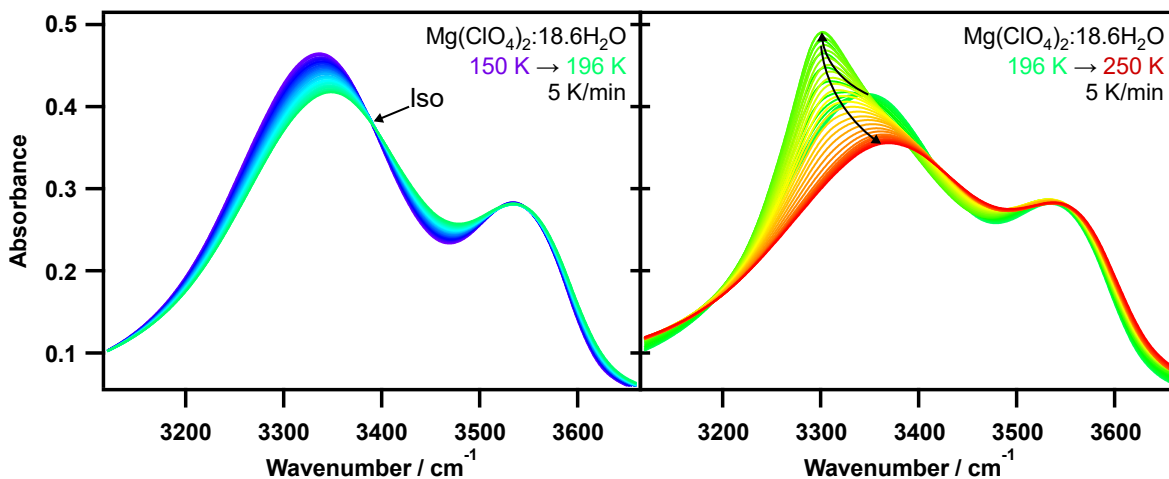


Figure 6.9. FTIR spectra of the OH stretch in $\text{Mg}(\text{ClO}_4)_2(\text{aq})$ on reheating.

FTIR spectra on heating at 5 K/min, split into two segments for greater clarity. **Left:** heating from (approximately) 150 K to 196 K, with an isobestic point marked. **Right:** heating from (approximately) 196 K to 250 K, with line-shape evolution marked with arrows. Solution is 44 wt% salt, resulting in $\text{Mg}(\text{ClO}_4)_2:18.6\text{D}_2\text{O}$ (H_2O doped).

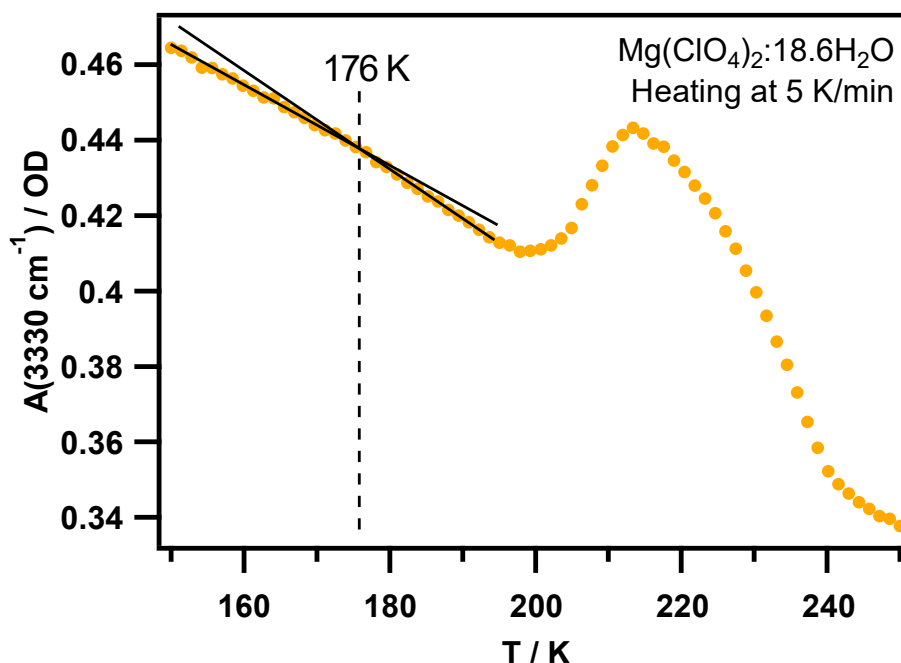


Figure 6.10. Temperature dependent OH stretch mode absorbance at 3330 cm^{-1} in $\text{Mg}(\text{ClO}_4)_2$ solution when reheated at a constant rate.

Data is fit to straight lines for high and low temperature ranges. The intercept occurs at 176 K, however the temperature scale is not exact due to experimental limitations.

On reheating the magnesium perchlorate solution, the first thing to note is the intensity decrease and blue-shift as shown in Figure 6.9 (left). The absorbance at a constant wavelength is plotted in Figure 6.10 which again exhibits a change in dA/dT , as identified by the slight ‘kink’ at 176 K. This occurs at 7 K *lower* on heating than on cooling which is nonsensical and provides further proof that the instrument sensor temperature is unreliable, and a direct measurement of the sample temperature is needed. Nonetheless this kink is likely due to heating above T_g , where the liquid reverts to an HDL-like phase. There is a

potential isosbestic point at lower temperature, however vitrification is considered a kinetic transition only and should not result in the conversion between distinct spectral populations. These isosbestic points were subtle to begin with, and clearly their validity as a reliable indicator of phase transitions is questionable. They may exist here purely as a fluke, resulting from continuous frequency and intensity shifts.

As shown in Figure 6.9 (right), liquefaction is followed directly by the formation of a sharp low-frequency shoulder band that resembles the crystallisation witnessed in HTFA (Figure 6.5), and finally the disappearance of the shoulder band—likely due to the dissolution of the precipitate. There is clearly plenty to discuss with regards to the dynamical and structural changes in this $\text{Mg}(\text{ClO}_4)_2$ solution, however there is no evidence of a LLT. Observations instead point towards a solution whose solute water is analogous to pure H_2O at pressures that inhibit the formation of LDL, and regular (I_h) ice for that matter.

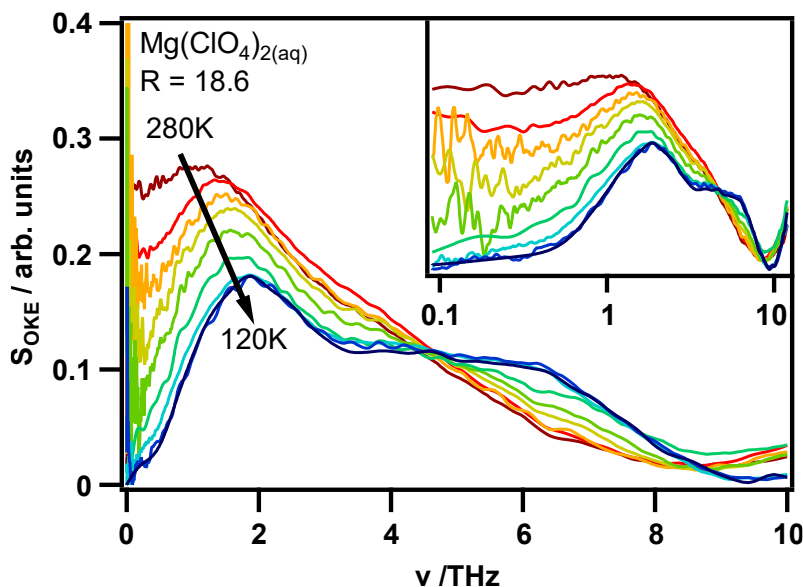


Figure 6.11. OKE spectra of $\text{Mg}(\text{ClO}_4)_2$ solution between 280 and 120 K.

Spectra are displayed on both a linear (main) and logarithmic (inset) frequency scale. Solution is 44 wt% salt, resulting in $\text{Mg}(\text{ClO}_4)_2:18.6\text{H}_2\text{O}$.

The OKE spectrum of magnesium perchlorate solution, shown in Figure 6.11, should be dominated by H_2O dynamics, with some smaller contribution from the solute Π^H term. Like the OKE spectra of HTFA solution, a 6 THz band emerges at low temperatures. Given that it is likely that no LLT is present in this liquid, this suggests that this similar band observed in HTFA is not related to the LLT. Turton *et al.*⁸³ observed that in $\text{LiCl}_{(\text{aq})}$ solution the H_2O LA phonon is red-shifted with respect to its frequency in pure water from ~ 5 to 4 THz, but blue-shifts to 6 THz and grows in intensity on cooling. This is consistent with the spectral evolution observed here. A *ca.* 2 THz band is also present, but its intensity decreases with decreasing temperature; this may be due simply to the freezing out of the diffusive sub-THz

modes. If there was an increase in tetrahedral ordering one might predict an increase in amplitude due simply to the greater proportion of H₂O molecules available to participate in a bending mode. Indeed, there is a small amplitude increase in the HTFA 2 THz band around the LLT, however as mentioned previously, the ion (especially TFA) librational bands complicate the interpretation of these spectra.

6.6 Thiocyanate-Probed Lithium Chloride Solutions

Lithium chloride solutions in particular have been studied as a proxy for neat water at high pressure.^{208,229,230} Turton *et al.* showed that the characteristic hydrogen-bond bend and stretch modes are maintained in LiCl solution at low temperature.⁸³ In vitreous (hyperquenched) LiCl solutions there is experimental evidence for a polyamorphic transition between HDA and LDA states,²³⁰ and for phase-separation having occurred.²³¹ By necessity the LDL phase expels solutes to facilitate the formation of four-coordinated water,²³² and computer simulations suggest that homogenous salt solutions will undergo nano-scale phase-segregation into LDL and salt-rich brine domains.²²⁹

LiCl solution has a liquidus temperature at its eutectic concentration of 6.76 M (7 H₂O molecules per ion pair) that is approximately 80 K less than neat water,^{233,234} and on further cooling the solution can be vitrified at ~140 K.²³⁵ LiSCN solution is actually very similar to this; at its eutectic concentration the liquidus temperature is suppressed by ~90 K.²³⁶ However, the thiocyanate ion is a powerful experimental probe: it has a strongly IR-active ν_{CN} stretch mode at 2040–2200 cm⁻¹ that is sensitive to its local electrostatic environment,^{237–239} and a large anisotropic polarisability, resulting in a strong OKE signal. The following section will study the IR spectra of LiCl solutions that are SCN⁻ doped, and sometimes D₂O doped as well; these will be often labelled as LiCl-SCN:nH₂O, where n = 7 corresponds to the eutectic composition. This is method, which is similar to that used by Yuan and Fayer for room temperature LiCl solution,²⁴⁰ can provide greater insight into the temperature-dependent structure of the solution.

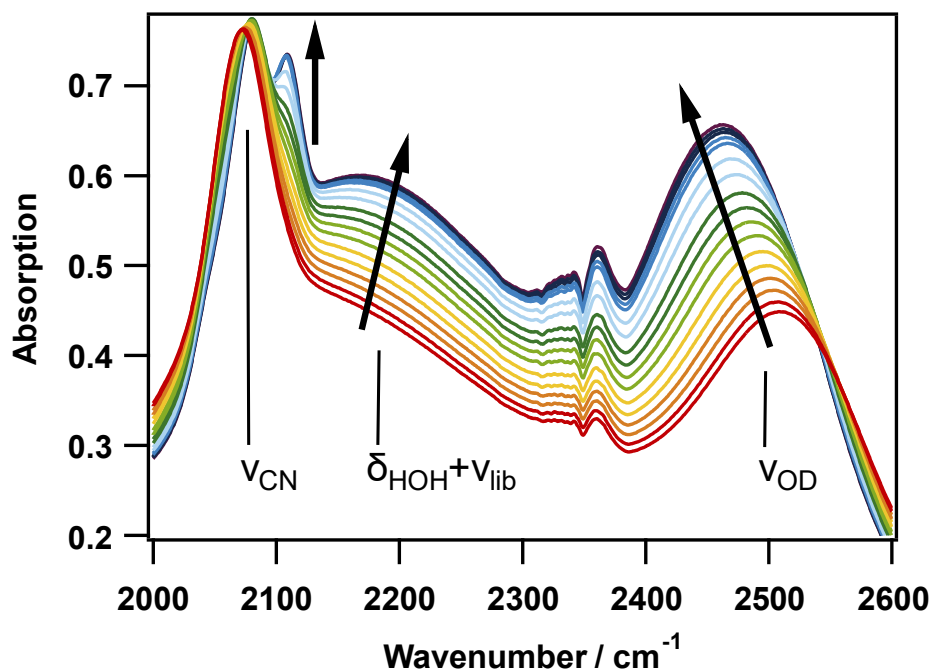


Figure 6.12. IR spectra of eutectic LiCl-SCN:7H₂O doped with D₂O at various temperatures.

Solution is measured between 253 and 93 K in 10 K intervals (direction of arrows). Labelled spectrum displaying a range of vibrational transitions: the thiocyanate CN stretching vibration ν_{CN} , a water combination band of H-O-H bending δ_{HOH} and librational mode ν_{lib} , and the O-D stretching transition ν_{OD} .

The FTIR spectra of the doubly doped LiCl_(aq) eutectic mixture are shown in Figure 6.12 on cooling. The 2000–2600 cm⁻¹ region is jam-packed with spectral features, containing from low to high frequency: the narrow ν_{CN} stretching mode, the broad H₂O combination band formed of the H-O-H bend mode (δ_{HOH}) and a librational mode (ν_{lib}), and finally the slightly less broad ν_{OD} stretching mode.

The temperature-dependent behaviour of the water component in the eutectic solution is indicated by the combination band and the OD stretching mode. Decreasing the temperature causes the former to shift to high frequency and latter to lower frequencies, while both increase in amplitude. The point at which the solution becomes vitreous is marked by the slow-down of these trends, which occurs at $T_g \approx 140$ K (see Figure 6.14).

The formation of ice should be readily identifiable as shown previously in D₂O doped pure water (Figure 6.3) by the growth of a narrow, lower-frequency OD stretch mode. Figure 6.13 shows the occurrence of crystallisation in a more dilute solution of doubly doped LiCl_(aq). Furthermore, the combination band line-shape can also be used as an indicator, where the presence of ice is observable as a higher frequency contribution to the band that does not exist in the more concentrated solution of Figure 6.12. This is largely due to the

stiffening of the ν_{lib} mode in ice.^{241,242} On heating, the sharp OD stretch peak vanishes at 233 K, consistent with the liquidus temperature of this solution.²³⁴

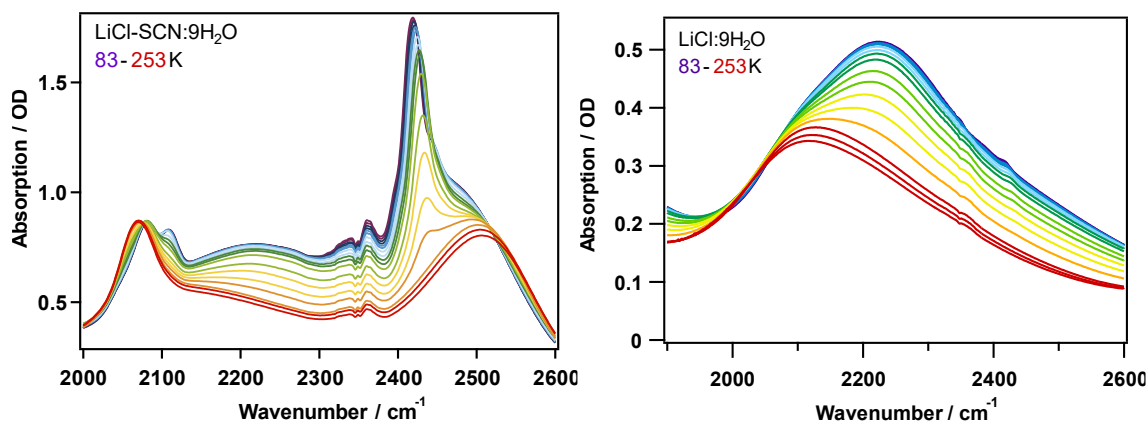


Figure 6.13. Temperature-dependent FTIR spectra of doped and undoped LiCl:9H₂O.

Left: D₂O and SCN⁻ doped solution. **Right:** Undoped solution showing the H₂O combination band only.

The ν_{CN} stretching mode appears as a single mode at room temperature peaking at 2070 cm^{-1} as opposed to 2055 cm^{-1} observed in fully water-solvated ions. This is consistent with the formation of Li⁺SCN⁻ contact ion pairs (CIPs), as expected at high concentration.^{237,243} Eventually a second, higher frequency shoulder mode $\sim 2105 \text{ cm}^{-1}$ appears on cooling. Figure 6.13 confirms that this shoulder peak is due to the thiocyanate probe and not the H₂O combination band. To characterise the temperature-dependence of the ν_{CN} stretching mode, the combination band was fit to Gaussian line-shape functions and subtracted from the spectra, leaving the isolated thiocyanate contribution. This was completed by Dr. Paul Lane, and thus Figure 6.14 is courtesy of his work.

As shown in Figure 6.14, the $\sim 2075 \text{ cm}^{-1}$ CIP ν_{CN} band shifts to higher frequency on cooling down to 180 K, consistent with an environment with increased hydrogen-bonding strength. Thereafter this blue-shift is arrested, and the ν_{CN} shoulder peak exhibits rapid intensity growth. This mode is not consistent with the spectrum of crystalline LiSCN,²⁴⁴ and has instead been previously identified as “aggregates”.^{237,243} The thiocyanate ions exist in dynamic equilibrium between solvated, CIPs, and aggregates, meaning that this apparent equilibrium shift therefore shows a segregation of a salt-rich (brine) phase.

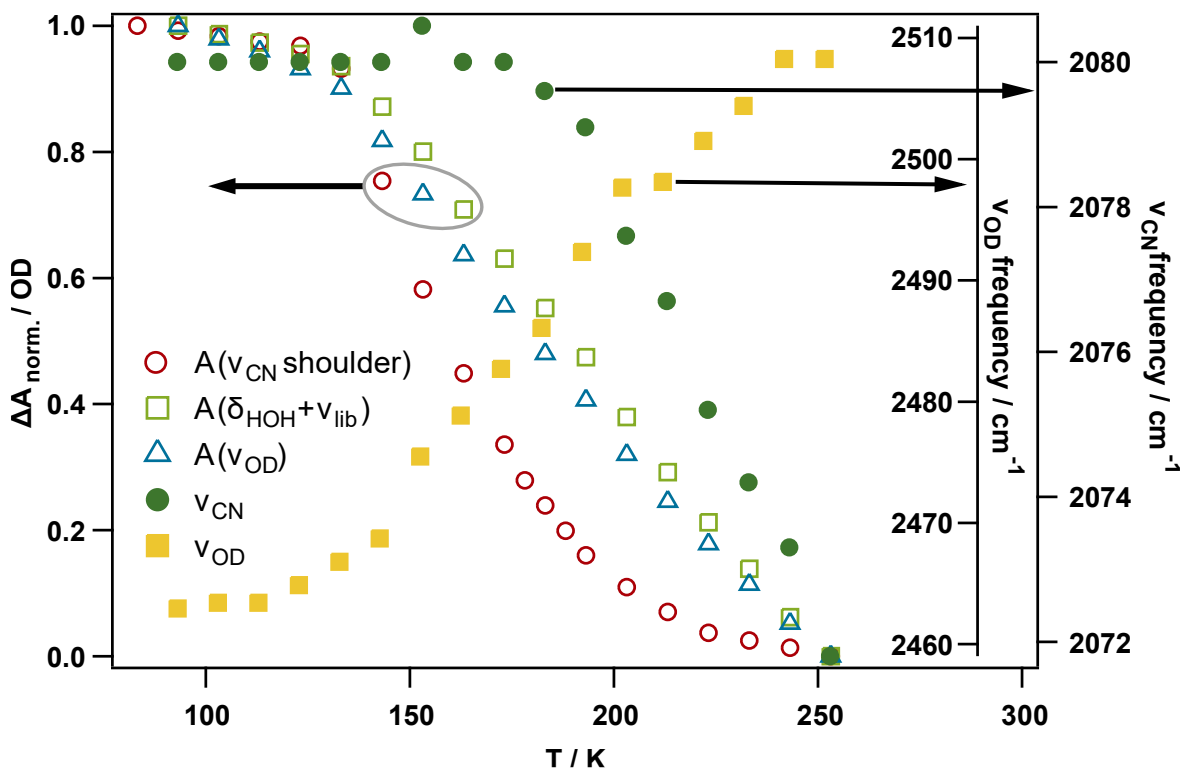


Figure 6.14. Fitting parameter trends for the T-dependent LiCl-SCN:7H₂O IR-spectra.

Normalised Gaussian amplitudes for the ν_{CN} shoulder (red \circ), the combination band (green \square), and the ν_{OD} mode (blue Δ) are plotted (left axis) against temperature. Frequencies of the ν_{CN} (green \bullet) and ν_{OD} (yellow \blacksquare) stretches are plotted (right axes, labelled) against temperature. Courtesy of Dr. Paul Lane.

As with the magnesium perchlorate solutions, there is no appreciable spectral line-shape evolution that would directly indicate a first-order LLT in this solution. The continuous aggregation upon cooling revealed by the increasing ν_{CN} shoulder intensity is indicative of the formation of an LDL phase that drives out solute into a salt-rich brine phase. In terms of the pure H₂O phase diagram, this effect suggests a Widom-line crossing. However, the presence of isosbestic points in the OD stretch is dubious at best (see Appendix I.1 for enlarged figure of potential isosbestic points), nor does it blue-shift to the same extent as that witnessed in HTFA solution indicating more tetrahedral H₂O ordering. Without definitive evidence of a LLT obtained *via* the ν_{OD} mode alternative explanations for these results must be offered.

Highly concentrated solutions of NaCl are known to form large aggregate clusters in solution that exclude water, whereas KSCN can form spatially extended networks that intertwine with the surrounding hydrogen bonding network.²⁴⁵ Regardless of the structure of the aggregates, the H₂O hydrogen-bonding structure at high salt concentration is different from that of pure water. Reduced water coordination in these solutions may explain the failure to witness a more tetrahedral H₂O structure. Furthermore, the simulations of Choi *et al.*²⁴⁵ showed that aqueous NaCl solutions exhibit CIP mole fractions that increase with salt

concentration up to 3 M, beyond which they remain constant as the solubility limit is approached. This is consistent with the relatively unchanging amplitude of the ν_{CN} CIP mode as the temperature is reduced (and thus the solubility limit is approached), coupled with the formation of aggregates.

6.7 Conclusion & Further Work

A conclusive, unambiguous observation of the LLT of water has proved elusive in this work. Aqueous salt solutions that can be supercooled into no man's land without crystallising are not particularly common (assuming these efforts are indicative). Those that do have this ability must also (to some extent) retain the hydrogen-bonding properties of neat water. Magnesium perchlorate solution seems to introduce local electrostatic fields that are too strong, comparable to neat water at high enough pressures such that LDL or LDA are not expected to exist.

It is difficult to say for certain why HTFA solution is apparently successful in showcasing the LLT in H_2O while others are not, however it is notable that it is a salt formed of ions that both form (arguably) water-like hydrogen bonds with solvent H_2O . For OKE spectroscopic studies there appear to be two potential avenues for further research, firstly is the continued search for a salt of isotropic ions that can suppress crystallisation without destroying the water characteristics. Perhaps other salts of the hydrazinium ion, such as hydrazinium perchlorate, may be worth exploring. The second option is to fully characterise the OKE spectra of HTFA through temperature and concentration studies. This would certainly be a time-consuming exercise, but if done correctly should enable the direct study of its GHz to THz dynamics throughout the HDL to LDL transition.

It would be interesting to effectively combine the work of sections 6.5 and 6.6 (magnesium perchlorate and thiocyanate probed lithium chloride). Recall that one of the major issues with the LiCl (3.5 H_2O molecules per ion) solution study was the reduced H_2O coordination numbers due to high salt concentration. This may have resulted in the failure of the formation of tetrahedral LDL water. As shown previously, a $\text{Mg}(\text{ClO}_4)_2$ solution containing 6 water molecules per ion can be supercooled beyond no man's land and into the glassy state. Lenton *et al.*²²³ suggest that this solution exhibits octahedral charge ordering, as opposed to nano-segregated dilute *vs.* briny domains for example. Regrettably, the water structure in this solution resembles that of pure water of ≥ 2 GPa, which is far too high, but perhaps lowering the cation charge density by replacing the magnesium ion with, *e.g.*, Ca^{2+} ,

may solve this problem (its charge density is approximately equal to Li^+). Indeed, eutectic $\text{Ca}(\text{ClO}_4)_2$ solution has been supercooled beyond no man's land without the need for excessive cooling rates.²⁴⁶ Probing these perchlorate solutions with the thiocyanate ion may be a worthwhile attempt to observe the LLT; other supercooled behaviours of the solution may be interesting within the context of Martian brine.

Finally, an improvement to the constant cooling/heating rate experiments used here would be the use of thermocouples (or similar) to directly probe the temperature of the sample to provide a more accurate temperature scale throughout.

7 CONCLUSION

This thesis has presented three spectroscopic studies on molecular dynamics and structure throughout a broad range of condensed matter systems. Materials ranging from hydrocarbon molecular liquids to the more exotic Ti:alkoxides (and Si analogue) glass formers, and finally to aqueous salt solutions.

Ultrafast optical-Kerr effect spectroscopy is the main technique that has been utilised throughout. This method applies transform-limited pulses to induce and probe a transient birefringence, producing a Bose-Einstein corrected depolarised Raman spectrum with an unrivalled SNR in the THz-GHz regime. These are the timescales of a broad range of intermolecular dynamics, the nature of which can be complex—even for relatively ‘simple’, weakly interacting liquids such as the *n*-alkanes and cycloalkanes. Fourier-transform infrared spectroscopy is also employed to observe the behaviour of much higher frequency (intramolecular) vibrational modes that are sensitive to their electrostatic environment; these are studied to deduce changes in local structure.

OKE spectroscopy has been a well-known and well-used technique for several decades now, however the output data is far more difficult to interpret. A few different methods of interpretation have emerged organically which have undoubtedly provided useful insights into intermolecular dynamics (and indeed provided a starting point for this work). However, upon closer scrutiny the current methods produce inconsistent and/or limited illustrations of the dynamics. No standard approach to the line-shape fitting exists to guide the interpretation of the relatively shapeless intermolecular bands; the complexity of these dynamics/spectra identify the need for a generic blueprint for the analysis of the GHz-THz part of the OKE spectrum—this is the focus of chapter 4. To accomplish this, the OKE spectra of many cheap and cheerful, weakly-interacting, molecular liquids had to be gathered and analysed *en masse*. These measurements are grouped into 4 series of experiments: *n*-alkanes, cycloalkanes, propane over temperature, and the 6-membered rings. Each series vary certain OKE-relevant properties (*e.g.* viscosity, polarisability) in a controlled manner, enabling the component line-shapes that comprise the spectra to be gradually deduced. Ultimately, after many iterations, a self-consistent solution was converged upon that can provide a coherent illustration of the intermolecular dynamics. This blueprint for spectral analysis may be useful

in instances where the current (albeit simpler) *ad hoc* methods become untenable, which, as argued within this chapter, can happen quite rapidly as more data is collected. No time was wasted in testing the utility of this work, which underpins the work of the following chapter.

One of the more arcane spectral features of glasses (but sometimes also liquids) observed in Raman (or X-ray, or neutron) scattering is the Boson peak; other than being transverse in nature, little is known of its origin. The BP is observable as one of many Raman-active bands in an often-overcrowded region of the spectrum. Consequently, most research into this anomalous band is complicated by its convolution with other spectral features, especially librations, making even its *assignment* difficult, let alone tracking its temperature-dependent line-shape with any confidence. Chapter 5 presents an optical-Kerr effect study on carefully selected glass-forming molecular liquids with near-isotropic polarisabilities. These were selected to simplify the intermolecular spectra, allowing the BP to be isolated enough to provide new insights into its nature and origin. It was found that vitreous titanium butoxide exhibits intermolecular spectra that can be explained using a single collision-induced molecular “cage-rattling” mode (labelled the fast- β in chapter 4). Such dynamics been suggested to originate from broadened van Hove singularities of the corresponding crystal, and in fact this has been a suggested origin of the BP itself; this result is therefore consistent with this outlook. Vitreous tetrabutyl orthosilicate however clearly exhibits not one but two fast- β modes. This second, lower frequency mode *may* result from molecular clusters (*i.e.* locally favoured structures), the presence of which has been touted as a major factor that influences whether a material will supercool and vitrify or simply crystallise. Further work is required to determine if this indeed the origin of the second intermolecular vibrational mode, e.g. X-ray or neutron scattering may reveal changes in the liquid structure over temperature, where clusters ought to form on cooling and disappear at higher temperatures.

The liquid-liquid transition in water is a product of a theoretical explanation to its divergent thermodynamic behaviour on supercooling, and has been a very controversial topic since its existence was postulated some 30 years ago. Since then, there has been a strong impetus for its experimental verification, however the LLT is believed to occur within a region of the H₂O phase diagram that is dominated by the onset of rapid crystal nucleation. To prevent this, aqueous salt solutions (esp. lithium chloride solution) have been investigated as an experimental proxy for neat water at high pressure, with the added benefit of impeding crystal nucleation. Recent work claims to have witnessed a LLT within an aqueous hydrazinium trifluoroacetate solution, revealed by the temperature dependent O-H stretching line-shape observed through FTIR spectroscopy. The work of chapter 6 approaches the LLT

on several experimental fronts: through both OKE and FTIR spectroscopies on HTFA_(aq), thiocyanate-doped LiCl_(aq), and Mg(ClO₄)_{2(aq)}. These solutions are closely studied at their lowest possible concentration that prevent ice nucleation on cooling. Results show the OKE-active intermolecular bands in HTFA_(aq) and Mg(ClO₄)_{2(aq)} exhibit very similar temperature dependences, which is surprising given that the evidence strongly suggests that the latter does not exhibit any LLT. Meanwhile LiCl_(aq) solution appears to undergo nanophase separation into a salt rich brine and more dilute phase. This however does not appear to be driven by a LLT, evidenced by the OH (or OD) stretching line-shape which does not change appreciably throughout. Meanwhile, magnesium perchlorate solution appears analogous to neat water at much higher pressure (too high to encounter an LLT), attributable to the high charge density of the cation. In summary and despite best efforts, no new evidence of an LLT in water has been observed in this work.

8 REFERENCES

- (1) Voth, G. A.; Hochstrasser, R. M. Transition State Dynamics and Relaxation Processes in Solutions: A Frontier of Physical Chemistry. *J. Phys. Chem.* **1996**, *100* (31), 13034–13049.
- (2) Weinstein, J. A.; Hunt, N. T. In Search of Molecular Movies. *Nat. Chem.* **2012**, *4* (3), 157–158.
- (3) Cholakova, D.; Denkov, N. Rotator Phases in Alkane Systems: In Bulk, Surface Layers and Micro/Nano-Confinements. *Adv. Colloid Interface Sci.* **2019**, *269*, 7–42.
- (4) James, H. M.; Keenan, T. A. Theory of Phase Transitions in Solid Heavy Methane. *J. Chem. Phys.* **1959**, *31* (1), 12–41.
- (5) de Gennes, P. Entangled Polymers. *Phys. Today* **1983**, *36* (6), 33–39.
- (6) Steinhoff, H. J.; Kramm, B.; Hess, G.; Owerdieck, C.; Redhardt, A. Rotational and Translational Water Diffusion in the Hemoglobin Hydration Shell: Dielectric and Proton Nuclear Relaxation Measurements. *Biophys. J.* **1993**, *65* (4), 1486–1495.
- (7) Perticaroli, S.; Comez, L.; Paolantoni, M.; Sassi, P.; Lupi, L.; Fioretto, D.; Paciaroni, A.; Morresi, A. Broadband Depolarized Light Scattering Study of Diluted Protein Aqueous Solutions. *J. Phys. Chem. B* **2010**, *114* (24), 8262–8269.
- (8) González-Jiménez, M.; Ramakrishnan, G.; Harwood, T.; Laphorn, A. J.; Kelly, S. M.; Ellis, E. M.; Wynne, K. Observation of Coherent Delocalized Phonon-like Modes in DNA under Physiological Conditions. *Nat. Commun.* **2016**, *7* (1), 11799.
- (9) Ramakrishnan, G.; González-Jiménez, M.; Laphorn, A. J.; Wynne, K. The Spectrum of Slow and Super-Slow (Picosecond to Nanosecond) Water Dynamics around Organic and Biological Solutes. *J. Phys. Chem. Lett.* **2017**, *8*, 2964–2970.
- (10) Dyson, F. J.; Lenard, A. Stability of Matter. I. *J. Math. Phys.* **1967**, *8* (3), 423–434.
- (11) Lenard, A.; Dyson, F. J. Stability of Matter. II. *J. Math. Phys.* **1968**, *9* (5), 698–711.
- (12) Lennard-Jones, J. E. Cohesion. *Proc. Phys. Soc.* **1931**, *43* (5), 461–482.
- (13) Atkins, P. W.; De Paula, J. *Atkins' Physical Chemistry*, 9th ed.; Oxford University Press: Oxford; New York, 2010.
- (14) Debye, P. Zur Theorie Der Spezifischen Wärmen. *Ann. Phys.* **1912**, *344* (14), 789–839.
- (15) Kittel, C. *Introduction to Solid State Physics*, 8th ed.; Wiley, 2004.
- (16) Turton, D. A.; Wynne, K. Stokes-Einstein-Debye Failure in Molecular Orientational Diffusion: Exception or Rule? *J. Phys. Chem. B* **2014**, *118* (17), 4600–4604.
- (17) Einstein, A. Über Die von Der Molekularkinetischen Theorie Der Wärme Geforderte Bewegung von in Ruhenden Flüssigkeiten Suspensierten Teilchen. *Ann. Phys.* **1905**, *322* (8), 549–560.
- (18) Debye, P. *Polar Molecules*; Chemical Catalog: New York, 1929.
- (19) Mutneja, A.; Karmakar, S. Translational Dynamics of a Rod-like Probe in Supercooled Liquids: An Experimentally Realizable Method to Study Stokes-Einstein Breakdown, Dynamic Heterogeneity, and Amorphous Order. *Soft Matter*

- 2021, 17 (23), 5738–5746.
- (20) Winther, L. R.; Qvist, J.; Halle, B. Hydration and Mobility of Trehalose in Aqueous Solution. *J. Phys. Chem. B* **2012**, 116 (30), 9196–9207.
- (21) Capaccioli, S.; Ngai, K. L. Relation between the α -Relaxation and Johari–Goldstein β -Relaxation of a Component in Binary Miscible Mixtures of Glass-Formers. *J. Phys. Chem. B* **2005**, 109 (19), 9727–9735.
- (22) Koenderink, G. H.; Zhang, H.; Aarts, D. G. A. L.; Lettinga, M. P.; Philipse, A. P.; Nägele, G. On the Validity of Stokes–Einstein–Debye Relations for Rotational Diffusion in Colloidal Suspensions. *Faraday Discuss.* **2003**, 123, 335–354.
- (23) Makuch, K.; Hołyst, R.; Kalwarczyk, T.; Garstecki, P.; Brady, J. F. Diffusion and Flow in Complex Liquids. *Soft Matter* **2020**, 16 (1), 114–124.
- (24) Reichenbach, J. Structure and Dynamics in Ionic Liquids and Concentrated Salt Solutions: An Ultrafast Spectroscopic Study, University of Glasgow, 2017.
- (25) Katayama, Y.; Mizutani, T.; Utsumi, W.; Shimomura, O.; Yamakata, M.; Funakoshi, K. A First-Order Liquid–Liquid Phase Transition in Phosphorus. *Nature* **2000**, 403 (6766), 170–173.
- (26) Sastry, S.; Austen Angell, C. Liquid–Liquid Phase Transition in Supercooled Silicon. *Nat. Mater.* **2003**, 2 (11), 739–743.
- (27) Henry, L.; Mezouar, M.; Garbarino, G.; Sifré, D.; Weck, G.; Datchi, F. Liquid–Liquid Transition and Critical Point in Sulfur. *Nature* **2020**, 584 (7821), 382–386.
- (28) Kurita, R.; Tanaka, H. On the Abundance and General Nature of the Liquid–Liquid Phase Transition in Molecular Systems. *J. Phys. Condens. Matter* **2005**, 17 (27), L293–L302.
- (29) Walton, F.; Bolling, J.; Farrell, A.; MacEwen, J.; Syme, C. D.; Jiménez, M. G.; Senn, H. M.; Wilson, C.; Cinque, G.; Wynne, K. Polyamorphism Mirrors Polymorphism in the Liquid–Liquid Transition of a Molecular Liquid. *J. Am. Chem. Soc.* **2020**, 142 (16), 7591–7597.
- (30) Tanaka, H.; Kurita, R.; Mataka, H. Liquid-Liquid Transition in the Molecular Liquid Triphenyl Phosphite. *Phys. Rev. Lett.* **2004**, 92 (2), 025701.
- (31) Woutersen, S.; Ensing, B.; Hilbers, M.; Zhao, Z.; Angell, C. A. A Liquid-Liquid Transition in Supercooled Aqueous Solution Related to the HDA-LDA Transition. *Science (80-.)*. **2018**, 359 (6380), 1127–1131.
- (32) Kim, K. H.; Amann-Winkel, K.; Giovambattista, N.; Späh, A.; Perakis, F.; Pathak, H.; Parada, M. L.; Yang, C.; Mariedahl, D.; Eklund, T.; et al. Experimental Observation of the Liquid-Liquid Transition in Bulk Supercooled Water under Pressure. *Science (80-.)*. **2020**, 370 (6519), 978–982.
- (33) Koechner, W. *Solid-State Laser Engineering*, 6th ed.; Springer Series in Optical Sciences; Springer New York: New York, NY, 2006; Vol. 1.
- (34) Shahsafi, A.; Xiao, Y.; Salman, J.; Gundlach, B. S.; Wan, C.; Roney, P. J.; Kats, M. A. Mid-Infrared Optics Using Dielectrics with Refractive Indices Below Unity. *Phys. Rev. Appl.* **2018**, 10 (3), 034019.
- (35) Shelby, R. A.; Smith, D. R.; Schultz, S. Experimental Verification of a Negative Index of Refraction. *Science (80-.)*. **2001**, 292 (5514), 77–79.
- (36) Kerr, J. XL. A New Relation between Electricity and Light: Dielectrified Media Birefringent. *London, Edinburgh, Dublin Philos. Mag. J. Sci.* **1875**, 50 (332), 337–348.
- (37) Kerr, J. LIV. A New Relation between Electricity and Light: Dielectrified Media

- Birefringent (Second Paper). *London, Edinburgh, Dublin Philos. Mag. J. Sci.* **1875**, 50 (333), 446–458.
- (38) Maker, P. D.; Terhune, R. W.; Savage, C. M. Intensity-Dependent Changes in the Refractive Index of Liquids. *Phys. Rev. Lett.* **1964**, 12 (18), 507–509.
- (39) Bancewicz, T. Rayleigh Light Scattering by Liquids Composed of Interacting Anisotropic Molecules: Spherical Tensor Approach within the Second Order Approximation of the DID Model. *Mol. Phys.* **1983**, 50 (1), 173–191.
- (40) Frenkel, D.; McTague, J. P. Molecular Dynamics Studies of Orientational and Collision-induced Light Scattering in Molecular Fluids. *J. Chem. Phys.* **1980**, 72 (4), 2801–2818.
- (41) Geiger, L. C.; Ladanyi, B. M. Higher Order Interaction-induced Effects on Rayleigh Light Scattering by Molecular Liquids. *J. Chem. Phys.* **1987**, 87 (1), 191–202.
- (42) Elola, M. D.; Ladanyi, B. M. Polarizability Response in Polar Solvents: Molecular-Dynamics Simulations of Acetonitrile and Chloroform. *J. Chem. Phys.* **2005**, 122 (22), 224506.
- (43) Frisch, M. J.; Trucks, G. W.; Schlegel, H. B.; Scuseria, G. E.; Robb, M. A.; Cheeseman, J. R.; Scalmani, G.; Barone, V.; Mennucci, B.; Petersson, G. A.; et al. Gaussian09. Gaussian, Inc.: Wallingford CT 2009.
- (44) Smith, N. A.; Meech, S. R. Optically-Heterodyne-Detected Optical Kerr Effect (OHD-OKE): Applications in Condensed Phase Dynamics. *Int. Rev. Phys. Chem.* **2002**, 21 (1), 75–100.
- (45) Farrer, R. A.; Loughnane, B. J.; Deschenes, L. A.; Fourkas, J. T. Level-Dependent Damping in Intermolecular Vibrations: Linear Spectroscopy. *J. Chem. Phys.* **1997**, 106 (17), 6901–6915.
- (46) Giraud, G. Ultrafast Vibrational Dynamics in Liquids and Proteins, University of Strathclyde, 2003.
- (47) Giraud, G.; Gordon, C. M.; Dunkin, I. R.; Wynne, K. The Effects of Anion and Cation Substitution on the Ultrafast Solvent Dynamics of Ionic Liquids: A Time-Resolved Optical Kerr-Effect Spectroscopic Study. *J. Chem. Phys.* **2003**, 119 (1), 464–477.
- (48) McMorrow, D. Separation of Nuclear and Electronic Contributions to Femtosecond Four-Wave Mixing Data. *Opt. Commun.* **1991**, 86 (2), 236–244.
- (49) Williams, G.; Watts, D. C. Non-Symmetrical Dielectric Relaxation Behaviour Arising from a Simple Empirical Decay Function. *Trans. Faraday Soc.* **1970**, 66, 80.
- (50) Kohlrausch, R. Theorie Des Elektrischen Rückstandes in Der Leidener Flasche. *Ann. Phys.* **1854**, 167 (2), 179–214.
- (51) Alvarez, F.; Alegria, A.; Colmenero, J. Relationship between the Time-Domain Kohlrausch-Williams-Watts and Frequency-Domain Havriliak-Negami Relaxation Functions. *Phys. Rev. B* **1991**, 44 (14), 7306–7312.
- (52) Havriliak, S.; Negami, S. A Complex Plane Analysis of α -Dispersions in Some Polymer Systems. *J. Polym. Sci. Part C Polym. Symp.* **1966**, 14 (1), 99–117.
- (53) Turton, D. A.; Martin, D. F.; Wynne, K. Optical Kerr-Effect Study of Trans- and Cis-1,2-Dichloroethene: Liquid–Liquid Transition or Super-Arrhenius Relaxation. *Phys. Chem. Chem. Phys.* **2010**, 12 (16), 4191.
- (54) McMorrow, D.; Lotshaw, W. T. Intermolecular Dynamics in Acetonitrile Probed with Femtosecond Fourier-Transform Raman Spectroscopy. *J. Phys. Chem.* **1991**, 95 (25), 10395–10406.

- (55) Turton, D. A.; Wynne, K. Structural Relaxation in the Hydrogen-Bonding Liquids N-Methylacetamide and Water Studied by Optical Kerr Effect Spectroscopy. *J. Chem. Phys.* **2008**, *128* (15).
- (56) Giraud, G.; Wynne, K. A Comparison of the Low-Frequency Vibrational Spectra of Liquids Obtained through Infrared and Raman Spectroscopies. *J. Chem. Phys.* **2003**, *119* (22), 11753–11764.
- (57) Giraud, G.; Karolin, J.; Wynne, K. Low-Frequency Modes of Peptides and Globular Proteins in Solution Observed by Ultrafast OHD-RIKES Spectroscopy. *Biophys. J.* **2003**, *85* (3), 1903–1913.
- (58) Heisler, I. A.; Mazur, K.; Meech, S. R. THz Raman Spectra of Aqueous Solutions of Hydrophiles and Amphiphiles. In *Ultrafast Phenomena and Nanophotonics XVII*; Betz, M., Elezzabi, A. Y., Song, J.-J., Tsen, K.-T., Eds.; SPIE, 2013; Vol. 8623, p 862302.
- (59) Bender, J. S.; Fourkas, J. T.; Coasne, B. Empirical Analysis of Optical Kerr Effect Spectra: A Case for Constraint. *J. Phys. Chem. B* **2017**, *121* (50), 11376–11382.
- (60) Bucaro, J. A.; Litovitz, T. A. Rayleigh Scattering: Collisional Motions in Liquids. *J. Chem. Phys.* **1971**, *54* (9), 3846–3853.
- (61) Farrell, A. J.; González-Jiménez, M.; Ramakrishnan, G.; Wynne, K. Low-Frequency (Gigahertz to Terahertz) Depolarized Raman Scattering Off n-Alkanes, Cycloalkanes, and Six-Membered Rings: A Physical Interpretation. *J. Phys. Chem. B* **2020**, *124* (35), 7611–7624.
- (62) Caporaletti, F.; Capaccioli, S.; Valenti, S.; Mikolasek, M.; Chumakov, A. I.; Monaco, G. A Microscopic Look at the Johari-Goldstein Relaxation in a Hydrogen-Bonded Glass-Former. *Sci. Rep.* **2019**, *9* (1), 1–10.
- (63) Cho, M.; Fleming, G. R.; Saito, S.; Ohmine, I.; Stratt, R. M. Instantaneous Normal Mode Analysis of Liquid Water. *J. Chem. Phys.* **1994**, *100* (9), 6672–6683.
- (64) Stratt, R. M. The Instantaneous Normal Modes of Liquids. *Acc. Chem. Res.* **1995**, *28* (5), 201–207.
- (65) Keyes, T. Instantaneous Normal Mode Approach to Liquid State Dynamics. *J. Phys. Chem. A* **1997**, *101* (16), 2921–2930.
- (66) Ryu, S.; Stratt, R. M. A Case Study in the Molecular Interpretation of Optical Kerr Effect Spectra: Instantaneous-Normal-Mode Analysis of the OKE Spectrum of Liquid Benzene †. *J. Phys. Chem. B* **2004**, *108* (21), 6782–6795.
- (67) Volterra, V.; Bucaro, J. A.; Litovitz, T. A. Molecular Motion and Light Scattering in Liquids. *Berichte der Bunsengesellschaft für Phys. Chemie* **1971**, *75* (3-4), 309–315.
- (68) Kudlik, A.; Benkhof, S.; Blochowicz, T.; Tschirwitz, C.; Rössler, E. The Dielectric Response of Simple Organic Glass Formers. *J. Mol. Struct.* **1999**, *479* (2–3), 201–218.
- (69) Lunkenheimer, P.; Schneider, U.; Brand, R.; Loidl, A.; Loidl, A. Glassy Dynamics. *Contemp. Phys.* **2000**, *41* (1), 15–36.
- (70) Geirhos, K.; Lunkenheimer, P.; Loidl, A. Johari-Goldstein Relaxation Far Below T_g: Experimental Evidence for the Gardner Transition in Structural Glasses? *Phys. Rev. Lett.* **2018**, *120* (8), 85705.
- (71) Götze, W.; Sperl, M. Nearly Logarithmic Decay of Correlations in Glass-Forming Liquids. *Phys. Rev. Lett.* **2004**, *92* (10), 105701.
- (72) Li, J.; Wang, I.; Fruchey, K.; Fayer, M. D. Dynamics in Supercooled Ionic Organic Liquids and Mode Coupling Theory Analysis. *J. Phys. Chem. A* **2006**, *110* (35), 10384–

- 1039I.
- (73) Nicolau, B. G.; Sturlaugson, A.; Fruchey, K.; Ribeiro, M. C. C.; Fayer, M. D. Room Temperature Ionic Liquid-Lithium Salt Mixtures: Optical Kerr Effect Dynamical Measurements. *J. Phys. Chem. B* **2010**, *114* (25), 8350–8356.
- (74) Schmidtke, B.; Petzold, N.; Kahlau, R.; Rössler, E. A. Reorientational Dynamics in Molecular Liquids as Revealed by Dynamic Light Scattering: From Boiling Point to Glass Transition Temperature. *J. Chem. Phys.* **2013**, *139* (8), 084504.
- (75) Schmidtke, B.; Rössler, E. A. Depolarized Light Scattering Spectra of Molecular Liquids: Described in Terms of Mode Coupling Theory. *J. Chem. Phys.* **2014**, *141* (4), 44511.
- (76) Sokolowsky, K. P.; Bailey, H. E.; Hoffman, D. J.; Andersen, H. C.; Fayer, M. D. Critical Slowing of Density Fluctuations Approaching the Isotropic-Nematic Transition in Liquid Crystals: 2D IR Measurements and Mode Coupling Theory. *J. Phys. Chem. B* **2016**, *120* (28), 7003–7015.
- (77) Pardo, L. C.; Lunkenheimer, P.; Loidl, A. Dielectric Spectroscopy in Benzophenone: The β Relaxation and Its Relation to the Mode-Coupling Cole-Cole Peak. *Phys. Rev. E* **2007**, *76* (3), 030502.
- (78) Lunkenheimer, P.; Pardo, L. C.; Köhler, M.; Loidl, A. Broadband Dielectric Spectroscopy on Benzophenone: α Relaxation, β Relaxation, and Mode Coupling Theory. *Phys. Rev. E* **2008**, *77* (3), 031506.
- (79) Janssen, L. M. C. Mode-Coupling Theory of the Glass Transition: A Primer. *Front. Phys.* **2018**, *6* (OCT), 1–18.
- (80) Fecko, C. J.; Eaves, J. D.; Tokmakoff, A. Isotropic and Anisotropic Raman Scattering from Molecular Liquids Measured by Spatially Masked Optical Kerr Effect Spectroscopy. *J. Chem. Phys.* **2002**, *117* (3), 1139–1154.
- (81) Zhong, Q.; Fourkas, J. T. Optical Kerr Effect Spectroscopy of Simple Liquids. *J. Phys. Chem. B* **2008**, *112* (49), 15529–15539.
- (82) Turton, D. A.; Senn, H. M.; Harwood, T.; Laphorn, A. J.; Ellis, E. M.; Wynne, K. Terahertz Underdamped Vibrational Motion Governs Protein-Ligand Binding in Solution. *Nat. Commun.* **2014**, *5*, 3999.
- (83) Turton, D. A.; Corsaro, C.; Martin, D. F.; Mallamace, F.; Wynne, K. The Dynamic Crossover in Water Does Not Require Bulk Water. *Phys. Chem. Chem. Phys.* **2012**, *14* (22), 8067.
- (84) Reichenbach, J.; Ruddell, S. A.; González-Jiménez, M.; Lemes, J.; Turton, D. A.; France, D. J.; Wynne, K. Phonon-like Hydrogen-Bond Modes in Protic Ionic Liquids. *J. Am. Chem. Soc.* **2017**, *139* (21), 7160–7163.
- (85) Lemmon, E.; McLinden, M.; Friend, D. Thermophysical Properties of Fluid Systems. In *NIST Chemistry WebBook*; Linstrom, P. J., Mallard, W. G., Eds.; Gaithersburg, MD.
- (86) Fischer, J.; Weiss, A. Transport Properties of Liquids VI. Viscosity, Excess Volumes, and Self-Diffusion of Nearly Athermal Mixtures. *Ber. Bunsenges. Phys. Chem.* **1986**, *90* (12), 1129–1141.
- (87) Kakinuma, S.; Shirota, H. Dynamic Kerr Effect Study on Six-Membered-Ring Molecular Liquids: Benzene, 1,3-Cyclohexadiene, 1,4-Cyclohexadiene, Cyclohexene, and Cyclohexane. *J. Phys. Chem. B* **2015**, *119* (13), 4713–4724.
- (88) Iglesias-Silva, G. A.; Guzmán-López, A.; Pérez-Durán, G.; Ramos-Estrada, M. Densities and Viscosities for Binary Liquid Mixtures of N-Undecane + 1-Propanol, + 1-Butanol, + 1-Pentanol, and + 1-Hexanol from 283.15 to 363.15 K at 0.1 MPa. *J. Chem.*

- Eng. Data* **2016**, *61* (8), 2682–2699.
- (89) Daugé, P.; Canet, X.; Baylaucq, A.; Boned, C. Measurements of the Density and Viscosity of the Tridecane + 2,2,4,4,6,8,8-Heptamethylnonane Mixtures in the Temperature Range 293.15–353.15 K at Pressures up to 100 MPa. *High Temp. - High Press.* **2001**, *33* (2), 213–230.
- (90) Quiñones-Cisneros, S. E.; Zéberg-Mikkelsen, C. K.; Stenby, E. H. Accurate Density and Viscosity Modeling of Nonpolar Fluids Based on the “f-Theory” and a Noncubic Equation of State. *Int. J. Thermophys.* **2002**, *23* (1), 41–55.
- (91) Santos, T. V. M.; Pereira, M. F. V.; Avelino, H. M. N. T.; Caetano, F. J. P.; Fareleira, J. M. N. A. Viscosity and Density Measurements on Liquid N-Tetradecane at Moderately High Pressures. *Fluid Phase Equilib.* **2017**, *453*, 46–57.
- (92) Perrin, F. Mouvement Brownien d'un Ellipsoïde (I). Dispersion Diélectrique Pour Des Molécules Ellipsoïdales. *Le J. Phys. le Radium* **1934**, *5*, 497–511.
- (93) Doi, M. Rotational Relaxation Time of Rigid Rod-like Macromolecule in Concentrated Solution. *J. Phys.* **1975**, *36* (7–8), 607–611.
- (94) Neild, A.; Padding, J. T.; Yu, L.; Bhaduri, B.; Briels, W. J.; Ng, T. W. Translational and Rotational Coupling in Brownian Rods near a Solid Surface. *Phys. Rev. E - Stat. Nonlinear, Soft Matter Phys.* **2010**, *82* (4), 1–10.
- (95) Hu, C.; Zwanzig, R. Rotational Friction Coefficients for Spheroids with the Slipping Boundary Condition. *J. Chem. Phys.* **1974**, *60* (11), 4354–4357.
- (96) Barron, L. D. *Molecular Light Scattering and Optical Activity*, 2nd ed.; Cambridge University Press, 2004.
- (97) Scaife, W. G.; Vij, J. K.; Evans, G.; Evans, M. The Complex Permittivity of Six N-Alkanes; Measurements in the Far Infrared. *J. Phys. D. Appl. Phys.* **1982**, *15* (7), 1279–1283.
- (98) Steffen, T.; Meinders, N. A. C. M.; Duppen, K. Microscopic Origin of the Optical Kerr Effect Response of CS₂-Pentane Binary Mixtures. *J. Phys. Chem. A* **1998**, *102* (23), 4213–4221.
- (99) Rajian, J. R.; Hyun, B.; Quitevis, E. L. Intermolecular Spectrum of Liquid Biphenyl Studied by Optical Kerr Effect Spectroscopy. *J. Phys. Chem. A* **2004**, *108* (46), 10107–10115.
- (100) Zhong, Q.; Fourkas, J. T. Searching for Voids in Liquids with Optical Kerr Effect Spectroscopy. *J. Phys. Chem. B* **2008**, *112* (29), 8656–8663.
- (101) Thomas, L. L.; Christakis, T. J.; Jorgensen, W. L. Conformation of Alkanes in the Gas Phase and Pure Liquids. *J. Phys. Chem. B* **2006**, *110* (42), 21198–21204.
- (102) Byrd, J. N.; Bartlett, R. J.; Montgomery, J. A. At What Chain Length Do Unbranched Alkanes Prefer Folded Conformations? *J. Phys. Chem. A* **2014**, *118* (9), 1706–1712.
- (103) Buckingham, R. A. The Classical Equation of State of Gaseous Helium, Neon and Argon. *Proc. R. Soc. London. Ser. A. Math. Phys. Sci.* **1938**, *168* (933), 264–283.
- (104) Turton, D. A.; Hunger, J.; Stoppa, A.; Thoman, A.; Candelaresi, M.; Hefter, G.; Walther, M.; Buchner, R.; Wynne, K. Rattling the Cage: Micro- to Mesoscopic Structure in Liquids as Simple as Argon and as Complicated as Water. *J. Mol. Liq.* **2011**, *159* (1), 2–8.
- (105) Shiota, H.; Moriyama, K. Low-Frequency Vibrational Motions of Polystyrene in Carbon Tetrachloride: Comparison with Model Monomer and Dependence on Concentration and Molecular Weight. *J. Phys. Chem. B* **2020**, *124* (10), 2006–2016.

- (106) Bounds, D. G.; Klein, M. L.; Patey, G. N. Molecular Dynamics Simulation of the Plastic Phase of Solid Methane. *J. Chem. Phys.* **1980**, *72* (10), 5348–5356.
- (107) Turton, D. A.; Sonnleitner, T.; Ortner, A.; Walther, M.; Hefter, G.; Seddon, K. R.; Stana, S.; Plechkova, N. V.; Buchner, R.; Wynne, K. Structure and Dynamics in Protic Ionic Liquids: A Combined Optical Kerr-Effect and Dielectric Relaxation Spectroscopy Study. *Faraday Discuss.* **2012**, *154*, 145.
- (108) Wiebel, S.; Wuttke, J. Structural Relaxation and Mode Coupling in a Non-Glassforming Liquid: Depolarized Light Scattering in Benzene. *New J. Phys.* **2002**, *4*, 356.
- (109) Corsaro, C.; Fazio, E.; Mallamace, D. The Stokes-Einstein Relation in Water/Methanol Solutions. *J. Chem. Phys.* **2019**, *150* (23).
- (110) Kawasaki, T.; Kim, K. Spurious Violation of the Stokes – Einstein – Debye Relation in Supercooled Water. *Sci. Rep.* **2019**, 1–9.
- (111) Becker, S. R.; Poole, P. H.; Starr, F. W. Fractional Stokes-Einstein and Debye-Stokes-Einstein Relations in a Network-Forming Liquid. *Phys. Rev. Lett.* **2006**, *97* (5), 2–5.
- (112) Kumar, S. K.; Szamel, G.; Douglas, J. F. Nature of the Breakdown in the Stokes-Einstein Relationship in a Hard Sphere Fluid. *J. Chem. Phys.* **2006**, *124* (21).
- (113) Rössler, E. Indications for a Change of Diffusion Mechanism in Supercooled Liquids. *Phys. Rev. Lett.* **1990**, *65* (13), 1595–1598.
- (114) Hodgdon, J. A.; Stillinger, F. H. Stokes-Einstein Violation in Glass-Forming Liquids. *Phys. Rev. E* **1993**, *48* (1), 207–213.
- (115) Bender, J. S.; Cohen, S. R.; He, X.; Fourkas, J. T.; Coasne, B. Toward in Situ Measurement of the Density of Liquid Benzene Using Optical Kerr Effect Spectroscopy. *J. Phys. Chem. B* **2016**, *120* (34), 9103–9114.
- (116) Hendrickson, J. B. Molecular Geometry. V. Evaluation of Functions and Conformations of Medium Rings. *J. Am. Chem. Soc.* **1967**, *89* (26), 7036–7043.
- (117) Kilpatrick, J. E.; Pitzer, K. S.; Spitzer, R. The Thermodynamics and Molecular Structure of Cyclopentane. *J. Am. Chem. Soc.* **1947**, *69* (10), 2483–2488.
- (118) MacPhail, R. A.; Variyar, J. E. Pseudorotation Dynamics in Liquid Cyclopentane by Raman Spectroscopy. *Chem. Phys. Lett.* **1989**, *161* (3), 239–244.
- (119) Kowalewski, P.; Frey, H. M.; Infanger, D.; Leutwyler, S. Probing the Structure, Pseudorotation, and Radial Vibrations of Cyclopentane by Femtosecond Rotational Raman Coherence Spectroscopy. *J. Phys. Chem. A* **2015**, *119* (45), 11215–11225.
- (120) Bocian, D. F.; Strauss, H. L. Conformational Structure and Energy of Cycloheptane and Some Related Oxepanes. *J. Am. Chem. Soc.* **1977**, *99* (9), 2876–2882.
- (121) McMorro, D.; Lotshaw, W. T. Evidence for Low-Frequency ($\approx 15 \text{ cm}^{-1}$) Collective Modes in Benzene and Pyridine Liquids. *Chem. Phys. Lett.* **1993**, *201* (1–4), 369–376.
- (122) Loughnane, B. J.; Scodinu, A.; Fourkas, J. T. Temperature-Dependent Optical Kerr Effect Spectroscopy of Aromatic Liquids. *J. Phys. Chem. B* **2006**, *110* (11), 5708–5720.
- (123) Rønne, C.; Jensby, K.; Loughnane, B. J.; Fourkas, J.; Nielsen, O. F.; Keiding, S. R. Temperature Dependence of the Dielectric Function of C₆H₆(l) and C₆H₅CH₃(l) Measured with THz Spectroscopy. *J. Chem. Phys.* **2000**, *113* (9), 3749–3756.
- (124) Cong, P.; Deuel, H. P.; Simon, J. D. Structure and Dynamics of Molecular Liquids Investigated by Optical-Heterodyne Detected Raman-Induced Kerr Effect Spectroscopy (OHD-RIKES). *Chem. Phys. Lett.* **1995**, *240* (1–3), 72–78.

- (125) Heisler, I. A.; Meech, S. R. Low-Frequency Isotropic and Anisotropic Raman Spectra of Aromatic Liquids. *J. Chem. Phys.* **2010**, *132* (17).
- (126) Beard, M. C.; Lotshaw, W. T.; Korter, T. M.; Heilweil, E. J.; McMorro, D. Comparative OHD-RIKES and THz-TDS Probes of Ultrafast Structural Dynamics in Molecular Liquids. *J. Phys. Chem. A* **2004**, *108* (43), 9348–9360.
- (127) Perrot, M.; Brooker, M. H.; Lascombe, J. Raman Light Scattering Studies of the Depolarized Rayleigh Wing of Liquids and Solutions. *J. Chem. Phys.* **1981**, *74* (5), 2787.
- (128) Ricci, M.; Bartolini, P.; Chelli, R.; Cardini, G.; Califano, S.; Righini, R. The Fast Dynamics of Benzene in the Liquid Phase. Part I. Optical Kerr Effect Experimental Investigation. *Phys. Chem. Chem. Phys.* **2001**, *3* (14), 2795–2802.
- (129) Dill, J. F.; Litovitz, T. A.; Bucaro, J. A. Molecular Reorientation in Liquids by Rayleigh Scattering: Pressure Dependence of Rotational Correlation Functions. *J. Chem. Phys.* **1975**, *62* (10), 3839–3850.
- (130) Neelakandan, M.; Pant, D.; Quitevis, E. L. Structure and Intermolecular Dynamics of Liquids: Femtosecond Optical Kerr Effect Measurements in Nonpolar Fluorinated Benzenes. *J. Phys. Chem. A* **1997**, *101* (16), 2936–2945.
- (131) Chang, Y. J.; Castner, E. W. Intermolecular Dynamics of Substituted Benzene and Cyclohexane Liquids, Studied by Femtosecond Non-Linear Optical Polarization Spectroscopy. *J. Phys. Chem.* **1996**, *100*, 3330.
- (132) Bender, J. S.; Coasne, B.; Fourkas, J. T. Assessing Polarizability Models for the Simulation of Low-Frequency Raman Spectra of Benzene. *J. Phys. Chem. B* **2015**, *119* (29), 9345–9358.
- (133) González-Jiménez, M.; Ramakrishnan, G.; Tukachev, N. V.; Senn, H. M.; Wynne, K. Low-Frequency Vibrational Modes in G-Quadruplexes Reveal the Mechanical Properties of Nucleic Acids. *Phys. Chem. Chem. Phys.* **2021**, *23* (23), 13250–13260.
- (134) Farrell, A. J.; González-Jiménez, M.; Tukachev, N.; Turton, D. A.; Russell, B. A.; Guinane, S.; Senn, H. M.; Wynne, K. Characterisation of the Boson Peak from the Glass into the Liquid. *chemrxiv* **2021**, Pre-print.
- (135) Angell, C. A.; Ngai, K. L.; McKenna, G. B.; McMillan, P. F.; Martin, S. W. Relaxation in Glassforming Liquids and Amorphous Solids. *J. Appl. Phys.* **2000**, *88* (6), 3113–3157.
- (136) Ediger, M. D. Spatially Heterogeneous Dynamics in Supercooled Liquids. *Annu. Rev. Phys. Chem.* **2000**, *51* (1), 99–128.
- (137) Martinez, L.-M.; Angell, C. A. A Thermodynamic Connection to the Fragility of Glass-Forming Liquids. *Nature* **2001**, *410* (6829), 663–667.
- (138) Debenedetti, P. G.; Stillinger, F. H. Supercooled Liquids and the Glass Transition. *Nature* **2001**, *410* (6825), 259–267.
- (139) Dyre, J. C. Colloquium : The Glass Transition and Elastic Models of Glass-Forming Liquids. *Rev. Mod. Phys.* **2006**, *78* (3), 953–972.
- (140) Yannopoulos, S. N.; Andrikopoulos, K. S.; Ruocco, G. On the Analysis of the Vibrational Boson Peak and Low-Energy Excitations in Glasses. *J. Non. Cryst. Solids* **2006**, *352* (42–49), 454I–455I.
- (141) Grigera, T. S.; Martín-Mayor, V.; Parisi, G.; Verrocchio, P. Phonon Interpretation of the “boson Peak” in Supercooled Liquids. *Nature* **2003**, *422* (6929), 289–292.
- (142) Winterling, G. Very-Low-Frequency Raman Scattering in Vitreous Silica. *Phys. Rev.*

- B* **1975**, *12* (6), 2432–2440.
- (143) Schober, H. R. Vibrations and Relaxations in a Soft Sphere Glass: Boson Peak and Structure Factors. *J. Phys. Condens. Matter* **2004**, *16* (27).
- (144) Shintani, H.; Tanaka, H. Universal Link between the Boson Peak and Transverse Phonons in Glass. *Nat. Mater.* **2008**, *7* (11), 870–877.
- (145) Schirmacher, W.; Ruocco, G.; Scopigno, T. Acoustic Attenuation in Glasses and Its Relation with the Boson Peak. *Phys. Rev. Lett.* **2007**, *98* (2), 025501.
- (146) Sokolov, A. P. Vibrations at the Boson Peak: Random- and Coherent-Phase Contributions. *J. Phys. Condens. Matter* **1999**, *11* (10A), A213–A218.
- (147) Schirmacher, W. Thermal Conductivity of Glassy Materials and the “boson Peak”. *Europhys. Lett.* **2006**, *73* (6), 892–898.
- (148) Chumakov, A. I.; Monaco, G.; Monaco, A.; Crichton, W. A.; Bosak, A.; Ruffer, R.; Meyer, A.; Kargl, F.; Comez, L.; Fioretto, D.; et al. Equivalence of the Boson Peak in Glasses to the Transverse Acoustic van Hove Singularity in Crystals. *Phys. Rev. Lett.* **2011**, *106* (22), 225501.
- (149) Taraskin, S. N.; Loh, Y. L.; Natarajan, G.; Elliott, S. R. Origin of the Boson Peak in Systems with Lattice Disorder. *Phys. Rev. Lett.* **2001**, *86* (7), 1255–1258.
- (150) Schober, H. R.; Buchenau, U.; Gurevich, V. L. Pressure Dependence of the Boson Peak in Glasses: Correlated and Uncorrelated Perturbations. *Phys. Rev. B* **2014**, *89* (1), 014204.
- (151) Parshin, D. A.; Schober, H. R.; Gurevich, V. L. Vibrational Instability, Two-Level Systems, and the Boson Peak in Glasses. *Phys. Rev. B* **2007**, *76* (6), 064206.
- (152) Gurevich, V. L.; Parshin, D. A.; Schober, H. R. Anharmonicity, Vibrational Instability, and the Boson Peak in Glasses. *Phys. Rev. B* **2003**, *67* (9), 94203.
- (153) Baggioli, M.; Zaccone, A. Universal Origin of Boson Peak Vibrational Anomalies in Ordered Crystals and in Amorphous Materials. *Phys. Rev. Lett.* **2019**, *122* (14), 145501.
- (154) Frank, F. Supercooling of Liquids. *Proc. R. Soc. London. Ser. A. Math. Phys. Sci.* **1952**, *215* (1120), 43–46.
- (155) Tanaka, H. Two-Order-Parameter Model of the Liquid-Glass Transition. III. Universal Patterns of Relaxations in Glass-Forming Liquids. *J. Non. Cryst. Solids* **2005**, *351* (43–45), 3396–3413.
- (156) Brodin, A.; Börjesson, L.; Engberg, D.; Torell, L. M.; Sokolov, A. P. Relaxational and Vibrational Dynamics in the Glass-Transition Range of a Strong Glass Former. *Phys. Rev. B* **1996**, *53* (17), 11511–11520.
- (157) Sokolov, A. P.; Rössler, E.; Kisliuk, A.; Quitmann, D. Dynamics of Strong and Fragile Glass Formers: Differences and Correlation with Low-Temperature Properties. *Phys. Rev. Lett.* **1993**, *71* (13), 2062–2065.
- (158) Surovtsev, N. V. Low-Frequency Raman Scattering in As₂S₃ Glass Former around the Liquid – Glass Transition. *J. Phys. Condens. Matter* **2003**, *15*, 7651–7662.
- (159) Kojima, S.; Novikov, V. N. Correlation of Temperature Dependence of Quasielastic-Light-Scattering Intensity and α -Relaxation Time. *Phys. Rev. B* **1996**, *54* (1), 222–227.
- (160) Bobovich, Y. S. Disordered Media and Materials: A Review of Recent Structural Data and Trends in Application of Raman Spectroscopy. *Glas. Phys. Chem.* **2003**, *29* (4), 331–344.
- (161) Wiedersich, J.; Surovtsev, N. V.; Rössler, E. A Comprehensive Light Scattering Study

- of the Glass Former Toluene. *J. Chem. Phys.* **2000**, *113* (3), 1143–1153.
- (162) Baran, J.; Davydova, N. A.; Drozd, M. The Role of Nucleation in Vitrification of Supercooled Liquids. *J. Phys. Condens. Matter* **2010**, *22* (15).
- (163) Wilding, M. C.; Wilson, M.; McMillan, P. F.; Benmore, C. J.; Weber, J. K. R.; Deschamps, T.; Champagnon, B. Structural Properties of Y₂O₃-Al₂O₃ Liquids and Glasses: An Overview. *J. Non. Cryst. Solids* **2015**, *407*, 228–234.
- (164) Rufflé, B.; Etrillard, J.; Toudic, B.; Ecolivet, C.; Coddens, G.; Ambroise, J. P.; Guéguen, E.; Marchand, R. Comparative Analysis of the Fast Dynamics in the Supercooled Nonfragile Glass-Forming Liquid Na_{0.5}Li_{0.5}PO₃ Observed by Coherent Neutron Scattering. *Phys. Rev. B* **1997**, *56* (18), 11546–11552.
- (165) Yannopoulos, S. N.; Kalampounias, A. G.; Chrissanthopoulos, A.; Papatheodorou, G. N. Temperature Induced Changes on the Structure and the Dynamics of the “Tetrahedral” Glasses and Melts of ZNCl₂ and ZnBr₂. *J. Chem. Phys.* **2003**, *118* (7), 3197–3214.
- (166) Tölle, A. Neutron Scattering Studies of the Model Glass Former Ortho-Terphenyl. *Reports Prog. Phys.* **2001**, *64* (11), 1473–1532.
- (167) Hong, L.; Begen, B.; Kisliuk, A.; Pawlus, S.; Paluch, M.; Sokolov, A. P. Influence of Pressure on Quasielastic Scattering in Glasses: Relationship to the Boson Peak. *Phys. Rev. Lett.* **2009**, *102* (14), 145502.
- (168) Ngai, K. L.; Sokolov, A.; Steffen, W. Correlations between Boson Peak Strength and Characteristics of Local Segmental Relaxation in Polymers. *J. Chem. Phys.* **1997**, *107* (13), 5268–5272.
- (169) Andrikopoulos, K. S.; Kalampounias, A. G.; Falagara, O.; Yannopoulos, S. N. The Glassy and Supercooled State of Elemental Sulfur: Vibrational Modes, Structure Metastability, and Polymer Content. *J. Chem. Phys.* **2013**, *139* (12).
- (170) Yannopoulos, S. N.; Andrikopoulos, K. S. Raman Scattering Study on Structural and Dynamical Features of Noncrystalline Selenium. *J. Chem. Phys.* **2004**, *121* (10), 4747–4758.
- (171) Caponi, S.; Fontana, A.; Rossi, F.; Baldi, G.; Fabiani, E. Effect of Temperature on the Vibrational Density of States in Vitreous SiO₂: A Raman Study. *Phys. Rev. B* **2007**, *76* (9), 92201.
- (172) Deschamps, T.; Martinet, C.; de Ligny, D.; Bruneel, J. L.; Champagnon, B. Low-Frequency Raman Scattering under High Pressure in Diamond Anvil Cell: Experimental Protocol and Application to GeO₂ and SiO₂ Boson Peaks. *J. Non. Cryst. Solids* **2012**, *358* (23), 3156–3160.
- (173) Schroeder, J.; Wu, W.; Apkarian, J. L.; Lee, M.; Hwa, L. G.; Moynihan, C. T. Raman Scattering and Boson Peaks in Glasses: Temperature and Pressure Effects. *J. Non. Cryst. Solids* **2004**, *349* (1–3), 88–97.
- (174) Zanatta, M.; Baldi, G.; Caponi, S.; Fontana, A.; Petrillo, C.; Rossi, F.; Sacchetti, F. Debye to Non-Debye Scaling of the Boson Peak Dynamics: Critical Behavior and Local Disorder in Vitreous Germania. *J. Chem. Phys.* **2011**, *135* (17).
- (175) Baldi, G.; Fontana, A.; Monaco, G.; Orsingher, L.; Rols, S.; Rossi, F.; Ruta, B. Connection between Boson Peak and Elastic Properties in Silicate Glasses. *Phys. Rev. Lett.* **2009**, *102* (19), 195502.
- (176) Wuttke, J.; Petry, W.; Coddens, G.; Fujara, F. Fast Dynamics of Glass-Forming Glycerol. *Phys. Rev. E* **1995**, *52* (4), 4026–4034.
- (177) Chumakov, A. I.; Sergueev, I.; van Bürck, U.; Schirmacher, W.; Asthalter, T.; Ruffer,

- R.; Leupold, O.; Petry, W. Collective Nature of the Boson Peak and Universal Transboson Dynamics of Glasses. *Phys. Rev. Lett.* **2004**, *92* (24), 245508.
- (178) Chumakov, A. I.; Monaco, G.; Fontana, A.; Bosak, A.; Hermann, R. P.; Bessas, D.; Wehinger, B.; Crichton, W. A.; Krisch, M.; Ruffer, R.; et al. Role of Disorder in the Thermodynamics and Atomic Dynamics of Glasses. *Phys. Rev. Lett.* **2014**, *112* (2), 025502.
- (179) Tanaka, H. Two-Order-Parameter Model of the Liquid–Glass Transition. II. Structural Relaxation and Dynamic Heterogeneity. *J. Non. Cryst. Solids* **2005**, *351* (43–45), 3385–3395.
- (180) Tanaka, H. Bond Orientational Order in Liquids: Towards a Unified Description of Water-like Anomalies, Liquid-Liquid Transition, Glass Transition, and Crystallization. *Eur. Phys. J. E* **2012**, *35* (10), 113.
- (181) Achibat, T.; Boukenter, A.; Duval, E. Correlation Effects on Raman Scattering from Low-energy Vibrational Modes in Glasses. II. Experimental Results. *J. Chem. Phys.* **1993**, *99* (3), 2046–2051.
- (182) Fontana, A.; Dell’Anna, R.; Montagna, M.; Rossi, F.; Viliani, G.; Ruocco, G.; Sampoli, M.; Buchenau, U.; Wischnewski, A. The Raman Coupling Function in Amorphous Silica and the Nature of the Long-Wavelength Excitations in Disordered Systems. *Europhys. Lett.* **1999**, *47* (1), 56–62.
- (183) Orsingher, L.; Baldi, G.; Fontana, A.; Rossi, F. The Raman Coupling Function in Permanently Densified GeO₂ Glasses. *Philos. Mag.* **2011**, *91* (13–15), 1857–1863.
- (184) Cho, M.; Du, M.; Scherer, N. F.; Fleming, G. R.; Mukamel, S. Off-resonant Transient Birefringence in Liquids. *J. Chem. Phys.* **1993**, *99* (4), 2410–2428.
- (185) Scott, D. W.; Guthrie, G. B.; Messerly, J. F.; Todd, S. S.; Berg, W. T.; Hossenlopp, I. A.; McCullough, J. P. Toluene: Thermodynamic Properties, Molecular Vibrations, and Internal Rotation. *J. Phys. Chem.* **1962**, *66* (5), 911–914.
- (186) Yamamuro, O.; Tsukushi, I.; Lindqvist, A.; Takahara, S.; Ishikawa, M.; Matsuo, T. Calorimetric Study of Glassy and Liquid Toluene and Ethylbenzene: Thermodynamic Approach to Spatial Heterogeneity in Glass-Forming Molecular Liquids. *J. Phys. Chem. B* **1998**, *102* (9), 1605–1609.
- (187) Alvarez-Ney, C.; Labarga, J.; Moratalla, M.; Castilla, J. M.; Ramos, M. A. Calorimetric Measurements at Low Temperatures in Toluene Glass and Crystal. *J. Low Temp. Phys.* **2017**, *187* (1–2), 182–191.
- (188) Wuttke, J.; Seidl, M.; Hinze, G.; Tölle, A.; Petry, W.; Coddens, G. Mode-Coupling Crossover in Viscous Toluene Revealed by Neutron and Light Scattering. *Eur. Phys. J. B* **1998**, *1* (2), 169–172.
- (189) Santarelli, V. A.; MacDonald, J. A.; Pine, C. Overlapping Dielectric Dispersions in Toluene. *J. Chem. Phys.* **1967**, *46* (6), 2367–2375.
- (190) Ibers, J. A. Crystal and Molecular Structure of Titanium (IV) Ethoxide. *Nature* **1963**, *197* (4868), 686–687.
- (191) Caughlan, C. N.; Smith, H. S.; Katz, W.; Hodgson; Crowe, R. W. Organic Compounds of Titanium. II. Association of Organic Titanates in Benzene Solution. *J. Am. Chem. Soc.* **1951**, *73* (12), 5652–5654.
- (192) Babonneau, F.; Doeuff, S.; Leautic, A.; Sanchez, C.; Cartier, C.; Verdagner, M. XANES and EXAFS Study of Titanium Alkoxides. *Inorg. Chem.* **1988**, *27* (18), 3166–3172.
- (193) Martin, R. L.; Winter, G. Structure of the Trinuclear Titanium (IV) Alkoxides. *Nature*

- 1960**, *188* (4747), 313–315.
- (194) Bradley, D. C.; Holloway, C. E. Nuclear Magnetic Resonance and Cryoscopic Studies on Some Alkoxides of Titanium, Zirconium, and Hafnium. *J. Chem. Soc. A Inorganic, Phys. Theor.* **1968**, No. 1316, 1316.
- (195) Zheng, Q.; Zhang, Y.; Montazerian, M.; Gulbitten, O.; Mauro, J. C.; Zanutto, E. D.; Yue, Y. Understanding Glass through Differential Scanning Calorimetry. *Chem. Rev.* **2019**, *119* (13), 7848–7939.
- (196) Lane, P. D.; Reichenbach, J.; Farrell, A. J.; Ramakers, L. A. I.; Adamczyk, K.; Hunt, N. T.; Wynne, K. Experimental Observation of Nanophase Segregation in Aqueous Salt Solutions around the Predicted Liquid–Liquid Transition in Water. *Phys. Chem. Chem. Phys.* **2020**, *22* (17), 9438–9447.
- (197) Brini, E.; Fennell, C. J.; Fernandez-Serra, M.; Hribar-Lee, B.; Lukšič, M.; Dill, K. A. How Water’s Properties Are Encoded in Its Molecular Structure and Energies. *Chem. Rev.* **2017**, *117* (19), 12385–12414.
- (198) Domínguez, C. M.; Ramos, D.; Mendieta-Moreno, J. I.; Fierro, J. L. G.; Mendieta, J.; Tamayo, J.; Calleja, M. Effect of Water-DNA Interactions on Elastic Properties of DNA Self-Assembled Monolayers. *Sci. Rep.* **2017**, *7* (1), 536.
- (199) Busch, S.; Bruce, C. D.; Redfield, C.; Lorenz, C. D.; McLain, S. E. Water Mediation Is Essential to Nucleation of β -Turn Formation in Peptide Folding Motifs. *Angew. Chemie Int. Ed.* **2013**, *52* (49), 13091–13095.
- (200) Levy, Y.; Onuchic, J. N. Water and Proteins: A Love-Hate Relationship. *Proc. Natl. Acad. Sci.* **2004**, *101* (10), 3325–3326.
- (201) Schwabe, J. W. The Role of Water in Protein–DNA Interactions. *Curr. Opin. Struct. Biol.* **1997**, *7* (1), 126–134.
- (202) Carpenter, W. B.; Fournier, J. A.; Lewis, N. H. C.; Tokmakoff, A. Picosecond Proton Transfer Kinetics in Water Revealed with Ultrafast IR Spectroscopy. *J. Phys. Chem. B* **2018**, *122* (10), 2792–2802.
- (203) Persson, E.; Halle, B. Cell Water Dynamics on Multiple Time Scales. *Proc. Natl. Acad. Sci. U. S. A.* **2008**, *105* (17), 6266–6271.
- (204) Gallo, P.; Amann-Winkel, K.; Angell, C. A.; Anisimov, M. A.; Caupin, F.; Chakravarty, C.; Lascaris, E.; Loerting, T.; Panagiotopoulos, A. Z.; Russo, J.; et al. Water: A Tale of Two Liquids. *Chem. Rev.* **2016**, *116* (13), 7463–7500.
- (205) Amann-Winkel, K.; Böhmer, R.; Fujara, F.; Gainaru, C.; Geil, B.; Loerting, T. Colloquium : Water’s Controversial Glass Transitions. *Rev. Mod. Phys.* **2016**, *88* (1), 011002.
- (206) Speedy, R. J.; Angell, C. A. Isothermal Compressibility of Supercooled Water and Evidence for a Thermodynamic Singularity at -45°C . *J. Chem. Phys.* **1976**, *65* (3), 851–858.
- (207) Poole, P. H.; Sciortino, F.; Essmann, U.; Stanley, H. E. Phase Behaviour of Metastable Water. *Nature* **1992**, *360* (6402), 324–328.
- (208) Bullock, G.; Molinero, V. Low-Density Liquid Water Is the Mother of Ice: On the Relation between Mesosstructure, Thermodynamics and Ice Crystallization in Solutions. *Faraday Discuss.* **2013**, *167*, 371.
- (209) Kim, W. -H.; Reinot, T.; Hayes, J. M.; Small, G. J. Nonphotochemical Hole Burning in Hyperquenched Glassy Films of Water: A Pronounced Deuteration Effect. *J. Chem. Phys.* **1996**, *104* (17), 6415–6417.

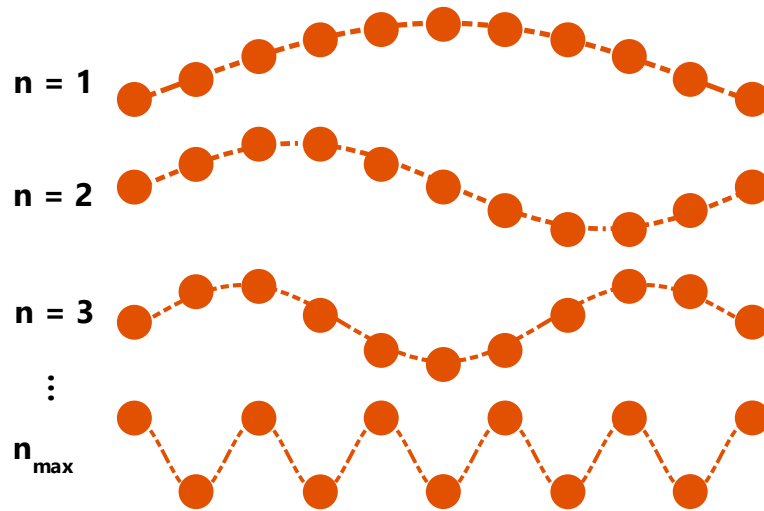
- (210) Mayer, E. New Method for Vitriying Water and Other Liquids by Rapid Cooling of Their Aerosols. *J. Appl. Phys.* **1985**, *58* (2), 663–667.
- (211) Perakis, F.; Amann-Winkel, K.; Lehmkuhler, F.; Sprung, M.; Mariedahl, D.; Sellberg, J. A.; Pathak, H.; Späh, A.; Cavalca, F.; Schlesinger, D.; et al. Diffusive Dynamics during the High-to-Low Density Transition in Amorphous Ice. *Proc. Natl. Acad. Sci.* **2017**, *114* (31), 8193–8198.
- (212) Murata, K.; Tanaka, H. Liquid–Liquid Transition without Macroscopic Phase Separation in a Water–Glycerol Mixture. *Nat. Mater.* **2012**, *11* (5), 436–443.
- (213) Popov, I.; Greenbaum (Gutina), A.; Sokolov, A. P.; Feldman, Y. The Puzzling First-Order Phase Transition in Water–Glycerol Mixtures. *Phys. Chem. Chem. Phys.* **2015**, *17* (27), 18063–18071.
- (214) Bruijn, J. R.; van der Loop, T. H.; Woutersen, S. Changing Hydrogen-Bond Structure during an Aqueous Liquid–Liquid Transition Investigated with Time-Resolved and Two-Dimensional Vibrational Spectroscopy. *J. Phys. Chem. Lett.* **2016**, *7* (5), 795–799.
- (215) Koop, T.; Luo, B.; Tsias, A.; Peter, T. Water Activity as the Determinant for Homogeneous Ice Nucleation in Aqueous Solutions. *Nature* **2000**, *406* (6796), 611–614.
- (216) Zhang, B.; Yu, Y.; Zhang, Y.-Y.; Jiang, S.; Li, Q.; Hu, H.-S.; Li, G.; Zhao, Z.; Wang, C.; Xie, H.; et al. Infrared Spectroscopy of Neutral Water Clusters at Finite Temperature: Evidence for a Noncyclic Pentamer. *Proc. Natl. Acad. Sci.* **2020**, *117* (27), 15423–15428.
- (217) Burnham, C. J.; Xantheas, S. S.; Miller, M. A.; Applegate, B. E.; Miller, R. E. The Formation of Cyclic Water Complexes by Sequential Ring Insertion: Experiment and Theory. *J. Chem. Phys.* **2002**, *117* (3), 1109–1122.
- (218) Heyden, M.; Sun, J.; Funkner, S.; Mathias, G.; Forbert, H.; Havenith, M.; Marx, D. Dissecting the THz Spectrum of Liquid Water from First Principles via Correlations in Time and Space. *Proc. Natl. Acad. Sci.* **2010**, *107* (27), 12068–12073.
- (219) Taschin, A.; Bartolini, P.; Marcelli, A.; Righini, R.; Torre, R. A Comparative Study on Bulk and Nanoconfined Water by Time-Resolved Optical Kerr Effect Spectroscopy. *Faraday Discuss.* **2013**, *167*, 293.
- (220) Walrafen, G. E. Raman Spectrum of Water: Transverse and Longitudinal Acoustic Modes below 300 cm^{-1} and Optic Modes above 300 cm^{-1} . *J. Phys. Chem.* **1990**, *94* (6), 2237–2239.
- (221) Hecht, M. H.; Kounaves, S. P.; Quinn, R. C.; West, S. J.; Young, S. M. M.; Ming, D. W.; Catling, D. C.; Clark, B. C.; Boynton, W. V.; Hoffman, J.; et al. Detection of Perchlorate and the Soluble Chemistry of Martian Soil at the Phoenix Lander Site. *Science* (80-.). **2009**, *325* (5936), 64–67.
- (222) Chevrier, V. F.; Hanley, J.; Altheide, T. S. Stability of Perchlorate Hydrates and Their Liquid Solutions at the Phoenix Landing Site, Mars. *Geophys. Res. Lett.* **2009**, *36* (10), L10202.
- (223) Lenton, S.; Rhys, N. H.; Towey, J. J.; Soper, A. K.; Dougan, L. Highly Compressed Water Structure Observed in a Perchlorate Aqueous Solution. *Nat. Commun.* **2017**, *8* (1), 919.
- (224) Hartman, K. A. The Structure of Water and the Stability of the Secondary Structure in Biological Molecules. An Infrared and Proton Magnetic Resonance Study. *J. Phys. Chem.* **1966**, *70* (1), 270–276.

- (225) Brink, G.; Falk, M. Infrared Spectrum of HDO in Aqueous Solutions of Perchlorates and Tetrafluoroborates. *Can. J. Chem.* **1970**, *48* (19), 3019–3025.
- (226) Loerting, T.; Schustereder, W.; Winkel, K.; Salzmann, C. G.; Kohl, I.; Mayer, E. Amorphous Ice: Stepwise Formation of Very-High-Density Amorphous Ice from Low-Density Amorphous Ice at 125 K. *Phys. Rev. Lett.* **2006**, *96* (2), 025702.
- (227) Kojima, S. Anomalous Behaviour of the O-H Stretching Vibrational Mode in the Liquid-Glass Transition of Glycerol. *J. Mol. Struct.* **1993**, *294*, 193–195.
- (228) Ruiz, G. N.; Amann-Winkel, K.; Bove, L. E.; Corti, H. R.; Loerting, T. Calorimetric Study of Water's Two Glass Transitions in the Presence of LiCl. *Phys. Chem. Chem. Phys.* **2018**, *20* (9), 6401–6408.
- (229) Le, L.; Molinero, V. Nanophase Segregation in Supercooled Aqueous Solutions and Their Glasses Driven by the Polyamorphism of Water. *J. Phys. Chem. A* **2011**, *115* (23), 5900–5907.
- (230) Mishima, O. Phase Separation in Dilute LiCl–H₂O Solution Related to the Polyamorphism of Liquid Water. *J. Chem. Phys.* **2007**, *126* (24), 244507.
- (231) Suzuki, Y.; Mishima, O. Two Distinct Raman Profiles of Glassy Dilute LiCl Solution. *Phys. Rev. Lett.* **2000**, *85* (6), 1322–1325.
- (232) Angell, C. A.; Sare, E. J. Liquid–Liquid Immiscibility in Common Aqueous Salt Solutions at Low Temperatures. *J. Chem. Phys.* **1968**, *49* (10), 4713–4714.
- (233) Elarby-Aouizerat, A.; Jal, J. F.; Chieux, P.; Letoffé, J. M.; Claudy, P.; Dupuy, J. Metastable Crystallization Products and Metastable Phase Diagram of the Glassy and Supercooled Aqueous Ionic Solutions of LiCl. *J. Non. Cryst. Solids* **1988**, *104* (2–3), 203–210.
- (234) Monnin, C.; Dubois, M.; Papaiconomou, N.; Simonin, J. P. Thermodynamics of the LiCl + H₂O System. *J. Chem. Eng. Data* **2002**, *47* (6), 1331–1336.
- (235) Angell, C. A. Insights into Phases of Liquid Water from Study of Its Unusual Glass-Forming Properties. *Science* (80-.). **2008**, *319* (5863), 582–587.
- (236) Schimmel, F. A. Solubilities of Lithium Chloride and Lithium Thiocyanate at Low Temperatures. *J. Chem. Eng. Data* **1960**, *5* (4), 519–520.
- (237) Schultz, P. W.; Leroi, G. E.; Popov, A. I. Solvation of SCN⁻ and SeCN⁻ Anions in Hydrogen-Bonding Solvents. *J. Am. Chem. Soc.* **1996**, *118* (43), 10617–10625.
- (238) Czurlok, D.; Gleim, J.; Lindner, J.; Vöhringer, P. Vibrational Energy Relaxation of Thiocyanate Ions in Liquid-to-Supercritical Light and Heavy Water. A Fermi's Golden Rule Analysis. *J. Phys. Chem. Lett.* **2014**, *5* (19), 3373–3379.
- (239) Lenchenkov, V.; She, C.; Lian, T. Vibrational Relaxation of CN Stretch of Pseudo-Halide Anions (OCN⁻, SCN⁻, and SeCN⁻) in Polar Solvents. *J. Phys. Chem. B* **2006**, *110* (40), 19990–19997.
- (240) Yuan, R.; Fayer, M. D. Dynamics of Water Molecules and Ions in Concentrated Lithium Chloride Solutions Probed with Ultrafast 2D IR Spectroscopy. *J. Phys. Chem. B* **2019**, *123* (35), 7628–7639.
- (241) Elton, D. C.; Fernández-Serra, M. The Hydrogen-Bond Network of Water Supports Propagating Optical Phonon-like Modes. *Nat. Commun.* **2016**, *7* (1), 10193.
- (242) Tassaing, T.; Danten, Y.; Besnard, M. Infrared Spectroscopic Study of Hydrogen-Bonding in Water at High Temperature and Pressure. *J. Mol. Liq.* **2002**, *101* (1–3), 149–158.
- (243) Park, S.; Ji, M.; Gaffney, K. J. Ligand Exchange Dynamics in Aqueous Solution

- Studied with 2DIR Spectroscopy. *J. Phys. Chem. B* **2010**, *114* (19), 6693–6702.
- (244) Gafurov, M. M.; Aliev, A. R.; Akhmedov, I. R. Raman and Infrared Study of the Crystals with Molecular Anions in the Region of a Solid–Liquid Phase Transition. *Spectrochim. Acta Part A Mol. Biomol. Spectrosc.* **2002**, *58* (12), 2683–2692.
- (245) Choi, J.-H.; Cho, M. Ion Aggregation in High Salt Solutions. II. Spectral Graph Analysis of Water Hydrogen-Bonding Network and Ion Aggregate Structures. *J. Chem. Phys.* **2014**, *141* (15), 154502.
- (246) Tu, S.; Lobanov, S. S.; Bai, J.; Zhong, H.; Gregerson, J.; Rogers, A. D.; Ehm, L.; Parise, J. B. Enhanced Formation of Solvent-Shared Ion Pairs in Aqueous Calcium Perchlorate Solution toward Saturated Concentration or Deep Supercooling Temperature and Its Effects on the Water Structure. *J. Phys. Chem. B* **2019**, *123* (45), 9654–9667.

9 APPENDICES

A. Phonons in a 1-Dimensional Chain



Appendix A.I. Phonon energy states from the lowest 3 to the maximum

Shown in terms of TA phonons for illustration, however this applies equally to LA phonons too.

The longest wavelength phonons are the lowest energy; the first phonon mode ($n = 1$) has a wavelength of $2L$, where L is the length of the chain. Clearly the length of the 1D chain, or volume of the 3D crystal, imposes a limit to the phonon wavelength. The lattice spacing imposes a lower limit to the phonon wavelength (and thus upper limit to the phonon frequency) as shown by n_{\max} . This in turn imposes a maximum (Debye) frequency, $\omega_D = v\pi/a$, where v is the speed of sound and a is the lattice spacing.

B. Hydrocarbon Molarities

<i>n</i> -Alkane C_nH_{2n+2}	Density [g/L] (at 20 °C)	Mol. weight (g/mol)	Molarity (mol/L)
5	626	72	8.694
6	659	86	7.663
7	684	100	6.84
8	703	114	6.167
9	718	128	5.609
10	730	142	5.141
11	740	156	4.744
12	749	170	4.406
13	756	184	4.109
14	763	198	3.854
15	769	212	3.627
16	773	226	3.420
17	777	240	3.238
20	789	254	3.106
Cycloalkane C_nH_{2n}	Density [g/L] (at 20 °C)	Mol. weight (g/mol)	Molarity (mol/L)
5	751	70	10.73
6	779	84	9.274
7	811	98	8.276
8	834	112	7.446
10	871	140	6.221
Cyclohexene	811	82	9.890
1,4-Cyclohexadiene	847	80	10.59
Benzene	876	78	11.23

Appendix B.I. Molarity of n-alkanes, cycloalkanes, and six membered rings from their density.

C. Hydrocarbon OKE Spectra Line-Shape Fitting Parameters

	α -relaxation			β -relaxation			Fast- β			Libration		
298K C_nH_{2n+2}	A_{iD} / 10^{-1}	τ / ps	Ω_I / THz	A_{iD} / 10^{-1}	τ / ps	Ω_I / THz	A_B / 10^{-1}	$\omega_0/2\pi$ / THz	$\gamma/2\pi$ / THz	A_B / 10^{-1}	$\omega_0/2\pi$ / THz	$\gamma/2\pi$ / THz
5	3.34	2.60	1.57	2.13	0.69	1.22	3.69	1.22	1.66	1.89	1.57	1.19
6	5.23	5.23	1.70	2.19	1.12	1.21	3.20	1.21	1.79	1.75	1.70	1.33
7	8.36	8.69	1.75	1.93	1.23	1.20	2.85	1.20	1.91	1.83	1.76	1.41
8	11.0	13.9	1.82	1.78	1.41	1.22	2.50	1.22	1.97	1.82	1.82	1.46
9	13.4	24.4	1.82	1.53	2.40	1.09	2.33	1.09	2.05	1.96	1.82	1.52
10	15.9	43.6	1.80	1.57	4.07	1.01	2.06	1.01	2.11	1.85	1.80	1.52
12	20.6	87.5	1.77	1.42	6.30	0.93	1.84	0.93	2.14	1.92	1.77	1.52
14	23.5	162	1.78	1.65	9.38	0.88	1.71	0.88	2.17	1.85	1.78	1.57
16	24.0	244	1.80	1.56	1.38	0.79	1.59	0.79	2.22	1.90	1.80	1.66

Appendix C.1. Fitting parameter values for n-alkane OKE spectra.

Ω_I are fixed values; α -relaxation Ω_I is fixed to the libration ω_0 and β -relaxation Ω_I is fixed to the fast- β ω_0 .

	α -relaxation			β -relaxation				Fast- β			Libration		
T / K	A_{iD} / 10^{-1}	τ / ps	Ω_I / THz	A_{iCC} / 10^{-1}	τ / ps	Ω_I / THz	β_{CC}	A_B / 10^{-1}	$\omega_0/2\pi$ / THz	$\gamma/2\pi$ / THz	A_G / 10^{-1}	$\omega_G/2\pi$ / THz	$\sigma_G/2\pi$ / THz
77.7	1.80	25.9	1.58	2.09	1.54	1.74	0.72	1.33	1.74	2.08	1.19	1.58	1.53
90	1.66	9.64	1.57	2.07	1.31	1.69	0.96	1.43	1.69	2.04	1.30	1.57	1.57
130	1.42	6.16	1.49	1.99	0.77	1.59	1	1.70	1.59	1.92	1.15	1.49	1.58
170	0.83	2.74	1.39	2.14	0.55	1.45	1	2.03	1.45	1.73	1.38	1.39	1.54
210	0.38	1.93	1.24	2.04	0.47	1.41	1	2.28	1.41	1.59	1.61	1.24	1.54

Appendix C.2 Fitting parameter values for propane OKE spectra.

Ω_I are fixed values; α -relaxation Ω_I is fixed to the libration ω_G and β -relaxation Ω_I is fixed to the fast- β ω_0 .

	α -relaxation			β -relaxation				Fast- β			Libration		
	A_{iD} / 10^{-2}	τ / ps	Ω_I / THz	A_{iCC} / 10^{-2}	τ / ps	Ω_I / THz	β_{CC}	A_B / 10^{-2}	$\omega_0/2\pi$ / THz	$\gamma/2\pi$ / THz	A_G / 10^{-2}	$\omega_G/2\pi$ / THz	$\sigma_G/2\pi$ / THz
298K cC _n H _{2n}													
5	3.55	0.50	0.95	7.88	0.89	1.23	1	28.8	1.23	1.26	11.0	0.95	1.60
6	5.46	1.30	1.02	6.96	1.41	1.22	1	24.5	1.22	1.64	14.9	1.02	1.47
7	10.8	6.52	1.10	13.9	1.55	1.22	1	22.7	1.22	2.13	14.6	1.10	1.30
8	9.47	10.6	1.05	13.4	2.19	1.17	1	22.0	1.17	2.56	14.5	1.05	1.20
10	32.8	47.9	0.97	28.4	4.57	1.04	0.84	19.0	1.04	2.50	13.1	0.97	1.17

Appendix C.3. Fitting parameter values for cycloalkanes OKE spectra

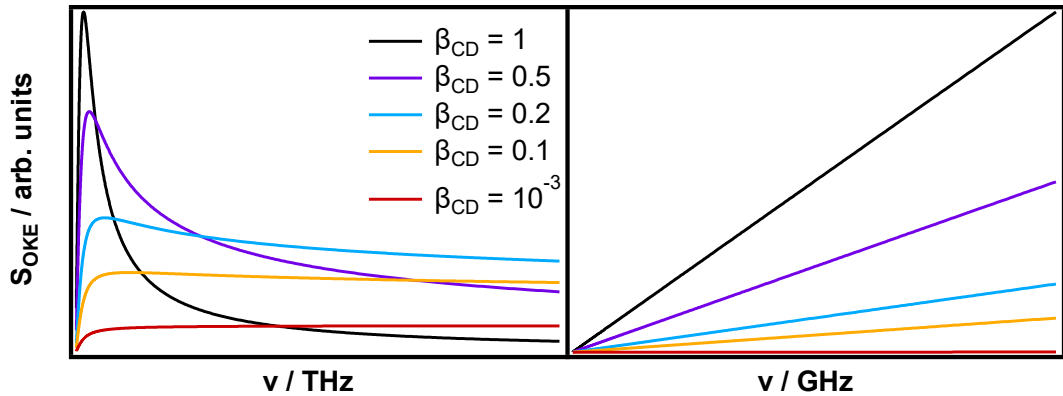
Ω_I are fixed values; α -relaxation Ω_I is fixed to the libration ω_G and β -relaxation Ω_I is fixed to the fast- β ω_0 .

	α -relaxation			β -relaxation			Fast- β			Libration		
	A_{iD} / 10^{-2}	τ / ps	Ω_I / THz	A_{iD} / 10^{-2}	τ / ps	Ω_I / THz	A_B / 10^{-2}	$\omega_0/2\pi$ / THz	$\gamma/2\pi$ / THz	A_G / 10^{-2}	$\omega_G/2\pi$ / THz	$\sigma_G/2\pi$ / THz
298K C ₆ rings												
C ₆ H ₁₂	5.46	1.30	1.02	6.96	1.41	1.22	24.5	1.22	1.64	14.9	1.02	1.47
C ₆ H ₁₀	104	3.35	1.05	95.9	0.88	1.21	87.9	1.21	1.75	33.1	1.05	1.48
1,4-C ₆ H ₈	290	2.88	1.22	201	0.76	1.20	160	1.20	1.85	64.8	1.22	1.62
C ₆ H ₆	296	3.05	1.77	192	0.74	1.26	175	1.26	1.90	107	1.77	1.68

Appendix C.4 Fitting parameter values for 6-membered ring OKE spectra.

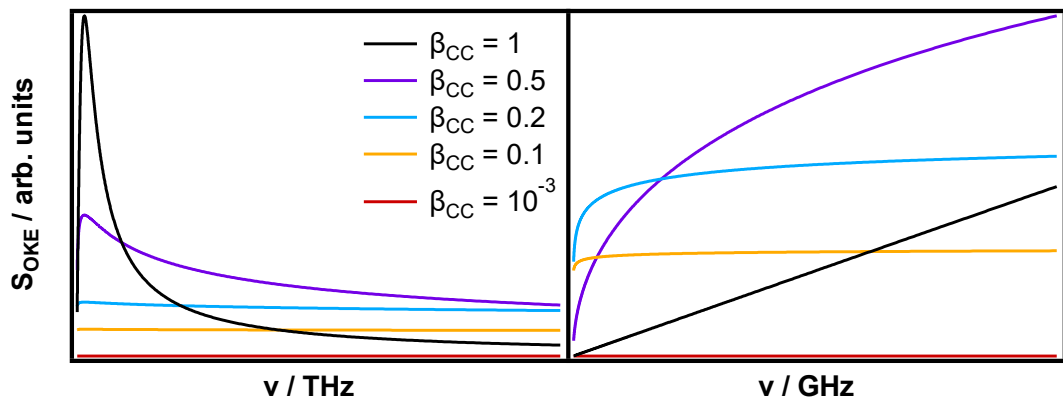
Ω_I are fixed values; α -relaxation Ω_I is fixed to the libration ω_G and β -relaxation Ω_I is fixed to the fast- β ω_0 .

D. Havriliak-Negami Line-Shape Proportionalities



Appendix D.1. The effect of the Cole-Davidson parameter on the Havriliak-Negami line-shape.

HN line-shapes with $\tau/ps = A_{HN} = \beta_{CC} = 1$, with linear frequency axes throughout. **Left:** The HN line-shapes at THz frequencies for various α_{CD} values. **Right:** The same HN line-shapes at GHz frequencies

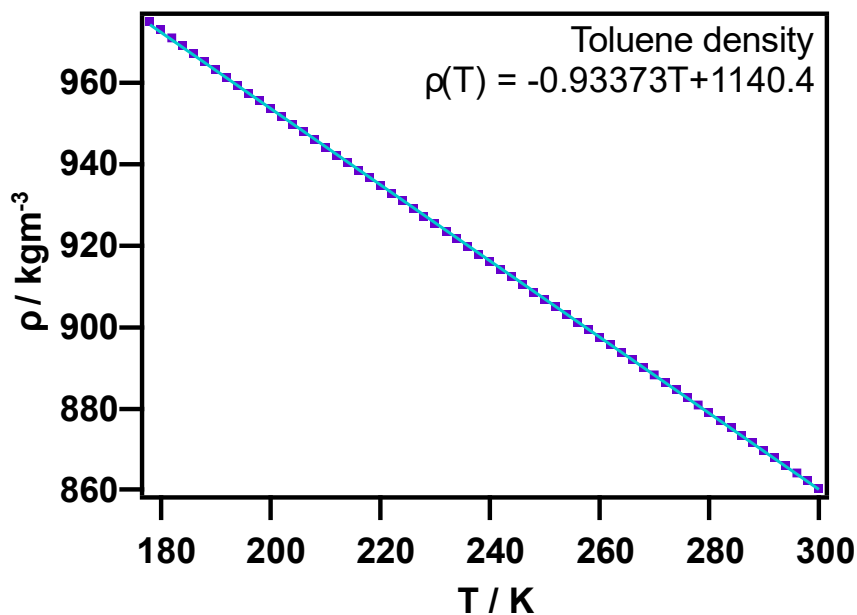


Appendix D.2. The effect of the Cole-Cole parameter on the Havriliak-Negami line-shape.

HN line-shapes with $\tau/ps = A_{HN} = \alpha_{CD} = 1$, with linear frequency axes throughout. **Left:** The HN line-shapes at THz frequencies for various β_{CC} values. **Right:** The same HN line-shapes at GHz frequencies

Both Cole-Davidson and Cole-Cole parameters broaden the HN line-shape but with different results (see Figure 3.3 for Cole-Cole line-shapes displayed with a logarithmic frequency axis). Focussing on the proportionality as $\nu \rightarrow 0$, it can be seen from Appendix D.1 (right) that the Cole-Davidson parameter does not affect the $\propto \nu$ relationship of the lineshape (for non-zero values). With regards to the Cole-Cole parameter, the line-shapes appears as $\propto \nu^n$ where $0 < n < 1$.

E. Toluene Supplementary Data



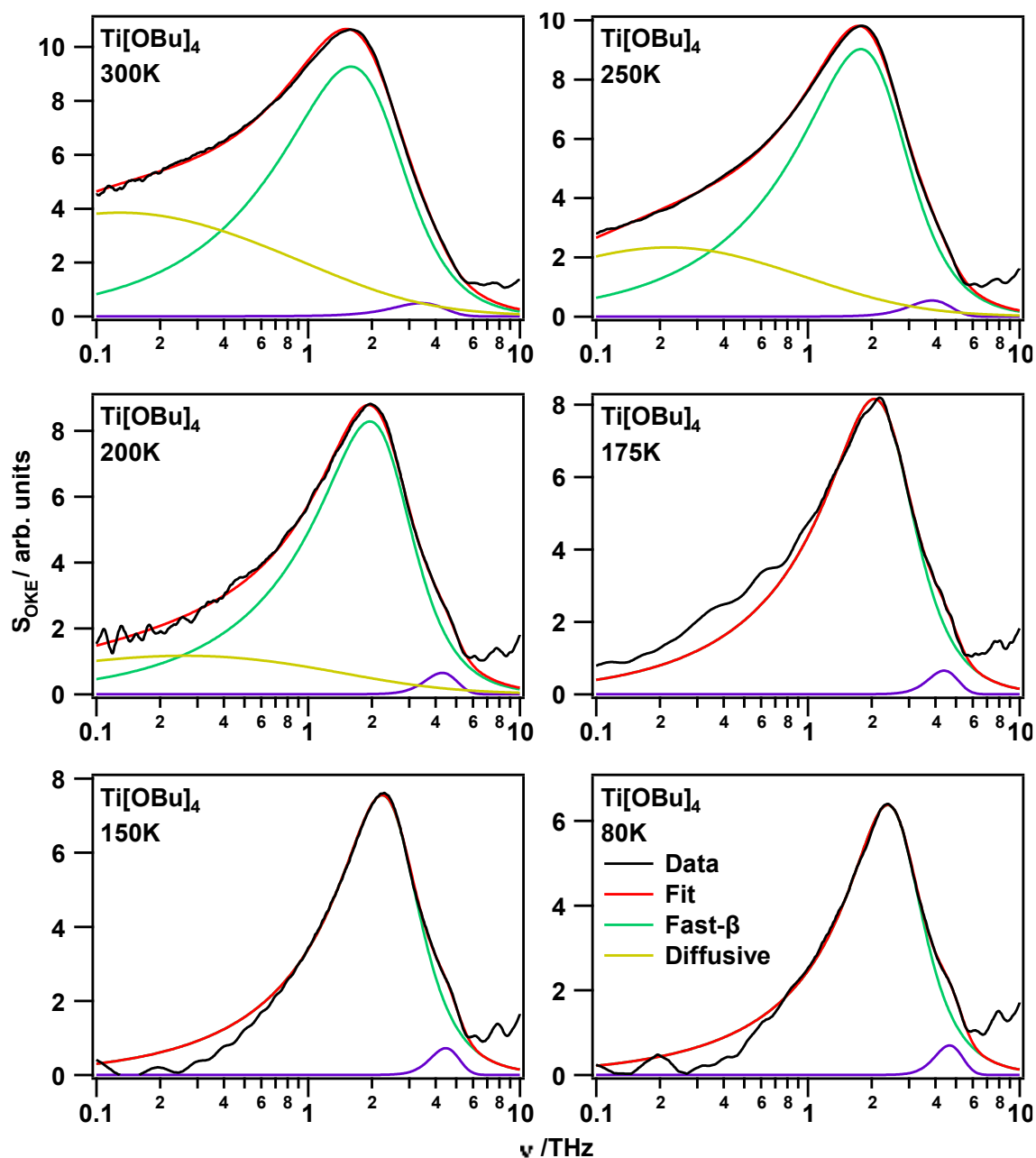
Appendix E.1. Toluene density as a function of temperature

Data taken from ref.⁸⁵ is fit with a linear trend, with result shown.

T / K	Orientational α			Translational α				Boson peak			Intramolecular mode		
	A_{iD}	τ / ps	$\gamma_{rise}/2\pi$ / THz	A_{iCC}	τ / ps	$\gamma_{rise}/2\pi$ / THz	β_{CC}	A_B	$\omega_0/2\pi$ / THz	$\gamma/2\pi$ / THz	A_G /10 ¹²	$\omega_G/2\pi$ / THz	$\sigma/2\pi$ / THz
300	196.1	5.072	1.867	67.72	1.501	1.367	1.000	299.3	1.367	3.962	72.96	1.867	0.959
250	248.9	10.19	2.053	68.19	1.950	1.398	0.864	278.7	1.398	3.679	74.90	2.053	0.927
200	271.7	46.55	2.263	121.3	6.391	1.455	0.703	243.2	1.455	3.613	73.40	2.263	0.875
150	193.8	1129	2.450	82.43	57.12	1.531	0.416	207.2	1.531	3.456	73.82	2.450	0.831
120	--	--	--	--	--	--	--	181.8	1.626	3.022	71.50	2.634	0.797

Appendix E.2. Fitting parameter values for the OKE spectra of toluene as a function of temperature

F. TiBuO Supplementary Data

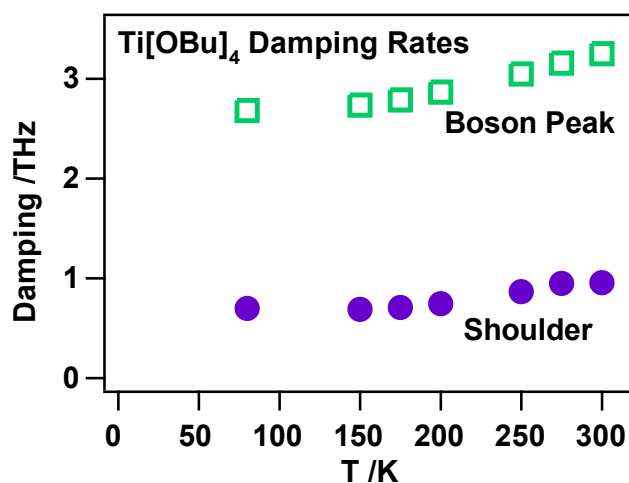


Appendix F.I. Line-shape fits to the temperature dependent OKE spectra of titanium butoxide with a logarithmic frequency scale.

Spectra taken from 300 K to 80 K (left to right).

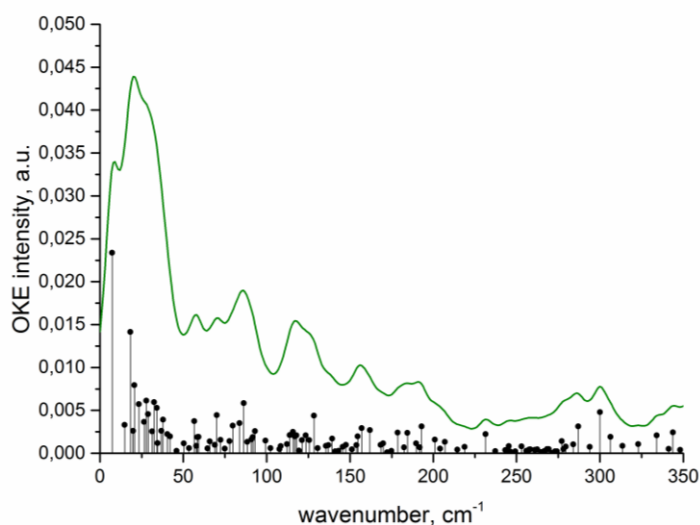
T /K	Translational diffusion				Fast- β			Intramolecular mode		
	A_{iCC}	τ / ps	$\gamma_{rise}/2\pi$ / THz	β_{CC}	A_B	$\omega_0/2\pi$ / THz	$\gamma/2\pi$ / THz	A_G / 10^{12}	$\omega_G/2\pi$ / THz	$\sigma/2\pi$ / THz
300	13.92	1.162	2.171	0.550	75.27	2.171	3.250	1.176	3.432	0.955
275	9.923	0.800	2.235	0.612	71.06	2.235	3.156	1.201	3.695	0.949
250	6.873	0.683	2.274	0.700	67.55	2.274	3.046	1.178	3.858	0.865
200	4.287	0.529	2.380	0.670	56.00	2.380	2.863	1.210	4.302	0.744
175	--	--	--	--	53.57	2.450	2.786	1.152	4.398	0.706
150	--	--	--	--	46.56	2.591	2.734	1.245	4.466	0.688
80	--	--	--	--	37.19	2.710	2.681	1.217	4.668	0.698

Appendix F.2. Fitting parameter values for the temperature dependent TiBuO spectra



Appendix F.3. Damping rates of the TiBuO line-shape fits with temperature.

Boson peak values correspond to the γ value of the Brownian oscillator, whilst the shoulder values are the σ values of the antisymmetrised Gaussian function



Appendix F.4. Calculated OKE spectrum of TiBuO trimer.

Calculation performed by Dr. Nikita Tukachev and Dr. Hans Senn. PBE-D3(BJ)/def2-SVP level of theory.

G. OKE Line-Shape Fitting Parameters for Titanium Tetrabutoxide, Tetraethoxide, and Their 1:1 Mixture.

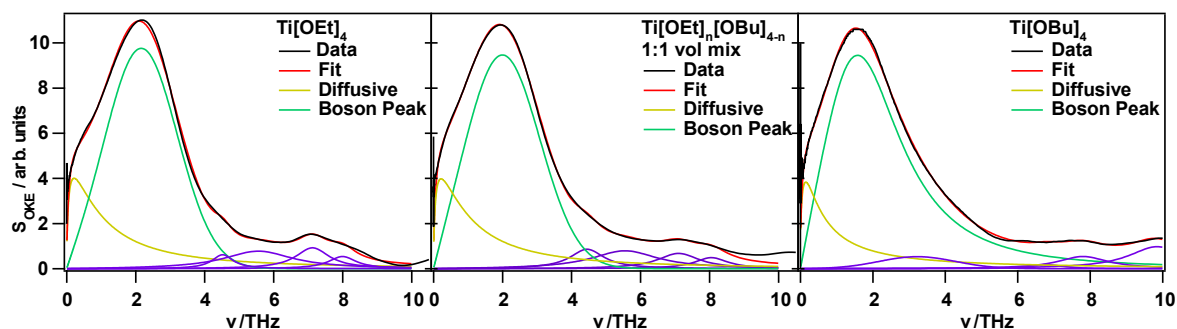
	Diffusive Mode				Boson Peak			Intramolecular Mode #1		
	A_{icc}	τ / ps	$\gamma_{\text{rise}}/2\pi$ / THz	β_{cc}	A^*	$\omega_0/2\pi$ / THz	$(\gamma \text{ or } \sigma)^\dagger / 2\pi$ / THz	A^*	$\omega_0/2\pi$ / THz	$(\gamma \text{ or } \sigma)^\dagger / 2\pi$ / THz
TiEtO	13.08	0.617	2.169	0.722	25.36	2.169	1.050	0.626	4.534	0.731
Ti[EtO] _n [BuO] _{4-n}	14.26	0.628	1.994	0.670	25.54	1.994	1.091	1.380	4.490	1.200
TiBuO	13.28	1.046	2.182	0.683	74.73	2.182	3.250	1.007	3.370	0.938
	Intramolecular Mode #2			Intramolecular Mode #3			Intramolecular Mode #4			
	A_B	$\omega_0/2\pi$ / THz	$\gamma / 2\pi$ / THz	A_B	$\omega_0/2\pi$ / THz	$\gamma / 2\pi$ / THz	A_B	$\omega_0/2\pi$ / THz	$\gamma / 2\pi$ / THz	
TiEtO	2.070	5.689	2.444	0.950	7.152	1.171	0.411	8.011	0.978	
Ti[EtO] _n [BuO] _{4-n}	1.921	5.671	2.357	0.853	7.142	1.467	0.442	8.073	1.184	
TiBuO	0.1518	6.817	1.025	0.729	7.849	1.687	1.176	9.895	1.903	

* Gaussian (shaded entries) amplitudes are in units of $\times 10^{12}$

† σ for Gaussians (shaded entries), otherwise γ for Brownians.

Appendix G.1. Fitting parameter values for Ti[BuO]₄, Ti[EtO]₄, and Ti[BuO]_n[EtO]_{4-n}

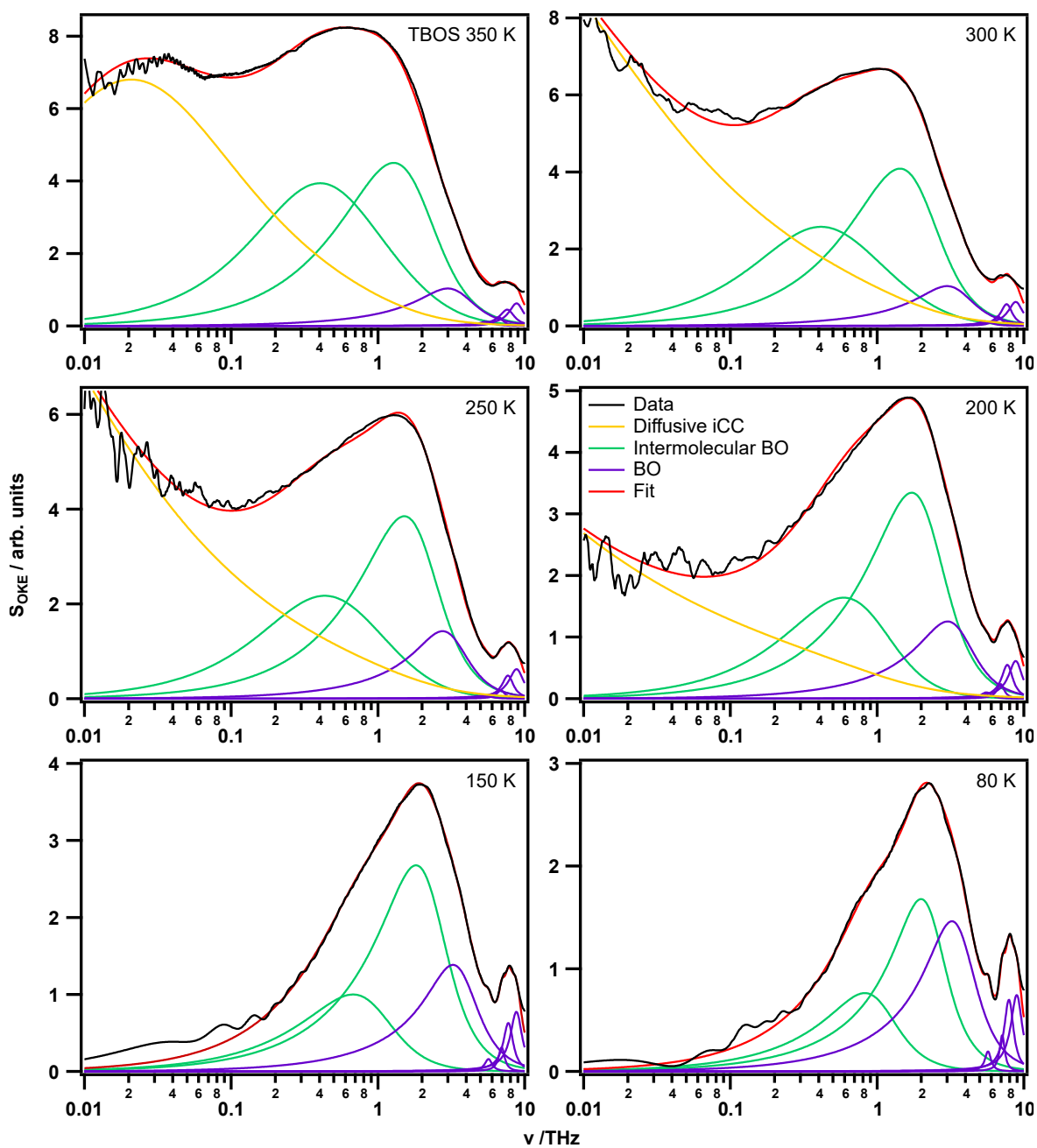
OKE spectra of these liquids were taken at room temperature.



Appendix G.2. OKE spectra of liquids Ti[BuO]₄, Ti[EtO]₄, and Ti[BuO]_n[EtO]_{4-n}

Spectra taken at room temperature. The mixture was made by mixing the two neat liquids in a 1:1 volume ratio.

H. TBOS Supplementary Data

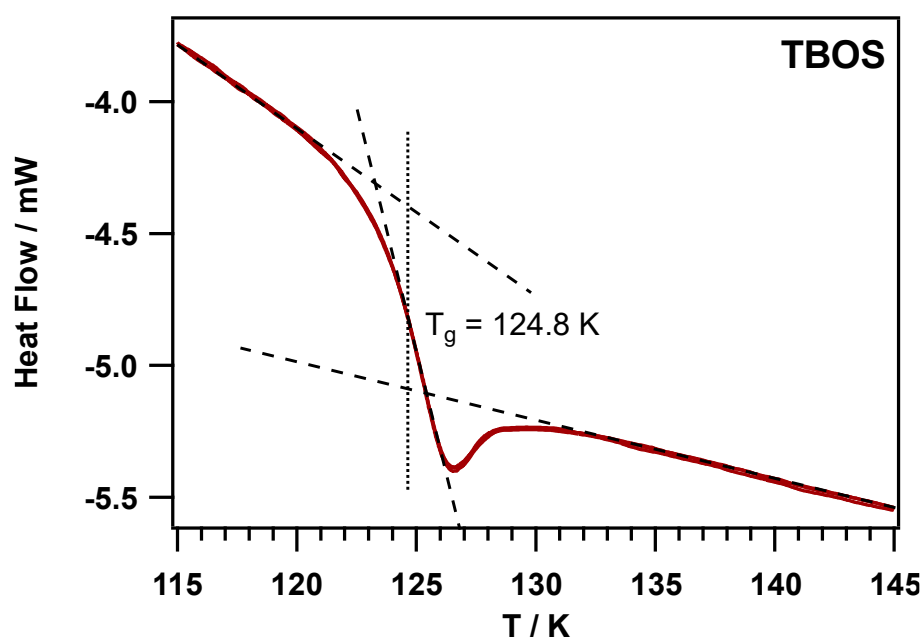


Appendix H.I. Line-shape fits for the TBOS OKE spectra shown on a logarithmic scale at various temperatures

Spectra taken from 300 K to 80 K (left to right), See legend for assignments; the high frequency shoulder mode (purple) is consistent with an intramolecular mode.

T /K	Translational diffusion				'Cluster' Fast- β			Fast- β		
	A_{icc}	τ / ps	$\gamma_{rise}/2\pi$ / THz	β_{CC}	A_B	$\omega_0/2\pi$ / THz	$\gamma/2\pi$ / THz	A_B	$\omega_0/2\pi$ / THz	$\gamma/2\pi$ / THz
350	0.211	7.635	1.876	0.730	0.441	1.102	3.310	0.392	1.876	3.114
300	0.543	125.9	2.012	0.506	0.287	1.097	3.229	0.341	2.012	3.110
250	0.756	975.2	2.056	0.422	0.233	0.986	2.531	0.304	2.056	3.079
200	1.000	3981	2.215	0.378	0.154	0.970	1.836	0.251	2.215	3.009
150	--	--	--	--	0.084	0.955	1.506	0.190	2.246	2.807
80	--	--	--	--	0.056	1.038	1.352	0.101	2.293	2.357

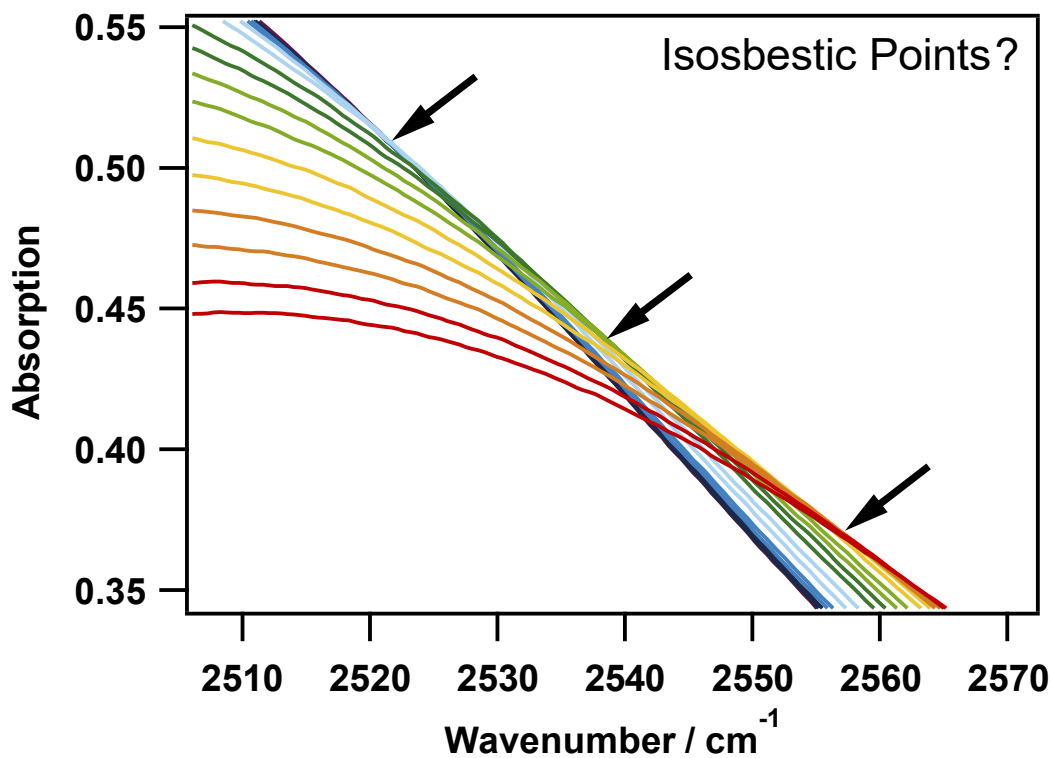
Appendix H.2. Fitting parameter values for the diffusive and two lowest frequency intermolecular modes of TBOS as a function of temperature



Appendix H.3. DSC measurements showing the glass transition in TBOS

Measurements taken by Dr. Ben Russell

I. Doped Lithium Chloride Solutions



Appendix I.I. Possible isosbestic points on the OD stretch mode of LiCl-SCN:7H₂O.

Spectra are taken over the temperature range of 253 to 93 K in 10 K intervals.

If one separates the temperature ramp into narrower ~50 K segments, multiple isosbestic points can be observed. It would make no physical sense to infer that this represents multiple transitions. Clearly care must be taken when making these links, especially for such subtle isosbestic points.